

**STUDIES ON COPPER - HYDROGEN BROMIDE (Cu-HBr) LASER  
AND ITS NONLINEAR FREQUENCY CONVERSION**

*By*

**RAMAKANTA BISWAL**

**PHYS03201004005**

**Raja Ramanna Centre for Advanced Technology, Indore**

*A thesis submitted to the*

*Board of Studies in Physical Sciences*

*In partial fulfillment of requirements*

*for the Degree of*

**DOCTOR OF PHILOSOPHY**

*of*

**HOMI BHABHA NATIONAL INSTITUTE**

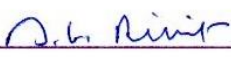
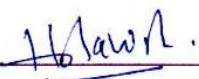
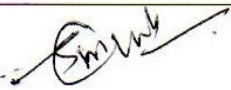
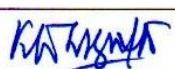
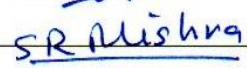
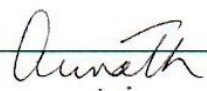


**May, 2015**

# Homi Bhabha National Institute

## Recommendations of the Viva Voce Committee

As members of the Viva Voce Committee, we certify that we have read the dissertation prepared by **Ramakanta Biswal** entitled "**Studies on Copper – Hydrogen Bromide (Cu-HBr) laser and its nonlinear frequency conversion**" and recommend that it may be accepted as fulfilling the thesis requirement for the award of Degree of Doctor of Philosophy.

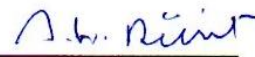
Chairman - Dr. S. M. Oak		16/10/2015
		Date
Guide/Convener - Dr. S. K. Dixit		16.10.2015
		Date
Member 1 - Dr. P. A. Naik		16/10/15
		Date
Member 2 - Dr. H. S. Rawat		16/10/2015
		Date
Member 3 - Dr. A. Chakrabarti		Date 16.10.15
Member 4 - Dr. S. M. Gupta		Date 16/10/15
Member 5 - Dr. K. Dasgupta		Date
Member 6 - Dr. S. R. Mishra		16-10-2015
		Date
External Examiner: Dr. A. K. Nath		Date 16.10.2015

Final approval and acceptance of this thesis is contingent upon the candidate's submission of the final copies of the thesis to HBNI.

I hereby certify that I have read this thesis prepared under my direction and recommend that it may be accepted as fulfilling the thesis requirement.

Date: 16<sup>th</sup> October, 2015

Place: RRCAT, Indore

Guide:   
(Dr. S. K. Dixit)

## **STATEMENT BY AUTHOR**

This dissertation has been submitted in partial fulfillment of requirements for an advanced degree at Homi Bhabha National Institute (HBNI) and is deposited in the library to be made available to borrowers under rules of the HBNI.

Brief quotations from this dissertation are allowable without special permission, provided that accurate acknowledgement of source is made. Requests for permission for extended quotation from or reproduction of this manuscript in whole or in part may be granted by the Competent Authority of HBNI when in his or her judgment the proposed use of the material is in the interests of scholarship. In all other instances, however, permission must be obtained from the author.

  
Ramakanta Biswal

## DECLARATION

I, hereby declare that the investigation presented in the thesis has been carried out by me. The work is original and has not been submitted earlier as a whole or in part for a degree / diploma at this or any other Institution / University.

  
Ramakanta Biswal

## List of Publications arising from the thesis

### Journal

1. “Studies on the generation of 1.5 W average power, 18 kHz repetition rate coherent mid-ultraviolet radiation at 271.2 nm”, **R. Biswal**, P. K. Agrawal, S. K. Dixit & S. V. Nakhe, *Applied Optics*, **2015** (In press: posted online on 15<sup>th</sup> October, 2015).
2. “Studies on the spatial, spectral and energy characteristics of Copper – Hydrogen Bromide laser radiations”, **R. Biswal**, P. K. Agrawal, O. Prakash, G. K. Mishra, S. K. Dixit & S. V. Nakhe, *IEEE Journal of Quantum Electronics*, **2014**, *50*(2), 112-119.
3. “Studies on the spectral purity of copper-hydrogen bromide laser radiations”, **R. Biswal**, G. K. Mishra, P. K. Agrawal, S. V. Nakhe & S. K. Dixit, *Applied Optics*, **2013**, *52*(14), 3269-3278.
4. “A study on the purification of hydrogen bromide gas by fractional distillation technique and its effect on improvement of copper-hydrogen bromide laser performance”, **R. Biswal**, P. K. Agrawal, S. K. Dixit & S. V. Nakhe, *Optical Engineering*, **2012**, *51*(11), art No.114203, 1-8.
5. “Analysis of pulsed discharge characteristics of solid state switch (IGBT) based 16 kHz repetition rate, 100 W average power Copper-HBr laser”, **R. Biswal**, P. K. Agrawal, G. K. Mishra, S. K. Dixit & S. V. Nakhe, *Journal of Russian Laser Research (Springer)*, **2012**, *33*(4), 319-335.
6. “A comparative study on thermal lensing characteristics of low (~500 °C) and high (~1500 °C) temperature variants of copper vapor laser”, **R. Biswal**, G. K. Mishra, G. S. Purbia, P. K. Agrawal, O. Prakash, S. K. Dixit and J. K. Mittal, *Optical Engineering*, **2011**, *50*(8), art. No. 084202, 1-8.

7. “Development of a 16 kHz repetition rate, 110 W average power Copper-HyBrID laser”  
**R. Biswal**, P. K. Agrawal, G. K. Mishra, S. V. Nakhe, S. K. Dixit & J. K. Mittal, *Pramana - Journal of Physics*, **2010**, 75(5), 953-959.

### Chapter in books and lecture notes

1. “Development of 15-27 kHz repetition rate, 30-60 W average power copper HyBrID laser”  
**R. Biswal**, P. K. Agrawal, S. V. Nakhe, S. K. Dixit and J. K. Mittal, *Laser and Bose Einstein Condensation Physics*, Manmohan et. al. eds., **2010**, 149-160 (Narosa).

### Conferences

1. “Development of 18 kHz repetition rate, watt level average power coherent UV sources at 255.3, 271.2 & 289.1 nm by frequency conversion of Cu-HBr laser radiations”, **R. Biswal**, P. K. Agrawal, G. K. Mishra, O. Prakash, S. K. Dixit & S. V. Nakhe, *Proc. DAE-BRNS National Laser Symposium*, RRCAT, Indore, Dec. 2-5, **2015** (Accepted).
2. “On the safety measures for hydrogen bromide gas in copper – hydrogen bromide (Cu-HBr) laser activity at RRCAT”, **R. Biswal**, S. Talwar, G. K. Mishra, S. K. Dixit & S. V. Nakhe, *32<sup>nd</sup> DAE Safety & Occupational Health Professionals Meet*, RRCAT, Indore, Oct. 5-7, **2015**, art. No. CP-06, CP-17-20.
3. “Studies on the green-yellow spectral distribution characteristics of a Copper-HBr laser”  
**R. Biswal**, P. K. Agrawal, O. Prakash, G. K. Mishra, S. K. Dixit & S. V. Nakhe, *Proc. DAE-BRNS National Laser Symposium*, Manipal University, Manipal, Jan. 8-11, **2014**, art No. CP-01-34.
4. “A real-time study on the spectral line-width characteristics of a Copper-HBr laser”, **R. Biswal**, G. K. Mishra, S. K. Agrawal, S. K. Dixit and S. V. Nakhe, *Proc. DAE-BRNS National Laser Symposium*, BARC, Mumbai, Feb. 6-9, **2013**, art No. CP-01-02.

5. “Development of a high specific average output power (70 W/l), high repetition rate (18 kHz) HBr additive based compact advanced copper laser”, **R. Biswal**, S. K. Agrawal, P. K. Agrawal, G. K. Mishra, S. K. Dixit and S. V. Nakhe, *Proc. DAE-BRNS National Laser Symposium*, CGC, Anna University, Chennai, Jan. 9-12, **2012**, 16-19.
6. “A comparative study on pulsed discharge characteristics of HBr additive based advanced and elemental copper vapour laser variants”, **R. Biswal**, P. K. Agrawal, O. Prakash, S. K. Dixit & S. V. Nakhe, *Proc. DAE-BRNS National Laser Symposium*, CGC, Anna University, Chennai, Jan. 9-12, **2012**, 12-15.
7. “A study on the pulsed discharge characteristics of a 100 W class advanced copper laser” **R. Biswal**, P. K. Agrawal, G. K. Mishra, S. K. Dixit and S. V. Nakhe, *Proc. DAE-BRNS National Laser Symposium*, CGC, Anna University, Chennai, Jan. 9-12, **2012**, 8-11.
8. “A comparative study on thermal lensing characteristics of a Copper-Hydrogen Bromide (Cu-HBr) laser and an elemental copper vapour laser”, **R. Biswal**, G. K. Mishra, G. S. Purbia, P. K. Agrawal, Om Prakash, S. K. Dixit and J. K. Mittal, *Proc. DAE-BRNS National Laser Symposium*, RRCAT, Indore, Dec.1-4, **2010**, art. No. CP-01-32.
9. “Development of 16 kHz repetition rate, 110 W average power Copper HyBrID laser” **R. Biswal**, P. K. Agrawal, G. K. Mishra, S. V. Nakhe, S. K. Dixit & J. K. Mittal, *Proc. DAE-BRNS National Laser Symp.*, BARC, Mumbai, Jan. 13-16, **2010**, art. No.: CP-01-26.
10. “Development of IGBT based high power (11 kW), high repetition rate (20 kHz) pulsed power supply for Copper HyBrID laser”, P. K. Agrawal, S. V. Nakhe, **R. Biswal** & J. K. Mittal, *Proc. DAE-BRNS National Laser Symposium*, BARC, Mumbai, Jan. 13-16, **2010**, art. No.: CP-01-06.

  
Signature of the student:

Date: 29/10/2015

## DEDICATIONS

*This thesis is dedicated to My Parents*

## ACKNOWLEDGEMENTS

It is a matter of great pleasure for me to express my gratitude to all those who have contributed, directly or indirectly, without whom the work would have been incomplete.

At the outset, I express my deep & sincere gratitude for my guide, *Dr. S. K. Dixit*, for his invaluable guidance, motivation, help & support in planning and shaping of the thesis.

I thank *Dr. P. D. Gupta*, Director, RRCAT for permitting me to pursue Ph. D. in HBNI. I thank all the members of the Doctoral committee (*Dr. S. M. Oak, Dr. P. A. Naik, Dr. K. Dasgupta, Dr. H. S. Rawat, Dr. A. Chakrabarti & Dr. S. M. Gupta*) as well as ex-members *Dr. S. K. Deb & Dr. G. S. Lodha*) for their valuable suggestions. I am very grateful to *Shri S. V. Nakhe*, Head, LSES, for his constant encouragement, motivation, help and overall support.

I am highly thankful to *Shri P. K. Agrawal* for development of electrical pulse power supplies for the Cu-HBr lasers. I acknowledge help & useful discussions with my senior colleague *Dr. Om Prakash*. I also thank *Shri G. K. Mishra* for experimental support. I am thankful to *Shri H. S. Vora* (senior colleague & present Head, LESD) for providing beam analysis software & many useful discussions. Useful discussions and helps from senior colleagues such as *Shri B. Singh* (present Head, LMPD), *Shri K. K. Sharangpani, Dr. R. Khare & Shri P. K. Shukla* are also duly acknowledged. I acknowledge helps & supports from glass blowing facility, laser workshop & optical workshop for fabrication of various components. I acknowledge helps from colleagues *S. Agrawal, R. K. Mishra, Jagdish Kumar, S. Talwar, U. Kumbhakar, R. Mahakud, Jitendra K. Madaan, Pankaj Kumar, Shailendra K. Singh* and all other members of this group for supporting in different ways in various stages of the work.

Special thanks are due to ex. Heads, LSED, *Dr. R. Bhatnagar* for initiation of the Cu-HBr laser activity, *Shri U. Nundy* for his keen interest & *Shri J. K. Mittal* for further guidance.

Last but not the least, I express my deep appreciation for my wife, *Reena* and kids, *Rinku* and *Rinki*, for their understanding, patience, whole-hearted support & co-operation.

# CONTENTS

	<b>Page No.</b>
<b>SYNOPSIS</b>	<b>1</b>
<b>LIST OF FIGURES</b>	<b>11</b>
<b>LIST OF TABLES</b>	<b>18</b>
<b>CHAPTER 1: REVIEW ON COPPER-HYDROGEN BROMIDE (Cu-HBr) LASER</b>	<b>19</b>
1.1 Introduction .....	19
1.2 Fundamentals of atomic copper laser .....	20
1.2.1 Energy levels & lasing transitions .....	20
1.2.2 Basic laser kinetics and performance limiting factors.....	21
1.2.2.1 Limitations due to high temperature (~1500 °C) operation.....	24
1.2.2.2 Limitation due to high pre-pulse electron density ( $n_{eo}$ ) .....	25
1.3 Additives in copper lasers – Emergence of Copper-HBr laser .....	26
1.3.1 High temperature copper laser .....	27
1.3.2 Low temperature copper laser .....	29
1.4 Physics and technology of Copper-HBr laser.....	32
1.4.1 Basic physical principles .....	32
1.4.1.1 Copper seeding mechanism.....	32
1.4.1.2 Lasing kinetics.....	34
1.4.1.3 Laser discharge characteristics.....	40
1.4.2 Engineering and technology .....	41
1.4.2.1 Laser design.....	42
1.4.2.2 Electrical excitation sources .....	44
1.4.2.3 Laser system performances.....	45
1.5 Current trends on technology and applications of copper lasers.....	48

## **CHAPTER 2: DEVELOPMENT AND STUDIES ON HIGH AVERAGE POWER**

	<b>(40 TO 110 W) Cu-HBr LASERS</b>	<b>51</b>
2.1	Introduction.....	51
2.2	Design & development of subsystems for Copper-HBrLs.....	51
2.2.1	Thermal design.....	51
2.2.2	Laser electrodes & discharge tubes.....	54
2.2.3	Precision gas mixing set up for HBr & Neon.....	55
2.2.4	High voltage electrical pulse power supply.....	56
2.2.5	Assembled Copper-HBr laser systems.....	59
2.3	Safety systems for HBr gas handling.....	61
2.4	The developed 40-110 W average power Copper-HBr lasers.....	63
2.5	Parametric studies for laser output power of the developed Cu-HBr lasers.....	65
2.5.1	Buffer gas pressure & flow rate.....	66
2.5.2	HBr concentration.....	68
2.5.3	Pulse repetition rate.....	70
2.5.4	Electrical input power (charging voltage).....	72
2.6	Scaling behaviour of the developed Cu-HBr lasers.....	73
2.7	Conclusions.....	75

## **CHAPTER 3: ANALYSIS OF ELECTRICAL PULSE PUMPING**

	<b>CHARACTERISTICS OF THE Cu-HBr LASERS</b>	<b>77</b>
3.1	Introduction.....	77
3.2	Theoretical background of the measurement and analysis.....	78
3.3	Electrical pulse pumping behaviour of Cu-HBrL.....	81
3.3.1	Time resolved characteristics.....	81

3.3.1.1	Measured laser head voltages and currents.....	81
3.3.1.2	Active discharge voltage.....	82
3.3.1.3	Active electrical input power & discharge resistance.....	84
3.3.2	Time averaged characteristics.....	85
3.3.2.1	Average discharge resistance & pre-pulse electron density.....	85
3.3.2.2	Average electrical power deposition in laser discharge.....	87
3.3.3	Role of other operating parameters.....	88
3.4	Pulse pumping behaviour with thyatron pulser.....	91
3.5	Comparison with the published results and further scope.....	94
3.6	Conclusions.....	95

## **CHAPTER 4: STUDIES ON HBr GAS PURIFICATION FOR PERFORMANCE**

	<b>ENHANCEMENT OF Cu-HBr LASER</b>	<b>97</b>
4.1	Introduction.....	97
4.2	The HBr gas purification by fractional distillation.....	98
4.2.1	Principle of purification process.....	98
4.2.2	Set up for HBr gas purification.....	99
4.2.3	Mass spectrometry of the HBr gases.....	100
4.3	Effect of purified HBr gas on the performance of Cu-HBr laser.....	103
4.3.1	Laser output performance.....	104
4.3.2	Laser discharge characteristics.....	105
4.3.3	Analysis and discussion.....	107
4.4	Conclusions.....	111

## **CHAPTER 5: STUDIES ON THERMAL LENSING BEHAVIOUR**

	<b>OF Cu-HBr LASER</b>	<b>113</b>
5.1	Introduction.....	113
5.2	Thermal lens and its measurement method.....	114
5.3	Experimental results on thermal lens power of Cu-HBrL and CVL.....	118
5.4	Analysis and discussion on thermal lens power.....	121
	5.4.1 Gas thermal lens.....	122
	5.4.2 Window thermal lens.....	124
	5.4.3 Combined thermal lens.....	127
5.5	Conclusions.....	128

## **CHAPTER 6: STUDIES ON SPECTRAL CHARACTERISTICS OF**

	<b>Cu-HBr LASER</b>	<b>129</b>
6.1	Introduction.....	129
6.2	Theory of spectral emission of a Cu-HBr laser.....	129
	6.2.1 Isotope shifts & hyperfine splitting.....	130
	6.2.2 Line broadening effects.....	132
6.3	Measurement of spectral characteristics of Cu-HBr laser lines.....	134
	6.3.1 Experimental arrangement and laser parameters.....	134
	6.3.2 Measurement principle.....	135
6.4	Experimental results and analysis on the spectral behaviour of Cu-HBr laser.....	136
	6.4.1 Parametric effects on spectral characteristics.....	136
	6.4.2 Analysis and discussion.....	139
6.5	Conclusions.....	146

## **CHAPTER 7: STUDIES ON THE BEAM DIVERGENCE AND POINTING**

<b>STABILITY OF Cu-HBr LASER</b>		<b>147</b>
7.1	Introduction.....	147
7.2	Measurement for Cu-HBr laser beam divergence & pointing stability.....	148
7.2.1	Set up for measurement.....	148
7.2.2	Principle of measurement and base data.....	150
7.3	Spatial beam quality behaviour of Cu-HBr laser with plane-plane resonator.....	152
7.3.1	Far-field beam divergence.....	152
7.3.2	Far-field beam pointing stability & intensity fluctuation.....	154
7.3.3	Radial and temporal intensity profiles.....	155
7.4	Spatial beam quality behaviour of Cu-HBr laser with confocal unstable resonators.....	158
7.4.1	Beam divergence & pointing stability behaviour.....	158
7.4.2	Radial and temporal intensity profiles.....	161
7.5	Analysis of observed beam quality behaviour of the Cu-HBr laser.....	162
7.5.1	Beam quality of Cu-HBrL vs. input power & HBr concentration.....	163
7.5.2	Beam quality of Cu-HBrL with plane-plane & unstable resonators.....	166
7.5.3	Far-field intensity variation.....	168
7.6	Conclusions.....	170

## **CHAPTER 8: REVIEW ON NONLINER FREQUENCY CONVERSION OF**

<b>COPPER LASERS</b>		<b>171</b>
8.1	Introduction.....	171
8.2	Basics of nonlinear frequency conversion.....	172
8.2.1	Nonlinear polarisation.....	172

8.2.2	Coupled wave equation.....	173
8.2.3	Second harmonic and sum frequency generation.....	174
8.2.4	Phase matching for SHG/SFG process.....	175
8.2.5	Beam walk-off.....	177
8.3	Issues in high average power high pulse repetition rate SHG/SFG.....	178
8.3.1	Effect of temperature.....	179
8.3.2	Effect of laser beam divergence and line-width.....	180
8.3.3	Pump beam depletion.....	182
8.4	Review of results on SHG & SFG of copper lasers.....	184
8.4.1	Nonlinear crystals.....	184
8.4.2	Pump focusing geometries – Spherical spot focusing & cylindrical line focusing.....	186
8.4.3	SHG & SFG at PRR ~5-10 kHz (conventional CVL).....	187
8.4.4	SHG & SFG at PRR ~10-20 kHz (Cu-HBrL, CuBrL & KE-CVL).....	190

## **CHAPTER 9: STUDIES ON SECOND HARMONIC AND SUM FREQUENCY**

### **GENERATION OF Cu-HBr LASER 193**

9.1	Introduction.....	193
9.2	Thermal considerations in SHG/SFG processes of a Cu-HBr laser.....	194
9.3	Set up for SHG/SFG of Cu-HBr laser.....	196
9.3.1	The experimental arrangement.....	196
9.3.2	Measurement techniques.....	197
9.4	Experimental results on SHG & SFG of Cu-HBr laser.....	198
9.4.1	Optimisation of focussing conditions.....	198
9.4.2	SHG of green radiation.....	201

9.4.3	SHG of yellow radiation.....	202
9.4.4	SFG of green & yellow radiations.....	203
9.5	Analysis of the result and discussion.....	204
9.5.1	Time averaged characteristics of SHG and SFG.....	204
9.5.2	Time resolved characteristics of SHG and SFG.....	209
9.6	Thermal effects on UV pulse train.....	212
9.7	Conclusions.....	216
<b>CHAPTER 10: SUMMARY AND FUTURE SCOPE</b>		<b>217</b>
10.1	Summary of the thesis.....	217
10.2	Scope for future work.....	224
<b>REFERENCES</b>		<b>227</b>

## LIST OF ABBREVIATIONS AND NOMENCLATURE USED

ADP	Ammonium Dihydrogen Phosphate (Nonlinear crystal)
ASE	Amplified Spontaneous Emission
BBO/ $\beta$ -BBO	Beta Barium Borate (Nonlinear crystal)
BSP	Beam Splitting cube Polariser
CCD	Charge Coupled Device (camera)
CLBO	Cesium Lithium Borate (Nonlinear crystal)
CT	Capacitor Transfer (storage-peaking capacitor arrangement)
CuBrL	Copper Bromide Laser
Cu-HBrL	Copper - Hydrogen Bromide Laser
Cu-HyBrID	Copper - Hydrogen Bromide In Discharge
CVL	Copper Vapour Laser
DA	Dissociative Attachment
DC	Direct Current
DCM	Dichroic Mirror
DKDP	Deuterated Potassium Dihydrogen Phosphate (Nonlinear crystal)
DL	Diffraction Limit
FBG	Fiber Bragg Grating
G	Green (510.6 nm radiation of copper laser)
GDFR	Generalised Diffraction Filtered Resonator (Optical)
HV	High Voltage
HyBrID	Hydrogen Bromide In Discharge
IC	Interacting circuit (electrical)
IGBT	Insulated Gate Bipolar Transistor

IP	Interacting peaking (electrical circuit)
IR	Infrared
KDP	Potassium Dihydrogen Phosphate (Nonlinear crystal)
KE-CVL	Kinetically Enhanced - Copper Vapour Laser
LBO	Lithium Borate (Nonlinear crystal)
LLL	Lower Laser Level
MA	Magnetic Assist
MOPA	Master Oscillator Power Amplifier
MOSFET	Metal Oxide Semiconductor Field Effect Transistor
MPC	Magnetic Pulse Compression
ND	Neutral Density
OSHA	Occupational Safety and Health Administration
OW	Optical Wedge
PBUR	Positive Branch Unstable Resonator (Optical)
PD	Photo Diode
PM	Power Meter (laser)
PPR	Plane-Plane Resonator (optical)
PRR	Pulse Repetition Rate
SCM	Scrapper Mirror
SFG	Sum Frequency Generation
SFUR	Self-Filtering Unstable Resonator
SHG	Second Harmonic Generation
SI	Saturable Inductor
SS	Stainless Steel
TLV	Threshold Limiting Value

TPA	Two Photon Absorption
ULL	Upper Laser Level
UR	Unstable Resonator (optical)
UV	Ultraviolet
Y	Yellow (578.2 nm radiation of copper laser)



# Homi Bhabha National Institute

Ph. D. PROGRAMME

<b>1. Name of the student</b>	<b>: Ramakanta Biswal</b>
<b>2. Name of the Constituent Institution</b>	<b>: Raja Ramanna Centre for Advanced Technology, Indore-452013</b>
<b>3. Enrolment Number</b>	<b>: PHYS03201004005</b>
<b>4. Title of the Thesis</b>	<b>: Studies on Copper - Hydrogen Bromide (Cu-HBr) laser and its nonlinear frequency conversion</b>
<b>5. Board of Studies</b>	<b>: Physical Sciences</b>

## SYNOPSIS

Copper - Hydrogen Bromide laser (Cu-HBrL), also known as Copper-HyBrID laser, is a low temperature ( $\sim 500$  °C) and an improved performance variant of the conventional high temperature ( $\sim 1500$  °C) copper vapour laser (CVL). A Cu-HBr laser is based on lasing transitions in copper atom. The additive HBr gas reacts with copper metal in the discharge tube to produce copper bromide molecules and their molecular complexes. These copper precursors subsequently dissociate under electron impact to provide copper atoms of necessary density for efficient lasing. The Cu-HBr lasers produce high pulse repetition rate (15-20 kHz), pulsed (40-50 ns), visible radiations (510.6 nm & 578.2 nm) of high average power (10-200 W), high electro-optic efficiency (2-3%) and high beam quality. The low temperature operation of a Cu-HBr laser has led to its compact & light-weight design and faster start-up/cool-down time (10-15 minutes) with ease of operation. With the improved laser characteristics and convenient design, a Cu-HBr laser scores favourably over the other well developed high temperature ( $\sim 1500$  °C) CVL and kinetically enhanced CVL (KE-CVL) as well as low temperature

(~500 °C) copper bromide laser (CuBrL). The Cu-HBrLs have enhanced the scope of applicability of atomic copper lasers in high pulse repetition rate (PRR) pumping of tunable visible-IR dye & Ti: Sapphire lasers for spectroscopic applications, in high PRR nonlinear frequency conversion for ultraviolet (UV: 255.3, 271.2 & 289.1 nm) generation for fast fabrication of photonic components such as fiber gratings as well as in high speed precision material processing and fast imaging. Presently, frequency doubled Q-switched solid-state lasers (Nd: YAG/Nd: YVO<sub>4</sub> laser: 532 nm, Yb: YAG laser: 515 nm) are emerging as compact and alternate high PRR visible laser sources. However, the features of high PRR Cu-HBrLs such as ease of average power scalability to 100s of watt in visible range without going through the route of nonlinear frequency doubling and capability to produce high quality laser beams are advantageous over the solid state lasers.

The technology development of Cu-HBr lasers involves the challenges associated with design/assembly of laser electrodes & discharge tubes, integration of gas & vacuum handling unit, handling & precision controlling of highly corrosive HBr gas, issues of material compatibilities, critical dependence of laser parameters on HBr concentration and issues related with high power & high PRR electrical excitation sources. Equally challenging is the frequency extension to the UV regime, by second harmonic and sum frequency generation at high PRR (~20 kHz) Cu-HBrLs. With these objectives in view, the present thesis is a dedicated research work on the technology development of high average power (upto ~110 W) and high PRR (16-18 kHz) Cu-HBrLs of different active volumes followed by its frequency extension to UV regions (watt level average power) through nonlinear frequency conversion. The core thesis works include detailed studies on the Cu-HBr laser system development, laser parameter studies with HBr concentration & electrical input power, analysis of electrical power deposition into laser medium, HBr gas purification for enhanced laser performance, evaluation of thermal lensing behaviour, studies on spatial & spectral beam quality characteristics for both the green

(510.6 nm) & yellow (578.2 nm) radiations with plane-plane & unstable optical resonators, generation of high quality laser beams and studies on wavelength extension to high the PRR coherent UV (255.3 - 289.1 nm) radiations of watt level average power through second harmonic and sum frequency conversions. The present thesis work has led to the successful technology development of Cu-HBrLs of various power levels, new research results into the field and efficient high PRR UV beam generation with high potential for utilization.

The overall thesis is organized into ten chapters as follows,

### **Chapter 1: Review on Copper-Hydrogen Bromide (Cu-HBr) laser**

The Cu-HBrL, first demonstrated by Livingstone et. al. in 1992, is an outcome of intense R & D efforts to improve the performance and design of conventional high temperature CVL, first reported by Walter et. al. in 1966. This chapter presents a comprehensive review on the R & D activities in the field of Cu-HBrLs. First, the lasing spectroscopy, kinetics and the associated performance limiting factors of conventional copper vapour laser are discussed. Next, the role of additives in the field of copper lasers leading to emergence of different variants particularly the low operating temperature, high PRR and high power Cu-HBrL, is brought out. The physics of Cu-HBrLs such as copper seeding mechanism, role of HBr in favourably affecting the plasma & laser kinetics, low temperature & high PRR operation, discharge characteristics, laser beam quality characteristics and power scaling behaviour are discussed in detail. The engineering and technology aspects of Cu-HBrLs such as laser design, high PRR electrical excitation sources and material compatibility issues are also presented. The review ends with the current status on the technology development, research and applications of copper-HBr / copper vapour lasers.

### **Chapter 2: Development and studies on high average power (40 to 110 W) Cu-HBr lasers**

A Cu-HBrL relies on successful development and integration of various subsystems followed by a systematic parametric optimization study. This chapter presents core of the thesis

works on the development of 40 to 110 W average power Cu-HBrLs. This study comprises of a detailed thermal design of the investigated Cu-HBr lasers, mechanical design of laser electrodes & discharge tubes vis-à-vis their material compatibility with HBr, design of precision gas mixing set up for HBr & Neon gases, design/development of high-PRR, high-voltage & fast-switching electrical excitation sources followed by their integration and parametric optimization of the laser output power. Thyatron and solid state IGBT (Insulated gate bipolar transistor) pulsers are employed for the electrical excitation. The parameters studied for the laser power optimization are electrical input power, PRR, buffer gas pressure & flow rate, HBr concentration and electrical storage/peaking capacitor ratios. These results on the different average output power (40, 70, 85 & 110 W) versions of developed Cu-HBrLs, differing mainly in their active volumes, are presented and discussed in detail. Overall, this chapter presents a comprehensive guideline for designing of Cu-HBrLs. These developed Cu-HBrLs have been utilized for carrying out further studies as presented in the subsequent chapters.

### **Chapter 3: Analysis of electrical pulse pumping characteristics of the Cu-HBr lasers**

This chapter presents both time-resolved & time-averaged analysis of the electrical pulse pumping characteristics of the developed Cu-HBrLs. This is carried out by numerical processing of the laser head voltage and current waveforms recorded for different laser operating parameters, laser active volumes, electrical excitation sources and active medium compositions. The processes controlling discharge/plasma parameters such as electrical inductance, electrical resistance, active laser head voltage, active electrical power, pre-pulse electron density & axial gas temperature are evaluated and a correlation is established with the observed Cu-HBrL performance. Average electrical power coupled to the laser discharge with various parametric conditions such as electrical input power, HBr concentration, buffer gas flow rate & pressure as well as PRR are evaluated and presented. Role of high voltage electrical

pulsed configuration with thyatron and IGBT switches are studied, analysed and presented. This is also supplemented with a comparative study on the electrical discharge characteristics of Cu-HBrL vs. CVL of identical tube geometry. The presented work has led to a technique for quick optimization of pulsed gas discharge lasers through on-line analysis of their head voltage-current waveforms, in addition to providing guide lines for efficient pumping.

#### **Chapter 4: Studies on HBr gas purification for performance enhancement of Cu-HBr laser**

The HBr gas purity is very important for optimized operation of a Cu-HBrL as it crucially controls the laser kinetics. Due to highly reactive nature, the HBr gas purity degrades during the overall process of its manufacturing, storage and handling. The generated impurities contaminate the laser discharge leading to degraded laser performance. In this perspective, this chapter presents the details of a purification process of HBr gas by fractional distillation and evaluation of the purified HBr gas in improving the developed Cu-HBr laser performance in a test set up. The principle of the purification technique, development of a suitable HBr gas purification set up and mass spectrometry analysis before/after the purification process are presented. The purified HBr gas is utilized for enhancement of the laser output power, followed by an analysis of its discharge characteristics, to understand the physical mechanism. Around 30% improvement in the laser output power of Cu-HBrL, has been demonstrated with purified HBr gas. The effects of the distilled HBr gas on the laser output power, efficiency and beam diameter are presented. The electrical discharge characteristics such as change in discharge impedance and electrical power coupled into the discharge are analysed for both the distilled/undistilled HBr gases. The underlying physics behind the improved laser performance with purified HBr gas is discussed. The presented work provided a guideline for the improved performance of a Cu-HBr laser.

## **Chapter 5: Studies on thermal lensing behaviour of Cu-HBr laser**

This chapter presents experimental studies and theoretical analysis on the thermal lensing characteristics of the developed Cu-HBrL using an interferometer technique. These results are also compared with that of a conventional CVL of identical discharge tube geometry and excitation conditions. The thermal lensing aspect of a Cu-HBrL is of crucial importance for applications requiring high beam quality laser output such as in nonlinear frequency conversion for UV generation. The chapter starts with a brief presentation on the theory of thermal lensing & its origin in a Cu-HBrL/CVL as well as the principle of its measurement and the associated experimental set-up. Next, the experimental results on thermal lens power due to contributions from both the gaseous medium & discharge sealing optical windows as well as separately that of optical windows are presented as a function of electrical input powers and gas mixture compositions. It is observed that the Cu-HBrL has much weaker thermal lens as compared to that in the CVL, out of which the contribution of the optical windows dominates over that of the gaseous active medium. A theoretical analysis on the gas thermal lens as well as the window thermal lens is presented taking into account the radial temperature distribution, thermal conductivity, temperature coefficient of the refractive indices of the media involved and the heat flux reaching the windows & its absorption. The analysis agrees well with the observed trends.

## **Chapter 6: Studies on spectral characteristics of Cu-HBr laser**

This chapter presents a detailed experimental study and the related theoretical analysis on the spectral emission characteristics of both the green (510.6 nm) and yellow (578.2 nm) radiations of the Cu-HBrL for different laser operating parameters. Knowledge of the spectral characteristics of a Cu-HBrL is essential while planning its utility for nonlinear frequency conversion to UV as carried out in this thesis. The chapter starts with a brief discussion on the theory of spectral emission/broadening characteristics copper laser radiations taking into

account isotope shift, hyperfine splitting and broadening effects (natural, resonance/self, Van der Waals, Doppler) associated with the energy levels of neutral copper atom. Details on the measurement technique, based on high precision Fizeau interferometer based wavelength meter and the underlying principle are presented. Experimental results on the Cu-HBr laser spectral emission characteristics, of both green and yellow radiation components, such as line-width, emission frequency & their stability for different electrical input powers, HBr concentrations & optical resonators (plane-plane & unstable), are presented in detail. A comprehensive theoretical analysis followed by simulation of the spectral line-shapes of both the radiations is carried out taking into account the relevant line broadening effects. The theoretical results, in conjunction with the temperature & laser gain distribution effects, agree well with the observed trends.

### **Chapter 7: Studies on beam divergence and pointing stability of Cu-HBr laser**

The laser beam divergence and pointing stability of Cu-HBr laser radiations are crucial parameters in applications requiring finely focused beams such as second-harmonic/sum-frequency UV generation as studied in the present thesis. With this perspective in view, this chapter presents a comprehensive study on these beam quality aspects of both the green and yellow radiations of the Cu-HBrL for different laser operating conditions. The chapter covers the basics and underlying principles of laser beam quality measurement. The experimental results on variation of far-field divergence and pointing stability with different electrical input powers, HBr concentrations and optical resonators (plane-plane & unstable) are presented in detail for both the radiation components of the developed Cu-HBrL. This experimental study is augmented with near-field spatial intensity profiles & temporal pulse shapes of both the radiations. The related analysis and discussion encompass the estimation of divergence for different resonators, role of spatio-temporal laser gain characteristics, thermally induced perturbations and effect of diffraction as well as spectral emission widths. The whole study

has culminated into generation of diffraction limited and highly stable Cu-HBrL beams as required for efficient UV generation through nonlinear optical conversion, as presented in chapter 9.

### **Chapter 8: Review on nonlinear frequency conversion of copper lasers**

This chapter reviews the works on the most commonly used nonlinear frequency conversion processes of the copper laser radiations, i.e., the second harmonic and sum frequency generation (SHG and SFG) leading to high repetition rate coherent UV (255.3, 271.2 & 289.1 nm) radiations. The fundamentals of SHG/SFG processes, relevant coupled wave equations and the phase matching conditions are presented. The criteria for choosing suitable nonlinear crystals for SHG/SFG based high repetition, high average power UV generation are presented taking into account the phase matching conditions, nonlinear coefficients, damage threshold, absorption at the involved optical frequencies, thermal effects, acceptance angle and beam walk-off effects. The experimental and theoretical works on the SHG/SFG processes of copper vapour laser which mostly carried out at PRR of 5-6 kHz are reviewed. The limited reported studies on the SHG of green radiations of 10-18 kHz PRR, as obtained from Cu-HBrLs, kinetically enhanced CVLs and CuBrL, are presented and discussed.

### **Chapter 9: Studies on second harmonic and sum-frequency generation of Cu-HBr laser**

This chapter presents detailed experimental studies and analysis on SHG of both the green (255.3 nm) and yellow (289.1 nm) radiations of the Cu-HBrL (PRR: 18 kHz) along with their SFG (271.2 nm) in critically phase matched, type-I  $\beta$ -BBO crystal. In order to prevent the crystal damage, the SHG/SFG study is limited to the fundamental beam average power of about 10 W. These nonlinear frequency conversion studies are performed for both for plane-plane and unstable resonator Cu-HBr laser of different beam quality. The spatial, temporal and spectral characteristics of the Cu-HBr laser radiations, relevant for the frequency conversion, have already been elaborated in chapters 5, 6 & 7. This chapter presents details of the

experimental set up as well as the results on optimization of SHG/SFG efficiency of the Cu-HBrL as a function of pump focusing conditions for different focusing geometry (spherical & cylindrical) & focal length of the focusing lens. Further, the experimental results on the UV average output power and conversion efficiency are presented with variation of fundamental beam optical power of the Cu-HBrL equipped with plane-plane and unstable resonators of different magnifications. Temporal variation of the SHG/SFG conversion coefficients and conversion efficiencies are evaluated from analysis based on optical pulses of the fundamental, depleted fundamental and generated UV beams. The SHG process is also studied with mechanically chopped fundamental beams and the results are analysed. The SHG/SFG average UV output powers of around 2 W, 1.5 W & 1 W are achieved at 255.3 nm, 271.2 nm & 289.1 nm respectively at 18 kHz PRR.

#### **Chapter 10: Summary and future scope**

This chapter is a summary of the works carried out in the present thesis on the technology development, experimental investigations and analysis on various aspects of Cu-HBr lasers and its nonlinear frequency conversion. The scope of future work, in the field, is also delineated.



## LIST OF FIGURES

<b>Figure No.</b>	<b>Title</b>	<b>Page No.</b>
Fig. 1.1	Energy level diagram of neutral copper atom showing the laser transitions	21
Fig. 1.2	Typical temporal variation of on-axis particle density in Cu-HBrL & CVL (a) Ground level copper density, (b) Electron density, (c) Upper laser level copper density and (d) Lower laser level copper density	38
Fig. 1.3	V, I & Laser pulses of Cu-HBrL (a) and CVL (b) at optimised condition	40
Fig. 2.1	Variation of estimated thickness of thermal insulation (a) and axial gas temperature (b) with electrical input power for Copper-HBr lasers of different tube dimensions	53
Fig. 2.2	In-house developed fused silica discharge tube for Cu-HBrL	55
Fig. 2.3	Developed Ne-HBr gas controlling set up (a) and halogen trap (b) used in Cu-HBrL	56
Fig. 2.4	Photographs of developed modulators based on (a) Thyatron and (b) IGBTs	58
Fig. 2.5	Schematic of the assembled Copper-HBr laser with (a) IGBT pulser and (b) Thyatron pulser	60
Fig. 2.6	Photographs of the assembled Copper-HBr laser systems	61
Fig. 2.7	Photographs of installed HBr sensor, oxygen monitor (a) & HBr alarm system (b)	62
Fig. 2.8	Photographs of the successfully developed high power Cu-HBrLs in operation (a) The Cu-HBrL 2 (70 W power) (b) The Cu-HBrL 4 (110 W power)	64

Fig. 2.9	Variation of Cu-HBrL power with buffer gas flow rate (a) and buffer gas pressure (b)	66
Fig. 2.10	Variation of output power with HBr concentration in Cu-HBrLs	68
Fig. 2.11	Variation of output power with pulse repetition rates in Cu-HBrLs	70
Fig. 2.12	Variation of output power (a) and efficiency based on input from storage capacitor (b) with $P_{in}$ for Cu-HBrLs	72
Fig. 3.1	(a) Cu-HBrL as simplified electrical circuit element (b) Typical laser head voltage & current pulses of Cu-HBr laser	78
Fig. 3.2	Typical discharge voltage & current waveforms recorded for copper lasers for (a) Cu-HBrL 1 at 42 W laser output power (optimised HBr concentration ~6%), (b) Cu-HBrL 2 at 110 W laser output power (optimised HBr concentration ~7%), (c) Cu-HBrL 2 with very low HBr concentration (~1%) with only greenish fluorescence, and (d) Conventional CVL (bore dia. 4.7 cm, length 150 cm, PRR 6.5 kHz, 33 W laser output power with thyatron pulser).	80
Fig. 3.3	Digitised electrical pulses of Cu-HBrL 4 for different $P_{in}$ : (a) Voltage and (b) Current	81
Fig. 3.4	Variation of discharge loop inductance (a) & active laser head voltage (b) of Cu-HBrL 4 with $P_{in}$	82
Fig. 3.5	Temporal variation of active electrical power (a) & discharge resistance (b) of Cu-HBrL 4 for different $P_{in}$	84
Fig. 3.6	Variation of average discharge resistance of Cu-HBrL 4 with $P_{in}$	86
Fig. 3.7	Variation of pre-pulse electron density of Cu-HBrL 4 with $P_{in}$	86
Fig. 3.8	Variation of (a) average electrical power transferred to the laser head, to the laser discharge & the active laser efficiency and (b) fractional	87

	electrical power transferred to the laser head, to the laser discharge & fractional power loss for Cu-HBrL 4 with $P_{in}$	
Fig. 3.9	Variation of transferred electrical power to the laser head ( $P_{head}$ ) & discharge ( $P_{dump}$ ) and average laser output power of Cu-HBrL 4 with (a) HBr concentration (b) buffer gas flow rate (c) buffer gas pressure and (d) pulse repetition rate	89
Fig. 3.10	Digitised recorded discharge voltage (a) & current (b) pulses for Cu-HBrL & CVL	92
Fig. 3.11	Temporal variation of active electrical power (a) and discharge resistance (b) of Cu-HBrL & CVL	93
Fig. 3.12	Radial intensity profiles (a) and laser power build up (b) in Cu-HBrL & CVL	94
Fig. 4.1	Schematic of the HBr gas purification set up used in Copper-HBr laser	99
Fig. 4.2	Quadrupole mass spectrum of (a) Distilled HBr gas (b) Undistilled HBr gas	101
Fig. 4.3	Variation of Cu-HBrL output power (a) and radial beam intensity profiles (b) with distilled and undistilled HBr gas	104
Fig. 4.4	Digitised version of the recorded laser head voltage (a) and current (b) waveforms of Cu-HBrL for distilled and undistilled HBr gas	105
Fig. 4.5	Temporal variation of deposited electrical powers (a) and discharge resistances (b) of Cu-HBrL for distilled and undistilled HBr gas	106
Fig. 5.1	Experimental set up for measuring thermal lens focal length of Cu-HBrL/CVL: (a) heated active medium & optical windows together and (b) only heated optical window	115

Fig. 5.2	Shear interferograms of combined thermal (active medium + windows) lens estimation at 0 kW - Cu-HBrL & CVL (a), at 2.7 kW - Cu-HBrL (b), at 4.6 kW - Cu-HBrL (c), at 2.7 kW – CVL (d), at 4.6 kW – CVL (e)	119
Fig. 5.3	Fringes due to window thermal lens of Cu-HBrL and CVL for different input powers: (a) Cu-HBrL and CVL for 0 kW, (b) Cu-HBrL for 4.6 kW and (c) CVL for 4.6 kW	120
Fig. 5.4	Variation of thermal lens power of Cu-HBrL and CVL with electrical input power	121
Fig. 5.5	Computed radial gas temperature profiles for Cu-HBrL and CVL (a) at equilibrium condition for electrical input of 4.6 kW and (b) immediately after the discharge is on	123
Fig. 5.6	Recorded shear fringes (a) Cold condition, no discharge (b) Cold condition, Cu-HBrL, discharge just on (c) Cold condition, CVL (no HBr) discharge just on.	124
Fig. 6.1	Hyperfine energy levels and transitions in copper atom relevant to Cu-HBrL	131
Fig. 6.2	The experimental set up for measurement of Cu-HBrL spectral characteristics	134
Fig. 6.3	Variation of laser output power of green and yellow component of Cu-HBr laser with (a) Electrical input power and (b) HBr concentration	135
Fig. 6.4	Typical wave meter traces recorded for Cu-HBrL radiations: (a) Green & (b) Yellow	137
Fig. 6.5	Variation on emission line-width and its fluctuation for green and yellow component of Cu-HBr laser with (a) Electrical input power and (b) HBr concentration	137

Fig. 6.6	Variation in fluctuation in transition frequencies of green and yellow line of Cu-HBrL with (a) Electrical input power and (b) HBr concentration	138
Fig. 6.7	Typical calculated spectral emission line shape with individual hyperfine components of Cu-HBr laser radiations for (a) Green line and (b) Yellow line	141
Fig. 6.8	The simulated convoluted line shapes of Cu-HBr laser emission at different average gas temperatures for (a) Green radiation and (b) Yellow radiation	142
Fig. 6.9	Variation of computed emission line-widths of green and yellow radiation of Cu-HBr laser with average gas temperature	143
Fig. 7.1	Schematic of the set up for studying the spatial & energy characteristics of Cu-HBrL	148
Fig. 7.2	Typical recorded composite pictures (horizontal stack, 512 pulses) of far-field spot for green and yellow component of Cu-HBr laser with PPR (a) and PBUR M=50 (b)	150
Fig. 7.3	Typical composite far-field intensity distributions (512 pulses) of green (a) and yellow (b) component of Cu-HBr laser with PPR	151
Fig. 7.4	Typical composite far-field intensity distributions (512 pulses) of green (a) and yellow (b) component of Cu-HBr laser with PBUR M=50	151
Fig. 7.5	Typical variations in single pulse far-field beam divergence of Cu-HBrL radiations with PPR: (a) Green and (b) Yellow	152
Fig. 7.6	Variation of $\langle\theta\rangle$ and $\Delta\theta$ of recorded 512 pulses of green and yellow component of Cu-HBrL with PPR for different (a) electrical input powers and (b) HBr concentrations	153

Fig. 7.7	Typical pulse to pulse variations in far-field beam pointing angle of Cu-HBrL radiations with PPR: (a) Green and (b) Yellow	154
Fig. 7.8	Typical pulse to pulse variations in far-field beam intensity fluctuations of Cu-HBrL radiations with PPR: (a) Green and (b) Yellow	154
Fig. 7.9	Variation of beam pointing instability ( $\delta$ ) and intensity fluctuations ( $\Delta I/I$ ) of green & yellow component of Cu-HBrL with (a) electrical input powers & (b) HBr concentrations	155
Fig. 7.10	Typical radial intensity profiles of green & yellow component of Cu-HBrL at 8 kW input power for (a) optimum HBr concentration (7%) and (b) low HBr concentration (5%)	156
Fig. 7.11	Temporal intensity profiles of green & yellow component of Cu-HBrL at 8 kW input power for optimum HBr concentration (a & b) and low HBr concentration (c & d)	156
Fig. 7.12	Variation of laser pulse width and laser beam diameter of Cu-HBr laser with (a) electrical input power and (b) HBr concentration	157
Fig. 7.13	Variation of single pulse far-field beam divergence, pointing angle & intensity for recorded 512 pulses of Cu-HBrL with PBUR M=50 : Green (a, c & e) and Yellow (b, d & f)	159
Fig. 7.14	Variation of the beam divergence & its fluctuation (a) and the pointing stability & intensity fluctuation (b) of Cu-HBrL radiations with different magnification of the PBURs	160
Fig. 7.15	Typical recorded intensity profiles of G & Y component of Cu-HBrL with PBUR (M=50): (a) radial profiles and (b) temporal profiles	161
Fig. 8.1	Index surfaces for type-I critically phase matched -ve uniaxial crystal	177
Fig. 8.2	Spatial beam walk-off in type-I critically phase matched	177

	-ve uniaxial crystal	
Fig. 8.3	Variation of $P_{2\omega}$ with deviation from phase matching temperature	180
Fig. 8.4	Variation of $P_{2\omega}$ with angular deviation from phase matching angle	180
Fig. 8.5	Variation of SHG and depleted-fundamental power with interaction length in a nonlinear crystal	183
Fig. 9.1	Schematic of the experimental set up for SHG of Cu-HBr laser (G component). For SHG of Y component, a suitable DCM is used. For SFG, a broadband plane mirror is used in place of DCM and $f_1$ & $f_2$ are achromatic lens pair of 10X demagnification.	196
Fig. 9.2	Photograph of the experimental set up for SHG of Cu-HBr laser	196
Fig. 9.3	Spectrum of SHG & SFG radiations of Cu-HBr laser (a) SHG of green (b) SHG of yellow & (c) SFG of green & yellow	198
Fig. 9.4	Variation of SHG UV power (a) & conversion eff. (b) of green component of Cu-HBrL with focal length of focusing cylindrical lens for PPR and PBURs $M=12.5, 50$ & $100$	199
Fig. 9.5	Variation of SFG UV output power (a) & conv. efficiency (b) of Cu-HBrL with focal length of the pump focusing cylindrical lens for PPR and PBURs $M=12.5, 50$ & $100$	200
Fig. 9.6	Variation of SHG UV output power [ $P_{2\omega}(g)$ ] (a) and conversion efficiency [ $\eta_{2\omega}(g)$ ] (b), with fundamental green input power [ $P_{\omega}(g)$ ] for PPR and PBURs $M = 12.5, 50$ & $100$	201
Fig. 9.7	Variation of SHG UV output power [ $P_{2\omega}(y)$ ] (a) & conversion efficiency [ $\eta_{2\omega}(y)$ ] (b), with fundamental green input power [ $P_{\omega}(y)$ ] for PPR and PBURs $M = 12.5, 50$ & $100$	202
Fig. 9.8	Variation of SFG UV output power [ $P_{\omega 3}$ ] (a) and conversion	203

efficiency [ $\eta_{\omega_3}$ ] (b) with fundamental input power [ $P_{\omega}(g) + P_{\omega}(y)$ ]  
for PPR and PBURs  $M = 12.5, 50 \text{ \& } 100$

Fig. 9.9	Variation of SHG/SFG UV conversion coefficients with fundamental input powers for PPR and PBURs $M=12.5, 50 \text{ \& } 100$ : (a) SHG of green and (b) SFG of green & yellow	208
Fig. 9.10	Variation of instantaneous pump power & UV output power and UV conv. eff. & conv. coefficients for Cu-HBrL with PBUR $M=50$ : (A) SHG of green (a, b), (B) SHG of yellow (c, d) and (C) SFG of green & yellow	210
Fig. 9.11	Schematic of the SHG with chopped beam (a) and fundamental green & generated SHG UV pulse trains at 4 W (b: 0 Hz), (c: 10 Hz), (d: 100 Hz), (e: 500 Hz) & 7 W (f: 500 Hz)	214

### LIST OF TABLES

Table No.	Title	Page No.
Table 2.1	General features of the developed 40 to 110 W output power Cu-HBrLs	63
Table 2.2	Optimised parameters of the developed 40 to 110 W output power Cu-HBrLs	63
Table 4.1	Vapour pressure of HBr & Br <sub>2</sub> and their ratios at different temperatures	99
Table 6.1	Frequency shifts and relative intensities of the hyperfine components of Cu-HBrL lines based on transitions in natural copper atom	132

# Chapter 1

## Review on Copper - Hydrogen Bromide (Cu-HBr) laser

### 1.1 Introduction

Copper-Hydrogen Bromide laser (Cu-HBrL), also known as Copper-HyBrID laser, is a low temperature ( $\sim 500$  °C) and an improved performance variant of conventional high temperature ( $\sim 1500$  °C) copper vapour laser (CVL). A Cu-HBr laser is based on lasing transitions in neutral copper atom. The Cu-HBrL, first demonstrated by Livingstone et. al. in 1992 [1], is an outcome of intense R & D efforts to improve the performance and design of the conventional high temperature CVL, first reported by Walter et. al. in 1966 [2, 3]. In a Cu-HBrL, the additive HBr gas reacts with hot copper metal, in the discharge tube, to produce copper bromide molecules and their molecular complexes. These copper precursors subsequently dissociate under electron impact to provide copper atoms of necessary density for efficient lasing. The Cu-HBr lasers produce high pulse repetition rate (15-20 kHz), pulsed (50-60 ns), visible radiations (510.6 nm & 578.2 nm) of high average power (10-200 W), high electro-optic efficiency (2-3%) and high beam quality [1, 4-13]. The low temperature operation of a Cu-HBrL leads to its compact & light-weight design and faster start-up/cool-down time (10-15 minutes) with ease of operation [1, 4, 7, 14]. With improved laser characteristics and convenient design, a Cu-HBr laser scores favourably over the other well developed high temperature ( $\sim 1500$  °C) CVL and kinetically enhanced CVL (KE-CVL) as well as over low temperature ( $\sim 500$  °C) copper bromide laser (CuBrL) [15]. The Cu-HBrLs enhance the scope of applicability of copper lasers in high pulse repetition rate (PRR) pumping of tunable visible-IR dye & Ti:Sapphire lasers for spectroscopic applications, in high PRR nonlinear frequency conversion for ultraviolet (UV: 255.3, 271.2 & 289.1 nm) generation for fast fabrication of photonic components, in high speed precision material processing and fast imaging [15-31].

This chapter presents a comprehensive review on the R & D activities in the field of Cu-HBr lasers. The review begins with lasing spectroscopy, kinetics and associated performance limiting factors of conventional CVL. Next, the role of additives in the field of copper lasers leading to emergence of different variants particularly, the low temperature, high PRR and high power Cu-HBrL, is brought out. The physics of the Cu-HBrLs such as the copper seeding mechanism, role of HBr in favourably affecting the plasma & laser kinetics, low temperature & high PRR operation, discharge characteristics, laser beam quality issues, power scaling behaviour and the performance limiting factors are discussed. The engineering and technology aspects of the Cu-HBrLs such as the laser design & high PRR electrical excitation sources and material compatibility issues are also discussed. The review ends with the current status on technology development, research and applications of Cu-HBr/copper-vapour lasers.

## 1.2 Fundamentals of atomic copper laser

### 1.2.1 Energy levels and the lasing transitions

Fig. 1.1 shows the simplified energy level diagram of copper atom with its important lasing transitions. The copper laser is a three level laser system with self-terminating lasing action. It involves primarily the ground state, first excited state (as lower laser level: LLL) and second excited state (as upper laser level: ULL). The electronic configuration of the ground state, first excited state as well as second excited state of copper atom with term values ( $^{2S+1}L_J$ , L: total orbital angular momentum, S: total spin angular momentum and J: total angular momentum) are  $4s^1 3d^{10}$  ( $^2S$ ),  $4s^2 3d^9$  ( $^2D$ ) and  $3d^{10} 4p^1$  ( $^2P$ ) respectively. The fine structure energy levels are represented as  $^2S_{1/2}$  (ground level),  $^2D_{3/2}$  &  $^2D_{5/2}$  (LLLs) and  $^2P_{3/2}$  &  $^2P_{1/2}$  (ULLs). From the ground level, the LLLs are situated at 1.39 eV ( $^2D_{5/2}$ ) & 1.64 eV ( $^2D_{3/2}$ ) and the ULLs are situated at 3.79 eV ( $^2P_{1/2}$ ) & 3.82 eV ( $^2P_{3/2}$ ) [3].

The  $^2P$  levels are resonantly coupled to the ground level ( $^2S_{1/2}$ ) with high excitation cross sections i.e.  $9.7 \times 10^{-16} \text{ cm}^2$  for  $^2S_{1/2} \rightarrow ^2P_{3/2}$  &  $4.5 \times 10^{-16} \text{ cm}^2$  for  $^2S_{1/2} \rightarrow ^2P_{1/2}$ , hence

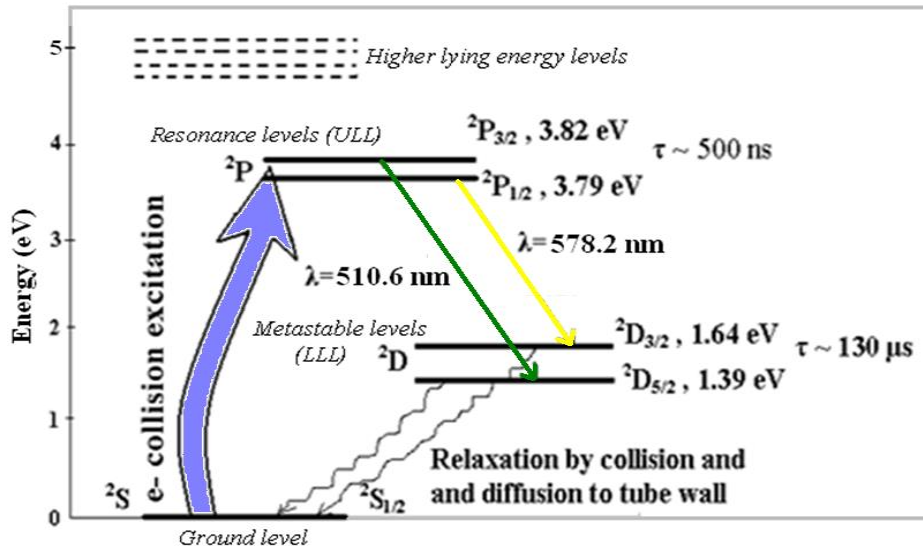


Fig. 1.1 Energy level diagram of neutral copper atom showing the laser transitions

subjected to strong radiation trapping [3]. The transitions between  ${}^2D$  and  ${}^2S_{1/2}$  levels are electrical dipole forbidden. In an isolated copper atom, the life times of the ULLs with respect to ground level are  $\sim 10$  ns [32]. However, in the active medium when the ground level copper atom density is high ( $\geq 10^{13}$   $\text{cm}^{-3}$ ), radiation trapping occurs and the life time of the ULLs w. r. t. the ground state increases to 12-13 ms, due to resonance absorption of  ${}^2P \rightarrow {}^2S$  transitions (324.8 & 327.4 nm) [32]. On the other hand, the life times of the ULLs w. r. t. the LLLs are  $\sim 500$  ns whereas the life times of the LLLs w. r. t. the ground level is  $\sim 130$   $\mu\text{s}$ . The electric dipole transition selection rules (i.e.  $\Delta L = \pm 1$  &  $\Delta J = 0, \pm 1$ ) allow only three optical transitions between  ${}^2P$  &  ${}^2D$  levels i.e.  ${}^2P_{3/2} \rightarrow {}^2D_{5/2}$  (510.6 nm),  ${}^2P_{1/2} \rightarrow {}^2D_{3/2}$  (578.2 nm) and  ${}^2P_{3/2} \rightarrow {}^2D_{3/2}$  (570 nm). The ratios of corresponding emission oscillator-strengths and intensities are 0.0051:0.0042:0.0012 and 9:5:1 respectively; hence the gain competition restricts the laser oscillations to 510.6 nm and 578.2 nm [15, 32]. The laser oscillation at 570 nm can be obtained by restricting the gain at the other two wavelengths [32], however it is not an attractive option.

### 1.2.2 Basic laser kinetics and performance limiting factors

In a copper laser, the copper atoms are pumped by fast ( $< 100$  ns rise time) discharge current pulses at high PRR in the inert/buffer (Neon) gaseous medium. The required ground

state copper atom density ( $n_{\text{Cu}} \sim 10^{15} \text{ cm}^{-3}$ ), for the efficient lasing, is produced through self-discharge heating & vaporization of copper metals at temperature of  $\sim 1500 \text{ }^\circ\text{C}$  [2]. In the rising part of high voltage excitation pulse, the ULLs ( $\text{Cu}^r$ ) are populated preferentially over the LLLs ( $\text{Cu}^m$ ) by direct electron impacts/collisions due to favourable average electron-temperature ( $T_e$ ) of 4-5 eV. The laser oscillation continues as long as the population inversion exists [2]. However, due to long life time of LLLs as compared to ULLs, bottlenecking of the population occurs. The population inversion between the laser levels [i.e.  $\Delta N = N_u - (g_u/g_l) N_l$ , where  $g_u$  &  $g_l$  are the level degeneracy factors and  $N_u$  &  $N_l$  are the population densities of the ULL & LLL respectively] reduces to zero shortly ( $< 100 \text{ ns}$ ) and then afterwards to negative values, thus making the laser self-terminating [2]. The ground state copper population is replenished by plasma relaxation during the inter-pulse period ( $\sim 100 \text{ } \mu\text{s}$ ), so as to start a new lasing cycle for the subsequent excitation pulse. The maximum PRR of the laser is decided by cumulative effects of recovery of ground state copper density & electron-ion ( $\text{e-Cu}^+$ ) neutralisation and the effective reduction of the pre-pulse electron density [15].

During the excitation and inter-pulse periods, the laser level populations deplete and recover through different processes, as evidenced by a number of theoretical and experimental studies [33-40]. The population densities in the ULL ( $N_u$ ) are proportional to the ground state copper density ( $n_{\text{Cu}}$ ). The  $N_u$  value is also proportional to the ratio of ground - ULL ( $\text{e} + \text{Cu} \rightarrow \text{e} + \text{Cu}^r$ ) excitation rate to ground - higher levels excitation/ionization ( $\text{e} + \text{Cu} \rightarrow \text{e} + \text{Cu}^{**}$  and  $\text{e} + \text{Cu} \rightarrow \text{e} + \text{e} + \text{Cu}^+$ ) rate. Here,  $\text{Cu}$ ,  $\text{Cu}^{**}$  and  $\text{Cu}^+$  refer to ground, higher lying levels above ULL and ionized state of the copper atom. With the onset of the excitation pulse, the  $N_u$  value starts to increase during first 10s of ns, attains a peak value and then starts falling. The fall in  $N_u$  is due to depletion of copper atoms through higher state excitation to both  $\text{Cu}^{**}$  &  $\text{Cu}^+$ , directly from ground state ( $\text{Cu}$ ) as well as resonance level ( $\text{Cu}^r$ ) and also due to the fall in  $T_e$ . During inter-pulse period,  $N_u$  relaxes almost completely due to super elastic collisions with

surrounding species ( $\text{Cu}^r + e \rightarrow e + \text{Cu}/\text{Cu}^m$ ) and radiation ( $\text{Cu}^r \rightarrow \text{Cu}/\text{Cu}^m + hc/\lambda$ ), with typical time scale of  $\sim 1 \mu\text{s}$  [36]. The populations of the LLLs decay principally by super elastic collisions with electrons ( $\text{Cu}^m + e \rightarrow \text{Cu} + e$ ), heavy body collisions with Ne/Cu ( $\text{Cu}^m + \text{Ne}/\text{Cu} \rightarrow \text{Cu} + \text{Ne}/\text{Cu}$ ) and diffusion to the discharge tube wall ( $\text{Cu}^m \rightarrow \text{Cu}$ ). The estimated time constants for the electron collision deactivation are  $\sim 5\text{-}10 \mu\text{s}$  (initial fast decay) and  $\sim 100 \mu\text{s}$  (slow decay later) whereas that of the heavy body collisions and diffusion processes are in the range of 5-10 ms [37, 38]. The rate constant of the dominant LLL relaxation mechanism (electron-atom super-elastic collision) is a function of electron density ( $n_e$ ) &  $T_e$  and inter-pulse period [34]. After the excitation pulse is over, the ground level population recovers through process of relaxation of LLLs, radiative & collisional decay of ULLs, three body collision induced electron-ion recombination followed by radiation & step wise collision decay ( $e + e + \text{Cu}^+ \rightarrow e + \text{Cu}^{**} \rightarrow e + \text{Cu}^*/\text{Cu} + hc/\lambda$ ) and diffusion of neutral copper atoms from wall to the tube axis. These laser kinetic processes crucially depend on the electron temperature, gas temperature and inter-pulse time which are again the function of laser operating parameters such as discharge voltage, electrical input power, discharge capacitance, PRR, buffer gas pressure etc. which also vary across the radial positions of the discharge tube [34, 35]. These parameters dictate the optical output power from a CVL.

The average output power of an atomic copper laser is given by,

$$P_{out} = E_o \cdot V \cdot f = \eta \cdot E_i \cdot V \cdot f \quad (1.1)$$

where  $E_i/E_o$  = specific input/output pulse energy,  $V$  = laser active volume ( $= \pi D^2 l/4$ :  $D$  = discharge tube bore diameter,  $l$  = discharge tube length),  $f$  = PRR and  $\eta$  = electro-optic conversion efficiency. For conventional copper lasers, the tube length scaling is usually limited to 100 – 150 cm owing to technological constraints in attaining uniform pulsed high electric field over the entire length as well as requirement of finite number of cavity round trips for high quality laser output within the short gain duration [15, 16]. On the other hand, the tube bore

diameter as well as the PRR is limited to ~3-5 cm and 5-6 kHz respectively, owing to increased spatio-temporal inhomogeneity of the applied electric field due to plasma skin-effect and increased gas heating effects, detrimental for efficient high quality laser output [34, 35, 41, 42]. The choice on specific output energy is limited by the discharge-excitation/laser-conversion efficiency (~1%) and maximum copper density employable ( $\sim 10^{15} \text{ cm}^{-3}$ ). This is further constrained by the requirement of fast-rise time, high voltage pulses as well as choice of discharge tube materials for high temperature operation. In order to understand the underlying limiting processes, a number of studies comprising of sophisticated computer simulation and rigorous experiments involving measurement of spatially & temporally resolved copper population densities, electron densities as well as comparing the laser performance with various trace gas additives have been carried out [33-42]. Based on these studies, the limiting performance of the conventional CVL has been attributed mainly to two factors – high temperature and high pre-pulse electron density in the gas-discharge plasma.

#### ***1.2.2.1 Limitation due to high temperature (~1500 °C) operation***

In conventional CVL, the laser copper atoms are produced by discharge heating and vapourisation of copper metals placed inside the discharge tube. Copper has melting point of 1083 °C. The demand of typical copper atom density ( $n_{\text{Cu}}$ ) of  $\sim 10^{15} \text{ cm}^{-3}$ , for optimum laser operation, requires the discharge tube temperature of ~1500 °C. Such high temperature operation places severe constraints on the laser design and performance. First, the laser start up time as well as the cool down time (after shut down) of the laser is of the order of an hour. Second, such high temperature operation causes complex engineering problems in terms of laser design and operation. Third, due to the high operating temperature, the axial gas temperature rises to ~3000 - 4000 °C [43, 44]. This adversely affects the inter-pulse recovery of the ground state copper atom density by preventing deactivation of the copper meta-stable levels as well as slowing down the electron-ion recombination process. This is because the

higher gas temperature slows down the relaxation of the  $T_e$  in the inter-pulse period and the electron-ion recombination process is very sensitive to  $T_e$  ( $\propto T_e^{-9/2}$ ) [34]. Therefore, incomplete relaxation of the CVL gas-discharge plasma results in significant depletion of the ground state copper density to meta-stable and ionization state. Studies indicate that about 10% of copper atoms are locked as ions due to inefficient recombination process alone, whereas typical LLL population of  $\sim 2.5\%$  is detrimental for the laser oscillation [15-17, 37]. The fractional remnant ionization is higher at the tube axis and increases as the PRR increases, which also lead to inefficient spatio-temporal coupling of the electrical energy to the CVL discharge plasma. So, the CVL performance is closely related to the gas temperature which affects the pre-pulse copper densities (in ground, meta-stable & ionization state), inter-pulse electron-ion recombination rate and impedance matching between the discharge tube & excitation circuit [15-17]. The high temperature operation of a CVL also adversely affects the laser beam quality. The high temperature leads to enhanced thermal lensing & optical aberration in the wavefront passing through the gain medium thereby increasing far-field divergence and pointing instability as well as annular near-field radial intensity profile with a central minimum [9, 45-52]. These beam quality attributes are not suited for many applications. Hence, it would be beneficial if the operating temperature of a copper laser is reduced.

### ***1.2.2.2 Limitation due to high pre-pulse electron density ( $n_{eo}$ )***

Electron density has crucial roles in deciding the performance of the pulsed gas discharge of copper lasers. The peak electron density and their energy spread decide the efficiency of ULL pumping. The pre-pulse electron density,  $n_{eo}$ , as well as its temperature (electron energy),  $T_e$ , decides the coupling of electrical energy into the CVL plasma and copper meta-stable relaxation rate, hence performance of CVL [34-37, 52-57]. Due to multi-kHz PRR operation, a significant residual electron density ( $n_{eo} \sim 10^{13} \text{ cm}^{-3}$ ,  $\sim 30\%$  of peak value) exists prior to the next electrical excitation pulse [36, 54]. This causes several detrimental effects on

the CVL performance. First, the optimized CVL operation is limited to a narrow range of PRR of about 4 to 8 kHz due to significant conductivity of pre-pulse CVL plasma. This is due to the fact that after a lasing pulse, the next electrical excitation pulse can only be applied after the plasma conductivity has decayed substantially. This limitation affects the laser power. Second, high electron density causes inhomogeneous spatio-temporal electrical power deposition in the CVL gain medium due to plasma skin effect [34, 35, 41, 56, 57], thereby affecting the laser intensity profile and beam quality. Third, significant  $n_{e0}$  value leads to improper impedance matching between the electrical power supply and the laser head. As a result, all the electrical energy at the source is not coupled to the laser active medium and part of it gets reflected back. So, considerable energy is wasted due to continuation of excitation pulse beyond the laser gain duration. This prevents the effective cooling of inter-pulse electrons and copper meta-stable relaxation, thereby affecting laser efficiency. Therefore, to improve the CVL performance, both the pre-pulse  $T_e$  &  $n_{e0}$  have to be reduced to a reasonable value.

### **1.3 Additives in copper laser - Emergence of Copper-HBr laser**

In the previous section, the high values of operating temperature, pre-pulse electron temperature and density are recognized to be performance limiting factors of a CVL. The most effective and practical way for lowering the CVL operating temperature was to use copper compounds of low vapourisation/sublimation temperature. It was also feasible to reduce pre-pulse electron density by using trace gas additive of high electron affinity. Another possibility was the use of additives which efficiently populate the ULLs and/or depopulates the LLLs due to matching energy levels with copper atom. At the same time, the additives should not absorb the laser radiations, should have negligible effect on the electron energy distribution in the discharge and should have high thermal conductivity to mitigate temperature issues. Based on these overall considerations, an intense R & D activity, in the field of additives with copper lasers, have been pursued to improve their performance. Several class of additives such as

hydrogen/halogens/hydrogen-halides ( $H_2$ ,  $Br_2$ ,  $Cl_2$ ,  $HBr$ ,  $HCl$ ,  $HI$ ) [15, 58-65], metallic vapours (Ag, Cs, Sc, Ni, Zn, Eu) [15, 66-72] as well as direct use of highly volatile copper compounds ( $CuBr$ ,  $CuCl$ ,  $CuI$  etc.) [15-17] have been studied to improve the copper laser performance. The halogen/hydrogen-halide additives improve the laser performance by altering the laser electrical characteristics (by reducing  $n_{eo}$ ) which favour the pumping mechanism and hence the population inversion. Hydrogen reduces inter-pulse  $T_e$ ,  $n_{eo}$  & peak gas temperature due to its high elastic collision cross section with electrons as well as due to high thermal conductivity [15, 59]. Copper halides act as low temperature source for copper atom whereas the halides/hydrogen-halides are effective for reducing  $n_{eo}$  due to their high electron affinity [15-17]. The metallic vapours additives control the population inversion by directly providing route(s) of additional excitation/de-excitation pathways for the laser levels; which act directly on the copper laser energy levels through the process of energy transfer collision. The metallic vapour additives such as Ag & Cs were reported to improve the laser performance by ~30% (57 to 76 W), owing to their closely matching energy levels with that of copper [66]. However, this approach (metallic vapour additives) was not very successful. Therefore, most of the copper laser technology development programs have been limited to the other two approaches. As a result, the copper lasers broadly work in two temperature regimes, depending on the choice of copper seeding mechanism and additives, (1) High temperature copper lasers (operating temperature ~1500 °C) e.g. conventional CVL & KE-CVL and, (2) Low temperature copper lasers (operating temperature ~500 °C) e.g.  $CuBrL$  &  $Cu-HBrL$ .

### ***1.3.1 High temperature copper laser***

Walter et. al. at TRG Inc. USA, in 1966, first reported pulsed lasing action in copper with He as buffer gas [2, 3]. This was based on an externally heated (~1500 °C) alumina discharge tube (1 cm bore & 80 cm long) giving average power only 20 mW at 660 Hz PRR & ~0.1% efficiency. Next major result, in the field, was reporting of self-heating action of

discharge tube in the electric discharge by Isaev et. al. in 1972, who demonstrated 15 W average output power at 15-18 kHz PRR from a 1.5 cm bore & 70 cm long alumina tube with efficiency of ~1% [73]. In the beginning, the efficient CVLs were limited to discharge tube of few mm bore diameter with He as buffer gas to promote deactivation of the LLLs through diffusion and subsequent collision with the discharge tube wall. Volume deactivation of metastable population by the discharge species in neon (Ne) as buffer gas, demonstrated by Bokhan et. al. in 1978 [74], opened up prospects for large bore (several cm bore diameter) CVLs. With improved electrical pulse power technology (high power solid-state switch and magnetic pulse compression based modulators) and laser design, output powers in excess of 100 W (110 W) were obtained from 8 cm bore, 122 cm long tube [75]. In parallel, an alternative and convenient way of average power scaling of CVLs with high quality laser output was reported by Anderson et. al. in 1975, through master oscillator power amplifier (MOPA) configuration [76]. A CVL MOPA system of 200 W average power were developed in Lawrence Livermore National Laboratory (LLNL), USA, in 1984, which were increased to 300 W, in 1985, using magnetic pulse compression (MPC) based modulators [77]; a total average power of 2 kW was generated from the installed CVL systems [78].

In 1980, Bokhan et. al. added H<sub>2</sub> in CVLs and demonstrated 20 to 67% increase in CVL output power in small-medium bore CVL of diameter 2.7 cm and 4 cm respectively with concurrent increase in optimum PRR and spatio-temporal laser beam characteristics [79]. Typical hydrogen concentration of 0.5-3%, depending on tube geometries and laser operating parameters, was found to improve the copper laser performance by 20-30% routinely [58-62]. The improved laser performance was attributed to rapid cooling & removal of inter-pulse electrons through inelastic collisions. This countered the plasma skin effect and favoured recovery of ground state copper density & rapid relaxation of the LLLs. In 1983, Kushner and Warner proposed a model for large bore diameter CVL and explained the performance in terms

of the discharge and excitation parameters [35]. Large bore devices demonstrated average power in excess of 100 W routinely [75, 80]. In 1994, Iseki et. al. and Chang et. al. independently reported the use of radiative gas cooling plates (called septa) in the discharge tube, in addition to H<sub>2</sub> addition, to further reduce the gas heating and plasma skin effect [81, 82]. Record average powers of 550 W/615 W from a single large bore CVL tube (8 cm bore, 350 cm long) as an oscillator/power-amplifier in Japan and ~750 W as a power amplifier in USA were demonstrated in 1995 [83,84]. A CVL MOPA chain, consisting of one oscillator of 30 W power & three power amplifiers of 500 W each, produced 1500 W [84].

In 1997-98, Withford et. al. demonstrated a major boost in the performance of conventional high temperature CVL (~1500 °C) by use of HCl (or HCl + H<sub>2</sub>) additive in discharge medium [62, 85-88]. This system was termed as kinetically enhanced CVL (KE-CVL). The KE-CVL presented an improved performance by a factor of 2-3 in average laser power, PRR and efficiency as compared to conventional CVL. The additive HCl gas changed the electrical discharge characteristics favourably by reducing the pre-pulse electron density. This, in turn, led to enhanced optimum PRR operation, increased ground state copper density & faster LLL relaxation as compared to that of elemental CVL with/without H<sub>2</sub> additive [89, 90]. In a specialized thermal/tube design, Mildren et. al. demonstrated more than 100 W power from a 3.2 cm bore & 100 cm long tube at 24 kHz PRR and 1.4% efficiency [91]. Average out power of 312 W (268 W, with addition of only H<sub>2</sub>) from a 8 cm bore, 300 cm long tube at 5 kHz PRR & 1.4 % efficiency using a high power (77 kW) pulser was demonstrated by Guyadec et. al. in 2005 [92]. However, the high temperature operation & related limiting factors, long start up time (60-90 minutes) as well as complex thermo-mechanical design are the problems associated with KE-CVLs.

### ***1.3.2 Low temperature copper laser***

Replacement of metallic copper by volatile copper bearing compound of low

vapourisation/sublimation temperature, which could dissociate readily in a pulsed discharge to produce free copper atoms for lasing, was proposed as a solution to the problems associated with high temperature CVL. Based on this, lasing action was obtained at temperature of 500-600 °C in copper atom via dissociation of CuI by Liu et. al. [93] and that of CuCl by Chen et. al. [94] in 1973-74 followed dissociation of CuBr by Sabotinov et. al. in 1974 [95]. These copper halide donors enabled the copper laser with less expensive fused silica discharge tube with much shorter start up time (~10 minutes) and with increased efficiency as well as optimum PRR as compared to the conventional CVL. A room temperature copper laser was demonstrated by Perry and Tobin in which the lasant copper atoms were produced by sputtering of the copper cathode which was then carried to the discharge region by flowing buffer gas [96]. Lasing action at 40 °C was also reported in copper acetylacetonate  $\text{Cu}(\text{C}_5\text{H}_7\text{O}_2)_2$  [97]. Of various copper compounds used, the highest laser power was obtained with CuBr followed by CuCl and CuI at typical output power ratio of 6:3:2 [98] and hence the R & D activities were mostly focused mostly on to the CuBr laser (CuBrL).

A strong effect of  $\text{H}_2$  in CuBrL, in terms of doubling of average output power and efficiency, was reported by Astadjov et. al. in 1985 [99]. It was attributed to the efficient inter-pulse plasma recovery by in-situ formed HBr (by reaction of H & Br) owing to its higher dissociative attachment (DA) rate constant than that of Br & H alone ( $\sim 10^{-9} \text{ cm}^3/\text{s}$  vs.  $\sim 10^{-11} \text{ cm}^3/\text{s}$  &  $\sim 10^{-16} \text{ cm}^3/\text{s}$ ) [100-102]. Important milestones were achieved in 1989 by Elaev et. al. with reporting of more than 100 W (112 W) average power  $\text{H}_2$ -CuBrL at 25 kHz PRR from 6 cm dia. & 150 cm long tube [103]. This was followed by Astadjov et. al. in 1997 with demonstration of 120 W average power sealed-off  $\text{H}_2$ -CuBrL from 6 cm bore & 200 cm long fused silica discharge tube using improved excitation circuit (interacting circuit) at PRR of 17.5 kHz and efficiency  $\sim 2.5\%$  [104]. Equivalent performance enhancement in CuBrL was observed, by using HBr additive in place of  $\text{H}_2$  in its active medium, by Shiyanov et. al. in 2004

[105-106]. It was observed that the required partial pressure of HBr was lower as compared to that of H<sub>2</sub> and has an implication for extension of discharge tube life time of CuBrL through self-cleaning action.

Despite the impressive performance of H<sub>2</sub>-CuBrL, the discharge stabilization in the presence of solid/liquid halides (CuBr), due to its proximity to the discharge and high sensitivity of the laser performance on the tube temperature, were major concerns [15, 95, 107]. Efforts were made to keep the CuBr source away from the discharge region by using multiple annular diaphragms and/or by using independent side finger arm reservoirs for CuBr [95,107-109]. The side arm temperature was precisely controlled by external heaters and was decoupled from that of the discharge tube. However, incorporation of these features modulates the laser output power with PRR due to action of acoustic resonances induced in the side-arms/diaphragms which alters the gas density and/or impedes the diffusion of CuBr vapour out of the reservoirs [110]. In addition, the construction of the discharge tube became quite complex due to incorporation of multiple side finger arms and/or diaphragms.

In an important alternative approach, to remove the deficiency of the copper halide lasers, in 1992, Livingstone et. al. generated CuBr vapour in-situ by reaction of HBr gas with the metallic copper inside the discharge tube itself by flowing HBr gas with Ne [1]. This was a hybrid architecture of elemental CVL (use of copper metal) and H<sub>2</sub>-CuBrL (use of CuBr as copper source & HBr for kinetic enhancement) and was coined as Cu-HyBrID (Copper-Hydrogen Bromide In Discharge) laser or Cu-HBrL, by Jones et. al. [4]. With this technique, the generation of CuBr density was decoupled from the tube temperature and was dependent on the HBr concentration (typically 5-10%). This made the tube construction much simpler (without diaphragms, CuBr reservoir finger), offered flexibility in the operating temperature over wide range of 450-850 °C unlike that of H<sub>2</sub>-CuBrL (500 ±10 °C) [111, 95]. Though other hydrogen halide gases such as HCl, HI and H<sub>2</sub> + Br<sub>2</sub> etc. have been used in architecture

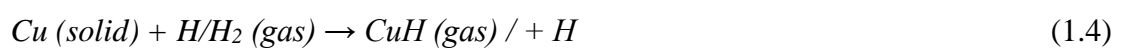
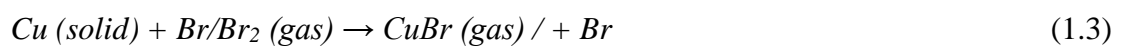
resembling the Cu-HBrL (in-situ generation of copper atoms at lower temperature), but the best performance has been obtained with HBr additive [112, 65]. The Cu-HBr laser has also produced one of the best performances among all the variant of copper lasers in terms of specific average output power, efficiency, spatial & spectral beam quality [113, 6-13]. The next section presents the physics and technology aspects of Cu-HBr lasers in detail.

## 1.4 Physics and technology of Copper-HBr laser

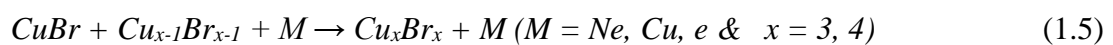
### 1.4.1 Basic physical principles

#### 1.4.1.1 Copper seeding mechanism

The number density of the lasant copper atoms in a Cu-HBr laser is controlled by the HBr additive, which is flown along with Ne buffer gas through the discharge tube. However, the exact mechanism of generation of the copper atoms in a Cu-HBrL is still not very well understood. Based on some experimental studies reported [111,114-116], the most accepted mechanism for the copper seeding process in a Cu-HBrL is as follows. The Ne-HBr gas mixture is passed through the discharge tube at a moderate flow rate (typical: 1-5 lit.-atm./hr) along the floor in which the copper metal pieces are placed. The laser discharge tube is self- heated to the desired temperature of 550-750 °C by multi-kHz PRR electric discharge, which fragments the HBr molecules to a large degree by cumulative dissociation. The HBr molecule & its dissociation products (Br, H: mostly Br) react with the hot copper metal pieces and produce CuBr & CuH vapour, as follows,



In the thermal equilibrium, the CuBr molecules polymerise mainly to Cu<sub>3</sub>Br<sub>3</sub> & Cu<sub>4</sub>Br<sub>4</sub> (as halides exist as polymers [117]) as follows,



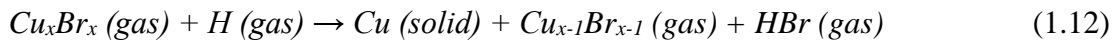
These macro-molecules diffuse into the discharge and then undergo dissociation mostly by electron impact collision and also partly by gas phase hydrogen reduction to produce free copper atoms for lasing, in a chain of chemical reactions, as follows [111,114-116],



The halide molecules lost by dissociation are replaced by molecules diffusing from the wall (in the form of  $Cu_xBr_x$ ). This process delivers further copper atoms to the discharge, because of slow re-association to form CuBr (in several hundreds of  $\mu s$ ) and even slower to form  $Cu_xBr_x$  [118]. Therefore, the number density of copper atoms, in the discharge, is governed by the number density of halogen species present and the electron temperature in discharge. The dissociation energies of the involved species are 3.76 eV (HBr), 3.43 eV (CuBr), 2.73 eV (CuH), 1.97 eV ( $Br_2$ ) and 4.52 eV ( $H_2$ ) [119]. The strongest chemical bond is between Cu and Br. The deeper the polymers ( $Cu_xBr_x$ ) penetrate into the discharge, the more of these will be fragmented to CuBr. Therefore the immediate source of copper atoms on the axis is CuBr, as observed in  $H_2$ -CuBrL [101]. Due to influence of gas heating and cumulative pulse-to-pulse dissociation, in the multi-kHz pulsed discharge, the relative populations of CuBr &  $Cu_xBr_x$  vary across the tube bore [114-115]. Near the wall, where the electron density and gas temperature are minimum, the number density of  $Cu_xBr_x$  dominates over that of CuBr. The number density of CuH decreases from the axis to the wall [115]. In the axial region, the electron collision dissociation of copper precursors (CuBr,  $Cu_xBr_x$ , CuH) dominates as copper seeding mechanism whereas on the wall region the gas phase hydrogen reduction (mostly of

$\text{Cu}_x\text{Br}_x$ ) dominates. These facts are established by studies based on absorption of 488 nm line from  $\text{Ar}^+$  laser by  $\text{CuBr}$  and absorption of 434 nm & 428 nm lines from Xe-lamp by  $\text{CuBr}$  &  $\text{CuH}$  respectively, followed by ab-initio calculations [114, 115].

The copper seeding mechanism in a Cu-HBrL best proceeds for typical tube (copper metal piece) temperature of 500-800 °C [111]. In this temperature range, the evaporation rate of copper bromide is higher than that of its generation. Then the rate of copper bromide vapour is controlled by rate of injection of HBr. For the temperature below 450 °C, the reaction of Br-bearing species with Cu will lead to solid copper bromide and their vapour pressure will be too low for seeding. On the other hand, for higher temperature (> 850 °C), both hydrogen reduction (equation 1.12) and thermal dissociation of the  $\text{Cu}_x\text{Br}_x$  (equation 1.13) become faster than the reaction to form  $\text{CuBr}$ . This leads to deposition of solid copper on the tube wall and fall in copper seeding into the discharge.



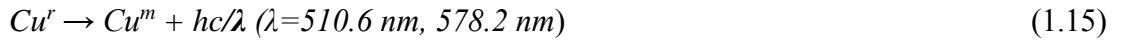
Then control over the  $\text{CuBr}$  vapour will be lost and discharge instability will start. The increased operating temperature also leads to increased axial gas temperature, which causes increased thermal dissociation of the HBr molecules ( $\text{HBr} \rightarrow \text{H}/\text{H}_2 + \text{Br}/\text{Br}_2$ ) and decrease of DA process for kinetic enhancement [7].

#### **1.4.1.2 Lasing kinetics**

The most crucial factor for the improved performance (high specific output power, efficiency & PRR) of a Cu-HBrL is the presence of HBr in its discharge medium [1, 120-122]. The HBr & its dissociation product  $\text{H}/\text{H}_2$  in a Cu-HBrL plasma significantly reduce the pre-pulse electron density. This translates into faster recovery of ground state copper density within inter-pulse period, decreased pre-pulse plasma electrical conductivity, spatio-temporal homogenisation of the applied electric field for efficient pumping, enhanced PRR operation

due to reduced plasma skin effects, increased pre-pulse discharge impedance favouring high-voltage hold-off, improved impedance matching & delaying the electron avalanche during the discharge that favours ULL excitation. These factors lead to vastly improved performance of a Cu-HBr laser.

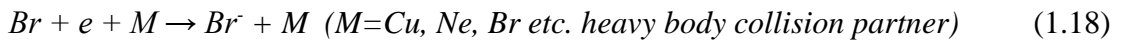
The Cu-HBr lasing kinetics are as follows. The generated copper atoms get excited to the ULLs due to fast electron-impacts/collisions in the rising part of the current pulse and produce lasing action (as discussed in section 1.2.2) as,



During the inter-pulse period, the LLLs (metastable-levels) decay to ground level and the electron temperature collapses, attaining the equilibrium temperature of 0.2-0.3 eV (2000-3000 °C). At this temperature (inter-pulse period), the HBr molecules combine with the residual electrons through dissociative attachment (DA) process as [120-121],



This is a resonant process with large cross section peak of  $\sim 10^{-16} \text{ cm}^2$  and rate constants of  $\sim 10^{-9} \text{ cm}^3/\text{s}$  at electron temperature of  $\sim 0.28 \text{ eV}$  [121]. The DA process is endothermic in nature and the energy required ( $\Delta E$ ) for maximum reaction rate is  $\sim 0.28 \text{ eV}$ , which is favourably available in the Cu-HBrL discharge during inter-pulse period. In addition, inter-pulse electrons also undergo radiative or three-body attachment with H & Br as well [120],



However, electron attachment to H via dissociation of HBr or to H<sub>2</sub> requires more energy ( $>3 \text{ eV}$ ) than that of HBr, hence are not dominant during the inter-pulse period. The three body electron attachment is intrinsically slow process by 2 to 3 orders of magnitude than that of the DA process [121]. The consequence of the electron attachment process is the

significant reduction in pre-pulse electron density, to  $\sim 10^{10}$ - $10^{11}$   $\text{cm}^{-3}$  from the peak value of  $10^{13}$  -  $10^{14}$   $\text{cm}^{-3}$ , as observed by Hogan et. al. [54] and was confirmed by estimation from its electrical characteristics [123, 124]. The DA rate constant decreases with increase in electron temperature ( $\sim T_e^{-0.9}$ ) [102, 121] and hence does not affect the electron population much during during the excitation period where the average electron temperature is typically 4-5 eV.

The loss of pre-pulse electrons, hence formation of  $\text{Br}^-$  &  $\text{H}^-$ , facilitates a rapid recovery of copper ground state density through the process of two body ion-ion neutralization as [120, 121],



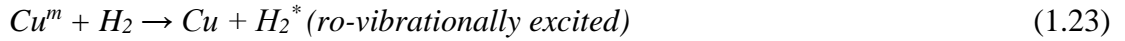
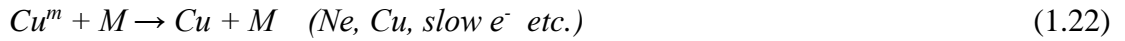
The above ion-ion neutralisation reactions are very fast with rate constant  $\sim 10^{-7}$   $\text{cm}^3/\text{s}$  with characteristic time  $\sim 100$  ns [102]. The other copper ground state copper recovery channel, operative in conventional CVL as well, is three body e -  $\text{Cu}^+$  recombination (1.21) which is a relatively slow process (rate constant  $\sim 10^{-10}$ - $10^{-11}$   $\text{cm}^3/\text{s}$ ) with typical time constant of  $\sim 10$   $\mu\text{s}$  [102, 121].



The rate constant of this three body neutralisation is highly sensitive to  $T_e$  ( $\sim T_e^{-4.5}$ ) and the inter-pulse  $T_e$  is lower in Cu-HBrL (owing to presence of hydrogen), hence effectiveness of this process is more in Cu-HBrL. Around 4.3 eV energy is released by neutralisation process (eq. 1.19) of  $\text{Cu}^+$  &  $\text{Br}^-$ , where part of the energy populates the ULL ( $\sim 3.8$  eV) and the rest may be taken away by metastable Br atoms ( $\sim 0.46$  eV) or as kinetic energy of Cu/Br atoms. Isaev et. al. [121] proposed that the DA process also play a crucial role in effective shaping the electron energy distribution during the early stage of the current pulse. Immediately after the onset of the applied voltage, when the applied voltage is low, the DA process impedes/delays the electron avalanche and the discharge current is delayed with respect to the voltage. The

delayed avalanche inhibits the early pumping of the LLLs and when the avalanche begins, the electron temperature is high and the ULLs are pumped efficiently. Also, the pre-pulse impedance increases to several kilo-ohms and hence higher discharge voltage is sustained across the laser head. Due to lower pre-pulse electron density, the pre-pulse plasma conductivity decreases and the plasma-skin effect (discussed in next section) reduces which facilitates the applied radial electric field to penetrate deeper into the axial region, hence providing spatio-temporally homogenous electrical excitation to the copper atoms. The decreased plasma conductivity also leads to better transfer of electrical energy from the pump electrical source to the discharge plasma and enables the Cu-HBrL to operate with high copper density ( $\sim 10^{15} - 10^{16} \text{ cm}^{-3}$  vs.  $10^{14} - 10^{15} \text{ cm}^{-3}$  in CVL) without breakdown [15-17].

In addition, the metastable levels also undergo a faster decay mostly via super-elastic collisions with other surrounding particles such as Ne, Cu and with low energy electrons as well as by energy transfer collisions with hydrogen present as dissociated product as [15],



The last reaction is important in the early inter-pulse period with a rate coefficient of  $\sim 10^{-13} \text{ cm}^3\text{s}$  [125]. The presence of  $\text{H}_2$  in Cu-HBrL has similar roles as in case of  $\text{H}_2$ -CVL/KE-CVL/ $\text{H}_2$ -CuBrL (section 1.3). The inter-pulse  $T_e$  is inversely proportional to elastic collision cross section ( $\sigma_{el}$ ) of electron & buffer gas atoms and is given by [15, 90],

$$\sigma_{el} \propto 2m_e n_j \frac{\langle \sigma_j v_e \rangle}{m_j} \quad (1.26)$$

where  $\sigma_j$  = momentum cross section,  $m_j$  = mass surrounding species,  $n_j$  = number density of surrounding species and  $v_e$  = speed of electrons. Therefore, due to lower mass as compared to other collision partner, and hence large elastic collision cross section, hydrogen speeds up

electron cooling and inter-pulse  $T_e$  approaches towards the average gas temperature. Hence, the overall the metastable levels relax faster as compared to CVL. These kinetic processes enables, a Cu-HBrL to be highly performing variant copper laser in terms of output power, efficiency and PRR operation.

The above discussed kinetic processes are supported thoroughly by experimental investigations by several authors [54, 114, 115, 126]. The temporally and radially resolved particle (copper ground level, ULL, LLL & electron density) density measurements, in a 2.5 cm bore Cu-HBrL were compared with that of 4.2 cm bore CVL by Hogan et. al. [54]. The comparative experimental trends are shown in Fig. 1.2. It was observed that the copper ground state density (Fig. 1.2a) recovered much faster as well as the pre-pulse electron reduced

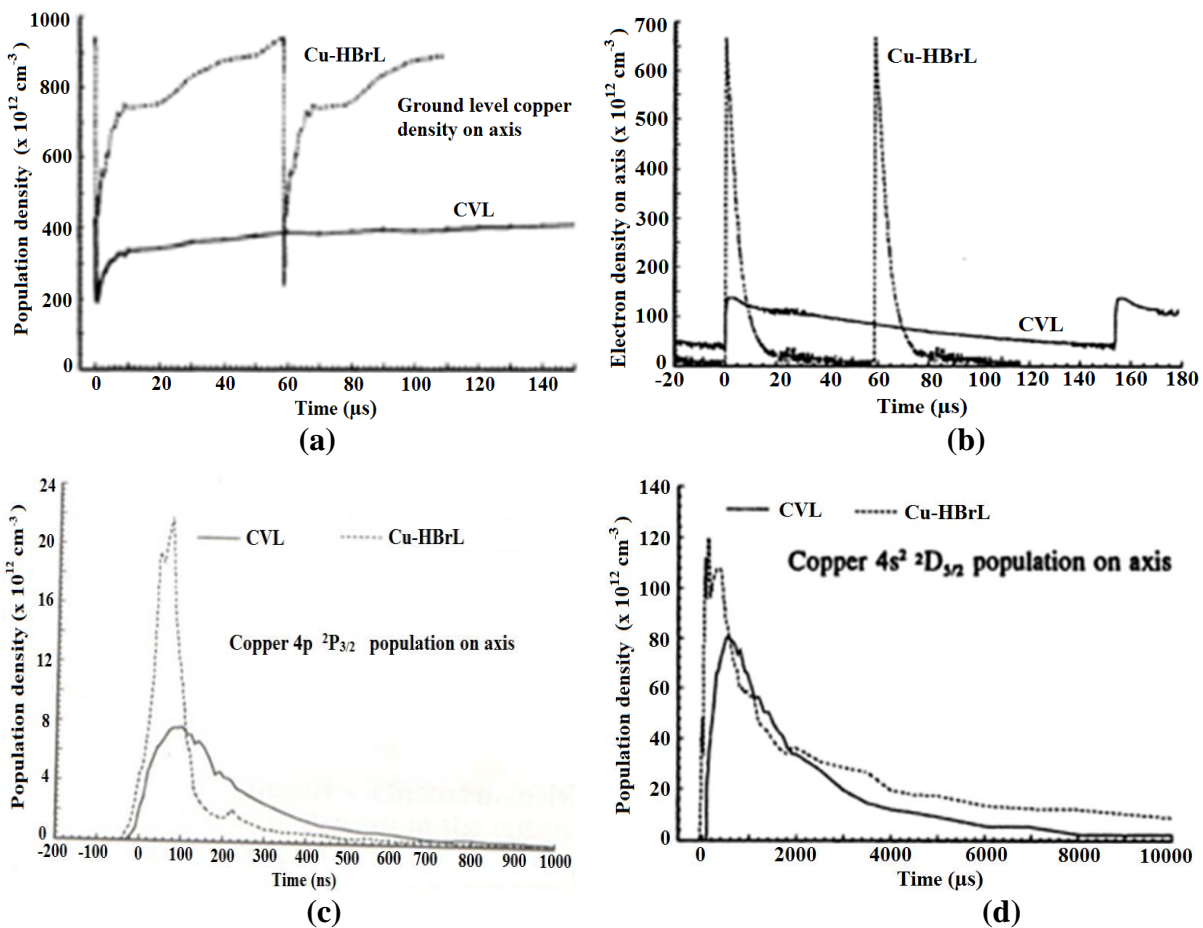


Fig. 1.2 Typical temporal variation of on-axis particle density in Cu-HBrL & CVL

(a) Ground level copper density, (b) Electron density, (c) Upper laser level copper density and (d) Lower laser level copper density [54]

to almost noise level in a Cu-HBrL (Fig. 1.2b). During excitation, the ULL population attained much higher value ( $\sim 3$  times) and relaxed much quicker than that of the CVL (Fig. 1.2c). However, the LLL population was higher in Cu-HBL but its decay was much faster than CVL (Fig. 1.2d). Similar study in a H<sub>2</sub>-CuBrL by Astadjov et. al. [104] revealed that the depletion of ground state copper density reduced to typically  $\sim 20\%$  from that of  $\sim 60\%$  without H<sub>2</sub> additive. This was due to higher DA rate constant of HBr (formed in situ) than that of Br/Br<sub>2</sub> ( $\sim 10^{-9}$  cm<sup>3</sup>/s vs.  $\sim 10^{-11}$  cm<sup>3</sup>/s). The dominant role of H<sub>2</sub> in CuBrL as compared to that of conventional CVL was attributed to higher DA rate constant of HBr than that of H<sub>2</sub> ( $\sim 10^{-9}$  cm<sup>3</sup>/s vs.  $\sim 10^{-16}$  cm<sup>3</sup>/s) [121].

The studies, on laser performance, were also carried out with other hydrogen halide gases HCl, HI in the Cu-HBrL architecture, i.e. in-situ generation of copper atoms in low temperature (500-600 °C) regime [112, 65]. In principle, these additives also favour the better laser kinetic processes [121]. However, the laser output power was 25-30% lower with HI and HCl additives as compared to HBr. The degraded performance of the low temperature laser performance with HCl and HI was attributed to their lower inter-pulse electron removal capability. This was because of lower DA cross section for HCl and lower electron affinity of Iodine atom as compared to HBr (3.06 eV vs. 3.36 eV) [112, 65]. It was also demonstrated that the addition of H<sub>2</sub> to Cu-HBrL led to decrease in laser output power as well as onset of discharge instability [113,127]. This was attributed to enhanced reduction of CuBr leading to precipitation of copper on the discharge tube wall i.e.  $\text{CuBr} + \text{H} \rightarrow \text{Cu} + \text{HBr}$ , thereby decreasing the available copper density for lasing and on setting of the discharge instability. Though the active medium of H<sub>2</sub>-CuBrL and Cu-HBrL contain same species, the composition of Cu-HBrL active medium was found to be optimum [121]. The enhanced performance of a Cu-HBrL was attributed to the high DA cross section of HBr for removal of the pre-pulse electrons and the favourable associated effects as brought out in the previous section.

### 1.4.1.3 Laser discharge characteristics

In a CVL, high pre-pulse electron density makes the electrical conductivity of the discharge tube to be relatively large which is only 2-3 order of magnitude smaller than that of a typical metal [118, 54]. Due to this pre-pulse conductivity, when a voltage pulse is applied to CVL, a large current flows without any significant increase in electron density for the first 10s of ns. This current, termed as phantom current by Hogan et. al. [118], is a signature of pre-pulse electron density in CVL and is identified as a characteristic step that often appears on the leading edge of the discharge current pulse (Fig. 1.3a). The electrons in phantom current don't reach the energy needed for significant rates of inelastic collision as required for ULL pumping. In addition, there is also significant pre-pulse ion density (mostly copper ions due to its lower ionisation energy of 7.73 eV) exist in the CVL tube. These charged species ( $e^-$  and  $Cu^+$ ) are efficiently removed/neutralised during the inter-pulse period by HBr additive gas in a Cu-HBr laser mostly through DA process. This is evidenced by observation of low phantom current in the Cu-HBrL discharge current pulse (Fig. 1.3b) [120]. The Cu-HBrL discharge current (I) is shorter & delayed as compared to CVL and starts near the peak of the tube voltage (V), consistent with delayed self-switching mechanism due to HBr. The laser output (O) starts along with start of the electron avalanche.

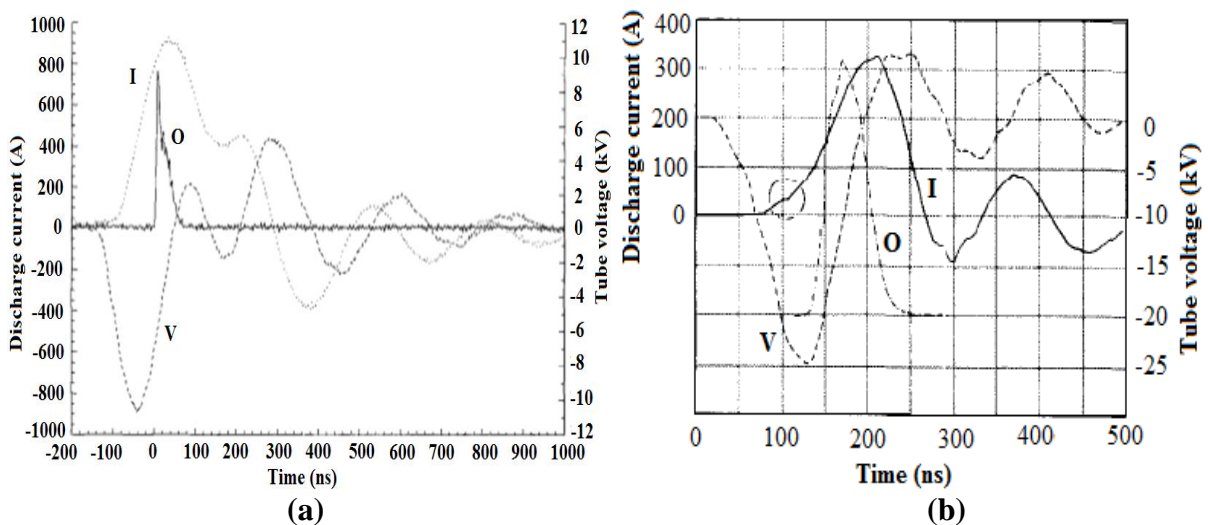


Fig. 1.3 V, I & Laser pulses of Cu-HBrL (a) [120] and CVL (b) [118] at optimised condition

One of the most significant manifestations of reduction in pre-pulse electron density is the reduced plasma skin-effect that enables a Cu-HBrL to operate at higher PRR than a CVL. In a high PRR pulsed electric discharge, plasma skin effect governs the spatio-temporal coupling of the electrical energy into the plasma. Due to this effect, the electric field varies both in time and radial direction from the surface to the axial region. The skin depth, i.e. 1/e penetration depth, of the radial electric field into the discharge tube axis is given by [35, 122],

$$\delta = \sqrt{\frac{2}{\omega \mu_0 \sigma}} \quad (1.27)$$

where  $\omega = 2\pi f$  such that  $f$  is the PRR,  $\mu_0$  is the permeability of free space,  $\sigma$  is the pre-pulse electrical conductivity of the CVL plasma which is given by,

$$\sigma = \frac{n_{e0} e^2}{m_e \nu_m} \quad (1.28)$$

where  $m_e$  = mass of electron and  $\nu_m$  = electron-atom collision frequency such that  $\nu_m = n \langle \sigma_m v_e \rangle$  with  $n$  is the buffer gas concentration,  $v_e$  is the speed of electrons and  $\sigma_m$  is the cross section of momentum transfer of collision partners with the electrons. The characteristic time ( $\tau$ ) for the electric field to penetrate towards the tube axis from the wall is given by [35, 122],

$$\tau = 0.15 R^2 \mu_0 \sigma \quad (1.29)$$

Therefore, more is  $n_{e0}$ , stronger is the plasma skin effect and more is the spatio-temporal in-homogeneity of the electric field coupled to the CVL active medium. This leads to spatio-temporal inhomogeneity of the laser emission hence affecting the laser performance. The lower value of  $n_{e0}$  (as in a Cu-HBr laser) leads to reduced plasma skin effect, improved electrical coupling to laser plasma, higher discharge voltage / peak electron temperature and thus improved Cu-HBr laser performance at high repetition rates.

#### 1.4.2 Engineering and technology

The Cu-HBrLs have complexities associated with corrosive nature of HBr gas, requirement of leak proof assembly, critical dependence of laser performance on HBr

concentration/flow rate, issues of material compatibilities as well as high temperature and high PRR operation. The laser engineering and technology development involve design, development and integration of laser electrodes, discharge tube, HBr + Neon gas precision flow unit, vacuum system, cooling system and high-PRR, high-voltage & fast-switching electrical excitation sources. Finally, the assembled laser system needs to be studied for laser output power, beam quality and reliability. This section presents an overview on these aspects of Cu-HBrL as reported by different researchers in the field.

#### ***1.4.2.1 Laser design***

Copper laser can be electrically excited both in longitudinal and transverse geometries [15, 16]. However, the longitudinal excited systems are more successful & widely studied. This is because, in transverse excitation geometries, the high-voltage lead-throughs & other vacuum seals fail due to high temperature at high electrical input power as well as high PRR operation [129]. In addition, it is difficult to maintain arcing-free uniform discharge in the gain region at high gas pressure and/or in the presence of halogen gases [129]. Hence, the Cu-HBrL development activities are limited to longitudinal excitation geometry only.

The Cu-HBrLs have wide operating temperature in the range on 500-800 °C. Fused silica is the material of choice for the discharge tube because it is cheap, inert to HBr, good electrical insulator, light-weight & robust, less prone to thermal shock, has low thermal conductivity & outgassing impurity, and can withstand the operating temperature of Cu-HBrL (softening temperature of fused silica is ~1000 °C) [7, 14, 113]. The recrystallized alumina ceramic tube sleeved within a fused silica tube, is also used as discharge tube in Cu-HBrL owing to its more robustness than fused silica [1, 4-6, 8-10]. However, it is quite expensive, difficult to make in large size and has relatively high outgassing impurity than that of fused silica. The choice of electrode material and its design in Cu-HBrL is also very important for stable discharge and flicker-free output beams. The electrode material should have high work-

function as well as be able to withstand high temperature. Tungsten, molybdenum, tantalum, copper and monel, in the form of pins and/or foil and/or bulk head, have been used as electrode material in Cu-HBrL [1, 4-10]. In copper halide lasers (Cu-HBrL & H<sub>2</sub>-CuBrL) electrodes of copper are preferred as its reaction with halogens is least likely to contaminate the discharge [6]. Similarly, Ne buffer gas and HBr additive are mixed either via needle valves or mass flow controllers of compatible material (SS 316) & high vacuum quality design before entering into the discharge. The gases are exhausted downstream at the cathode end via halogen filter and rotary vacuum pump.

The early designs of Cu-HBrLs were based on alumina discharge tube sleeved within fused silica tube which was wrapped with a thin layer of alumina fibre insulation to attain the desired operating temperature. The electrodes were hollow cylinders of molybdenum foil push fitted into water cooled stainless steel flanges or stainless steel cylindrical water cooled electrodes [1, 4, 5]. This configuration produced average output power as high as 120 W. The high specific output power Cu-HBrL, reported by Sabotinov et. al., was based on fused silica discharge tube side-arm tungsten electrodes engulfed within copper fillings [113]. The 200 W average power Cu-HBrL was based on cylindrical copper electrodes fitted into water cooled SS flanges [6]. In this model, the discharge tube was made of alumina sleeved within fused silica tube whereas the end-window attachments were made of fused silica. The wetted parts were ensured to be copper or fused silica or alumina to prevent generation of any impurity through reaction with HBr. The stable discharge operation was promoted by use of spot fixer. The spot fixer was a fused silica insert which lined with the copper electrode except for small hole drilled on one side of the insert. Attachment of the discharge was restricted to small area by the hole giving flicker-free discharge and stable output beam. Subsequently, all the high power designs were limited to cylindrical electrodes of high purity copper, fitted into water cooled SS flanges. An alternative and more complicated end-flange assembly was reported by

Mildren et. al., where an electrode of small area protruded in from one side and was electrically isolated from the end flanges and the discharge was made to anchor onto the electrode tip [10]. Guyadec et. al., for their 216/280 W Cu-HBrL, used discharge tube made up of fused silica and electrodes made up of monel cylinders fitted into water cooled SS flanges [7]. Average power in excess of 100 W with fused silica discharge tube and copper electrodes with conventional design has also been reported [14]. In all these designs, to prevent contamination by the CuBr due to diffusion from the discharge region, the end windows were attached at 30-40 cm away from the electrode tips.

#### ***1.4.2.2 Electrical excitation sources***

Electrical excitation sources have played a very crucial role in successful technology development of copper lasers in general and Cu-HBrL in particular. The Cu-HBrLs require high average power, high PRR, high voltage, fast-rising electrical pulses for efficient excitation. For maximum laser output power in Cu-HBrLs, typical required characteristic electric fields in the discharge is in the range of 3.5 to 5 V/cm-mbar at PRR of 15-25 kHz [4]. This translates into peak discharge voltages ( $V_b$ ) of 15-25 kV, peak discharge currents of 200-500 A, rise time of less than 100 ns and shortest possible over all duration. The typical Cu-HBr laser power supply consists of a suitable combination of low ripple ( $< \pm 1-2\%$ ) DC/switch-mode power supply, capacitor charge transfer (CT)/LC inversion/interacting peaking (IP)/interacting (IC) circuit and fast high voltage thyatron/solid-state switch in conjunction with MPC and/or magnetic assists (MA) [15]. The voltage & current magnitude is primarily decided by laser discharge tube length, its diameter as well as the laser operating pressure. In the beginning, most of the Cu-HBrLs were based on CT-circuit with a single thyatron (EEV CX 1535, EG & G HY-3001 etc.) modulator [1, 4, 5,130]. For higher power (>100 W) version Cu-HBrLs, requiring higher electrical inputs as well as higher tube voltages, high performing variant thyatrons e.g. EEV CX 1835 coupled with inductive snubber (to protect the thyatron

failure and/or its losses) and CT/IC excitation circuits have been used [6]. Mildren et. al. [10] have used single thyatron (ITT F-162) + MPC based modular in their ~125 W output power version Cu-HBrL. Guyadec et. al. [7] have used a 50 kW all solid state pulser based on MOSFET switch arrays, pulsed step-up transformer and several MPC stages to sharpen the excitation pulses. For kinetic study, Girard et. al. [115] have used 5 cm bore, 165 cm long tube Cu-HBrL producing ~45 W which was pumped by LC-inversion circuit based electrical excitation source employing several MOSFET switches and an MPC. The 1 kW average power Cu-HBrL, proposed by Little et. al., is based on multiple thyatron (3 to 5 in parallel) based 50 kW average power pulser equipped with MA and multi-stage MPCs [131]. The IC/IP circuits are more efficient due to their capability of better matching with the discharge [132,133] and hence have produced more than 25 % increase in output power (160 W to 201 W) in a Cu-HBrL [6]. However, use of these circuits are limited as both the discharge electrodes remain in high voltage floating conditions, posing risk of potential hazard.

#### ***1.4.2.3 Laser system performances***

The first Cu-HBrL, reported by Livingstone et. al. [1], was based on 1.3 cm bore, 30 cm active length producing average power of 7.8 W at PRR of 16 kHz and had laser start up time less than a minute (45 s). Jones et. al. reported average laser powers of 94 W/ 40 W with 1.5% / 2.7% efficiency at respective charging voltages of 19 kV / 14.4 kV and PRR of 21 kHz from a discharge tube of 4.5 cm bore and 120 cm length [4]. The laser start up time was 15-20 minutes. A single thyatron (EEV CX 1535) based conventional resonant-charging CT-circuit, capable of delivering electrical powers of 7 kW at PRR up to 27 kHz was used. In the following year, 1993-94, the same group scaled the tube length to 150 cm and achieved average laser power of 100 W /121 W with 2.6% / 2.2 % efficiency at 18 kHz PRR and 17.6 kV charging voltage [5]. About 21% enhancement in output power was obtained by eliminating parasitic stimulated emission due to back reflection from the fused silica discharge tube window [5]. In

the same year, Sabotinov et. al. generated record specific average output power of  $2 \text{ W/cm}^3$  from a Cu-HBrL (9.5 W average power at 60 kHz PRR from a 0.45 cm bore, 30 cm long tube) [113] which was significantly higher as compared to  $1.3 \text{ W/cm}^3$  for CVL [134] and  $1.4 \text{ W/cm}^3$  for H<sub>2</sub>-CuBrL of same active tube dimension [135].

A record average output power of 200 W with 1.9 % efficiency and 120 W with 3.2% efficiency at 17 kHz PRR from 6 cm bore & 200 cm long tube was obtained [6]. The laser incorporated specialised design ensuring least possible impurity (wetted parts were copper and alumina/fused-silica only), least possible window/cavity loss (as described in previous paragraph) and improved electrical excitation circuit (IC-circuit). An improved version thyratron (EEV CX 1835), capable of delivering average electrical power upto 10 kW with charging-voltage/PRR of 25-27 kV/ 25 kHz was used in both conventional CT-circuit & IC-circuit. Average laser power of about 160 W & 201 W were obtained at charging voltages of 26 kV & 26.5 kV and PRR of 17 kHz respectively for CT & IC circuits. The improved performance with IC-circuit was due to better matching between the circuit and the laser discharge. This enabled higher tube voltage (26.5 kV vs. 26 kV) and higher-peak/faster discharge current (405 A vs. 375 A & 78 ns vs. 87 ns) which favoured better ULL pumping [6]. However, another study reported by Coutance et. al. in 1995 [9], with tube of similar dimension but conventional cavity geometry as well as CT-circuit for electrical excitation produced 110 W average power at PRR of 16 kHz. Mildren et. al., in 1998, employed MPC with standard CT-circuit based on single thyratron (ITT F-162) and obtained 127 W average power from 235 cm long & 6 cm bore tube at charging voltage of 20.5 kV & PRR of 12.5 kHz [10]. In 1999, Guyadec et. al. [7] reported 216 W average output power at 2.7% efficiency as an oscillator and 280 W at 3.8% efficiency as a power amplifier at 18 kHz PRR from 8 cm bore, 300 cm long discharge tube employing 50 kW solid state pulser. The coupled electrical power to the discharge tube was about 8 kW, with tube charging voltage of 42 kV and current

pulse rise-time of ~40 ns. Coupled in MOPA configuration (40 W master oscillator + 1 amplifier), total average output power of 320 W was demonstrated. The performances of all these Cu-HBrLs differed due to employment of different active volumes, parametric and electrical excitation conditions. Little et. al. have projected Cu-HBrL of 1 kW average power with 2% efficiency at 17-18 kHz PPR from a 25 cm bore & 300 cm long, gas cooling septa based discharge tube & standard electrical excitation scheme [131].

The Cu-HBrLs are characterised by axially peaked gain, quasi-Gaussian radial intensity profiles (vs. flat top or centrally deep profile in CVL) as well as longer (50 to 100%) gain durations as compared to CVL [15]. These led to better output beam quality from a Cu-HBr laser. The plane-plane resonators (PPRs) were the most commonly used for maximum laser power extraction from Cu-HBr lasers. However, the output beam divergence was usually high in range of several mrad which also scaled up with increase in tube bore diameter. The beam divergence was usually expressed in terms of diffraction limit (DL) or  $M^2$  factor. The diffraction limited divergence is given as  $\theta_{DL} = \beta_p \lambda/D$  where  $D$  = beam diameter and  $\lambda$  = wavelength of the radiation involved. The factor  $\beta_p$  is a constant which depends on near-field laser beam intensity profile. This factor is 2.44 for flat top profile and 1.27 for Gaussian profile. Brown et. al. [8] have carried out a detailed calculation for DL of Cu-HBrL beam with observed quasi-Gaussian near-field radial intensity profile and evaluated the DL divergence to be  $3.05 \lambda/D$  ( $\beta_p = 3.05$ ) containing 92 % of the beam power. This is unlike that of a flat top CVL beam where the DL divergence is taken as  $2.44 \lambda/D$  ( $\beta_p = 2.44$ ) containing 84% of the beam power [8]. The reported beam divergence values of Cu-HBrLs with the PPR were in the range 20-30 times DL. For lowering the beam divergence close to DL (~ few tens of  $\mu$ rad), as needed in certain applications, confocal unstable resonators (UR) of different magnifications ( $M$ ) were used in Cu-HBrL. Coutance et. al. [9] used on-axis UR of  $M = 20$  in a 6 cm bore Cu-HBrL and generated 100 W average power at 16 kHz PPR (110 W with PPR), out of which ~80 W was

within 3.5 DL. Brown et. al. [8] employed a UR of  $M=190$  in a 6 cm bore, 220 cm long tube Cu-HBrL (106 W with PPR at a low input power) and produced 65 W with average beam divergence of 2 DL. In a similar study with 6 cm bore, 235 cm long tube, Mildren et. al. [10] incorporated high magnification UR ( $M = 280$ ) and 125 W laser power was obtained out of which 101 W (80% of total) was high beam quality output. Out of this more than 88% laser power was within 1.6 DL and more than 66% power was within DL. Isaev et. al. [136] used both PPR ( $M=1$ ) and UR  $M=54$  with their 2 cm bore, 80 cm long tube Cu-HBrL and obtained same 18-19 W average power with pulse averaged divergence around 1.5 DL for the UR. Huot et. al. [137] incorporated UR  $M=20$  in their Cu-HBrL and obtained output beam of  $M^2 \sim 7$ . Brown et. al. [8] used confocal negative branch UR with intra-cavity diffraction filtering aperture (self-filtering unstable resonator: SFUR) with a 2.5 cm bore, 80 cm long tube and obtained 20 W average power at average beam divergence of 1.3 DL. This SFUR Cu-HBrL master oscillator was further coupled with a 6 cm bore, 220 cm long tube Cu-HBrL (with UR  $M = 190$ ) in injection seeded scheme and 120 W average power with average beam divergence of 2.3 DL was obtained.

### **1.5 Current trends on technology and applications of copper lasers**

Copper lasers have almost matured in technology development over the span of about fifty years since its invention. Currently, the focus is more on the applications of developed copper laser systems. At the same time, the R & D programs are also continuing in different laboratories with final aim towards specific applications. The copper laser based multi-kHz PRR, pulsed ( $\sim 10$ s of ns) dye lasers & their frequency up-converted tunable UV sources are still the basis of selective photo-ionisation studies of elements in many laboratories. Recently, visible radiations of copper laser have been demonstrated in efficient, highly sensitive and real-time detection & monitoring of molecular Iodine-129/Iodine-127 in fast nuclear reactors, spent nuclear fuel reprocessing plants and radiochemical plants [25]. The copper lasers are being

used to reduce radio toxicity of Cesium/Uranium, with potential application for laser-induced radioactive waste disposal [26, 139]. About 70% decrease in radio toxicity of the Cs-137 nuclides (gold target within aqueous Cs-137) and 50% decrease in radio toxicity of U-235 & U-238 (Beryllium target in aqueous uranyl chloride solution) have been demonstrated. The CVL based 255.3 nm UV source are being utilized for efficient writing of fiber Bragg gratings [20, 31] for various sensor and photonic applications. The CuBrL are being utilized for single pulse imaging laser projection system for non-destructive testing of materials and processes shielded by intense background lighting such as plasmas [27, 30]. The flow and combustion characteristics of biofuels by high speed time resolved imaging of the spray and flame luminous intensity (shoot) is being pursued with CVLs [28].

The 271.2 nm UV radiation obtained by SFG of copper laser, has been used for space-selective enhancement of blue (460 nm) photoluminescence in gallium germano-silicate glass through laser-induced nano-structuring, with a potential for developing novel solar-blind UV detectors [29]. The copper lasers are also used for local crystallisation of glasses with precipitation of active phases, with aim of developing active elements of integrated optics [140]. The layered organo-inorganic copper nano-composites are synthesised by copper laser ablation in liquid media, with potential for device applications [22]. In an innovative approach, the synthesis of silica-core silver nanoshells is carried out by irradiating copper laser pulses on a colloidal solution containing silver and silica nanoparticles [141]. Efficient ablation of several material such as Mg, Ag, Au, Zn etc., using copper lasers, have been carried out for synthesis and characterisation of nanoparticles in colloidal solutions [21, 22, 142]. Successful restoration of ancient art works on papers and marbles, by using copper laser based surface irradiation/ablation, have also been carried out [143]. Copper lasers are utilized for treatment of scars [144, 145] and vascular lesions [144, 146, 147].

On the device development side, a reversible HBr source is developed for sealed-off

applications of copper lasers and successfully tested in a CuBrL [148]. In a novel approach, AgCl and CuCl were embedded inside the thermal insulation to exploit the KE-action without the need of extra HCl source [149]. Multi-wavelength (11 wavelengths from 0.43 to 6.45  $\mu\text{m}$ ) CuBrL is developed with addition of Strontium in discharge tube [150]. The Au along with Cu in segmented zone is used to develop three colours (510.6, 578.2 & 627.8 nm) metal vapour laser for spectroscopic applications [151]. A small bore CuBrL with record PRR of 700 kHz has been demonstrated [152]. Presently, frequency doubled Q-switched solid-state lasers are emerging as compact and alternate high PRR visible laser sources. However, the features of the advanced variant copper lasers such as ease of average power scalability to 100s of watt in visible range, even at the high PRRs, without going through the route of nonlinear frequency doubling and capability to produce highly stable diffraction limited laser beams are advantageous over the solid state lasers.

## Chapter 2

### Development and studies on high average power (40 to 110 W)

#### Cu-HBr lasers

##### 2.1 Introduction

The technology development of Cu-HBr lasers critically depends on successful development and integration of various subsystems followed by systematic parametric optimization studies. It involves the challenges associated with design and assembly of suitable laser electrodes, discharge tubes, gas & vacuum control system, issues of material compatibilities vis-à-vis safety system for handling highly corrosive HBr gas & precision control of its concentration and issues related with high power/voltage & high PRR electrical excitation sources. With this perspective in view, the current chapter presents development and studies on Cu-HBrL comprising of thermal design of the laser, mechanical design of the laser electrodes & discharge tubes, design of precision gas mixing set up for the Ne and HBr gases, design/development of high-PRR, high-voltage & fast-switching electrical excitation sources followed by their integration and parametric optimization of the laser output power. The thyatron and solid state IGBT (Insulated Gate Bipolar Transistor) pulsers are employed for the electrical excitation of the Cu-HBrLs. The parameters studied for the laser power optimization are the electrical input power, PRR, buffer gas pressure & flow rate, HBr concentration and electrical storage/peaking capacitors. These results on different average output power (40, 70, 85 & 110 W) versions of the developed Cu-HBrLs, differing mainly in their active volumes, are presented and discussed in detail.

##### 2.2 Design & development of subsystems for Cu-HBrLs

###### 2.2.1 Thermal design

The operation of a Cu-HBrL requires repetitive deposition of electrical energy in the discharge tube containing the mixture of active species, neon and HBr gases. A small part (~

2-3%) of the deposited energy is utilized to dissociate copper precursors, present in the discharge tube, to generate copper atoms of necessary density and subsequently excite them for lasing action. The rest is utilized for maintaining the desired discharge tube temperature of around 600 °C. The heat is finally released to the surrounding or taken away by water circulation through an annular SS jacket that encloses the discharge tube.

The thermal design of a Cu-HBrL discharge tube consists of wrapping a thin layer of suitable thermal insulation around the discharge tube to maintain the required tube temperature during the laser operation. For a given diameter and length of Cu-HBrL tube, the thermal design analysis is carried out as a function of coupled input electrical power, keeping in mind the laser tube operating temperature as well as the axial gas temperature. The analysis is based on solving the Fourier heat conduction equation as follows. In a Cu-HBrL, the electrical energy is deposited into the discharge medium in the form of short electrical pulses (~150-200 ns duration) at 15-20 kHz PRR. The pulsation of the medium is very small (duty cycle  $\sim 10^{-3}$ ). Then, the assumption of stationary heat conduction is valid and the steady state heat conduction equation is given as [153],

$$\nabla^2 T + \left( \frac{W_{in}}{K} \right) = 0 \quad (2.1)$$

where  $K = \alpha T + \beta$  is the thermal conductivity of alumina fiber insulation such that  $\alpha = 1.29 \times 10^{-4} \text{ W m}^{-1} \text{ K}^{-2}$  &  $\beta = 2.05 \times 10^{-2} \text{ W m}^{-1} \text{ K}^{-1}$  [154] and  $W_{in}$  is the electrical input power density. For the high aspect ratio ( $\frac{l}{2R} \gg 1$ :  $l$  = tube length &  $R$  = tube bore radius) cylindrically symmetrical discharge tube in steady state, the equation (2.1) reduces to give the heat flow per unit length as,

$$\frac{\delta \cdot P_{in}}{l} = -2\pi K r \frac{dT}{dr} \quad (2.2)$$

where  $\delta$  = fraction of electrical energy deposited,  $l$  = discharge tube length,  $r$  = radial coordinate,  $P_{in} = \frac{1}{2} C_s V_{Cs}^2 f$ , is the electrical input power such that  $C_s$ ,  $V_{Cs}$  &  $f$  are electrical storage

capacitance, storage capacitor voltage & PRR respectively. The solution of the above equation with boundary conditions,  $T(R) = T_w$  (wall temperature) and  $T(R') = T_o$  (fiber blanket outer temperature) & its simplification gives the required thickness (d) of the thermal insulation as,

$$d = R' - R = R \left[ \exp. \left[ \left( \frac{\pi l}{\delta \cdot P_{in}} \right) \{ \alpha(T_w^2 - T_o^2) + 2\beta(T_w - T_o) \} \right] - 1 \right] \quad (2.3)$$

The radial gas temperature profile  $T_g(r)$  and hence the axial gas temperature [ $T_g(0)$ ], can be calculated by solving the equation (2.1) in a similar fashion as [43,155],

$$T_g(r) = \left[ T_w^{m+1} + \frac{(m+1) \cdot \delta \cdot P_{in}}{4\pi R^2 K_o l} (R^2 - r^2) \right]^{\frac{1}{m+1}} \quad (2.4)$$

$$T_g(0) = \left[ T_w^{m+1} + \frac{(m+1) \cdot \delta \cdot P_{in}}{4\pi K_o l} \right]^{\frac{1}{m+1}} \quad (2.5)$$

where for the active medium gas mixture (HBr + Ne), the thermal conductivity of the gas is given as  $K = K_o T^m$  such that  $m = 1.54$ ,  $K_o = 1.8 \times 10^{-6} \text{ W m}^{-1} \text{ K}^{-1}$  for Ne-HBr mixture [7,126].

Fig. 2.1 shows the results of thermal analysis on discharge tubes differing in radius (R) and length (l), as employed in the present thesis work.

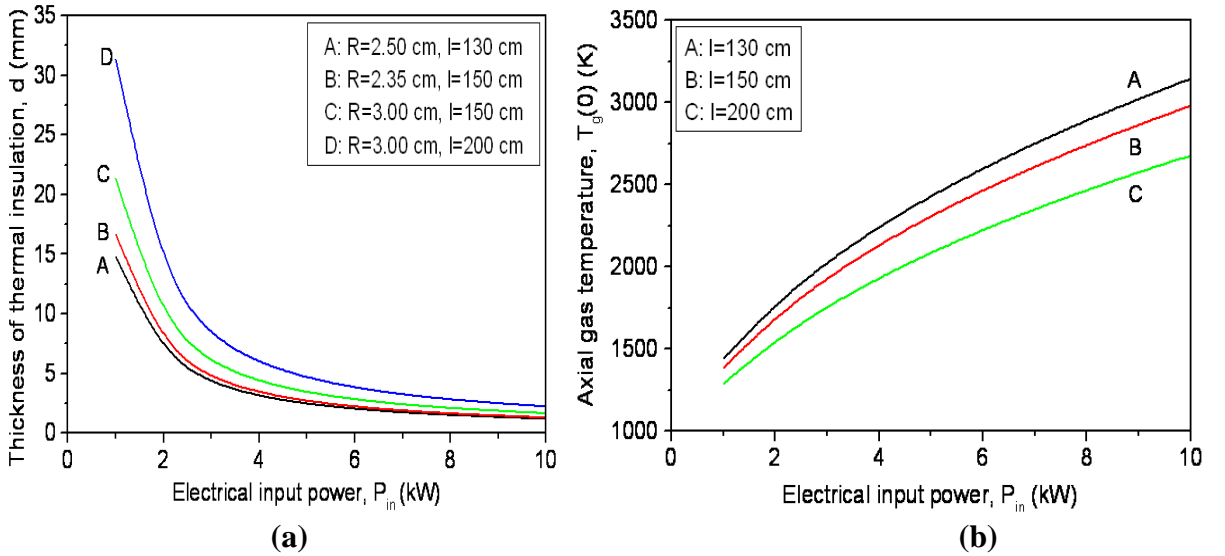


Fig.2.1 Variation of estimated thickness of thermal insulation (a) & axial gas temperature (b) with electrical input power for Copper-HBr lasers of different tube dimensions

Fig. 2.1a shows the variation of thickness of fiber insulation at various electrical input powers for the laser tubes ( $T_o = 450 \text{ K}$ ,  $T_w = 900 \text{ K}$ ,  $\delta = 0.85$ ). The required insulation thickness

reduces as the input power increases, as expected. It is also clear that for normally used average electrical of 4 to 5 kW in Cu-HBr lasers, the alumina fiber insulation thickness is in close range of a few mm for discharge tube of different lengths and diameters. The same is true irrespective of material of discharge tube such as fused silica or alumina, as the temperature drop due the discharge tube material/thickness is negligibly small. Fig. 2.1 b shows the variation of axial gas temperature with increases in input power for discharge tube of different lengths. The axial gas temperature increases with input power, as expected. However, for the typical input power (4 to 5 kW), the estimated axial gas temperature is less than 2500 K, as desired. This is to prevent the excessive dissociation of HBr molecules into H and Br, which is detrimental for the laser performance [7]. The thermal insulation thickness, for the laser tubes employed in the thesis work, has been suitably chosen as per the presented analysis.

### ***2.2.2 Laser electrodes & discharge tubes***

The electrode and discharge tube are the main parts of a Cu-HBrL. The gas discharge plasma and active medium are confined in the discharge tube within two electrodes. The discharge tubes of high purity (99.9%) fused silica ( $\text{SiO}_2$ ) and/or re-crystallised alumina of four different active volumes, (i) Fused silica:  $R = 2.5$  cm &  $l = 130$  cm, (ii) Alumina:  $R = 2.35$  cm &  $l = 150$  cm, (iii) Alumina:  $R = 3$  cm &  $l = 150$  cm and (iv) Fused silica:  $R = 3$  cm &  $l = 200$  cm, have been used. Both the materials are good electrical insulators, highly resistant to thermal shock, chemically inert to HBr, of low thermal conductivity and work reliably in the working temperature range (500-800 °C) of Cu-HBrLs. The fused silica tube has advantages of low cost, light weight, low outgassing impurity, better surface finish suitable for vacuum sealing and ease of fabrication for large sizes. However, the alumina discharge tube is mechanically more robust than that of fused silica. Fig. 2.2 shows the typical fused silica discharge tube/envelope, designed and fabricated in-house, used for Cu-HBrLs. The tubes have both their ends flared to protect thermal failure of the O-rings used for vacuum sealing with the electrodes. For the



*Fig. 2.2 In-house developed fused silica discharge tube for Cu-HBrL*

Cu-HBrLs with alumina discharge tubes, similar flare-ended fused silica envelopes are used with electrodes attached at their ends.

The discharge electrodes (Figs. 2.5 & 2.6) of the Cu-HBrLs consist of hollow copper cylinders of about 5 mm thick wall, each of which has a blind small hole (~3 mm diameter, ~5 mm deep) drilled on the face. Electrodes of high purity (99.99%) copper have been used as its reaction with HBr will not produce any new impurity in the discharge medium [6]. The small blind holes on the faces the electrodes serve to promote stable discharge attachment and flicker free laser operation. These copper cylinders are press-fitted into double walled, water cooled, stainless steel end flanges and are projected 5-10 cm into the discharge region and vacuum sealed at its both ends using Viton O-rings. For reason of minimising unwanted impurity due to chemical reaction with HBr, all the wetted parts have been ensured to be either copper or inert alumina/fused-silica, similar to the reported design [6]. At the low voltage side, there is a provision to inject HBr & Ne gas mixture just at the starting of the discharge region. The gas mixture is injected just at the beginning of gain medium. This is carried out through an “L” shaped fused silica capillary tube, either fused at one end of silica discharge tube (Fig. 2.2) or punctured through the electrode end flange for the case of Cu-HBrL with alumina discharge tube [156].

### ***2.2.3 Precision gas mixing set up for HBr & Neon***

One of the key issues associated with development of Cu-HBrLs is the reliable and precision control of HBr concentration inside the active discharge region. For this purpose, two different types of precision gas mixing set-ups are designed & developed. The first one is a

complete microprocessor based design (Fig. 2.3a), consisting of two thermal mass flow controllers for controlling Ne and HBr mass flow rate/concentration. The second one is a hybrid version, where the Ne flow rate is controlled by a mass flow controller (Bronkhorst: F-201 CV-100-AGD-22-V) & the HBr flow is controlled by an ultra-precision fine needle-valve (Parker: 4A-HOL-V-SS-TC). Both the units have ultra-high-vacuum compatible SS-316 tube fittings and are tested for helium leak integrity of better than  $10^{-10}$  mbar-lit./s. With these units, the gas flow rates upto 6 std.-lit./hr. and HBr concentration from 0.5 to 10% with accuracy of 0.5% is possible.

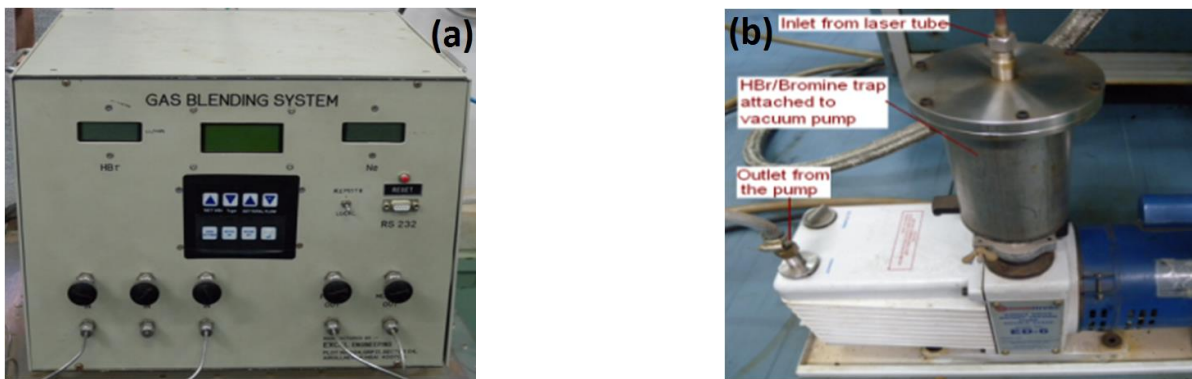


Fig. 2.3 Developed Ne-HBr gas controlling set up (a) and Halogen trap (b) used in Cu-HBrL

The Ne (99.99% purity) and HBr (98% purity) gases are pre-mixed before injecting into the laser discharge at the low voltage side and are taken out at the high voltage side through halogen neutralization chamber and rotary vacuum pump (Fig. 2.3b). The halogen neutralization chamber is a stainless steel vessel containing activated charcoal, silica gel & pellets of calcium hydroxide/carbonate. This ensured the neutralization of HBr/Br<sub>2</sub> exiting from the Cu-HBrL tube which is finally released as exhaust to outside the room in open atmosphere through a pipe.

#### 2.2.4 High voltage electrical pulse power supply

The electrical pumping pulse power technology plays a very crucial role in deciding the performance of Cu-HBrLs. Two types of high PRR, high voltage electrical pulse power supplies, differing mainly in terms of switching elements (thyatron or IGBT) are designed and

developed [157,158]. In both the cases, the resonant capacitor charge transfer (CT) circuit configurations are employed. The whole unit consists of a HV DC power supply, charging inductor ( $L_c$ ), blocking diode bank ( $D_b$ ), thyatron, storage capacitor ( $C_s$ ), peaking capacitor ( $C_p$ ), bypass inductor ( $L_b$ ) and the laser tube load. The electrical energy from the DC source is fed to the  $C_s$  through LC-resonant charging. The charging time of  $C_s$  is kept less than the laser inter-pulse period ( $1/f$ ). The blocking diode,  $D_b$ , prevents discharging of  $C_s$  before the switch is triggered. The voltage across  $C_s$  varies as [159],

$$V_{C_s} = V_o (1 - \cos \omega t) = 2V_o \sin^2 \frac{\omega t}{2} \quad (2.6)$$

where  $V_o$  is the input DC voltage. The charging current  $i$  and the resonance frequency  $\omega$  are,

$$i = V_o \sqrt{\frac{C_s}{(L_c + L_b)}} \sin \omega t \quad (2.7)$$

$$\omega = \frac{1}{\sqrt{(L_c + L_b)C_s}} \quad (2.8)$$

At the onset of storage capacitor charging;  $t = 0$ ,  $V_{C_s} = 0$  and  $i = 0$ . The maximum value of  $V_{C_s}$  is attained at  $t = \pi/\omega$ , known as charging time ( $\tau$ ). This is given as,

$$\tau = \pi \sqrt{(L_c + L_b)C_s} \quad (2.9)$$

At this time  $t = \tau$ , the  $V_{C_s}$  attains a value of  $2V_o$  while the circuit current goes to zero. The blocking diode  $D_b$  prevents reversal of current and the  $V_{C_s}$  remains equal to  $2V_o$  until the switch is triggered to conduct. The charging time is therefore determined by the upper limit of the laser PRR to be employed. The  $C_p$  is connected across the electrode and mounted as close as possible to the discharge tube. It makes the voltage pulse sharper and provides a still higher voltage across the discharge tube. When the thyatron is triggered, the charge on  $C_s$  is transferred to  $C_p$ . Then the voltage appears on the high voltage electrode and the breakdown takes place in the gain medium. By energy conservation principle, the maximum voltage possible at the  $C_p$  is given by,

$$V_{Cp} = V_{Cs} \sqrt{\frac{C_s}{C_p}} \quad (2.10)$$

In the present case, the thyatron based electrical power supply for Cu-HBrL consists of a 10 kV & 1 A rated, variac based DC power supply, oil-cooled high voltage modulator tank and thyatron trigger unit. The modulator tank consists of a charging inductor  $L_c = 150$  mH, hydrogen thyatron (E2V CX1535), its circuitry and storage capacitor(s) (Figs. 2.4a & 2.5b). This tank generates a lot of heat and hence, it is cooled through an oil circulation pump along with the water heat exchanger. The whole system is vertically mounted on a movable standard 19 inch rack. This power supply is capable of delivering average power of about 4-5 kW at required PRR of 15-20 kHz. However, higher PRR operation upto  $\sim 27$  kHz has been demonstrated but at the average electrical power limited to less than 3 kW [160].

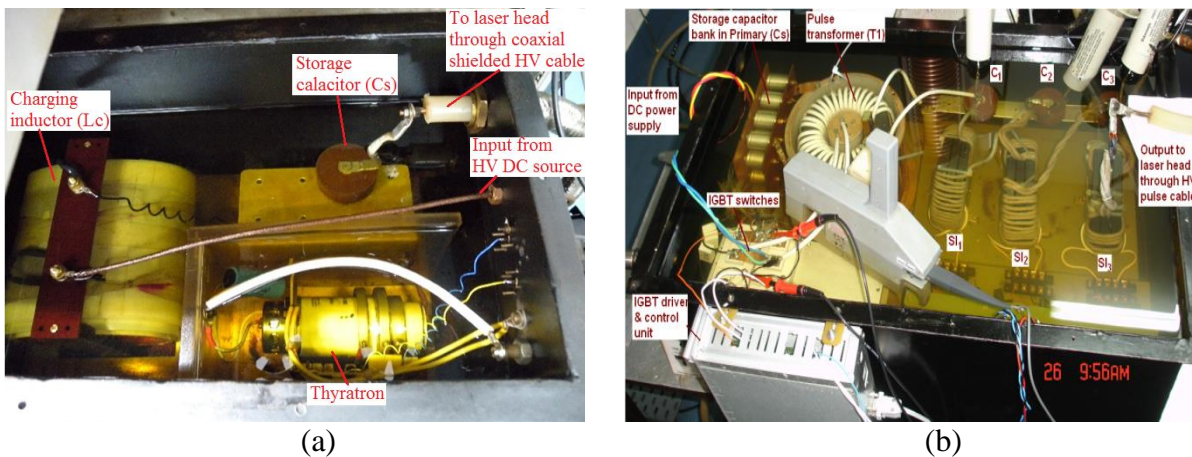


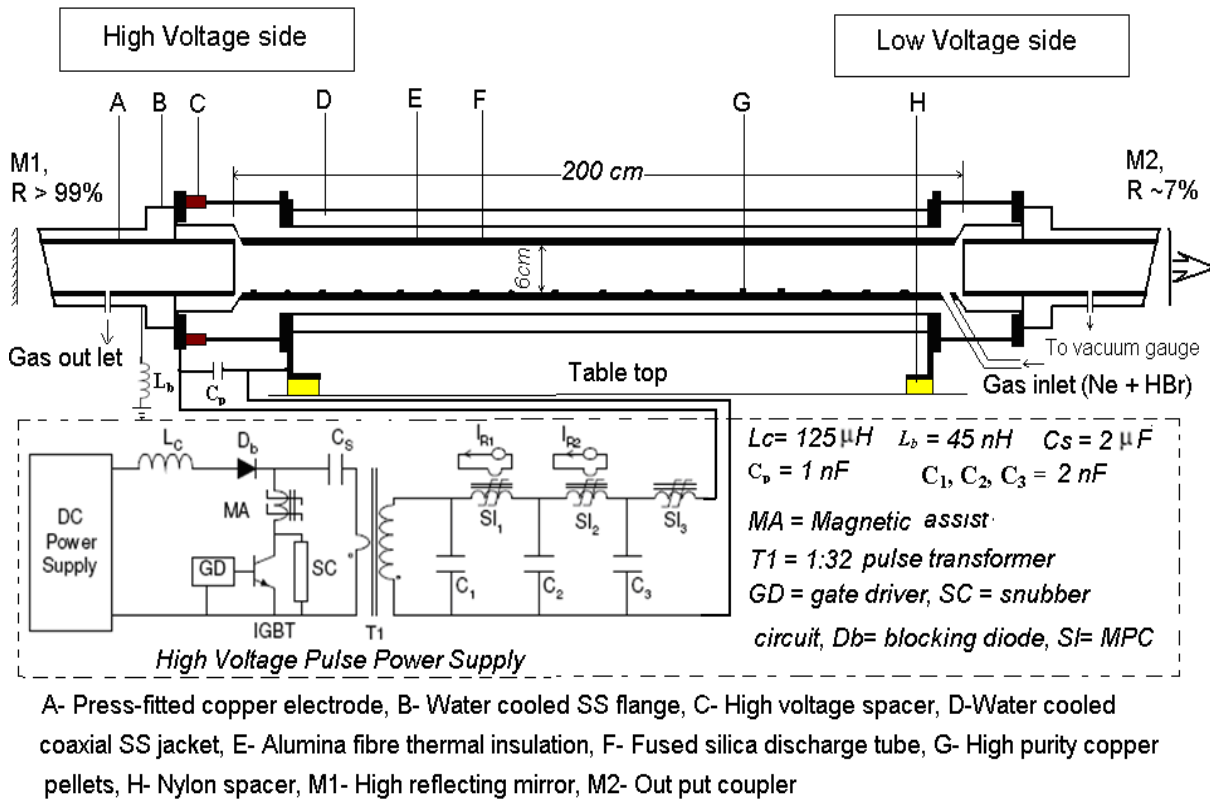
Fig. 2.4 Photographs of developed modulators based on (a) Thyatron and (b) IGBTs

The other type of pulsed power supply, designed & developed, is based on low voltage IGBT semiconductor switches (Figs. 2.4b & 2.5a). It mainly consists of a regulated DC power supply, a charging inductor ( $L_c$ ), a storage capacitor bank ( $C_s$ ), a magnetic assist (MA), several (4 Nos.) IGBT switches in parallel followed by a pulse step-up transformer (1:32) and three stages of MPCs in cascade. This excitation source functions as follows. As soon as the storage capacitor,  $C_s$  ( $\sim 2$   $\mu$ F) is resonantly charged to a maximum voltage from the DC power supply through  $L_c$  (200  $\mu$ H), the IGBT switches are triggered simultaneously. Then, the stored energy

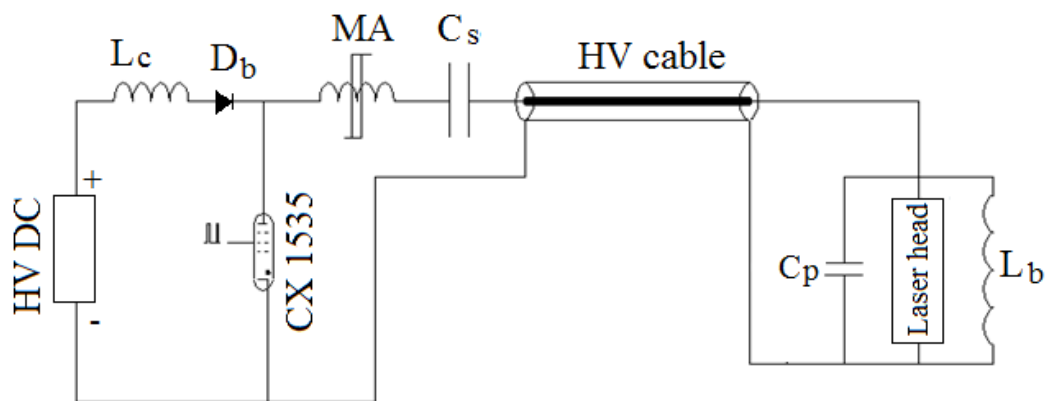
at  $C_s$  is transferred to the input capacitor ( $C_1$ ) of the first stage of MPC ( $SI_1$ ) through the MA, IGBTs and the transformer. The voltage build up at the  $C_1$  saturates  $SI_1$  and the energy is transferred to  $C_2$  resulting in compression of the current pulse. This process is repeated at  $SI_2$  and  $SI_3$  resulting an overall compression gain of the excitation pulses at the laser head. The power supply could be operated at average switched electrical power of 5-10 kW at PRR of 16-18 kHz, peak tube voltage of 15-25 kV with rise time of 70-80 ns. The overall power supply is assembled in the similar architecture as discussed for thyatron based supply. A bypass inductor of self-inductance ( $L_b$ ) (Fig. 2.5) about 40-50  $\mu$ H, which is made up of long copper tube & is connected across the laser tube, enables the laser tube to recover during inter-pulse period. This also serves as a path for gas exhaust from the Cu-HBrL tube, before the halogen neutralisation chamber, in addition with facilitating controlling of gas flow and pressure in the discharge tube. In the present thesis, the thyatron based system has been employed in low power (40 W) version of Cu-HBrL and the higher output power version lasers are based on IGBT solid state pulsers. The Cu-HBr laser power optimisation has been studied with the developed power supplies and the results are detailed in the section 2.5.

### ***2.2.5 Assembled Copper-HBr laser systems***

Following the successful development and testing of the subsystems, these are assembled and the overall systems are checked for vacuum and leak integrity better than  $10^{-8}$  mbar-lit./s. Fig. 2.5a shows the schematic of an assembled Cu-HBrL system, based on fused silica discharge tube, along with circuit diagram of IGBT switch based electrical excitation power supply, typically used in our 100 W average power class Cu-HBrL [14,124,158,161,162]. Fig. 2.5b shows the circuit diagram of the thyatron switch based electrical power supply which is used for our low power (40 W) version of the Cu-HBrL [158,160]. The laser is vacuum sealed at the electrodes by a pair of fused silica circular disks (thickness  $\sim$  1 cm, diameter  $\sim$  7.5 cm) attached to the electrode ends (other side of discharge)



(a)



(b)

Fig. 2.5 Schematic of assembled copper-HBr laser with (a) IGBT pulser (b) Thyatron pulser

by Viton O-rings at  $\sim 5^\circ$  inclination with respect to the laser tube axis, which also serve as end windows for optical beam exit. To prevent contamination by diffused CuBr molecules from the discharge region, the end windows are placed at about 30-40 cm from the electrode tips. Several high purity copper pieces ( $15 \times 10 \times 3 \text{ mm}^3$ ), machined for surface smoothness and are placed inside the discharge tube along its floor at regular intervals of  $\sim 10 \text{ cm}$ . A corrosion

resistant stainless steel diaphragm vacuum gauge (Leybold DIAVAC DV 1000) is used to monitor the pressure of buffer gas mixture. Depending on the input power level used, a thin layer of alumina fiber insulation is wrapped on the fused silica tube for the desired temperature. The optical resonator consists of a high reflecting plane mirror ( $R > 99\%$ ) and an anti-reflection coated fused silica blank (Reflectivity  $\sim 3.5\%$ ), which is used for the purpose of maximum power extraction from the gain medium. However, for high beam quality output, unstable resonators are used (Chapter 7 & 9). The 40 W class Cu-HBrL system is based on the conventional thyatron based pulse power supply, whereas all the other three high power versions are based on IGBT-solid state pulsers with minor modifications in  $C_s$  &  $C_p$  depending the tube geometry. For example, the 70 W version Cu-HBrL uses  $C_s \sim 1.5 \mu\text{F}$  &  $C_p \sim 2 \text{ nF}$ , the 85 W Cu-HBrL uses  $C_s \sim 2 \mu\text{F}$  &  $C_p \sim 1.3 \text{ nF}$  whereas the 110 W Cu-HBrL uses  $C_s \sim 2 \mu\text{F}$  &  $C_p \sim 1 \text{ nF}$ . Fig. 2.6 shows the photographs of the assembled Cu-HBrL systems.

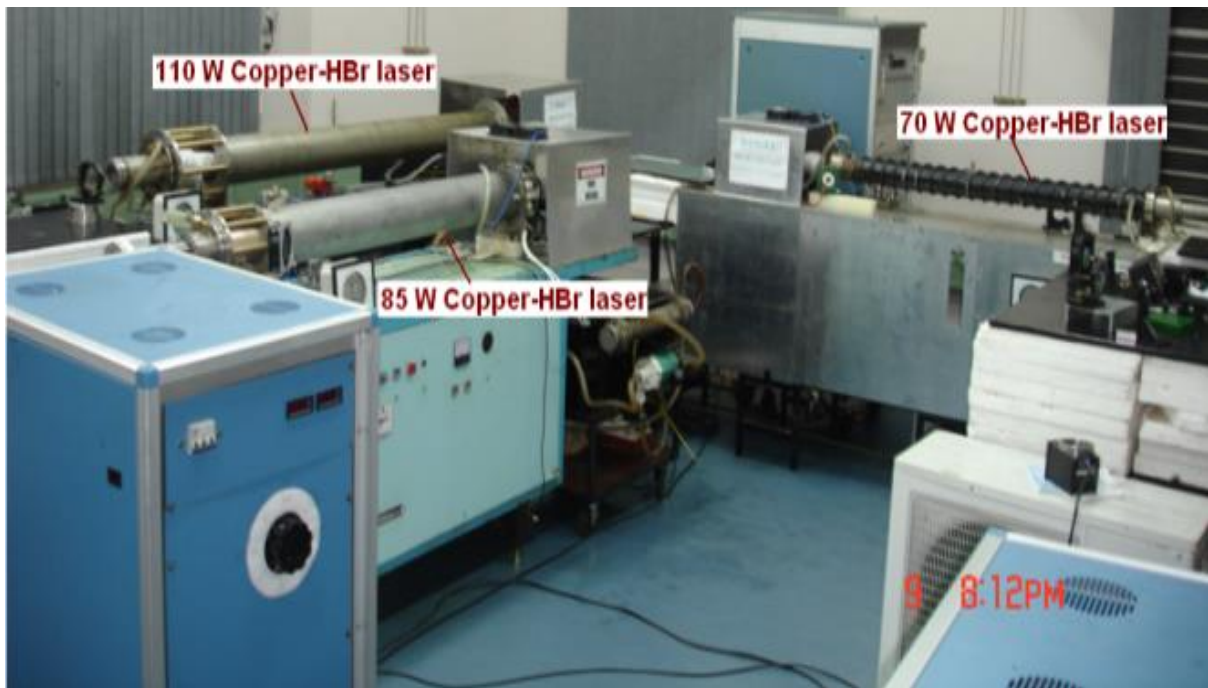


*Fig. 2.6 Photographs of the assembled Copper-HBr laser systems*

### **2.3 Safety systems for HBr gas handling**

HBr gas is a highly corrosive, colourless & odourless gas with very low threshold

limiting value (TLV) of about 3 ppm [163]. It is heavier than air and displaces oxygen. In the presence of moisture, it reacts violently & corrodes/degrades most of the materials. Therefore use of this gas involves risks of component failure as well as serious health hazards. In the present work, proper safety measures have been taken up. All the wetted parts of the involved systems are of corrosion resistant material (SS-316) with ensured helium leak integrity of the joints/assemblies better than  $10^{-8}$  mbar-lit./s. In addition, all the components are periodically purged with dry inert gases ( $N_2/Ar$ ) and checked for vacuum/pressure withstanding integrity.



Fig. 2.7 Photographs of installed HBr sensor, oxygen monitor(a) & HBr alarm system (b)

In order to handle the accidental leakage in the laboratory, proper detection & monitoring system for HBr are installed. Figs. 2.7a & b show the systems for monitoring HBr leakage (accidental) & ambient oxygen level in the laboratory and their relay & alarm system respectively. The HBr leak monitoring system (Make: Draeger, Germany & detection limit: 0-30 ppm with accuracy/resolution of 0.1 ppm) consists of an electrolyte as sensor element which produces current signal when HBr reacts with it. The amount of current generated is proportional to the HBr concentration. The alarm system, designed & developed in house, consists of dual stage alarm system with different audible range. The first alarm (80 dB) is actuated for HBr concentration of 3-13 ppm, whereas the second alarm (120 dB) is actuated for higher HBr concentration. In addition, the laboratory is equipped with personal protective

equipment such as protective mask with HBr neutralizing canister, breathing apparatus, chemical protective goggles & rubber clothing at par with OSHA standards [164].

#### 2.4 The developed 40-110 W average power Copper-HBr lasers

Based on the designed and assembled subsystems, as discussed in the previous section, four different Cu-HBrL systems are developed delivering maximum average laser powers of 40 W, 70 W, 85 W and 110 W at about 18 kHz PRR [14,124,158,160-162,165]. Tables 2.1 and 2.2 summarise the general and optimised technical features of the developed Cu-HBrLs, named for convenience of discussion as Cu-HBrL 1, 2, 3 & 4.

*Table 2.1 General features of the developed 40 to 110 W output power Cu-HBrLs*

Sl. No.	Laser tube dimension (Inner radius R x length l)	Laser tube material	Electrical switch	Laser output power @ PRR
Cu-HBrL 1	2.50 cm x 130 cm	Fused silica	Thyratron	40 W @ 18 kHz
Cu-HBrL 2	2.35 cm x 150 cm	Alumina	IGBT	70 W @ 18 kHz
Cu-HBrL 3	3.00 cm x 150 cm	Alumina	IGBT	85 W @ 18 kHz
Cu-HBrL 4	3.00 cm x 200 cm	Fused silica	IGBT	110W @ 18 kHz

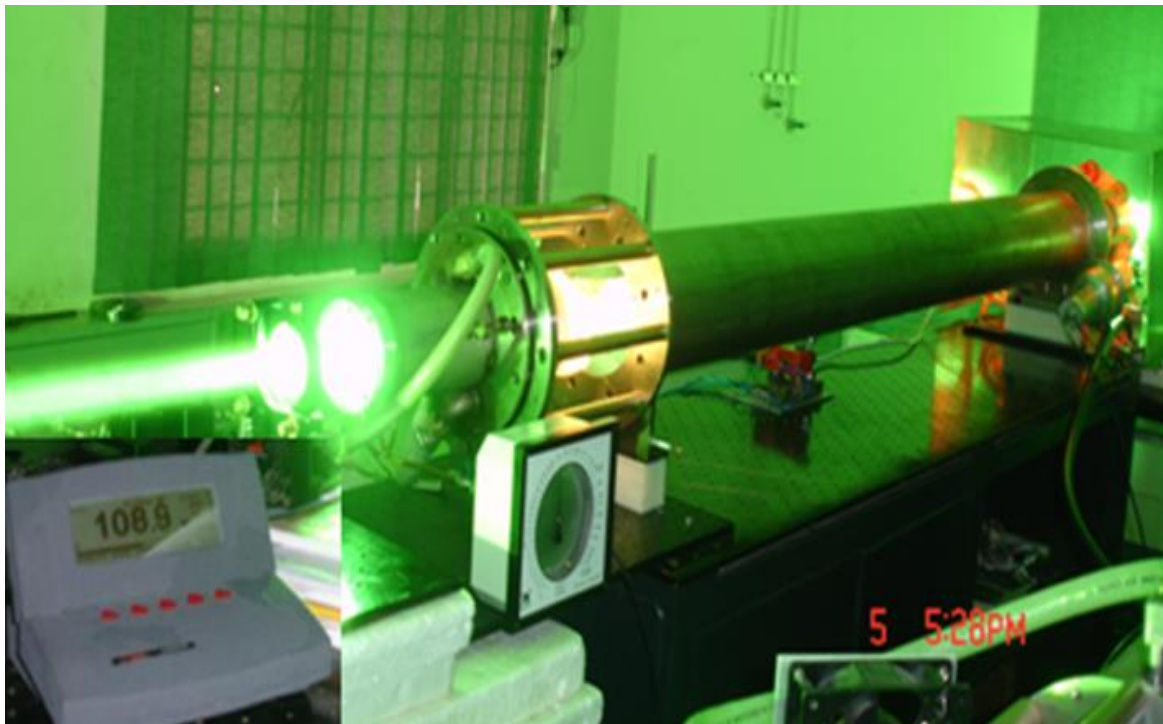
*Table 2.2 Optimised parameters of the developed 40 to 110 W output power Cu-HBrLs*

Sl. No.	P (mbar)	$\phi$ (lit.- atm./hr)	C <sub>s</sub> (nF)	C <sub>p</sub> (nF)	f (kHz)	V <sub>Cs</sub> / V <sub>b</sub> (kV)	P <sub>in</sub> (kW)
Cu-HBrL 1	~30	~ 3.5	2	1.3	18	14.4 /15	~3.7
Cu-HBrL 2	~25	~ 5	1540	2	18	0.75/17.3	~7.8
Cu-HBrL 3	~35	~ 6	1980	1.3	18	0.72/17.5	~9.2
Cu-HBrL 4	~35	~ 6	1980	1	16 - 18	0.80 - 0.76 / 23.3	~10.1 - ~10.3

Here, the parameters P = buffer gas pressure (Ne + HBr),  $\phi$  = buffer gas flow rate (Ne). Figs. 2.8 show the two representative photographs of the successfully developed high power Cu-HBrLs (Fig. 2.8 a 70 W Cu-HBrL & Fig. 2.8 b 110 W Cu-HBrL) in operation in our laboratory.



(a)



(b)

*Fig. 2.8 Photographs of the successfully developed high power Cu-HBrLs in operation*

*(a) The Cu-HBrL 2 (70 W power) (b) The Cu-HBrL 4 (110 W power)*

## 2.5 Parametric studies for laser output power of the developed Cu-HBr lasers

The average output power of a Copper-HBr laser has a complex dependence on the operating parameters such as buffer gas flow rate & pressure, HBr concentration, electrical input power, charging voltage, discharge capacitance (storage & peaking) and PRR. The Cu-HBr laser optimization is an iterative process where the output power is studied by varying one operating parameter at a time while keeping the others fixed. Depending on the laser discharge tube volume/dimension, the optimised values of these parameters, for maximum laser output power, also differ. In view of this, a detailed experimental study on the variation of average output powers of the developed Cu-HBrLs is carried out with respect to the associated operating parameters. For all the four investigated Cu-HBrLs 1 to 4, the same PPR, consisting of a high reflectivity (99.9%) hard di-electric coated mirror as high reflector & an AR coated fused silica disc (~3.5% reflectivity) as output coupler is used. The resonator length is kept at minimum possible distance between mirrors which is in range 2.0 to 2.8 meter.

The laser conversion efficiencies are calculated based on energy stored in the storage capacitor ( $C_s$ ). Values of the peaking capacitors ( $C_p$ ) are kept nearly half that of the  $C_s$  [1, 4-6, 166]. The storage capacitor charging voltages ( $V_{C_s}$ ) and laser-head discharge voltages ( $V_b$ ) are monitored, by using high voltage probes (Tektronix P6015A, band-width: 75 MHz), across  $C_s$  and  $C_p$  respectively. The laser discharge currents are monitored using a fast current transformer (Pearson 2878, band-width: 70 MHz) whereas the laser optical pulses are monitored using bi-planar vacuum photo-diodes (Hamamatsu: R1193U-52; 0.27 ns rise-time). These waveforms are recorded using a digital oscilloscope (Model: Tektronix-TDS 540 D or Lecroy-Waverunner 6050A; band-width: 500 MHz). The average laser output power was measured using a thermal power meter (Gentech TPM 300 CE or Ophir-LaserStar-FL250A-RP-SH). The temperatures of the discharge-tubes/discharge-tube-envelopes are monitored using a floating K-type thermocouple, attached onto the discharge tube. The laser discharge tubes are maintained at

almost constant temperature level of  $\sim 900$  K at all the input powers used, by suitably manipulating the amount of thermal insulation and additional cooling arrangement.

### 2.5.1 Buffer gas pressure & flow rate

Figs. 2.9a & b show the variations in laser output power with buffer (Ne) gas flow rates ( $\phi$ ) and pressures (P) for the Cu-HBrLs 1 to 4. Neon gas flow rates upto 6 lit.-atm./hr., limited by the present gas flow systems, have been used. At each operating point, the HBr concentration has been adjusted suitably for maximum laser output power. All other parameters are kept constant at their optimized values as given in table 2.2. It is seen that for all the investigated Cu-HBrLs, initially the output power scales up almost linearly as buffer gas flow rate increases. After a certain flow rate, which is different for different Cu-HBrLs, the laser power either saturates or changes the slope of increment or falls. The optimum flow rates for Cu-HBrL 1 and Cu-HBrL 2 are  $\sim 3.5$  lit.-atm./hr and  $\sim 5$  lit.-atm/hr with corresponding average laser output powers of 42 W and 72 W respectively. For Cu-HBrL 3 and Cu-HBrL 4, the maximum output powers are 86 W and 110 W respectively, for flow rate of  $\sim 6$  lit.-atm./hr. The variation of the output power with respect to the buffer gas flow rate is faster for Cu-HBrL 4 as compared to that of Cu-HBrL 3. On the other hand, for the variation in the buffer gas

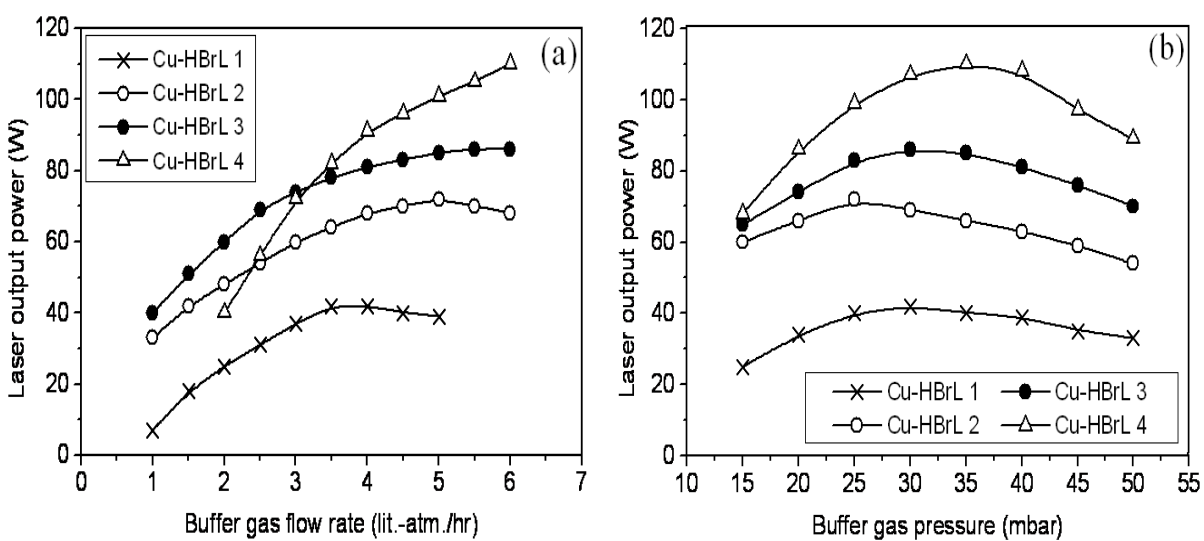


Fig. 2.9 Variation of Cu-HBrL power with buffer gas flow rate (a) & buffer gas pressure (b)

pressure in the investigated range, from 15 to 50 mbar, the laser output powers are maximum at 25-35 mbar (Fig. 2.9b). The optimum buffer gas pressures are 25-30 mbar, ~25 mbar, ~30 mbar and ~35 mbar for Cu-HBrL 1, Cu-HBrL 2, Cu-HBrL 3 and Cu-HBrL 4 respectively. These experimental results and their trends can be understood as follows.

In a Cu-HBrL, the role of buffer gas flow is to supplement/replenish the laser gain medium continuously with the active bromine species (HBr, Br & Br<sub>2</sub>) as well as for homogenisation of the copper precursors as HBr reacts mostly from upstream end [116, 130, 167]. The thermally dissociated bromine species, in the heated active medium, are lost due to diffusion towards the cooler end-window regions [130, 167]. The attained laser performance is a balancing act between the inlet HBr concentration and loss of bromine species by diffusion as well as inefficient homogenisation of copper precursors. In a steady-state optimum condition, the typical density of atomic bromine present in the discharge tube is about  $10^{15}$  cm<sup>-3</sup> [116, 130, 131]. Hence, when the flow rate of HBr is less than optimum level, the net available density of the bromine bromine species reduces. This in turn lowers the laser copper atom density in the active medium and the output power reduces. On the other hand, the decrease in output power at the higher flow rates is attributed to loss of bromine species by increased convective transport away from the gain region, leading to decrease in ground state as well as excited state copper density during the excitation phase [130, 167]. Also, the bromine diffusion speed is a function of active tube length (gain length), operating pressure & gas temperature [167]. Hence, the trends in laser power vs. buffer gas flow rates are different for Cu-HBrL 1 to 4. These considerations lead to typical volume replacement time of 1 to 2 minutes. This in turn requires optimised gas flow rates in Cu-HBrLs. At equivalent input power loading & same bore diameter tubes, longer the tube length more is the requirement of entrainment of the bromine species. Hence the gas flow rate in Cu-HBrL 4 is more than that in Cu-HBrL 3. This led to faster rise of laser output power in Cu-HBr 4 as compared to Cu-

HBrL 3, hence there is a cross-over in power curves (Fig. 2.9a). Similarly, the buffer gas pressure has important role in dictating the impedance matching from the laser circuit to the gain medium and deciding the peak electron temperature. The fall in the Cu-HBr laser output power at higher pressure, beyond an optimum (Fig. 2.9b) is likely due to decrease in peak electron temperature (due to increased collision), leading to relatively inefficient laser excitation. This seems to have a dominating effect over the increased impedance matching due to high pressure. At the same time, the decrease in laser output power at lower pressure, below optimum, is likely due to reduced electron temperature and deteriorated impedance matching. A marginal variation, in optimum pressure for the different Cu-HBrLs used, may be attributed to differences in the active electric fields ( $E/P$ , where  $E$  is electric field across the tube) and/or different impedances offered due to differing tube length & diameter [41].

### 2.5.2 HBr concentration

Fig. 2.10 shows the variation of average output power of the Cu-HBrL 1 to 4 as a function of HBr concentration from 2 to 10% of Ne-HBr mixture. The HBr gas concentration (its mass flow rate or pressure) is varied with the developed precision HBr gas mixing set up as described in section 2.2.3. The HBr flow rate and its partial pressure have been varied together with the buffer gas flow rate at fixed pressure. In the beginning, the discharge tubes

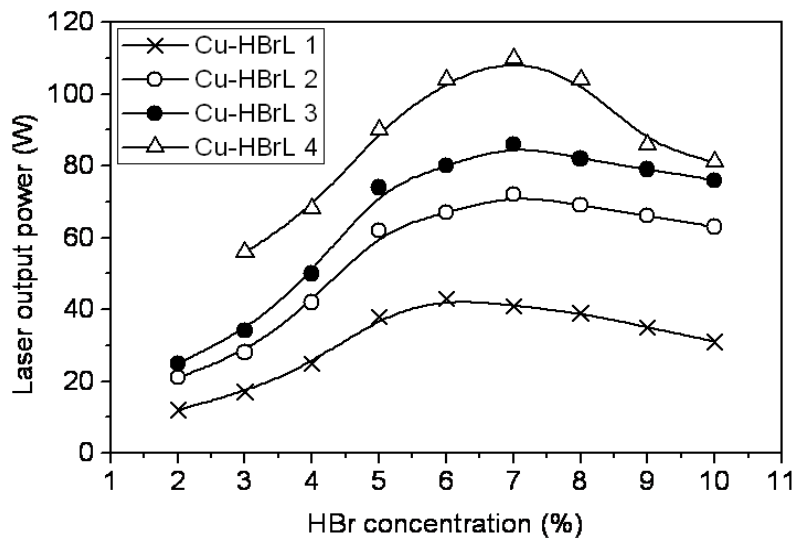


Fig. 2.10 Variation of output power with HBr concentration in Cu-HBrLs

are heated with only Ne buffer gas to around  $\sim 600$  °C and then the HBr gas is mixed and injected into the tubes. The Ne gas pressures as well as its flow rates are set at their corresponding optimal values as shown in Figs. 2.9a & b. For all the Cu-HBrLs, the laser output power increases rapidly as the HBr concentration increases from 2 to 5-6%, attains peak in the range of 5-8% and then falls slowly. For the HBr concentration beyond  $\sim 8\%$ , the instabilities in the laser discharge start. Then the laser beams are gradually quenched with increase in the proportion of yellow radiation, differing from green & yellow beam ratio in the optimal conditions. For Cu-HBrL 1, the output power increases quickly from  $\sim 12$  W at  $\sim 2\%$ , attains maximum of  $\sim 42$  W at  $\sim 6\%$  and the falls to  $\sim 31$  W at 10% HBr concentration. Similarly for Cu-HBrL 2 to 4, the output powers increase monotonically from  $\sim 21$  W,  $\sim 25$  W &  $\sim 50$  W for  $\sim 2\%$  concentration and attain the maximum levels of  $\sim 72$  W,  $\sim 85$  W &  $\sim 110$  W at  $\sim 7\%$  HBr concentration. These observations can be explained as follows.

The HBr concentration in a Cu-HBrL active medium has twin roles. First, it seeds the active medium with laser copper atoms through chemical reaction with metallic copper and second, it enhances the laser kinetics favouring plasma relaxation during the inter-pulse period [120,121]. The variation in the laser output behaviour is a balance between increase in laser copper density and decrease in electron temperature & electron density. In the beginning as the HBr concentration increases, available copper atom density in the active medium increases. This leads to the increase in laser power due to enhanced population inversion. However, for HBr concentrations above optimum level, the increased production of copper atoms in the active medium leads to reduced average electron temperature below the optimal value of 4-5 eV. This is responsible for the increased population to the LLLs and hence reduced population inversion & laser output power [32-35]. This is the possible reason why the laser output beam turns yellow for higher HBr concentration as the population inversion corresponding to the green line is terminated first due to its proximity to the ground level [12, 13]. In addition, for

higher HBr concentration, the electron density is quenched below the critical value for stable discharge ( $\sim 10^9\text{-}10^{10} \text{ cm}^{-3}$ ), owing to electron scavenging property of Br. This leads to impedance mismatch (high impedance) and discharge instability.

### 2.5.3 Pulse repetition rate

Figs. 2.11a & b show the variation of the laser output power with PRR for Cu-HBrL 1 and Cu-HBrLs 2 to 4 respectively. For Cu-HBrL 1, the variation in the PRR is carried over a wide range of PRR (15-28 kHz) by changing the values of  $C_s$ . The corresponding  $C_p$  values are also changed accordingly to about  $C_s/2$ , for efficient circuit matching. However, for Cu-HBrLs 2 to 4, which are based on IGBT + MPC based electrical power supplies, wide variation in PRR is not possible. This is because the MPCs are designed for almost fixed PRR operation with very narrow tolerance, which otherwise would cause increased losses in the modulator and onset of occasional voltage spikes at the IGBTs leading to their failure [168-170]. The Cu-HBrLs of 4 to 8 cm bore diameters are optimised mostly at 15-20 kHz PRR [4-7,160]. Therefore, the Cu-HBrLs 2 to 4 are designed to operate in the PRR range of around  $17 \pm 2$  kHz. For Cu-HBrL 1, three different pairs of  $C_s/C_p$  (2 nF / 1 nF, 1.6 nF / 0.8 nF & 1 nF / 0.5 nF) have been used corresponding to resonant charging frequencies (equation 2.8) of  $\sim 18$  kHz,  $\sim 20.5$  kHz &  $\sim 26$  kHz respectively. It is observed that for Cu-HBrL 1, the maximum output power

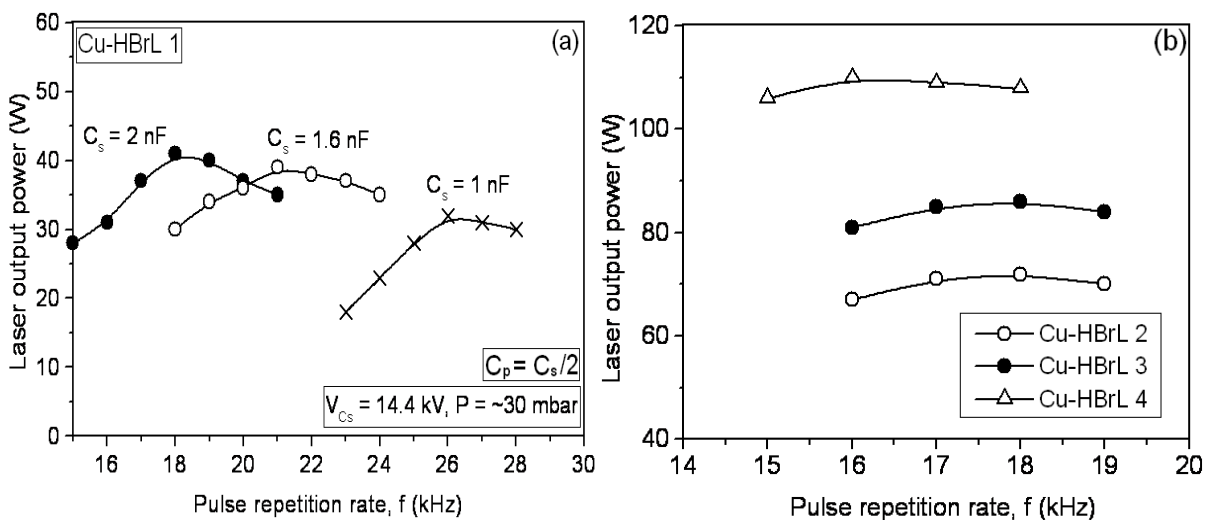


Fig. 2.11 Variation of the laser output power with pulse repetition rates in Cu-HBrLs

of ~42 W is obtained at  $C_s = 2\text{nF}$  for 18 kHz PRR. For lower  $C_s$  values of 1.6 nF & 1 nF, the corresponding maximum output powers decrease to ~39 W & ~32 W at PRR of 21 kHz & 26 kHz respectively. For  $C_s = 2\text{nF}$ , the PRR is varied over 15 to 21 kHz, leading to corresponding laser output of ~28 to ~35 W. For higher value of  $C_s = 2.6\text{ nF}$ , the laser output power reduces (not shown) to ~39 W at 16 kHz PRR. On other hand, for lower values of  $C_s = 1.6\text{ nF}$  and  $C_s = 1\text{ nF}$ , the PRR is varied over 18 to 24 kHz and 23 to 28 kHz respectively, producing corresponding laser output powers of ~30 to ~35 W and ~18 to ~30 W respectively. Hence, the Cu-HBrL 1 is operated over PRR range of 15-28 kHz with laser output power of 30-40 W [160]. Similarly for Cu-HBrL 2 & 3, with the variation in PRR from 16 to 19 kHz, the laser output power vary from ~67 to ~70 W with maximum of ~72 W and ~81 to ~84 W with maximum of ~86 W, both at 18 kHz PRR, respectively. On the other hand, for Cu-HBrL 4, the output power varies within ~106 to ~108 W for 15-18 kHz PRR, with maximum of ~110 W. The observed trends can be explained as follows.

The  $C_s$  values in a Cu-HBrL decide the rate of rise of voltage across laser tube, tube breakdown voltage & hence electron temperature and input electrical pulse energy [33-35]. The observed optimum value of  $C_s$  is linked to the achieved optimum electron temperature favouring the efficient upper laser level excitation [33-35]. Higher  $C_s$  value than optimum leads to increased heating effects & copper ionisation, thereby, inefficient laser excitation while the lower  $C_s$  value reduced the input pulse energy. This laser power reduces in both the cases. For a given  $C_s$ , the reduction of output power at either side of the resonant frequency maxima is attributed to lowering of average input power (for lower PRR) and non-optimal charging of  $C_s$  (for higher PRR). For Cu-HBrL 2 to 4, the laser power remains almost a constant level of 104-110 W within the scanned narrow PRR range. This constancy of laser power is most likely due to the counterbalancing acts of input power and gas temperature in averaging out the laser gain in the narrow range PRR scan.

### 2.5.4 Electrical input power (charging voltage)

Figs. 2.12a & b show the variation of laser output power and laser efficiency (based on input from storage capacitor). The electrical input powers ( $P_{in} = 0.5 C_s V_{Cs}^2 f$ ) are varied by changing the storage capacitor charging voltage ( $V_{Cs}$ ) at 18 kHz PRR. For the Cu-HBrL 1,  $V_{Cs}$  is varied from 11 to 17 kV, which corresponds to variation in  $P_{in}$  from ~2.2 to ~5.2 kW. The laser output power increases rapidly from 10 to 42 W for input power variation from ~2.2 to ~3.7 kW. Then, it reaches slowly to 50 W at ~5.2 kW. The corresponding laser efficiency varies from 0.46% to 0.96% respectively with a maximum of ~1.13% at 42 W laser output. For Cu-HBrL 2, the  $V_{Cs}$  is varied from ~650 to ~800 V that corresponded to variation in  $P_{in}$  from ~5.9 to ~8.9 kW at 18 kHz PRR. The corresponding laser power increases monotonically from ~33 to ~72 W (at ~8.2 kW) and attains a constant level of 71-72 W, thereafter. The efficiency also scales with  $P_{in}$ , from 0.56% to 0.80%, with a maximum of ~0.88% at 72 W laser output. Similarly for Cu-HBrL 3, as the  $V_{Cs}$  is varied from ~600 to ~760 V ( $P_{in}$  from ~6.4 to ~10.3 kW), the laser corresponding power increases concurrently from 59 to 85-86 W and the efficiency remains at almost constant level of 0.92-0.95% (upto 83 W) and then slowly decreases to ~0.82%. On the other hand, for Cu-HBrL 4, the laser output power and efficiency

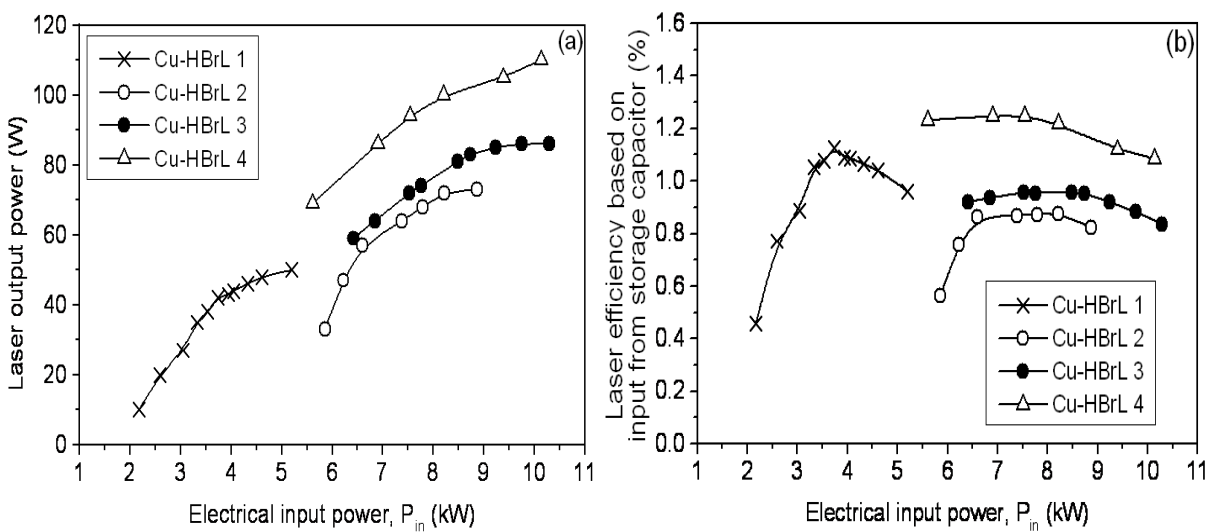


Fig. 2.12 Variation of output power(a) and efficiency based on input from storage capacitor (b) with  $P_{in}$  for Cu-HBrLs

are studied for different values of  $V_{Cs}$  varying from ~600 to ~800 V ( $P_{in}$  from ~5.7 to ~10.1 kW) at 16 kHz PRR. The corresponding laser output power rapidly rises from ~70 W to ~110 W, with a constant level of efficiency of ~1.2% at 70-100 W output level and then decreases slowly to ~1% at ~110 W output. Similar exercise, carried out at 18 kHz PRR level, albeit at proportionately reduced  $V_{Cs}$ , produces almost similar results.

In all the four lasers studied, it is clear that as  $V_{Cs}$  or  $P_{in}$  increases, the laser output increases monotonically upto certain level and then its slope reduces. This may be explained as follows. With the increase of the electrical input power, the HBr concentration is also made to increase which produces larger amount of copper bromide vapour. Therefore, larger fraction of copper atoms contributes to population inversion, hence the laser output power increases. In addition, higher the input power/voltage, higher is the rate of pumping to ULL of copper. On the other hand, the larger input power also results in larger current density through the discharge tube. This decreases the fraction of the upper laser level pumping due to cumulative effect of increased rate of ionization of copper and meta-stable population [34, 35]. In addition, increased input power results in higher average gas temperature. This in turn alters the equilibrium/optimal concentration of HBr and its dissociation products (H, Br) [7]. Therefore the beneficial effect of HBr i.e. faster reduction of inter-pulse electron density by process of dissociative attachment with low energy electrons ( $HBr + e \rightarrow H + Br^-$  or  $H^- + Br$ ) followed by recovery of ground state copper density by ion-ion neutralization ( $Cu^+ + Br^- \rightarrow Cu + Br$  &  $Cu^+ + H^- \rightarrow Cu + H$ ), is suppressed [7, 124]. Hence the laser efficiencies decrease beyond certain input powers. A detailed analysis of the pulse discharge characteristics and associated processes of these Cu-HBrLs are presented in chapter 3.

## **2.6 Scaling behaviour of the developed Cu-HBr lasers**

It is understood that for Cu-HBr laser, the power scaling behaviour is a complicated process due to complex dependency of the laser performance on HBr gas purity [124],

chemistry associated with HBr & its reaction products [7,15,124], discharge tube construction & optical resonator configuration [1, 4-7], excitation techniques [6, 7] etc. In addition, the operating parameters of Cu-HBrLs critically affect the laser performance as elaborated in section 2.5. However, based on our studies on four Cu-HBrLs (1 to 4), typical scaling laws for designing & developing Cu-HBr laser may be put forward as follows. The developed Cu-HBrLs differ in terms of their active volumes due to different discharge tube bore diameters ( $D' = 2R$ ) and lengths ( $l$ ) i. e.  $D' = 50$  mm &  $l = 130$  cm,  $D' = 47$  mm &  $l = 150$  cm,  $D' = 60$  mm &  $l = 150$  cm and  $D' = 60$  mm &  $l = 200$  cm. It is also important to note that in all the cases the laser output beam diameters ( $D$ ) are about 60% of the tube bore diameters due to discharge constriction [13]. Taking this fact into account, the specific optical (laser) output energy of the Cu-HBrLs is  $\sim 2.5 \mu\text{J}/\text{cm}^3$ . The maximum laser average output power scales as  $P_{out}(W) \approx l(\text{cm}) \cdot D'(\text{mm})/k$ , where  $k$  is constant that depends on various factors such as tube bore diameter, excitation scheme/circuitry, laser tube construction & resonator cavity configuration, HBr purity etc. For typical bore diameter of 50-60 mm (as in our case) with conventional capacitor transfer electrical excitation circuit, the value of  $k$  is about 100. This law form is in line with the typical power scaling behaviour of conventional CVLs [15].

In the present study on Cu-HBrLs, the typical electrical input power (average) per unit tube length is  $\sim 2.5$  kW/m for the maximum output power of the Cu-HBrLs. This value is a compromise between tube heating effects and laser pumping rate. The typical discharge voltage per unit length (electric field:  $E$ ) required is found to be in the range of 12 - 15 kV/m whereas the typical buffer gas pressure ( $P$ ) is in the range of 25 - 35 mbar with HBr partial pressure in the range of 1.5 - 2 mbar. These values translate to the typical value of the discharge characterising electric field parameter  $E/P = V_b/P \cdot l \approx 4 - 5$  V/cm-mbar, which essentially decides the average electron temperature in the discharge. The PRR corresponding to maximum average laser output power is  $f_{max} \approx 15 - 20$  kHz. Typical value of  $f_{max} = 17 \pm 1$

kHz is a good compromise between decrease in output pulse energy due to increased plasma heating effect as well as power loss at the high voltage pulse modulator for higher PRR vis-à-vis increased output pulse energy at lower PRR. Typically 6-7% HBr concentration i.e. 6-7% HBr + Neon (balance) is the optimized value in most of the reported Cu-HBr lasers. Similarly, the optimised buffer gas flow rate corresponds to volume replacement time of typically 1-2 minutes. Requirement of low output beam divergence from Cu-HBr laser demands the discharge tube aspect ratio ( $l/D'$ ) to be about 25 – 35. Constraints in achieving the required electric field over long tube length and requirement of output beam of low divergence by allowance of 3-4 number cavity round trip (limited by the laser gain duration), limits the value of length,  $l$ , to be less than 300 cm (typically 100-200 cm). These scaling trends are more or less consistent with the reported values in the field.

## **2.7 Conclusions**

In conclusion, this chapter presented a comprehensive study on design, construction/development and laser output power optimisation for different output power versions Cu-HBrLs (Cu-HBrL 1 to 4). These included detailed thermal design of the laser, mechanical design of the laser electrodes & discharge tubes, design of precision gas mixing set up for the HBr & Ne gases, design/development of high-PRR, high-voltage & fast-switching electrical excitation sources. These subsystems are successfully developed, assembled/integrated into realisation of 40 to 110 W average output power versions of Cu-HBrLs operating at 16-18 kHz PRR. Two types of electrical power supplies e.g. the thyatron and IGBT switch based pulsers are employed for the electrical excitation of these lasers. The safety handling of HBr is also addressed through incorporation of suitable HBr sensor and alarm system. The laser output powers have been studied for different buffer gas pressures & flow rates, HBr concentrations, pulse repetition rates and switched electrical input powers. The results for the four developed Cu-HBrLs are presented and discussed.



## Chapter 3

### Analysis of electrical pulse pumping characteristics of the Cu-HBr lasers

#### 3.1 Introduction

Studying the electrical discharge pulse pumping characteristics of a high power Cu-HBr laser is of crucial importance for performance optimization as well as evaluation and understanding of the ongoing plasma processes inside the active medium. These are linked with issues of impedance matching & electrical power deposition patterns in the active medium of a Cu-HBrL and are still not very well understood in the field. A limited study on the pulsed discharge characteristics of low power (10-20 W) Cu-HBrL and copper bromide (CuBr/CuBr-H<sub>2</sub>) lasers have been reported with a conventional thyatron based pulser [121, 126]. The pulsed discharge characteristics has also been studied and analyzed in a conventional CVL with thyatron and IGBT pulsers based excitation schemes under different input power conditions [168]. The average electrical power deposition into the laser constituents has been estimated by calorimetric methods in different copper laser variants [7, 169]. However, no such time resolved or averaged power deposition study is available in the case of a high average power (40-100 W) class Cu-HBrL in general and specifically with a solid state pulser.

This chapter presents a comprehensive analysis, both time resolved & time averaged, on the electric discharge characteristics of solid state switch (IGBT) based high average power (100 W class), high pulse repetition rate (16 kHz) Copper-HBr laser at various excitation conditions. Various discharge plasma parameters such as electrical inductance, resistance, active laser head voltage, active electrical power, pre-pulse electron density and axial gas temperature are evaluated by numerical processing of the measured laser head voltage-current waveforms. During transfer of energy to the laser discharge plasma, fractional losses in the high voltage pulse modulator and effective energy coupling for the laser excitation process are evaluated. The average laser performances at various input powers are correlated with both its

time resolved as well as average gas discharge parameters. Role of other Cu-HBrL operating parameters such as HBr concentration, buffer gas pressure, buffer gas flow rate and pulse repetition rate as well as the laser active volume are studied. The study is also augmented with a comparison on electrical input coupling behaviour with different electrical pulsers (thyatron vs. solid state) as well as active medium composition (Cu-HBrL vs. CVL).

### 3.2 Theoretical background of the measurement and analysis

A Cu-HBrL, as an electrical circuit element, can be represented (Fig. 3.1a) as a series combination of laser tube inductance ( $L$ ) and gas discharge resistance ( $R_d$ ) [121,126,128]. Therefore, the instantaneous voltage measured across the laser tube i.e.  $V(t)$ , is sum of the voltage across  $L$  i.e.  $V_L(t)$ , and the voltage across  $R_d$  i.e.  $V_d(t)$ . This can be expressed as,

$$V(t) = V_d(t) + V_L(t) \Rightarrow V_d(t) = V(t) - L \frac{dI(t)}{dt} = I(t) \cdot R_d(t) \quad (3.1)$$

For laser tube of fixed geometry at a given operating condition, the laser tube inductance  $L$  is constant and can be determined from the laser head voltage & current waveforms (Fig. 3.1 b).

At the first zero of the current waveform i.e. at  $t = t_0$ ,  $[I(t)]_{t=t_0} = 0 \Rightarrow [V_d(t)]_{t=t_0} = 0$ .

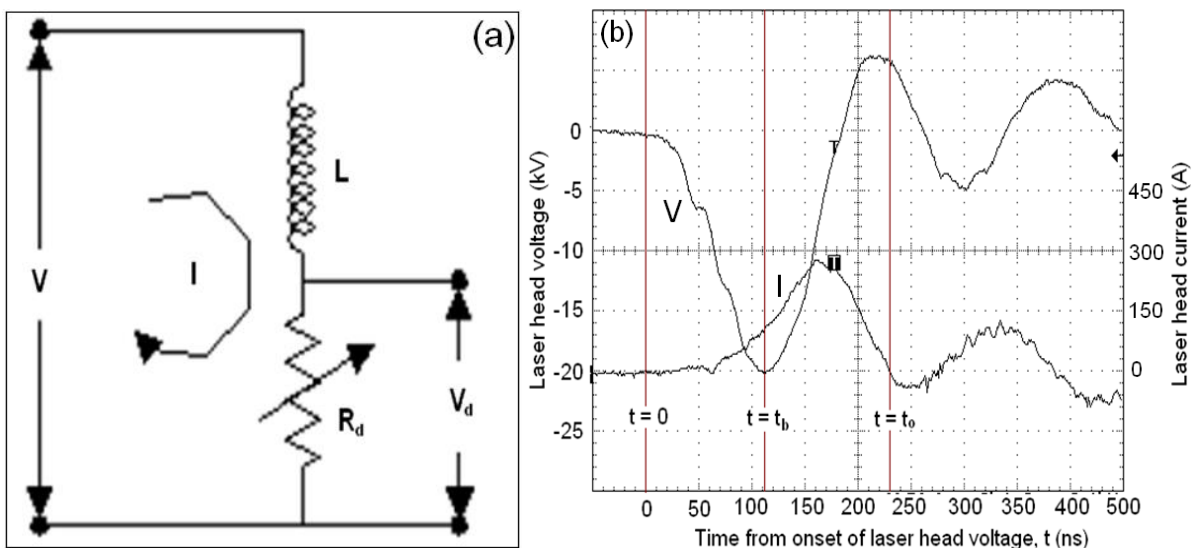


Fig. 3.1 (a) Cu-HBrL as simplified electrical circuit element (b) Typical laser head voltage & current pulses of Cu-HBr laser

Hence from equation 3.1, the laser tube/circuit loop inductance can be calculated as,

$$L = \frac{[V(t)]_{t=t_0}}{[(dI/dt)]_{t=t_0}} \quad (3.2)$$

The instantaneous electric power,  $P_a(t)$ , deposited into the Cu-HBrL discharge (also called the active peak input power), and the dynamic discharge resistance,  $R_d(t)$  are estimated as,

$$P_a(t) = V_d(t) \cdot I(t) \quad (3.3)$$

$$R_d(t) = \frac{V_d(t)}{I(t)} \quad (3.4)$$

The deposited active electrical pulse energy ( $E_p$ ), average active electrical power ( $P_{dump}$ ) and the average discharge resistance ( $\langle R_d \rangle$ ) of the Cu-HBrL are given as [121,171],

$$P_{dump} = f \cdot E_p = f \cdot \left[ \int_0^T V_d(t) \cdot I(t) dt \right] \quad (3.5)$$

$$\langle R_d \rangle \approx \frac{V_{d(p)}}{I_p} \quad (3.6)$$

where  $V_{d(p)}$  &  $I_p$  are the peak active/resistive discharge voltage and peak discharge current respectively. The discharge characteristics are analysed for different switched electrical input power ( $P_{in}$ ). This is varied by changing the voltage across the storage capacitor ( $C_s$ ) connected across the switch (IGBTs/thyratron) and is estimated using the relation,

$$P_{in} = \frac{1}{2} C_s \cdot V_{C_s}^2 \cdot f \quad (3.7)$$

where  $f$  is the PRR. The electrical power delivered from  $C_s$  is preferred as the input power because of its better reproducibility and good accuracy. The electrical power reaching at the laser head ( $P_{head}$ ) in such case is given as,

$$P_{head} = f_s \cdot \left[ \int_0^T V(t) \cdot I(t) dt \right] \quad (3.8)$$

where  $V(t)$ ,  $I(t)$  &  $T$  are the measured instantaneous head voltage, measured instantaneous discharge current and inter-pulse time ( $T = 1/f$ ) respectively. The difference in estimated values from equations 3.5, 3.7 & 3.8, gives a fair estimation of power loss across laser constituents.

This way of estimation for power deposition in the laser discharge is in good agreement with

that of the calorimetric methods used [7]. In addition, the analysis provides temporal pattern of energy deposition, estimation of which is very crucial for optimized copper laser operation.

The estimation of the electrical power deposited into the laser discharges vis-a-vis other associated laser discharge parameters is carried out by digitisation and numerically analysing

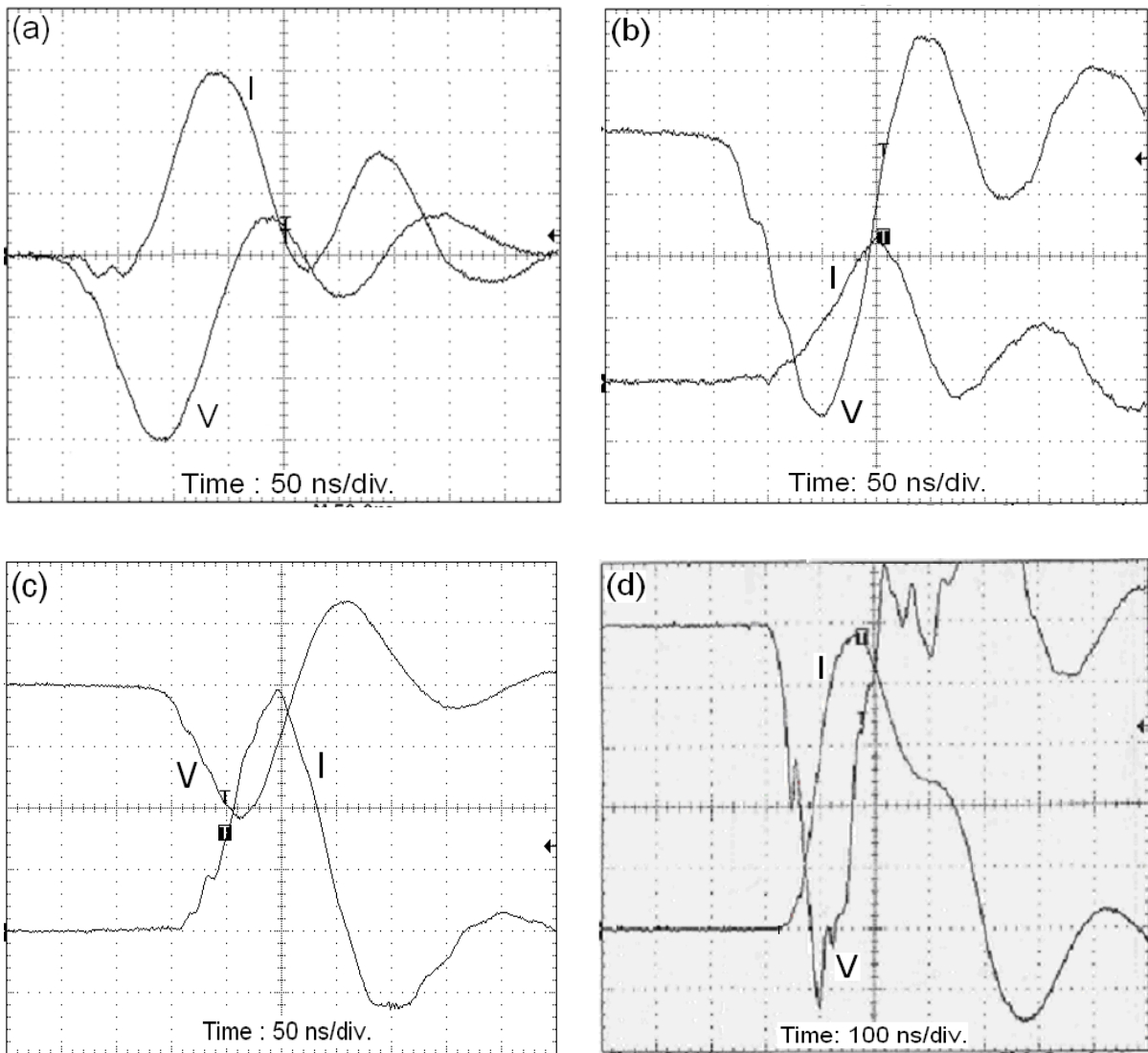


*Fig. 3.2 Typical discharge voltage & current waveforms recorded for copper lasers for (a) Cu-HBrL 1 at 42 W laser output power (optimised HBr concentration ~6%), (b) Cu-HBrL 2 at 110 W laser output power (optimised HBr concentration ~7%), (c) Cu-HBrL 2 with very low HBr concentration (~1%) with only greenish fluorescence, and (d) Conventional CVL (bore dia. 4.7 cm, length 150 cm, PRR 6.5 kHz, 33 W laser output power with thyatron pulser).*

the recorded laser discharge voltage (V) and current (I) waveforms. The temporal power deposition characteristics in the initial half of the discharge pulse and specifically, within  $< 100$  ns from the onset of discharge pulse, is the major deciding factor of copper laser performance. This is owing to the short population inversion time ( $< 100$  ns) of copper lasers. Therefore, the time resolved analysis ( $\sim 10$  ns resolution) of the electrical pulse pumping behaviour are carried out for different time limits by suitably changing the upper limit of integration of equations (3.5) & (3.8). Figs. 3.2 a-d show the typical laser discharge V & I pulses recorded for Cu-HBrL/CVL in different operating conditions as detailed in figure caption. These experimental V/I waveforms are the basis of further analysis/calculations. Specifically in the section 3.3, a detailed analysis is presented for our developed 100 W class Cu-HBrL (Cu-HBrL 4). Section 3.4 presents a comparative analysis on discharge pumping characteristics of a Cu-HBrL (Cu-HBrL 1) and a standard CVL of almost same dimension, both excited using thyatron pulser.

### 3.3 Electrical pulse pumping behaviour of Cu-HBrL

#### 3.3.1 Time resolved characteristics

##### 3.3.1.1 Measured laser head voltages and currents

Figs. 3.3a & b show the temporal variation of the digitised version of the laser (Cu-HBrL 4) head voltage and current waveforms respectively, recorded at different electrical input

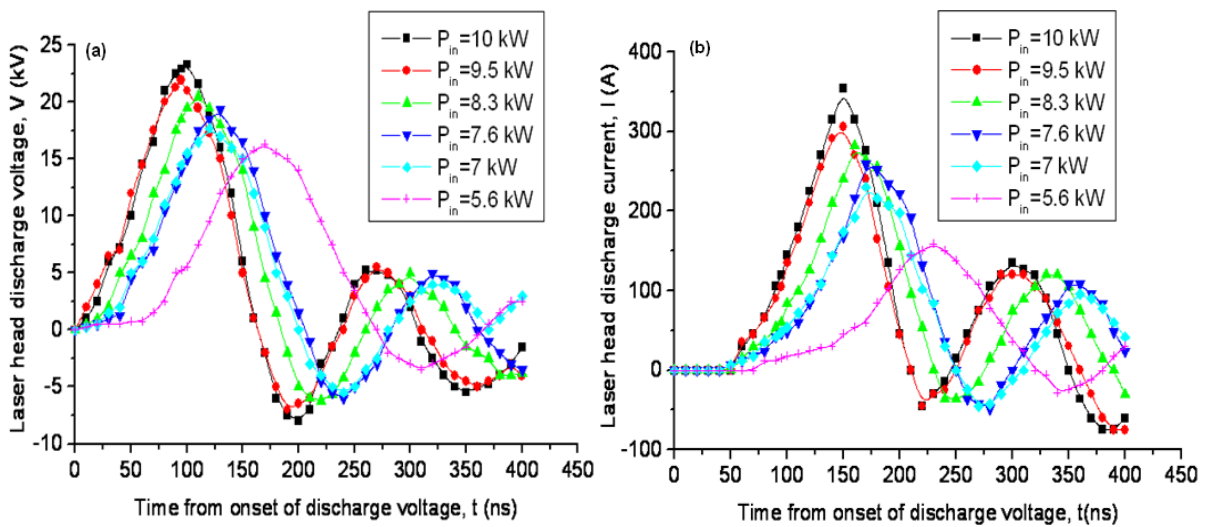


Fig. 3.3 Digitised electrical pulses of Cu-HBrL 4 for different  $P_{in}$ : (a) Voltage (b) Current

powers ( $P_{in}$ ). With increase in  $P_{in}$ , the HBr concentration is also concurrently increased to achieve the maximum average laser output power at a given  $P_{in}$  or  $V_{Cs}$ . The temporal characteristics of the laser head voltage-current waveforms show a typical onset delay of ~50 ns between them. As  $P_{in}$  increases from 5.6 kW to 10 kW, the peak values of the laser head voltage as well as that of the current increase from 16.3 kV to 23.3 kV and 160 A to 354 A respectively. With the increase of  $P_{in}$ , the rise time of V & I pulses become faster and the current pulse duration (at the base, corresponding to first half sinusoidal) also becomes shorter. For example, at  $P_{in}=5.6$  kW, the current pulse rise time is ~130 ns and its duration is ~250 ns whereas for  $P_{in}=10$  kW, the corresponding values are within 75-80 ns and ~150 ns respectively.

### 3.3.1.2 Active discharge voltage

The active laser discharge voltage is the actual voltage which decides the electron energy distribution in the Cu-HBrL plasma and hence the laser performance [34, 35]. However, it depends on the laser discharge loop inductance ( $L$ ). Therefore, to have a quantification of this parameter,  $L$ , is computed from the analysis of the recorded V & I waveforms, for different  $P_{in}$  using the equation 3.2. The variation in loop inductance and active laser head voltage are shown in Figs. 3.4 a & b respectively. Initially at  $P_{in}$  of 5.6 kW,  $L$  is ~1.8  $\mu$ H and then for

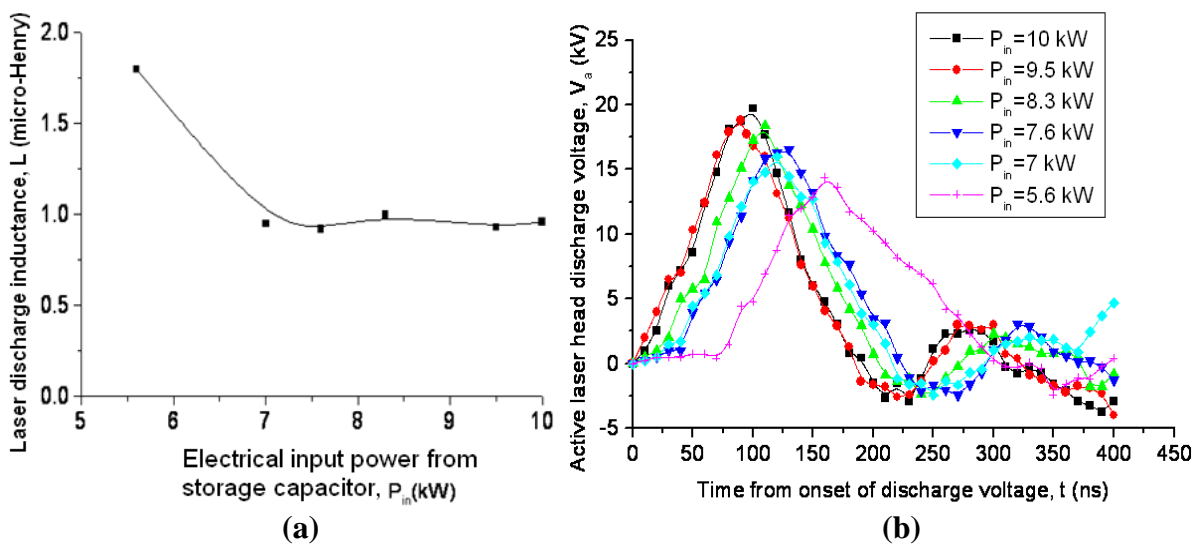


Fig. 3.4 Variation of discharge loop inductance (a) & active laser head voltage (b) of Cu-HBrL 4 with  $P_{in}$

higher input powers, it decreases to almost a constant level of  $\sim 1 \mu\text{H}$ . These values are comparable to the reported values of  $\sim 0.7 \mu\text{H}$  for a CuBr-H<sub>2</sub> laser of tube length of 50 cm and bore diameter of 2 cm, operating at  $P_{in} = 1.2 \text{ kW}$  with thyatron & CT-circuit based pulser [126]. Similar calculations carried out for conventional CVL of bore diameter 4.2 cm & length 150 cm have resulted  $L = 0.45 \mu\text{H}$  [168]. Similarly, as  $P_{in}$  increases from 5.6 kW to 10 kW, the peak values of  $V_d(t)$  vary from 14.4 kV to 19.7 kV. The corresponding voltage drop due to the laser discharge loop inductance is in the range of 10-15% of its peak value.

The laser discharge tube inductance, for longitudinally excited coaxial discharge tube geometry with uniform discharge current, is given as [41],

$$L = \frac{\mu_0 l}{2\pi} \left[ \frac{1}{4} + \ln \left( \frac{r_2}{r_1} \right) \right] \quad (3.9)$$

where  $\mu_0 = 4\pi \times 10^{-7} \text{ H/m}$ , is the permeability of free space,  $l$  is the discharge tube length,  $r_2$  is the inner radius of the coaxial current return conductor and  $r_1$  is the radius of the inner conductor. However, if the current through the tube exhibits on axis maximum, as in case of a Cu-HBrL, then the inductance will be higher than that indicated by the equation 3.9. Unlike the conventional CVL, the discharge current has axial peaking in a Cu-HBrL due to negligible plasma skin effect and enhanced ion-ion recombination leading to discharge constriction [12]. As  $P_{in}$  increases, the electron density also enhances and the filling of the tube cross section by the discharge current also increases. This leads to increase of  $r_1$  with increase of  $P_{in}$  as observed in the present study and by others too [122]. Therefore,  $L$  is expected to decrease as observed. It may be noted that the actual value of  $L$  may be 50 to 100% more than that of estimated by formula 3.9, depending on the fact that how closely and tightly the peaking capacitor is fitted in the laser head [41, 131]. For example, in our case, the calculated value of  $L$  is  $\sim 0.5 \mu\text{H}$  for  $r_1 \sim 2 \text{ cm}$  (the laser beam radius at  $P_{in} = 10 \text{ kW}$ ),  $r_2 \sim 6 \text{ cm}$  and  $l \sim 200 \text{ cm}$ . The placement factor (tightness & closeness to the laser head) of the peaking capacitor leads to an additional inductance of  $\sim 0.3 \mu\text{H}$ . Thus, taking into account the fact that Cu-HBrL has axially peaking

current, the net value of  $L$  could be close to around  $1 \mu\text{H}$  which is in line with present observation.

### 3.3.1.3 Active electrical input power & discharge resistance

Figs. 3.5 a & b show the temporal variation of the deposited electrical power into the laser discharge and the dynamic laser discharge tube resistance, calculated by using equations 3.3 & 3.4 respectively. The temporal power deposition pattern is the manifestation of effective coupling of electrical energy into CVL/Cu-HBrL discharge plasma. This is reflected in terms of the laser output power and efficiency. On the other hand, the temporal variation in the laser discharge resistance is an indication of how fast the discharge electrons gain energy. This ultimately decides the maximum voltage hold-off across the discharge tube & energy transfer to it. It is clear that the temporal variation pattern of the active electrical power deposition changes with  $P_{in}$ . As  $P_{in}$  increases, the energy deposition becomes faster. For example, as  $P_{in}$  increases from 5.6 kW to 10 kW, the durations of active electrical power deposition (corresponding to first half sinusoidal) reduces from  $\sim 240$  ns to  $\sim 140$  ns. The active electrical power depositions within the first half sinusoidal are 1.7 kW, 2.4 kW, 2.7 kW, 3 kW, 3.3 kW

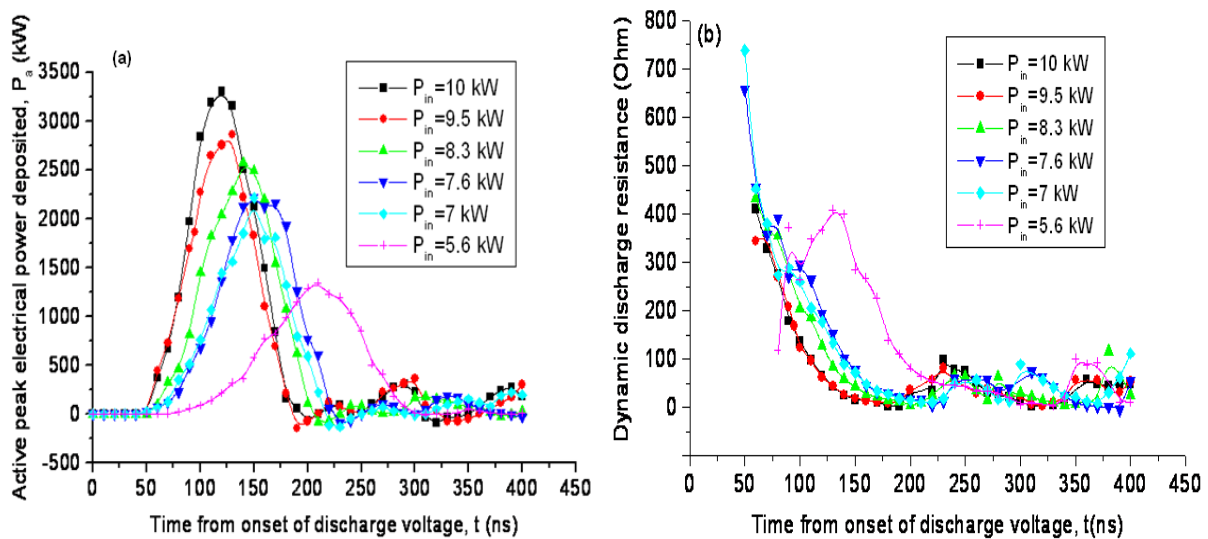


Fig. 3.5 Temporal variation of active electrical power (a) & discharge resistance (b)

of Cu-HBrL 4 for different  $P_{in}$

& 3.6 kW whereas their peak values are 1345 kW, 2215 kW, 2260 kW, 2575 kW, 2865 kW & 3300 kW respectively for  $P_{in}$  of 5.6 kW, 7 kW, 7.6 kW, 8.3 kW, 9.5 kW & 10 kW. Further, the power deposition corresponding to first 100 ns from the onset of the power deposition are estimated using equation 3.5 (putting the upper limit of integration =100 ns), for each  $P_{in}$ . The effective dumped input power are 0.6 kW, 1.36 kW, 1.58 kW, 2 kW, 2.8 kW & 3.1 kW corresponding to  $P_{in}$  of 5.6 kW, 7 kW, 7.6 kW, 8.3 kW, 9.5 kW & 10 kW respectively. These values account for ~35%, ~57%, ~59%, ~67%, ~85% & ~86% of the power deposition corresponding to first half sinusoidal durations respectively. This is linked with collapse of dynamic discharge resistances (Fig. 3.5 b) almost exponentially from sub kilo-ohms to tens of ohms during excitation pulse duration. The corresponding rates of input power deposition (active input power within first 100 ns duration/100 ns) are 6 GW/s, 13.6 GW/s, 15.8 GW/s, 20 GW/s, 28 GW/s & 31 GW/s respectively. This is consistent with the fact that the dynamic discharge resistances collapse at a much faster rate for higher values of  $P_{in}$  (Fig. 3.5 b). Faster rate of active energy deposition results in faster rate of electron multiplication and quicker collapse of the discharge tube resistance.

### 3.3.2 Time averaged characteristics

#### 3.3.2.1 Average discharge resistance & pre-pulse electron density

Fig. 3.6 shows the variation of the average discharge resistance ( $\langle R_d \rangle$ ) with  $P_{in}$ , calculated using equation 3.6. The value of  $\langle R_d \rangle$  decreases from ~90  $\Omega$  to ~56  $\Omega$  as  $P_{in}$  increases from 5.6 kW to 10 kW. This is comparable with typically reported values of 65  $\Omega$ , 48  $\Omega$  and 37  $\Omega$  for Cu-HBrL of 4 cm, 6 cm and 8 cm bore diameter respectively [171]. However, for a conventional CVL of bore diameter around 4 cm has  $\langle R_d \rangle$  ~25  $\Omega$  [168]. The average discharge tube resistance of a longitudinally excited CVL/Cu-HBrL is given as [41],

$$\langle R_d \rangle = K' \frac{l.P}{n_e(0). T_g(0)} \quad (3.10)$$

where  $P$  = pressure of neon buffer gas,  $n_e(0)$  = axial peak electron density,  $T_g(0)$  = axial gas

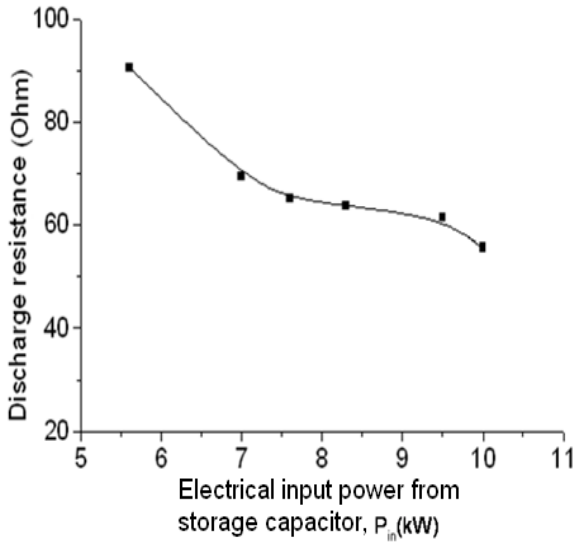


Fig. 3.6 Variation of average discharge resistance of Cu-HBrL 4 with  $P_{in}$

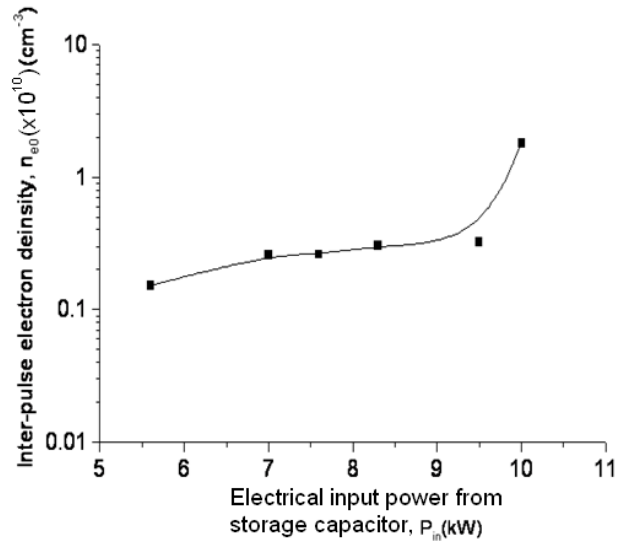


Fig. 3.7 Variation of pre-pulse electron density of Cu-HBrL 4 with  $P_{in}$

temperature and  $K'$  is a constant (depends on electron temperature). Therefore, for a given laser tube/system, the tube resistance is inversely proportional to the electron density and gas temperature. This peak electron density is also a function of pre-pulse electron density ( $n_{e0}$ ) as it grows from the  $n_{e0}$ . The pre-pulse electron density and the electron energy distribution function, hence the electron temperatures, are closely related and depend on the electrical discharge parameters [34, 35]. The  $n_{e0}$  can be evaluated from the laser discharge V & I pulses and is given as [123],

$$n_{e0} = \frac{1}{eV_L} \int_0^{t_b} I(t) dt \quad (3.11)$$

where  $e$  is the charge of electron,  $V_L = \pi r_l^2 l$ , is the laser active volume and  $t_b$  is the time at which break down occurs (Fig. 3.1b). Fig. 3.7 shows the variation of the estimated  $n_{e0}$  with  $P_{in}$ . With the increase of  $P_{in}$  from 5.6 kW to 10 kW,  $n_{e0}$  increases by an order from  $\sim 10^9$  to  $\sim 10^{10} \text{ cm}^{-3}$ . This figure is 2-3 order lower than the conventional CVL and is accounted by resonant DA process of the low-energy/inter-pulse electrons with HBr (equation 1.16) [120,121]. Similarly, to have an assessment of gas temperature effect on laser discharge resistance, axial gas temperatures are calculated for different  $P_{in}$ , using equation 2.5. The

estimated values of  $T_g(0)$  are 1935 K, 2075 K, 2175 K, 2225 K, 2295 K & 2385 K for the  $P_{in}$  of 5.6 kW, 7 kW, 7.6 kW, 8.3 kW, 9.5 kW & 10 kW respectively for Cu-HBrL 4. It is evident that both the parameters,  $n_e(0)$  and  $T_g(0)$ , increase with increase of  $P_{in}$  and hence are responsible for decrease in the tube resistance.

### 3.3.2.2 Average electrical power deposition in laser discharge

Fig. 3.8 a shows the variation of the average values of transferred electrical power from the pulser to laser head (calculated ignoring  $L$ , using equation 3.8), to the Cu-HBrL discharge plasma (calculated taking  $L$  into account, using equation 3.3) and the active laser efficiency ( $=P_{out}/P_{dump}$ ). As  $P_{in}$  increases from 5.6 kW to 10 kW, the electrical power transferred to the laser head increases from ~2.3 kW to ~4.7 kW, out of which the corresponding electrical power coupled to the laser discharge are ~2.2 kW to ~4 kW respectively. The corresponding laser

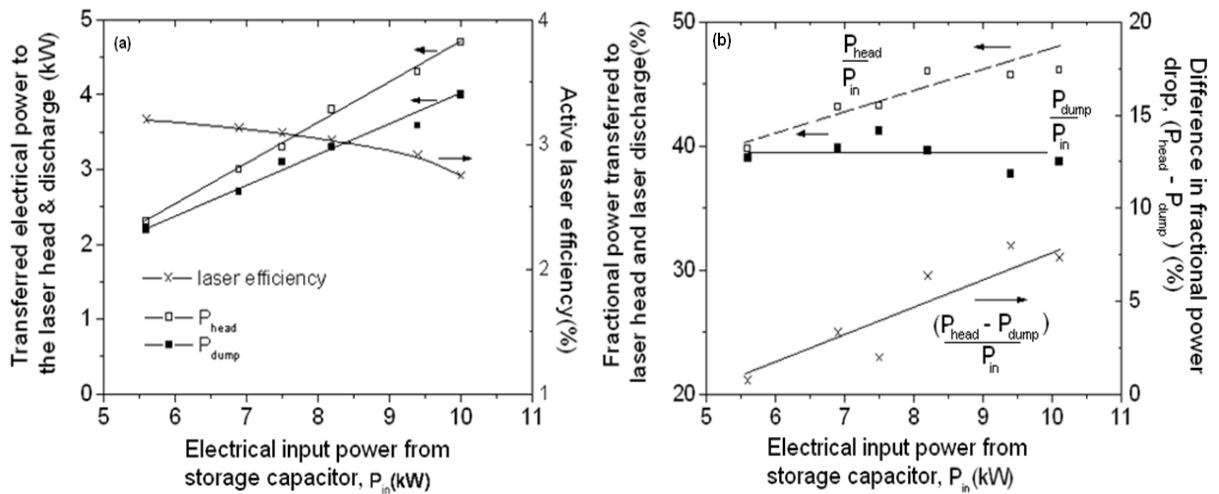


Fig. 3.8 Variation of (a) average electrical power transferred to the laser head, to the laser discharge & the active laser efficiency and (b) fractional electrical power transferred to the laser head, to the laser discharge & fractional power loss for Cu-HBrL 4 with  $P_{in}$

tube conversion efficiency decreases from ~3.2% to ~2.8% even though the laser output power increases from 70 W to 110 W. However, the corresponding fraction of the electric power coupled to the laser plasma ( $P_{dump}/P_{in}$ ) remains almost at a level of ~40%, even though the

fractional power transferred to the laser head ( $P_{head}/P_{in}$ ) keeps on increasing from ~40% to ~47% as  $P_{in}$  increases from 5.6 kW to 10 kW (Fig. 3.8 b). It is interesting to note that at the lower  $P_{in}$  of 5.6 kW, though  $L$  is the highest but the fractional drop of the electrical input, accounted for the distributive stray circuit elements, is less than 1% and keeps on increasing upto ~7% at  $P_{in}$  ~10 kW. This is consistent with the fact that for  $P_{in}$  of 5.6 kW,  $dI/dt$  (10 - 90%) is  $\sim 1 \times 10^9$  A/s against  $\sim 3.6 \times 10^9$  A/s for input power of 10 kW. The differing values of  $L$  and  $dI/dt$ , for different  $P_{in}$ , account for a voltage drop of 1.8-1.9 kV and 3.5-3.6 kV for  $P_{in}$  of 5.6 kW and 10 kW respectively. Therefore, the analytical results are in agreement with observed trends of laser output power and laser tube efficiency.

### 3.3.3 Role of other operating parameters

The influence of other experimental parameters such as HBr concentration, buffer gas flow rate, gas pressure and PRR are also analysed in a similar fashion from the recorded V-I waveforms. Figs. 3.9 show the variation in transferred electrical power to laser head & discharge along with average laser output power with HBr concentration (Fig. 3.9 a), buffer gas flow rate (Fig. 3.9 b) and buffer gas pressure (Fig. 3.9 c). For these conditions, the data have been recorded/analysed at  $V_{Cs}$  fixed at 770 V corresponding to  $P_{in}$  of 9.5 kW at 16 kHz PRR on Cu-HBrL 4. It is observed that the HBr concentration affects significantly the energy coupling behaviour to the Cu-HBrL discharge. With the variation of HBr concentration from 3% to 10%, the average laser out power varies from 54 to 77 W with a peak of 105 W at around 7% HBr concentration. Interestingly,  $P_{head}$  also varies from 2.8 to 3.8 kW with a peak of 4.4 kW at 7 -8% HBr concentration. On the other hand, the average electrical power coupled to the Cu-HBrL discharge changes from 2.2 kW to 2.9 kW with maximum deposition of ~3.7 kW. This corresponds to variation of fractional energy dumping ( $P_{dump}/P_{in}$ ) of ~23% to ~31% with maximum of ~39%. Similarly, with the variation of flow rate from 2 to 6 lit.-atm./hr., the laser power changes from ~40 W to ~105 W at constant  $P_{in}$  of 9.5 kW. The corresponding

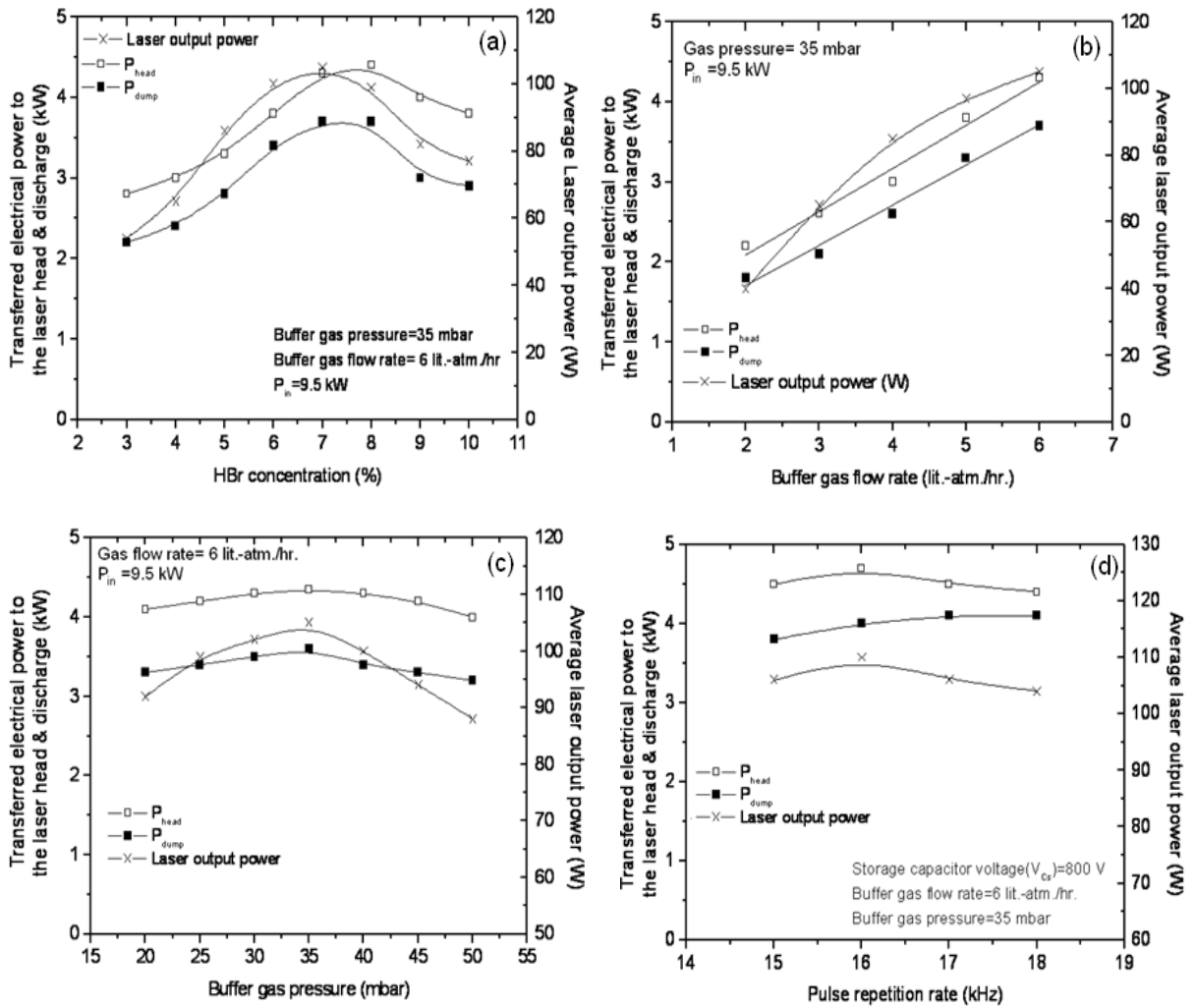


Fig. 3.9 Variation of transferred electrical power to the laser head ( $P_{head}$ ) & discharge ( $P_{dump}$ ) and average laser output power of Cu-HBrL4 with (a) HBr concentration (b) buffer gas flow rate (c) buffer gas pressure and (d) pulse repetition rate

variations in  $P_{head}$  and  $P_{dump}$  are  $\sim 2.2$  to  $\sim 4.3$  kW and  $\sim 1.8$  to  $\sim 3.7$  kW respectively. This corresponds to variation in the fractional energy dumping from  $\sim 19\%$  to  $\sim 39\%$ . As the buffer gas pressure is varied from 20 to 50 mbar, the laser power changes from 95 to 88 W with a peak of 105 W at  $\sim 35$  mbar. This is in accordance with maximum power transferred to the laser head (4.4 kW) as well as to the laser discharge plasma (3.7 kW) at  $\sim 35$  mbar pressure. This corresponds to the fractional energy coupling of  $\sim 39\%$ . At the other extremes of 20 & 50 mbar, the corresponding values are 4.1 kW, 3.3 kW, 35% & 4 kW, 3.2 kW, 34% respectively.

Fig. 3.9 d shows the effect of PRR on  $P_{head}$ ,  $P_{dump}$  and laser output power for Cu-HBrL

4. The PRR is varied from 15 to 18 kHz, in a step of 1 kHz, at fixed  $V_{Cs}$  of ~800 V, which corresponds to variation in  $P_{in}$  from ~9.5 to ~11 kW. The corresponding values of  $P_{head}$ ,  $P_{dump}$  and laser output power increased from ~4.4 to ~4.7 kW, ~3.8 to ~4.1 kW and ~104 to ~110 W respectively. However, the fractional energy dumping into laser active medium changed from ~40% to ~37%. These variations in the fractional energy coupling and laser output power are mainly attributable to variation of discharge impedance and/or lasant copper density for the different operating parameters. Similar rigorous analysis of electrical power coupling for Cu-HBrL 2 & 3 is also carried out. It is observed that the energy coupling trends are similar to that of Cu-HBrL 4 presented above [156]. At the optimum condition, about ~40 % of the switched input power is coupled to the laser plasma, in both the Cu-HBrL 2 & 3. Based on this, the laser tube efficiencies of Cu-HBrL 2 and Cu-HBrL 3 are ~2.2% and ~2.3% against that of ~2.8% for Cu-HBrL 4. The corresponding specific electric input power coupled becomes ~3.1 kW/lit., ~2.6 kW/lit. and ~1.6 kW/lit. for Cu-HBrL 2 to 4 respectively (for respective active pumping zone or laser beam output diameters of ~3 cm, ~3.5 cm & ~4 cm). The respective specific output powers come out to be ~70 W/lit., ~60 W/lit. and ~45 W/lit. These observations are in line with the fact that for higher specific input power the laser efficiency decreases due to increased gas heating effects [172].

The behaviour of power coupling efficiency, for the solid state pulser used, can be understood as follows. The solid state pulser (Fig. 2.5a) contains several IGBT switches (4 Nos.), a pulsed transformer and three stages of MPCs. These elements introduce losses (core loss:  $P_{core}$ , copper loss:  $P_{copper}$  etc.) when the electrical power is transferred from the storage capacitor ( $C_s$ ) to the laser head. For example, the losses for an MPC stage are given as [170],

$$P_{core} = M' \cdot V_T \cdot E_d \cdot f \quad (3.12)$$

$$P_{copper} = 2.923 \times 10^{-7} \sqrt{\frac{C^3}{2L_{tot}} \frac{V^2 f^{3/2} l_{wire}}{d_{wire}}} \quad (3.13)$$

where  $M'$  = number of torroids used in the MPC,  $V_T$  = volume of one torroidal core,  $E_d$  = energy dissipated per pulse per  $m^3$ ,  $C$  = capacitance of the storage capacitor of the MPC,  $V$  = peak voltage on the capacitor of the MPC,  $l_{wire}$  = length of the wire and  $d_{wire}$  = diameter of the wire used in the torroid. The volume of MPC core ( $M.V_T$ ) is dependent on several parameters such as compression ratio, energy per pulse handled by MPC, magnetic flux amplitude on core, core packing factor and magnetic permeability of core material [170]. It is obvious that for a given MPC the loss increases with increase of PRR (equations 3.12 & 3.13). MPCs used in conventional CVLs typically at PRR of about 5 kHz introduce 10-20% power loss per stage [168-170]. On the other hand Cu-HBrLs operate at around 3-4 times higher PRR as well as  $C$  and  $V$  values are different. The losses with Cu-HBrL per stage of MPC will be higher than that in a CVL. This is consistent with the observed large fraction losses in three stage MPC based power supply as employed in the present work on Cu-HBr lasers.

### 3.4 Pulse pumping behaviour with thyatron pulser

The electrical discharge analysis of Cu-HBrL (Cu-HBrL 1) vis-à-vis conventional CVL of equivalent tube geometry and excitation circuits (thyatron based CT-circuit) is also carried out and compared. Both the Cu-HBrL 1 and CVL consist of discharge tube of almost equivalent dimension i.e. bore dia. 5 cm vs. 4.7 cm & length 130 cm vs. 150 cm (Table 2.1). The Cu-HBrL produces 42 W average power @ 18 kHz PRR with 1.1% efficiency (based on  $P_{in}$ ) operating with neon gas pressure of ~30 mbar,  $C_s/C_p = 2$  nF / 1.2 nF &  $L_c = 1500$  mH. On the other hand, the CVL produces 33 W output power @ 6.5 kHz PRR with 0.7% efficiency operating at with neon gas pressure of ~25 mbar,  $C_s/C_p = 5$  nF / 2 nF &  $L_c = 400$  mH.

Figs. 3.10 a & b show the digitized version of recorded V/I waveforms of Cu-HBrL & CVL at their respective maximum power conditions. The recorded actual pulses are shown in Figs. 3.2 a & d. It is seen that there is a delay between the onset of the discharge voltage and current pulses in both the lasers. However, the delay is ~65 ns in case of the Cu-HBrL as

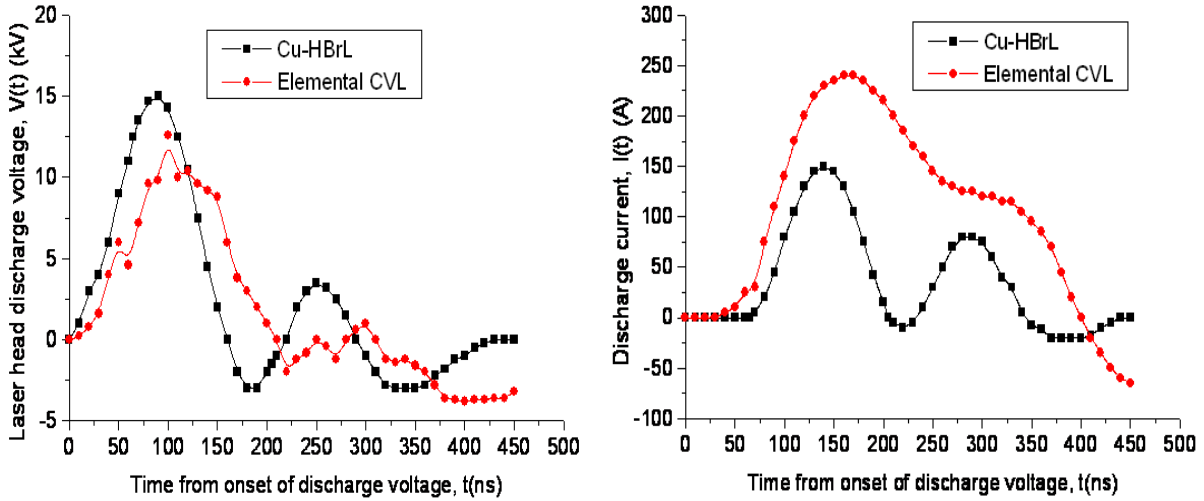


Fig. 3.10 Digitised recorded discharge voltage (a) & current (b) pulses for Cu-HBrL & CVL

compared to  $\sim 30$  ns in CVL. More interestingly, in case of Cu-HBrL, the process of avalanche of the discharge electrons takes place at  $\sim 15$  ns before the maxima of the discharge voltage/break-down whereas the same occurs at  $\sim 80$  ns in case of the CVL. The discharge voltage attains a peak of  $\sim 15$  kV &  $\sim 12.6$  kV whereas the discharge current attains a peak of  $\sim 150$  A &  $\sim 240$  A respectively for the Cu-HBrL and CVL. The rise time & half period of the current pulse duration are  $\sim 60$  ns &  $\sim 130$  ns respectively for the Cu-HBrL and  $\sim 130$  ns &  $\sim 350$  ns respectively for the CVL. The estimated values of  $L$ , using equation 3.2, are  $\sim 750$  nH and  $\sim 500$  nH for the Cu-HBrL & CVL respectively. The larger  $L$  value in the Cu-HBr laser is expected due to discharge quenching phenomena (equation 3.9). The higher value of discharge current in CVL as compared to Cu-HBrL is attributed to higher value of  $C_s$  used (5 nF vs. 2 nF) as well as higher  $n_{eo}$  in CVL ( $\sim 10^{13}$   $\text{cm}^{-3}$  vs.  $\sim 10^{11}$   $\text{cm}^{-3}$ , estimated using equation 3.11). On the other hand, shorter current pulse rise time in a Cu-HBrL is a combined effect of use of low value  $C_p$  (1 nF vs. 2 nF) as well as role of DA action of HBr for removal of pre-pulse electrons [33,121].

Based on the calculated discharge loop inductance values, the corresponding active peak voltages,  $V_{d(p)}$  are estimated to be  $\sim 13.2$  kV and  $\sim 11$  kV respectively for the Cu-HBrL and CVL. These values are about 12-13% less as compared to measured peak discharge voltages.

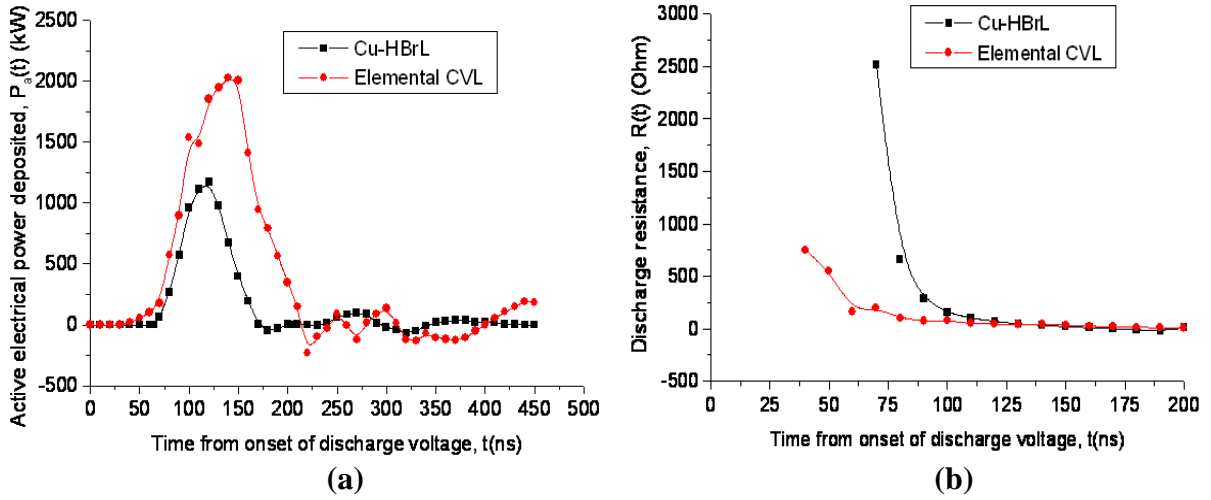


Fig. 3.11 Temporal variation of active electrical power (a) & discharge resistance (b)

for Cu-HBrL & CVL

Figs. 3.11a & b show the temporal characteristics of the active electrical power and discharge resistances respectively for both the lasers under investigation. The peak deposited electrical powers & the duration of power deposition are around 1115 kW & 100 ns for Cu-HBrL and 2030 kW & 170 ns for CVL respectively. The pulse energy deposited, till any time  $t$ , can be evaluated from the area under the  $P_{dump}$  vs.  $t$  curve (Fig. 3.11 a). For self-terminating, short inversion time Cu-HBr and CVL, it is the energy deposited in the initial fast rising part of the curve (Fig. 3.11 a) that dictates the laser power achieved. The calculated rate of active power deposition is  $\sim 1.08$  MW/s ( $= 65$  mJ/60 ns) for Cu-HBrL and  $\sim 0.77$  MW/s ( $= 100$  mJ/130 ns) for CVL. This faster rate of power deposition in Cu-HBr laser is consistent with its faster collapse of discharge resistance (Fig. 3.11 b) as compared to CVL. This is in line with the observed higher laser power & efficiency for the Cu-HBrL as compared to the CVL of almost same dimension.

The Cu-HBr laser has also scores over the CVL in terms of better beam profile & faster attainment of full laser power as shown in Figs. 3.12 a & b respectively, for the present investigated case. The radial intensity profile of CVL has on-axis minimum as compared to on-axis maximum (quasi-Gaussian profile) for the Cu-HBrL (Fig. 3.12a). The output beam width

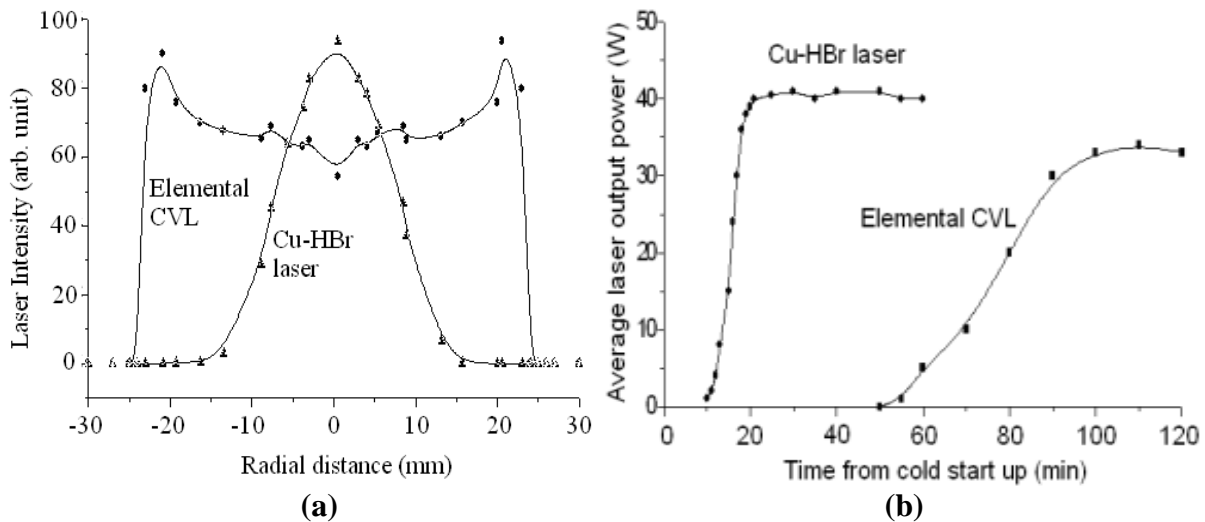


Fig. 3.12 Radial intensity profiles (a) and laser power build up (b) in Cu-HBrL & CVL

is almost same as the discharge tube diameter for CVL while it is ~60% of the discharge tube diameter for Cu-HBrL. These differences are due to axial peaked nature of laser gain and discharge quenching phenomena in a Cu-HBr laser, as explained earlier (sections 1.4 & 3.3). The laser start-up and subsequent power build-up time of the Cu-HBrL is almost one third that of the CVL (Fig. 3.12 b). This is due to lower working temperature as well as better coupling of electrical energy from the pump source to laser the discharge in a Cu-HBrL.

### 3.5 Comparison with the published results and further scope

The analysis of the discharge characteristics and performance of laser system presented here is consistent with the published related results on high power copper lasers. For a high power, large bore Cu-HBrL (216 W from 8 cm bore, 300 cm long tube) system based on MOSFET array & 3 stages of MPC combinations, the fractional power deposited in the laser tube was in the range of 20 - 40% for different electrical input powers (33-36 kW) and PRR of 16-18 kHz [7]. The power deposition fraction for a high average power large bore KE-CVL (312 W @ 5 kHz PRR from 8 cm bore, 300 cm long tube) using similar pulser (IGBT-MPC) configuration was ~30% [92]. These losses have been ascertained by calorimetric methods.

Similar studies with conventional CVL (30 W @ 5 kHz from 4.2 cm bore, 150 cm long

tube) with a solid state pulser of similar configuration (IGBT + 3 stages of MPC) confirmed that ~50% of  $P_{in}$  was deposited into the laser tube [168]. Though IGBT-MPC based pulser is less efficient in depositing energy in CVLs, they are preferred due to their high average power handling at high PRR, long life times and operational reliability [168]. Therefore our analysis of power deposition of ~40% for Cu-HBrL 2 to 4, ~80% for Cu-HBrL 1 and ~70% for the CVL in the laser tubes are within the range of the reported results and is even better than similar high power 15-20 kHz repetition rate copper laser device. The difference in values of various deposition fractions is due to difference in employed topology, power handling, MPC volume and hence stray inductance etc. as obvious from equations 3.12 & 3.13. We believe that the coupling fraction of electrical input power into discharge plasma can be increased by better design of modulator. This can be achieved by making the MPC more compact to reduce stray inductance and allowing the compression ratio to be retained for smaller core volumes as well as by sharpening the current pulse rise time by lowering  $L$ . However higher power handling is always associated with higher MPC volume and hence more power loss. The laser performance presented is also comparable with similar 100 W class Cu-HBrL systems [5, 6, 9, 10]. The different laser systems differed in terms of excitation schemes (CT scheme or IC scheme) and laser volumes used. It is also interesting to note that part of the  $P_{dump}$  (10-15%) is also lost in the heating of the electrodes [172]. Though we have not carried out analysis for the power lost in the electrodes, but assuming ~90% of the  $P_{dump}$  is used in heating the laser plasma, the active laser tube efficiency would be more than 3.5% at the maximum laser output power level. Further 15-20% enhancement in laser extraction efficiency can be realised by avoiding the parasitic cavity losses due to discharge sealing end windows [5, 6].

### 3.6 Conclusions

In conclusion, this chapter presented a comprehensive analysis (both time resolved & time averaged) on the electrical pulse pumping characteristics of the developed 40 to 110 W

average power Cu-HBrLs (Cu-HBrL 1 to 4). The analyses are carried out by numerically processing of the laser head voltage and current waveforms, for various laser operating parameters and active volumes. During transfer of energy to the laser discharge plasma, fractional losses at the modulator are evaluated. The average laser performances at various input powers are correlated with evaluated gas discharge parameters. A comparative performance study between Cu-HBrL & CVL of equivalent geometry, pumped by thyatron pulser, is also carried out. It is concluded that for IGBT-MPC solid state pulser, the energy coupling to the active medium is ~40% and for the thyatron pulser this value is 70-80%. For the solid state pulser the energy loss is due to loss in MPCs, pulse transformer & IGBT used whereas for thyatron pulser it is due to the switch itself. Between the Cu-HBrL & CVL, the energy coupling in the Cu-HBrL is better than that of CVL (~80% vs. ~70%) and is attributed to better impedance matching behaviour for the former. This study provides guideline for the efficient electrical pulse pumping of a Cu-HBrL vis-à-vis quick laser power optimisation by monitoring and online analysis of the laser discharge voltage & current waveforms.

## Chapter 4

### Studies on HBr gas purification for performance enhancement of

### Cu-HBr laser

#### 4.1 Introduction

It has already been pointed out that HBr gas is the most crucial component of a Cu-HBrL and is responsible for its success with high-performance. Just to recapitulate, the HBr reacts with copper metals in the discharge region to produce molecular complexes of copper bromide which dissociate to produce lasant copper atoms at low temperature [111]. It also lowers the pre-pulse electron density of the discharge by dissociative attachment (DA) reaction [120, 121]. Out of the various gases used for copper laser performance enhancement, HBr gives the best result owing to its higher DA cross section and stability [65, 112]. Therefore, any impurity present in HBr gas, is very likely to poison the discharge due to its deleterious effects on the evolution of intra-pulse electron energy distribution and discharge parameters. This will affect the laser kinetics adversely and degrade the laser performance. Due to extremely corrosive/reactive nature of HBr, the impurities such as dissociation and reactant products creep in during the overall process of its manufacturing, storage and handling [163, 173-175]. For this reason, industrially processed HBr gas has typical shelf-life of about six months which is mainly limited by catalytic disintegration of HBr molecule into hydrogen and bromine [163]. In this context, in a Cu-HBrL, the HBr gas used should be devoid of free hydrogen and bromine components. Hence, it is essential to check the purity of HBr gas prior to its use in a Cu-HBrL and devise a methodology to remove residual impurities present, which are detrimental to the laser output performance. However, this issue has not been paid sufficient attention in the field.

This chapter presents the details of a purification process of HBr gas by fractional distillation technique and evaluation of the purified HBr gas for improving the performance of developed Cu-HBr laser in a test set up. The principle of the purification technique,

development of a suitable HBr gas purification set up and mass spectrometry analysis before/after the purification process are presented. The purified HBr gas is utilized for enhancement of the laser output power, followed by an analysis of its discharge characteristics to understand the physical mechanism. More than 30% improvement in the laser output power of Cu-HBrL, has been demonstrated with the purified HBr gas. The effects of the distilled HBr gas on the laser output power, efficiency and beam diameter are presented. The electrical discharge characteristics such as change in discharge impedance and electrical power coupled into the discharge are analysed for both the distilled/undistilled HBr gases. The underlying physics responsible for the improved laser performance with purified HBr gas is discussed.

## **4.2 The HBr gas purification by fractional distillation**

### ***4.2.1 Principle of purification process***

The principle of HBr gas purification is to reduce the residual concentration of hydrogen and bromine. The purification process is based on fractional distillation of the constituents. It utilizes the fact that the vapour pressure of gases is a function of temperature as well as its nature/type. In the present case, a two-step fractional distillation is used which can be understood as follows. The vapour pressure data of HBr and Br<sub>2</sub> as well as their ratios at various temperatures are given in table 4.1 [176]. At temperature of -196 °C, both HBr and Br<sub>2</sub> are solid as their melting points (MP) are -87 °C and -7 °C respectively [175, 177]. However, at this temperature, H<sub>2</sub> remains in gaseous state as its MP is -253 °C [175]. Hence at -196 °C (liquid nitrogen temperature) the H<sub>2</sub> molecules are sucked out leaving behind the solid form HBr and Br<sub>2</sub> in the container. Then the temperature of the vessel containing the residual HBr & Br<sub>2</sub> is increased to about -20 °C (ice-salt temperature). At this temperature, the HBr is in gaseous form as its boiling point is at -67 °C whereas Br<sub>2</sub> remains solid and is trapped on the wall of container. The HBr gas obtained after this distillation process is almost free from hydrogen and is expected to have the Br<sub>2</sub> content of less than 0.5%.

Table 4.1 Vapour pressure of HBr & Br<sub>2</sub> and their ratios at different temperatures [176]

Temperature (°C)	P <sub>HBr</sub> (torr)	P <sub>Br<sub>2</sub></sub> (torr)	P <sub>Br<sub>2</sub></sub> / P <sub>HBr</sub>
-196	~10 <sup>-6</sup>	<10 <sup>-13</sup>	-
-171	~10 <sup>-2</sup>	~10 <sup>-13</sup>	~10 <sup>-11</sup>
-151	~10 <sup>-1</sup>	~10 <sup>-9</sup>	~10 <sup>-8</sup>
-85	~10 <sup>2</sup>	~10 <sup>-2</sup>	~10 <sup>-4</sup>
-64	~10 <sup>3</sup>	~10 <sup>-1</sup>	~10 <sup>-4</sup>
-20	~10 <sup>4</sup>	~10	~10 <sup>-3</sup>
0	~10 <sup>4</sup>	~10 <sup>2</sup>	~10 <sup>-2</sup>
25	~2 x 10 <sup>4</sup>	~10 <sup>2</sup>	~0.5 x 10 <sup>-2</sup>

#### 4.2.2 Set up for HBr gas purification

Based on the above principle and vapour pressure data (table 4.1), an experimental set up is designed for HBr gas purification. Fig. 4.1 shows the schematic of the purification set up and its use in Cu-HBrL. It consists of two independent cooling units for cooling down to temperature of -196 °C and -20 °C. The first unit/stage of the distillation set up consists of a

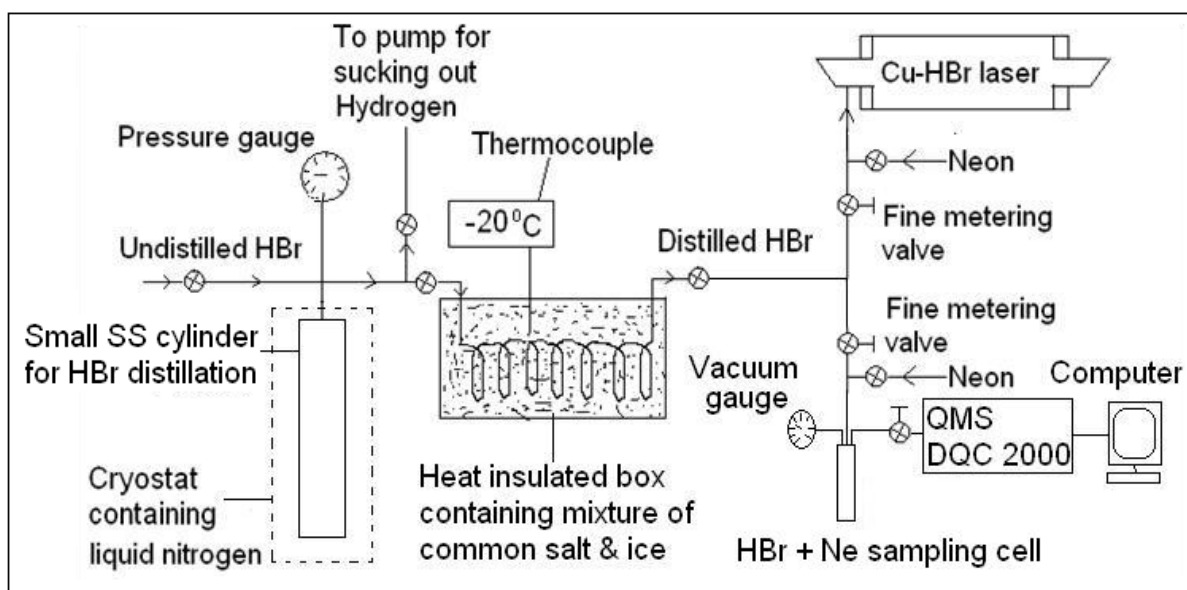


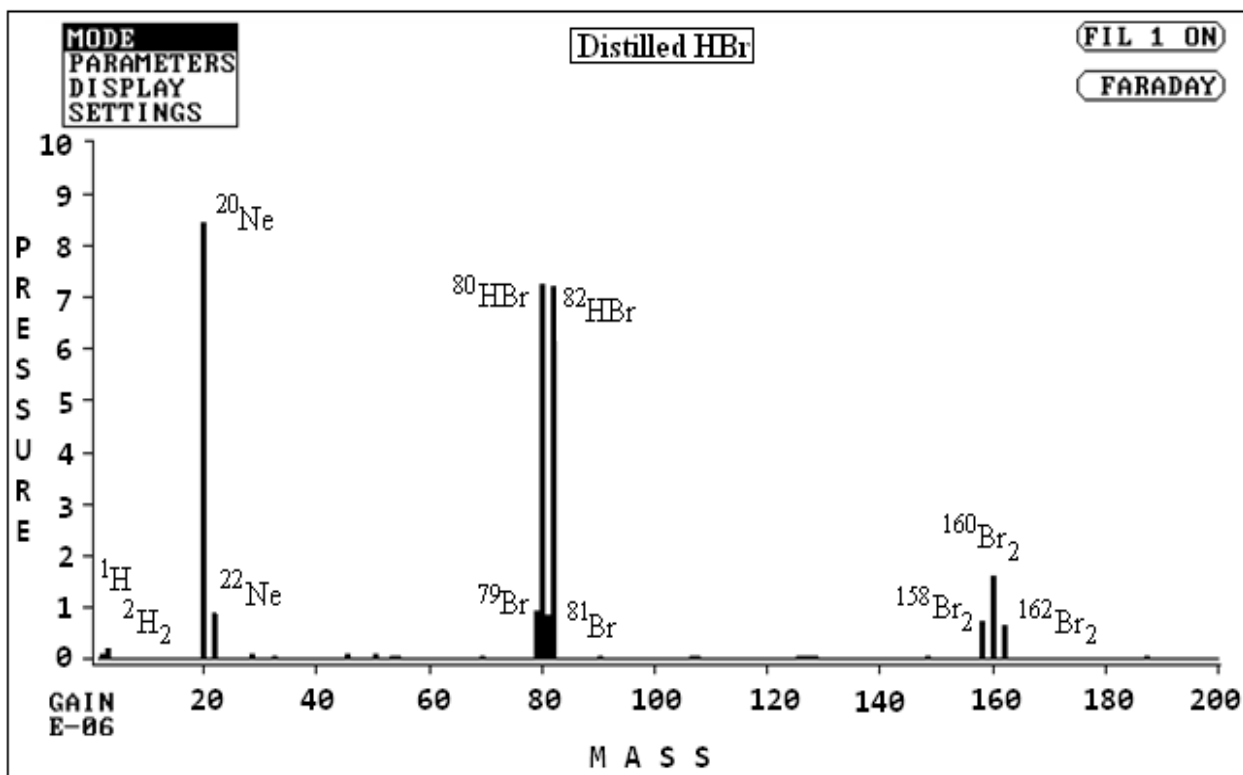
Fig. 4.1 Schematic of the HBr gas purification set up used in Copper-HBr laser

cryocan containing liquid nitrogen. The second unit consists of a heat insulated box containing crushed ice with added common salt to lower the temperature to  $-20\text{ }^{\circ}\text{C}$ . The temperature is constantly monitored using a thermocouple based temperature sensor. The lowering of the temperature of the salt-ice mixture (from  $0$  to  $-20\text{ }^{\circ}\text{C}$ ) is understood on the basis of shifting of equilibrium of chemical potentials of the species involved [178].

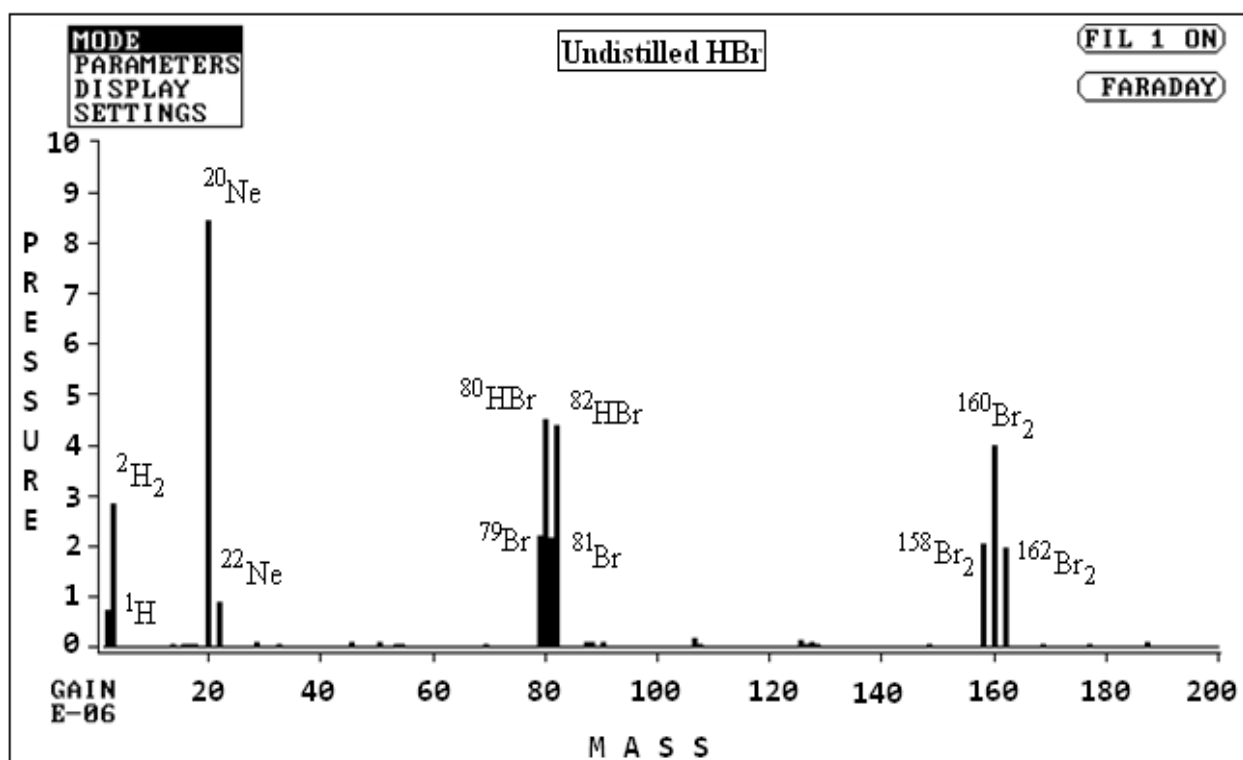
The whole HBr purification process is as follows. Some quantity of HBr gas (Air products, UK) is filled in a clean and leak proof (Helium leak rate  $< 10^{-9}$  mbar-lit./s, tested using a Helium mass spectrometer leak detector) small stainless steel cylinder of volume about  $350\text{ cm}^3$  (length  $\sim 50$  cm, bore diameter  $\sim 3$  cm). This cylinder is then immersed in a cryocan containing liquid nitrogen to cool it down to temperature of  $-196\text{ }^{\circ}\text{C}$ . At this temperature, the residual gases present in vapour phase are removed from the cylinder by a vacuum pump. Then the HBr container is taken out of the cryocan. The temperature of the cylinder goes up and so also the vapour pressure of its constituents. The gas mixture, left in the steel cylinder, is passed through a long ( $\sim 20$  m), thin walled stainless steel capillary (outer diameter  $\sim 3$  mm) coil placed in the second stage of the distillation unit, the box containing common salt & ice mixture. The long capillary coil is chosen to promote the effective entrapment action at its inner wall due to its high ratio of surface area to volume. The purified HBr (largely devoid of  $\text{H}_2$  &  $\text{Br}_2$ ) gas coming out of the capillary is injected into the Cu-HBrL discharge medium through the developed precision HBr gas mixing set up (section 2.2.3). A small part of the distilled gas, obtained after second stage, is collected and diluted with Neon gas (1 mbar HBr + 10 mbar Neon) measured using a stainless steel diaphragm vacuum gauge for mass spectrometric analysis. This analysis is then carried out using a quadrupole mass spectrometer (Larimax DQC 2000: Anglo Scientific Instruments, UK).

#### ***4.2.3 Mass spectrometry of the HBr gases***

Figs. 4.2 a & b show the recorded mass spectra of the distilled and the undistilled HBr



(a)



(b)

Fig. 4.2 Quadrupole mass spectrum of (a) Distilled HBr gas (b) Undistilled HBr gas

gases respectively, taken with the quadrupole mass spectrometer. The vacuum chamber, with which the spectrometer is attached, has equal bleeding gas mixture pressure of  $\sim 3 \times 10^{-5}$  mbar in both the cases of HBr studied. Both the spectra show the distinguished peaks of Neon, HBr, H<sub>2</sub>, H, Br<sub>2</sub> and Br very well. The peaks at mass numbers 1 and 2 correspond to atomic and molecular hydrogen respectively. The peaks at mass numbers 20 and 22 are of two natural isotopes of neon. The peaks at 79 and 81 are of natural isotopes of atomic bromine, whereas peaks at mass numbers 158, 160 and 162 are that of molecular bromine of different isotopic composition. The other smaller peaks observed are possibly resulted from back streaming rotary & diffusion pump oil, reaction products of HBr with the vacuum chamber/spectrometer wall material, reaction of trace carbon compounds with trace oxygen at the heated filament of the mass spectrometer ion source as well as filament of the ion gauges and the presence of trace atmospheric impurities [179]. It is seen that in case of the distilled HBr, the peaks of H, H<sub>2</sub>, Br and Br<sub>2</sub> are of much lower strength as compared to that of the undistilled HBr gas. In addition, the peak heights of HBr in distilled case are also higher as compared to that of the undistilled one. This confirms that after the fractional distillation the residual impurities (H/H<sub>2</sub>, Br/Br<sub>2</sub>) present in the HBr gas are considerably reduced.

The observed mass spectrum can be understood as follows. In a quadrupole mass spectrometer, molecules of a gas mixture undergo ionization and/or dissociation-ionization due to collisions with electrons energised by the applied electric field. The ions are separated by the quadrupole mass filter depending on their mass to charge ratio [179]. Hence, in the mass spectra of molecules in a quadrupole mass spectrometer, which is characteristic of gas composition, peaks of both the molecules as well as their dissociation products are expected. Therefore, the exact concentration of the residual impurity present (H<sub>2</sub> & Br<sub>2</sub>) cannot be quantified using this mass spectrometry technique. However, in a comparative study as carried in our case, this spectrometry gives fairly good relative information. In both the spectra of the

Figs. 4.2 a & b, several peaks of differing heights corresponding to a given species are observed. These are attributable to their different isotopes as well as abundances [180]. For example, the two peaks of atomic bromine, at mass number of 79 and 81, are almost of equal heights and is a consequence of the fact that atomic bromine has two natural isotopes at the above mass numbers with their natural abundances of 51% and 49% respectively. Based on statistical analysis, molecular bromine is expected to have three distinguished peaks at mass numbers 158, 160 and 162 with typical ratios of 1 : 2 : 1 i.e.  $^{79}\text{Br}-^{79}\text{Br} : ^{79}\text{Br}-^{81}\text{Br} : ^{81}\text{Br}-^{81}\text{Br} = 1 : 2 : 1$ . Similar arguments can also be extended to explain two observed peaks of almost equal heights for HBr. Here the hydrogen atom (with one major natural stable isotope of mass number 1, abundance 99.985%) combines with two bromine isotopes to form HBr molecules of mass number 80 and 82 i.e.  $^1\text{H}-^{79}\text{Br}$  &  $^1\text{H}-^{81}\text{Br}$ .

It is worth mentioning that, being highly corrosive and moisture sensitive in nature, the shelf life of HBr gas depends on several factors such as handling, cylinder material used and the leak integrity of the systems involved. Though it is not feasible always to carry out purity check before use and neither is it practical too, but a tell-tale sign of the laser head voltage-current waveforms can be taken as an indicative to adjudge the HBr purity. This is discussed in the next section.

#### **4.3 Effect of purified HBr gas on the performance of Cu-HBr laser**

The purified HBr gas is used in Cu-HBrL to see the effect of purification on the laser performance as compared to that of with unpurified case. The study is carried out in Cu-HBrL 1. The laser output powers and near-filed radial beam intensity profiles (by knife edge scan, immediately after the beam exit window) are studied. The laser discharge voltage and current waveforms are recorded, for both the cases, in the similar way as discussed in chapter 2. The laser operating parameters (input power, buffer gas pressure & flow rates) are maintained at same optimum level corresponding to undistilled HBr gas i.e. input power = ~3.7 kW, buffer

gas pressure = ~30 mbar, HBr concentration = ~6%, buffer gas flow rate = ~3.5 lit.-atm/hr. (see table 2.2, Cu-HBrL 1). The uncertainties in HBr partial pressure and gas flow rate, which are mainly guided by the control electronics of the mass flow controller and resolution of the ultra-precision (flow coefficient  $\approx 0.0004$ ) needle valve used, are around 1%. However, the measured laser output powers along with the laser voltage-current waveforms have been used as an additional reference for ensuring the repeatability of the experimental conditions.

### 4.3.1 Laser output performance

With the use of the distilled HBr gas, the maximum average laser output power obtained is 55 W at switched electrical input power  $P_{in}$  ~3.7 kW (Fig. 4.3a). On the other hand, at this condition with undistilled HBr gas, the maximum average laser output power is 40 W. This corresponds to an increase of about 37%. The corresponding increase in the laser efficiency is from ~1.1% to ~1.5%. The stability of the average laser output power, observed over a period of one hour, is also better with the distilled HBr case as compared to the undistilled one i. e.,  $\pm 1\%$  ( $55 \pm 0.5$  W) vs.  $\pm 2.5\%$  ( $40 \pm 1$  W). In both the cases, the laser spatial intensity profiles are axially peaked and very smooth Gaussian like (Fig. 4.3 b). However, for the case of purified HBr gas, the axial concentration of laser output power is more as compared to that of the

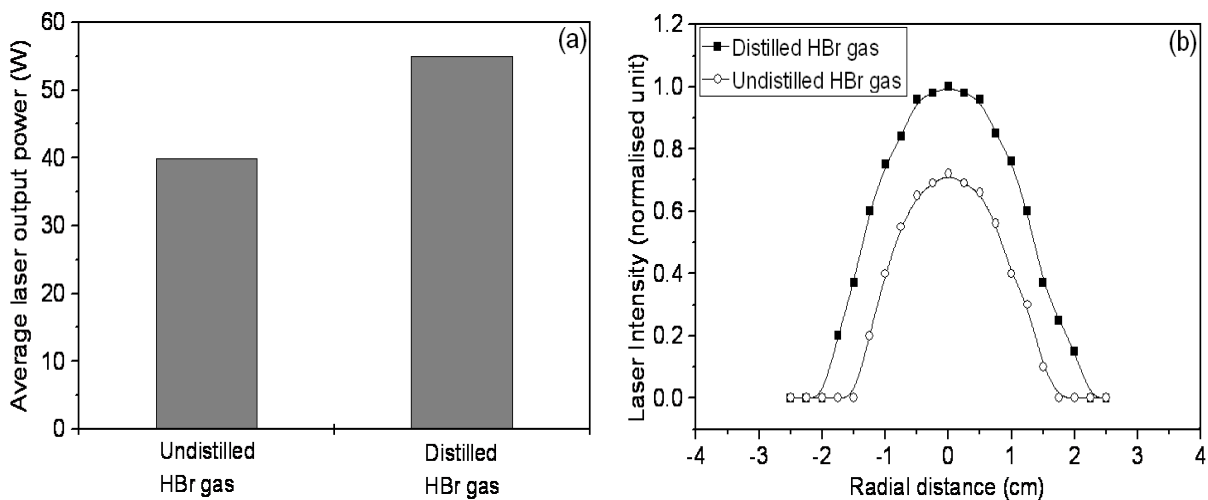


Fig. 4.3 Variation of Cu-HBrL output power (a) and radial beam intensity profiles (b) with distilled and undistilled HBr gas

undistilled HBr case. The laser discharge is less quenched in case of the purified HBr gas and the beam output diameter is found to be increased to ~4 cm (purified HBr gas) from ~3 cm (unpurified HBr gas).

#### 4.3.2 Laser discharge characteristics

In a Cu-HBrL, the improvement of laser performance has been attributed to improvement in electrical discharge characteristics resulting from addition of HBr, as discussed in chapter 3. These include increase in laser head voltage, lowering of pre-pulse electron density, better penetration of radial electric field into the discharge region and better impedance matching [7, 120, 121]. In view of this, the laser head voltage-current waveforms are recorded and analysed, in a similar way as discussed in chapter 3 (section 3.2). Figs. 4.4a & b show the digitised version of the measured laser head voltage and current waveforms respectively for both the cases of HBr. The temporal characteristics of the head voltage and current are different for the two types of HBr gas used. The maximum laser head voltage for the case of distilled HBr is ~17 kV, which is about 13% more than that of the undistilled case, i.e. ~15 kV. Also, the falling edge of the head voltage is slightly faster and beyond the half sinusoidal period,

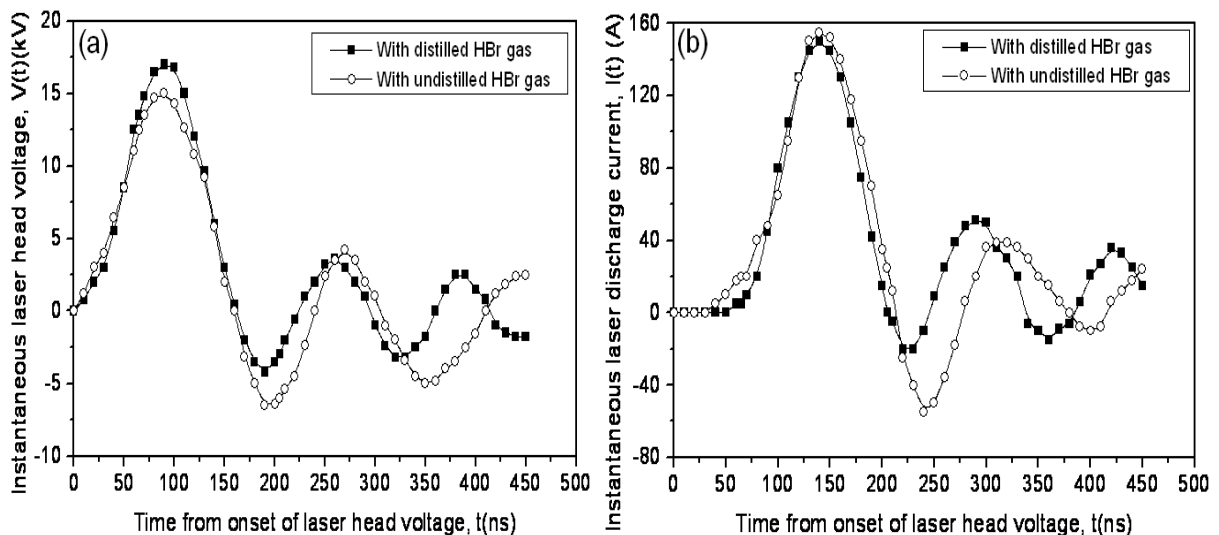


Fig. 4.4 Digitised version of the recorded laser head voltage (a) and current (b) waveforms of Cu-HBrL for distilled and undistilled HBr gas

its magnitude is lower in case of the distilled HBr gas as compared to the undistilled one. Similarly, the discharge current rise-time (5-95%), in case of the distilled HBr gas, is ~60 ns against ~80 ns with that of the undistilled one. Additionally, beyond the half sinusoidal period, its magnitude is also lower in case of the distilled HBr. However, there is only minor increase (~3%) in the peak discharge current ( $I_p$ ), from ~150 A to ~155 A, for the case of undistilled HBr gas against that of the distilled HBr gas.

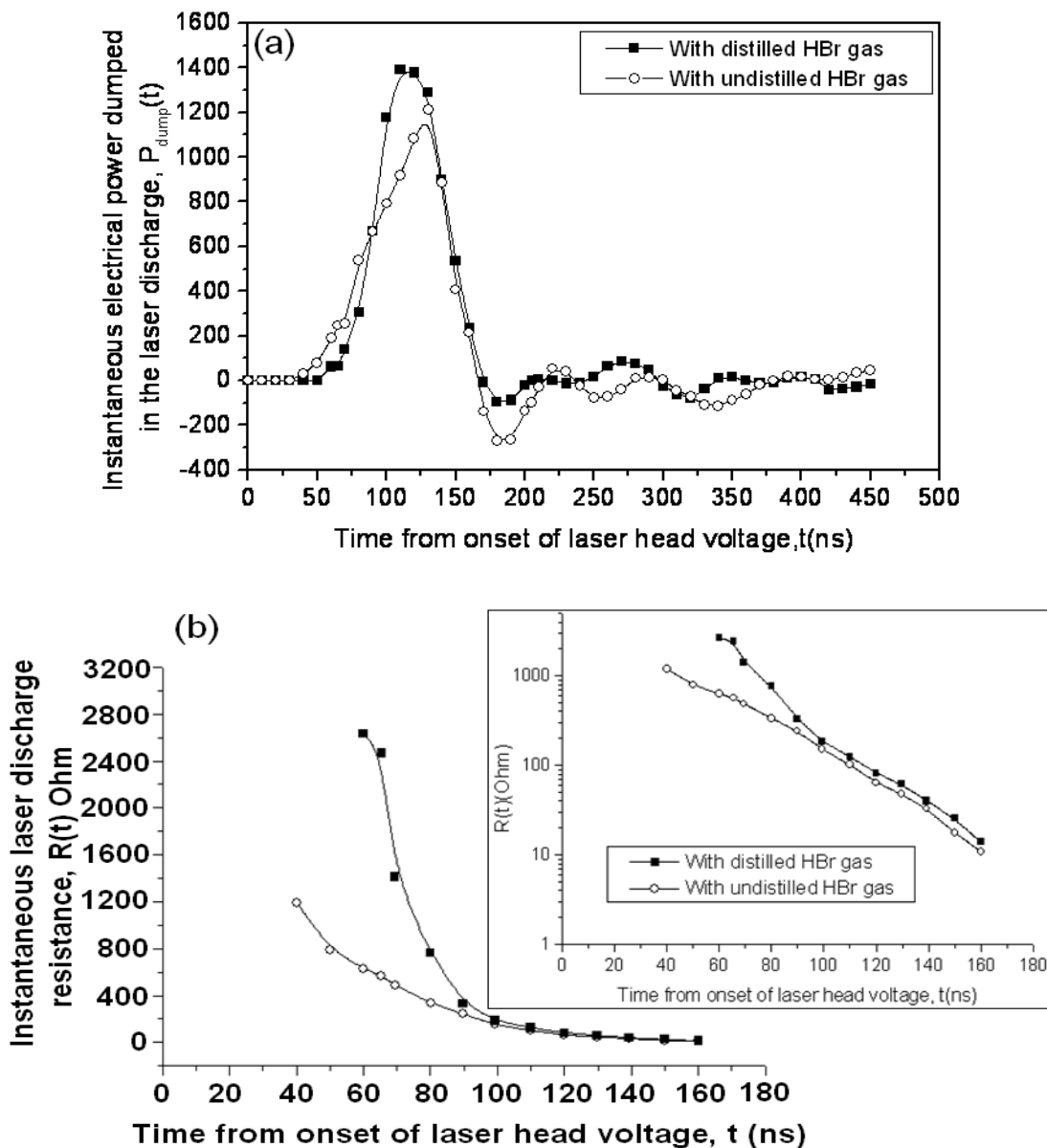


Fig. 4.5 Temporal variation of deposited electrical powers (a) and discharge resistances (b) of Cu-HBrL for distilled and undistilled HBr gas

The active electrical pulse power depositions into the discharge in both the cases are evaluated. The value of discharge loop inductances ( $L$ ), calculated using the equation 3.2, are  $\sim 900$  nH and  $\sim 700$  nH respectively for the case of undistilled HBr and distilled HBr gases. Based on this estimation and using equation 3.1, the corresponding peak active voltages are  $\sim 13.9$  kV and  $\sim 15.3$  kV. Figs. 4.5 a & b show the temporal variation of active electrical power and discharge resistance. The peak active electrical power (equation 3.3) increases from  $\sim 1211$  kW to  $\sim 1391$  kW whereas the dynamic discharge resistance (equation 3.4) undergoes a swing from  $\sim 1190$  to  $\sim 11$  ohm and  $\sim 2465$  to  $\sim 14$  ohm when distilled HBr gas is substituted by the undistilled gas. In addition, the collapse of the dynamic discharge resistance occurs at a much faster rate in case of distilled HBr gas as compared to the undistilled one i.e.  $\sim 2450$  ohm within 100 ns vs.  $\sim 1180$  ohm within 120 ns. Similarly, the average value of the discharge resistance, given as the ratio of peak value of active voltage to peak value of the discharge current (equation 3.6), are  $\sim 90$  ohm and  $\sim 102$  ohm respectively for the undistilled and distilled HBr gases. The average electrical power deposited into the laser plasma (estimated using equation 3.5) are  $\sim 3.2$  kW and  $\sim 2.9$  kW respectively for the case of distilled HBr gas and undistilled HBr gas. More importantly, the active electrical power within first 100 ns of the excitation pulse, which plays a vital role in deciding the laser performance, are  $\sim 3$  kW and  $\sim 2.6$  kW respectively for the distilled and undistilled HBr gases.

#### ***4.3.3 Analysis and discussion***

The improvement in the discharge characteristics and hence the laser performance of the Cu-HBrL can be understood by considering the discharge plasma kinetics with undistilled and distilled HBr gases. In a Cu-HBrL, it has been demonstrated that the optimum laser performance is crucially linked to the HBr partial pressure and its flow rate [130, 167]. In another study on CuBr laser with HBr and H<sub>2</sub> additives, it has been concluded that the optimal conditions of gas mixtures are necessary for improving the laser performance [181]. In a Cu-

HBr laser, the HBr partial pressure/flow rate governs the ground state copper atom density whereas its flow rate replenishes the diffusion loss of atomic bromine [15, 167]. In the case of undistilled HBr gas, the injected gas component consists of HBr molecules and their dissociation products i.e. H<sub>2</sub> and Br<sub>2</sub>. It has also been demonstrated, from both the experimental results and numerical calculations, that impurities such as excess concentration (atomic/molecular) of bromine and/or hydrogen poison the copper laser discharge in general and adversely affect its performance [62, 90, 99, 182]. The toxic effects of free hydrogen and bromine on Cu-HBrL are manifested through many interlinked processes as detailed below.

(a) *Reduced optimal DA process*: As outlined previously, out of various gaseous additive used for CVL performance improvement e.g. H<sub>2</sub>, Br<sub>2</sub>, Cl<sub>2</sub>, HBr, HCl and HI etc., HBr gives the best performance owing to its higher DA rate constants during inter-pulse period as well as its stability [65,121]. For example, at electron temperature of 0.2-0.25 eV (typical during inter-pulse period), the DA rate constants for H<sub>2</sub>, Br<sub>2</sub> and HBr are  $\sim 10^{-17}$  cm<sup>3</sup>/sec,  $\sim 10^{-11}$  cm<sup>3</sup>/sec and  $\sim 10^{-9}$  cm<sup>3</sup>/sec respectively [121]. Therefore at the same concentration of undistilled HBr and distilled HBr gas ( $\sim 1.5$  mbar in our case), the effective DA rate of the undistilled HBr (mixture of HBr, H<sub>2</sub> & Br<sub>2</sub>) is expected to be lower than that of the distilled one (mixture of  $\sim 0.5\%$  Br<sub>2</sub> and HBr). This, in turn, is reflected in terms of higher phantom current [118, 120] (current flowing through the laser tube prior to discharge break down, reflected as a kink in current pulse) and delayed collapse of discharge resistance in Cu-HBrL with undistilled HBr gas as observed in our case (Figs. 4.4 a & b). This is also the reason why the discharge resistances (both average and dynamic values), laser head voltage as well as the electrical power coupled (both peak as well as average values) to the laser discharge, are higher in case of distilled HBr as compared to the undistilled one. These considerations lead to the poorer laser performance with impure HBr gas.

(b) *Reduced ground state copper density:* It is expected that the ground state copper density, available prior to onset of the excitation pulse, would be less in case of Cu-HBrL with undistilled HBr gas as compared to that of distilled one. This is because of three reasons. First, more efficient DA process in case of distilled HBr is also expected to lead to a better recovery of the ground state copper density through the process of fast two body neutralisation of copper ions with bromine and hydrogen ions (equations 1.19 & 1.20) [120,121]. Second, excess concentrations of hydrogen and bromine in Cu-HBrL discharge (in case of undistilled HBr gas) are likely to deplete/lock the ground state copper density in the form of CuBr and CuH i.e.,  $\text{Cu} + \text{Br}/\text{H} \rightarrow \text{CuBr}/\text{CuH}$  [99]. These processes of locking of copper atoms are expected to be lower in Cu-HBrL with distilled HBr gas. Third, the partial pressure of pure HBr gas injected into the laser discharge is expected to be more than that of undistilled HBr gas consisting of three components (HBr, Br<sub>2</sub> & H<sub>2</sub>). This, in turn, contributes more copper ground state density for efficient lasing [167]. So, possibly the reduced ground state copper density along with slower discharge pulse rise time (~ 80 ns vs. ~ 60 ns.: Fig. 4.4b) in case of Cu-HBrL with undistilled HBr gas lead to lower laser power, as observed.

(c) *Adverse electron energy distribution:* In case of undistilled HBr gas, the presence of excess free Br<sub>2</sub> and H<sub>2</sub>, may also lead to the electron energy distribution function unfavourable for efficient laser level pumping. This is because of the inefficient DA process and higher plasma conductivity. This leads to slower build-up of electron temperature during initial part of the excitation pulse that results in poorer laser performance [121]. In addition, Cu-HBrL discharge plasma with pure HBr contains adequate amount H/Br concentration for efficient laser kinetics. So any excess concentrations of the free Br<sub>2</sub> and H<sub>2</sub>, present in Cu-HBrL discharge, are also expected to share the electron energy during the pumping process through additional routes of increased inelastic collisions thus making the laser pumping inefficient [121, 90, 182].

The increase in radial extent of the Cu-HBrL discharge with distilled HBr gas can be attributed to be a combination of increased penetration of the radial electric field into the discharge and effect of reduced discharge quenching. The lower phantom current in case of the distilled HBr gas (Fig. 4.4b) is a signature of lower pre-pulse electron density and hence increased skin depth of the radial electric field into the plasma [122]. In addition, in a Cu-HBrL, the negative ions formed by the DA process i.e.  $\text{Br}^-$  and  $\text{H}^-$ , constrict the discharge by enhancing their volume recombination with copper ions e.g.  $\text{Cu}^{++} + \text{Br}^-/\text{H}^- \rightarrow \text{Cu} + \text{Br}/\text{H}$ . This takes place around the axial region of the discharge tube because of higher degree of ionization of copper atoms on the tube axis as compared to the tube wall [122,124]. Both these factors contribute to increase in the overall laser gain. As the input power coupled into the plasma increases, the electron density during the excitation pulse also increases which lead to increased filling of the discharge tube cross section by the discharge current. This explains the increase of spatial extent of the electrical discharge/near-field laser beam diameter in case of distilled HBr gas. Additionally, lowering of free hydrogen and bromine concentration in distilled HBr gas reduce the discharge quenching effect [90, 99]. All these effects are expected to be responsible for increase in laser output beam diameter as observed in the present study and by others too [124, 99, 118].

Further, the increase in spatial extent of the electrical discharge in a given laser system not only increases the laser gain volume but also leads to reduction of  $L$  (discharge inductance) as estimated [124, 41]. The reduction of  $L$  further sharpens the rise of the discharge current as its rise time goes as  $\sqrt{LC_p}$ , where  $C_p$  is the capacitance of the peaking capacitor mounted on the Cu-HBrL head [41,131]. This in turn favours the increase in fractional electrical energy coupling during first 100 ns of discharge period, as observed. Additionally, substantial increase of discharge channel diameter vis-à-vis marginal increase in peak discharge current lead to decrease in current density ( $\sim 21 \text{ A/cm}^2$  to  $\sim 12 \text{ A/cm}^2$ ), which further lowers the depletion of

ground state copper density through lowering of ionization of copper atoms. So, increase of ground state copper density together with faster current pulse favours higher laser gain and hence higher laser power as observed with distilled HBr gas. Therefore, the improvement in the Cu-HBrL performance with distilled HBr gas is attributed to lowering of concentration of free bromine and hydrogen. This is mainly manifested as the increased average electrical energy coupling to the discharge and improved laser kinetics. The reduced skin effect and increased volumetric ion-ion recombination increase the radial extent of electric discharge that led to larger laser beam diameter.

Similar observations of degradation of laser performance due to excessive concentration of  $H_2$  and  $Br_2$  has also been reported in CuBr- $H_2$  laser and special electrode designs have been considered to trap the excessive bromine [126,104]. Degradation of Cu-HBrL performance at high specific electrical input power ( $\sim 3$  kW/m), that lead to thermal dissociation of HBr molecule due to increased gas temperature, has also been reported [14]. With addition of  $Br_2$  to elemental CVL, continuous degradation of the average laser output power has also been observed [90]. In a separate experiment by us, the degradation of the Cu-HBrL average output power from 40 W to 27 W has been observed, as hydrogen gas is added along with undistilled HBr gas.

#### **4.4 Conclusions**

In conclusion, this chapter presented a study on purification process of HBr gas by fractional distillation technique and its use for performance enhancement of Cu-HBrL. The residual impurities in HBr, mostly its catalytically dissociated products such as hydrogen and bromine, are removed/suppressed by two step process at temperature of  $-196$  °C and  $-20$  °C respectively. This is confirmed by comparing the mass spectrograph of the HBr gas before and after distillation. The effect of such purified HBr gas on the Cu-HBrL discharge and output performance characteristics such as the average output power, energy coupling efficiency and

output beam diameter are studied. More than 37% improvement in the laser output power and 33% increase in beam diameter are observed by use of this distilled HBr gas as compared to that of the undistilled gas. The underlying mechanisms of the enhancement are analysed by comparing the electrical discharge characteristics. The improvement in the Cu-HBrL performance with distilled HBr gas is attributed to lowering of bromine and hydrogen concentration. This is mainly manifested as the increased average electrical energy coupling to the discharge and improved laser kinetics. The presented work provides a guideline for the improving performance of a Cu-HBr laser.

## Chapter 5

### Studies on thermal lensing behaviour of Cu-HBr laser

#### 5.1 Introduction

For the applications of copper lasers such as pump source of tunable lasers, nonlinear frequency conversion for generation of coherent ultraviolet radiation and precision material processing etc., one of the issues is to ensure the high quality of laser wavefront [16, 17]. This involves consideration of thermal lensing and wavefront aberrations due to inhomogeneous radial temperature distribution. This results in the spatial variation of particle density and hence refractive index of the heated laser active medium. For conventional CVL, the thermal lensing issues have been studied adequately [43, 45-47]. It is established that thermal lensing leads to change in design parameters of the optical resonator in an oscillator, converging beams in CVL MOPA systems and non-spherical aberrated laser wavefront leading to poor laser beam quality [49, 183, 184]. However, these aspects have not been studied in case of a Cu-HBr laser. It is expected that Cu-HBr laser will have different thermal lensing behaviour, as compared to CVLs, due to its lower operating temperature and different discharge medium composition.

This chapter presents the experimental studies and theoretical analysis on the thermal lensing characteristics of developed Cu-HBrL using an interferometer technique. These results are also compared with that of a CVL of identical discharge tube geometry and excitation conditions. The experimental results on thermal lens power due to contributions from both the gaseous medium & discharge sealing optical windows as well as separately that of optical windows are presented as a function of electrical input powers and gas mixture compositions. A theoretical analysis, on the gas as well as window thermal lens, is presented taking into account the radial temperature distribution, thermal conductivity, temperature coefficient of the refractive indices of the media involved and the heat flux reaching the windows & its absorption.

## 5.2 Thermal lens and its measurement method

When a medium is heated, spatial variation in its particle density is created due to inhomogeneous spatial temperature distribution across its cross section. This is due to finite thermal conductivity of the medium involved and boundary conditions imposed by the surroundings. For high aspect ratio cylindrically symmetric heated tube, such as in Cu-HBrL/CVL, the radial component of the temperature variation dominates leading to radial variation in particle density and hence refractive index. When a collimated probe laser beam passes longitudinally through such a medium, it suffers focussing or defocusing action. This focussing or defocusing (lensing) action created by the heated medium is called thermal lensing. The strength and nature of the thermal lens of a medium is dependent on the magnitude of variation of particle density as well as its thermo-optic coefficient. Though there are several methods available for measuring the thermal lens of a medium, an interferometer based technique [185] is used in the present thermal lensing study of Cu-HBrL/CVL. This technique is preferred due to its better precision and accuracy, particularly for long focal length measurement.

The heated gaseous active medium of Cu-HBrL/CVL is vacuum sealed by pair of fused silica disks, acting as windows for the laser beam exit. Figs. 5.1 a & b show the experimental set up for measuring the combined focal length of the heated active medium and optical windows (Fig. 5.1a) and focal length of only the heated optical window (Fig. 5.1b). An expanded and collimated probe He-Ne laser beam, matching the internal diameter of discharge tube, is passed through the laser (active medium + windows) and is incident on a shear plate at 45°, after exit (Fig. 5.1a). The reflected beams, from both faces of the shear plate, produce interference pattern in the overlapping region [185]. When the Cu-HBrL/CVL, is in cold condition (no electrical input), the shear plate is set to produce horizontal fringes. On the application of electrical input power, the Cu-HBrL/CVL (active medium + end windows) is

heated up to produce thermal (refractive index) gradient. The laser beam passing through it, at such condition, undergoes convergence or divergence, resulting in change in its wavefront curvature. The exit beam, incident on the shear plate, produces straight fringes with rotation.

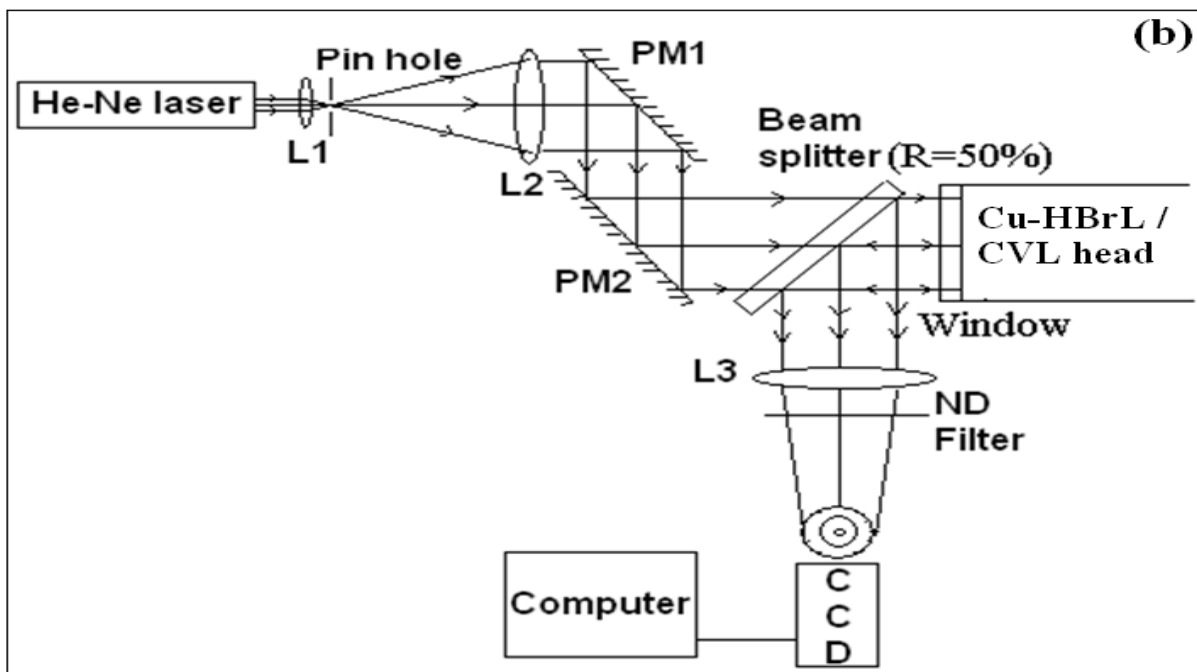
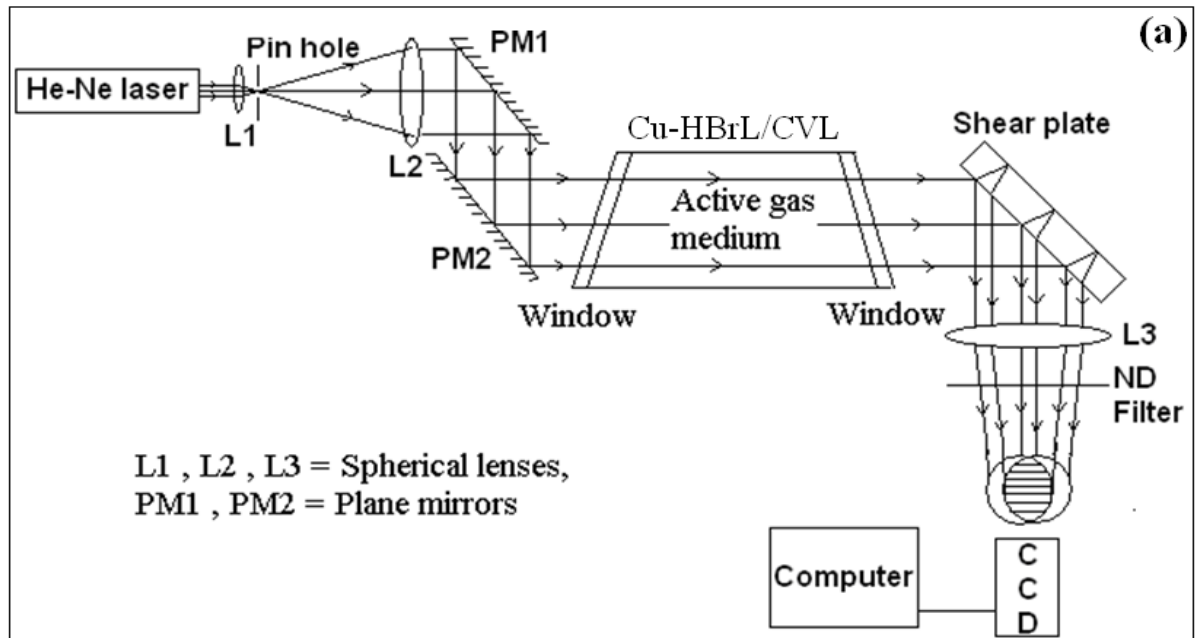


Fig. 5.1 Experimental set up for measuring thermal lens focal length of Cu-HBrL/CVL:  
(a) heated active medium & optical windows together and (b) only heated optical window

The angular extent of rotation, at the observation plane, is the measure of the focal length of the lensing action offered by the laser. The focal length of net/combined thermal lens ( $F_c$ ) is estimated from the degree of rotation of fringes and is given by [185],

$$F_c = \frac{S d'}{\lambda \sin \theta} \quad (5.1)$$

Here,  $S$  = the lateral shear and  $d'$  = the fringe spacing produced by shear plate, given as,

$$S = \frac{t' \sin 2i}{\sqrt{(n^2 - \sin^2 i)}} \quad (5.2)$$

$$d' = \frac{\lambda}{2 n \alpha} \quad (5.3)$$

where  $\lambda$  = wavelength of the He-Ne laser (632.8 nm),  $\theta$  = rotation angle of the fringes,  $t'$  = average thickness of the wedge plate used (10 mm),  $i$  = the angle of incidence ( $45^\circ$ ),  $n$  = refractive index of the wedge plate material BK-7 glass (1.515 @ 632.8 nm) and  $\alpha$  = the angle of the wedge plate (20 arc-sec). Experimentally,  $\theta$  is measured by recording the shear interferograms using a CCD camera with a frame grabber card interfaced to a computer.

For measurement of window thermal lens (Fig. 5.1b), the expanded/collimated He-Ne laser beam is incident normal to the optical window of the Cu-HBrL/CVL. The fringes, due to overlap of reflections from front and back surfaces of the optical window, are viewed at a screen. At cold condition, the fringes produced are straight. As the optical window is heated up (due to electrical input power to the laser), it behaves as a lens which results the fringes to develop curvature. The measure of the radius of the curvature of the fringes is the thermal lens due to a window. The thermal lens focal length,  $F_w$ , due to both the windows combined, is given as [45],

$$F_w = \frac{(r_p^2 - r_q^2)}{2(p-q)\lambda} \quad (5.4)$$

where  $r_p$  and  $r_q$  are the radii of the  $p^{\text{th}}$  and  $q^{\text{th}}$  fringes respectively. Then, these focal lengths

are converted to corresponding lens powers/diopters by taking inverse of  $F_c$  and  $F_w$  i.e.  $D_c = F_c^{-1}$  and  $D_w = F_w^{-1}$ . The gas thermal lens power is then  $D_g = D_c - D_w$ .

The dioptric lensing power of an optical medium,  $D$ , is proportional to spatial variation of the optical thickness ( $n.l$ ) of the medium, transverse to the direction of the optical beam propagation, i.e.

$$D \propto \frac{\partial(n.l)}{\partial r} \quad (5.5)$$

where  $n$  and  $l$  are the refractive index and thickness/length of the medium respectively and  $r$  is the radial co-ordinate. The active medium ( $l$ ) of Cu-HBrL/CVL is practically constant, largely independent of operating conditions. In such cases, for the non-uniformity of  $n$  across the medium cross-section resulting from non-uniform heating, the  $D$  value is proportional to the magnitude of spatial variation of refractive index i.e.

$$D \propto \frac{\partial n}{\partial r} \quad (5.6)$$

For a composite media consisting of gaseous as well as solid media as the case of a CVL/Cu-HBrL, equation 5.6, for combined lens diopter ( $D_c = D_g + D_w$ ) can be written as,

$$D_c \propto \left[ \left( \frac{\partial n}{\partial r} \right)_g + \left( \frac{\partial n}{\partial r} \right)_w \right] \quad (5.7)$$

such that the gas thermal lens power,  $D_g \propto \left( \frac{\partial n}{\partial r} \right)_g$  or  $(\partial n_g / \partial r)$  and the window thermal lens power,  $D_w \propto \left( \frac{\partial n}{\partial r} \right)_w$  or  $\partial n_w / \partial r$ , where  $n_g$  and  $n_w$  are the refractive indices of the gaseous active medium and window material respectively. So, the net thermal lens power of a Cu-HBrL/CVL is the inter-play of thermal lens power due to the active medium and thermal lens power due to the end windows, which in turn depend upon the radial variations of respective refractive indices. These are further related to radial variation of temperature ( $\partial T / \partial r$ ) as well as temperature coefficients of their respective refractive indices ( $\partial n / \partial T$ ) and are given as,

$$\left(\frac{\partial n}{\partial r}\right)_g = \left(\frac{\partial n}{\partial T}\right)_g \cdot \left(\frac{\partial T}{\partial r}\right)_g \Rightarrow D_g \propto \frac{\partial T_g(r)}{\partial r} \cdot \frac{\partial n_g}{\partial T} \quad (5.8)$$

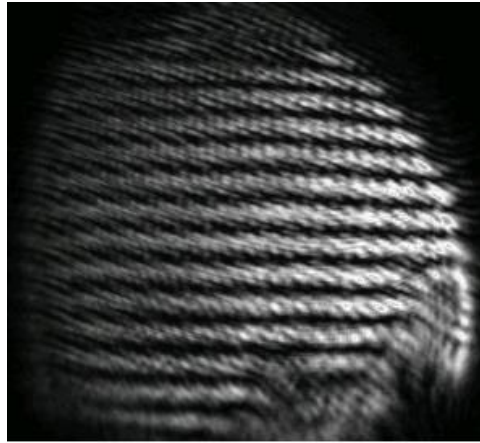
and,

$$\left(\frac{\partial n}{\partial r}\right)_w = \left(\frac{\partial n}{\partial T}\right)_w \cdot \left(\frac{\partial T}{\partial r}\right)_w \Rightarrow D_w \propto \frac{\partial T_w(r)}{\partial r} \cdot \frac{\partial n_w}{\partial T} \quad (5.9)$$

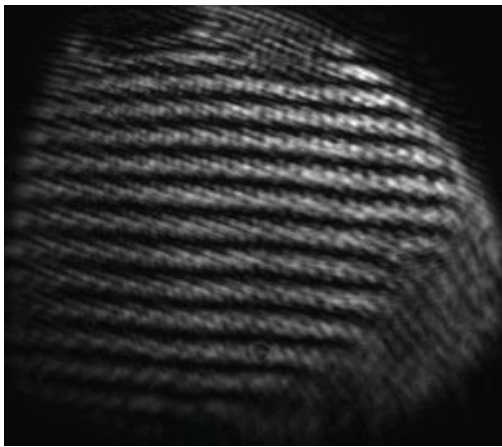
The thermal lensing nature (focussing or defocussing) is decided by the sign of thermo-optic coefficient,  $dn/dT$ . These theoretical considerations are very important for explaining the thermal lensing behaviour of Cu-HBrL/CVL as discussed in section 5.3 onwards.

### 5.3 Experimental results on thermal lens power of Cu-HBrL and CVL

The measurements of thermal lens power are carried out in both Cu-HBrL and CVL, separately. Both the lasers (Cu-HBrL & CVL) under investigation are based on identical discharge tubes of internal diameter 4.7 cm and length 150 cm. Identical fused silica optical windows are placed at ~30 cm from discharge tube ends to vacuum seal the laser discharge. Both the lasers are excited using thyatron switch (EEV CX 1535) based resonantly charged CT-circuit, up to electrical input power of 4.6 kW, and are operated in controlled buffer gas flow condition for efficient operation. Figs. 5.2 a - e show the typical shear interferograms recorded for estimation of combined focal length of thermal lens due to Cu-HBrL (a, b & c) and CVL (a, d & e) at electrical input power of 0 kW (cold condition), 2.7 kW and 4.6 kW respectively. The interferograms are recorded at equilibrium condition of the tube and window temperature. Initially, in cold condition (0 kW), the shear fringes of the He-Ne laser are set parallel to the x-axis for both the Cu-HBrL & CVL (Fig. 5.2a). As the input power is increased, the fringes start tilting. At electrical input power of 2.7 kW, the tilt of the shear fringe of Cu-HBrL is negative (clock wise rotation w.r.t. to Fig. 5.2 a) whereas for CVL, the observed tilt is positive (anti-clock wise rotation w.r.t. to Fig. 5.2a). As the input power increases further to 4.6 kW, the fringes have positive tilt for both the lasers. However, the tilt is much smaller for Cu-HBrL (Fig. 5.2c) as compared to that of CVL (Fig. 5.2e).



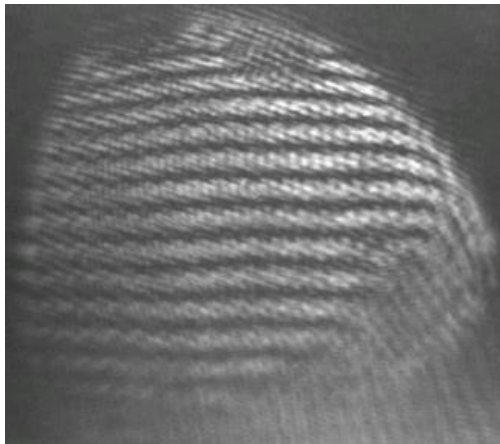
(a) Zero tilt ( $\theta \approx 0^\circ$ )



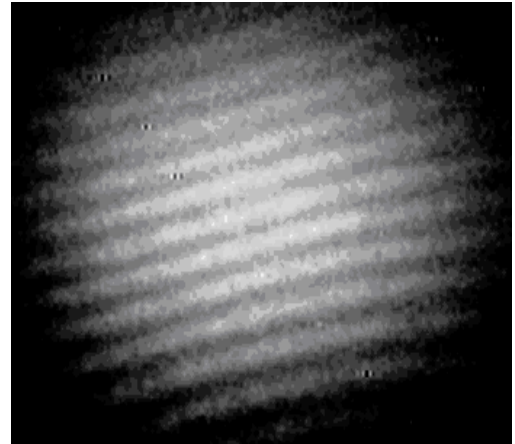
(b) Negative tilt ( $\theta \approx -2^\circ$ )



(d) Positive tilt ( $\theta \approx +2^\circ$ )



(c) Positive tilt ( $\theta \approx +1.4^\circ$ )



(e) Positive tilt ( $\theta \approx +19.3^\circ$ )

*Fig. 5.2 Shear interferograms of combined thermal (active medium + windows)*

*lens estimation at 0 kW - Cu-HBrL & CVL (a), at 2.7 kW - Cu-HBrL (b),*

*at 4.6 kW - Cu-HBrL (c), at 2.7 kW - CVL (d), at 4.6 kW - CVL (e)*

Figs. 5.3 a - c show the interferograms recorded for focal length estimation of optical windows thermal lens of the Cu-HBrL and CVL. Again at the cold condition (0 kW) the fringes are set straight (Fig. 5.3a). As the input power is increased to 4.6 kW, the interferograms of the Cu-HBrL window show a very minute (non-estimable) change in curvature (Fig. 5.3b) against a drastic change in case of CVL (Fig. 5.3c).

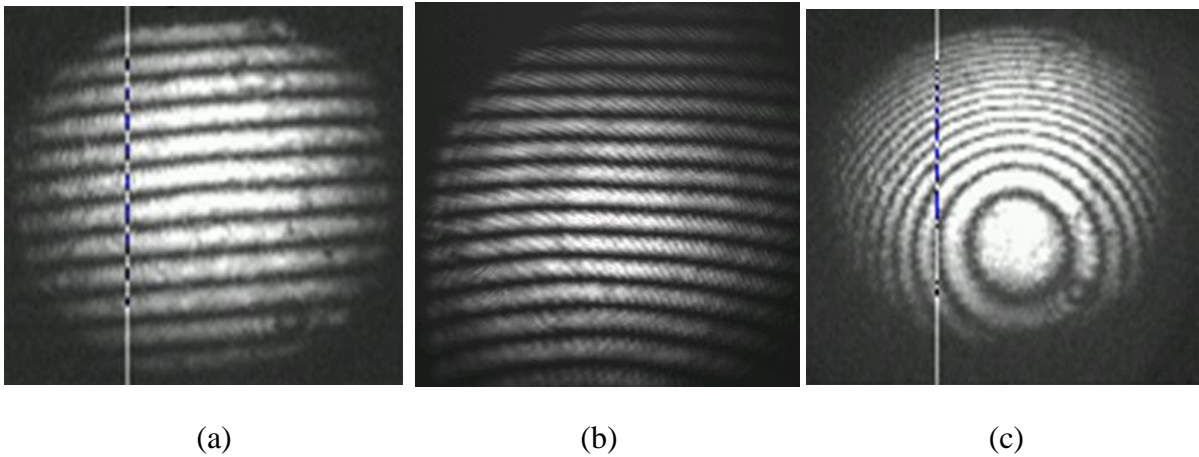


*Fig. 5.3 Fringes due to window thermal lens of Cu-HBrL and CVL for different input powers: (a) Cu-HBrL and CVL for 0 kW, (b) Cu-HBrL for 4.6 kW and (c) CVL for 4.6 kW*

Fig. 5.4 shows the variation of estimated combined (active medium + windows) lens diopter ( $D_c$ ) with electrical input powers for both the lasers. As the input power increases from 2.7 kW to 4.6 kW,  $D_c$  varies from  $-1.4 \text{ km}^{-1}$  to  $+0.94 \text{ km}^{-1}$  for the Cu-HBrL and from  $+1.4 \text{ km}^{-1}$  to  $+13 \text{ km}^{-1}$  for the CVL. Regarding the thermal lens of the windows, the curvature of the fringes in case of Cu-HBrL (Fig. 5.3b) is too large to be measured and hence no estimation of focal length has been possible even at the highest electrical input power (4.6 kW) used. However, for the CVL, the window thermal lens power ( $D_w$ ) dominates the overall thermal lensing behaviour and it varies from  $+3 \text{ km}^{-1}$  to  $+15 \text{ km}^{-1}$  as the input power increases from 2.7 kW to 4.6 kW. An error analysis of the measured results is carried out. The smallest possible measurable tilt/rotation of the fringes (resolution limit of measurement) corresponds to the angular separation of one fringe width at the focal plane of the lens L3 (Fig. 5.1) where the

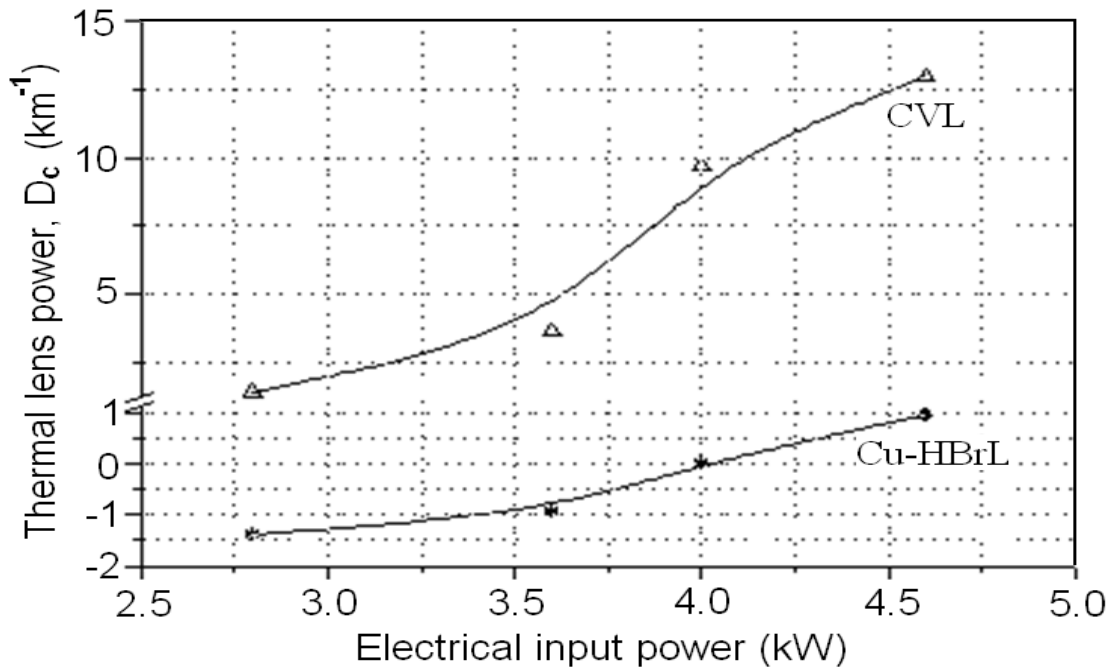


Fig. 5.4 Variation of thermal lens power of Cu-HBrL and CVL with electrical input power

CCD is placed for recording. In the present experimental set ups, the measured fringe width at CCD is about 2 mm, while the lens L3 of focal length is 25 mm. This corresponds to the lowest measurable tilt/rotation angle ( $=$  fringe width/lens focal length) of about  $0.5^\circ$ . Using equation 5.1, this angular fringes resolution corresponds to the dioptric power resolution of about  $0.35 \text{ km}^{-1}$ . Hence the dioptric power variation from  $-1.4 \text{ km}^{-1}$  to  $+13 \text{ km}^{-1}$ , for both the lasers, is well resolved by the present setup.

#### 5.4 Analysis and discussion on thermal lens power

As outlined in section 5.2, the observed thermal lens behaviour in Cu-HBrL/CVL is a combined effect of thermal lens due to the gaseous active medium and solid end windows. The lensing behaviour of these two media is different due to differences in particle density gradient (due to different temperature) and temperature coefficient of refractive indices. Therefore, these two lensing effects are first treated separately and then combined to explain the experimental results.

### 5.4.1 Gas thermal lens

The thermal lensing behaviour of gaseous active medium of copper lasers is a complex phenomenon which depends on many factors such as discharge tube geometry, gas pressure, wall temperature and thermal conductivity as well as the thermo-optic coefficients of the gaseous medium [43,45-47,51]. For typical laser operating conditions of Cu-HBrL/CVL, as used in the present study, the thermo-optic coefficients of the gaseous constituents ( $\partial n_g/\partial T$ ), dominated by that of neon buffer gas, is  $\sim -10^{-10} \text{ K}^{-1}$  [43,45,175,186]. Therefore, the radial variation of gas temperature,  $\partial T_g(r)/\partial r$ , is expected to play a crucial role in resolving the anomalies of thermal lens behaviour of the two lasers under investigation (equation 5.8). To understand the effect of gas temperature profile, the radial gas temperature distribution for both the lasers are computed using equation 2.4 (as discussed in chapter 2) with differing values of gas thermal conductivity  $K$  ( $K = K_o.T_g^m$ ) relevant for Cu-HBrL and CVL. For gas mixture of CVL,  $m = 0.685$  &  $K_o = 9.7 \times 10^{-4}$  and for gas mixtures of a Cu-HBrL,  $m = 1.54$  &  $K_o = 1.84 \times 10^{-6}$  [45, 7]. The tube wall temperatures are  $\sim 900 \text{ K}$  and  $\sim 1800 \text{ K}$  for Cu-HBrL and elemental CVL respectively.

Fig. 5.5a shows the variation of  $T_g(r)$  with the radial distance,  $r$ , for the highest input power of 4.6 kW. The estimated peak/axial gas temperatures are  $\sim 2360 \text{ K}$  and  $\sim 3100 \text{ K}$  for Cu-HBrL and CVL respectively. The gas temperature gradient is calculated for central 90% of the tube cross-section ( $r = -2.0 \text{ cm}$  to  $+2.0 \text{ cm}$ ), omitting the boundary points ( $r = \pm 2.35 \text{ cm}$ ). It is seen that the slope of the graphs,  $\partial T_g(r)/\partial r$ , is higher in case of the CVL as compared to Cu-HBrL. For example, at spatial locations of 0.5 cm, 1 cm, 1.5 cm and 2 cm from the tube axis, the gas temperature gradients (evaluated each time with respect to the temperature at the tube axis) are  $102 \text{ K.cm}^{-1}$ ,  $208 \text{ K.cm}^{-1}$ ,  $322 \text{ K.cm}^{-1}$ ,  $451 \text{ K.cm}^{-1}$  for the CVL and  $80 \text{ K.cm}^{-1}$ ,  $165 \text{ K.cm}^{-1}$ ,  $267 \text{ K.cm}^{-1}$ ,  $416 \text{ K.cm}^{-1}$  for the Cu-HBrL. It is clear that in CVL, the radial variation of gas temperature is more than that of Cu-HBrL. Physically this is also expected because

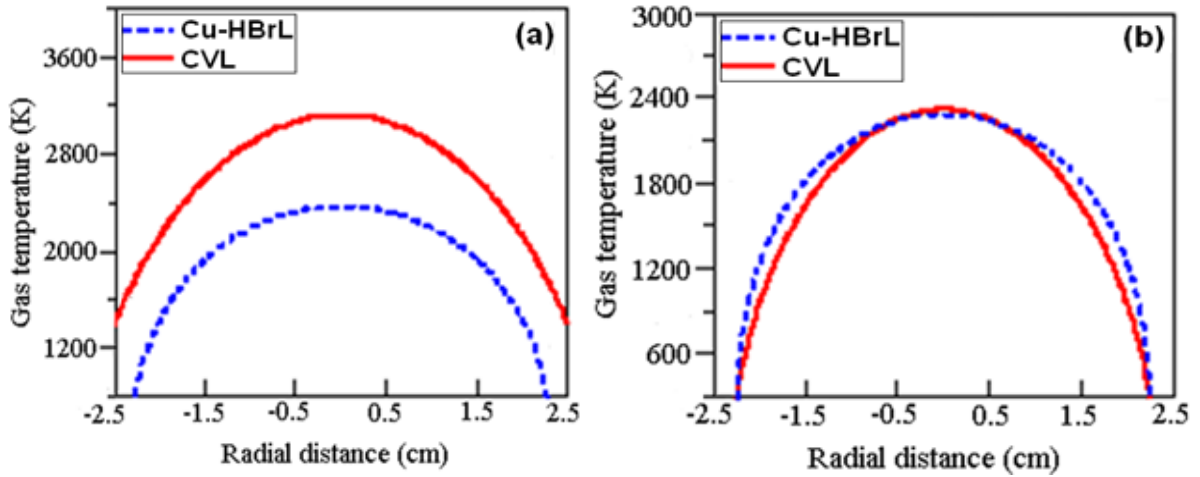
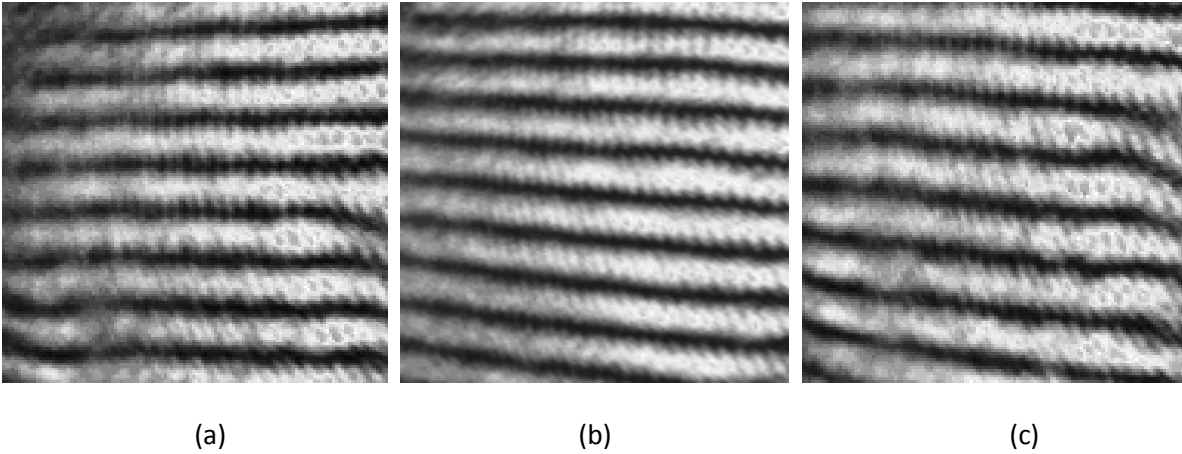


Fig. 5.5 Computed radial gas temperature profiles for Cu-HBrL and CVL (a) at equilibrium condition for electrical input of 4.6 kW and (b) immediately after the discharge is on

presence of hydrogen as a dissociation product of HBr in a Cu-HBrL plasma. The presence of hydrogen molecules in the gas mixture increase the thermal conductivity, hence increased radial heat transfer in Cu-HBrL as compared to CVL of identical configuration [59, 175]. This makes the gas temperature distribution of Cu-HBrL to be relatively flatter than that of CVL. Therefore, the spatial gradient of the active medium particle density is expected to be larger in CVL [43].

For the CVL,  $D_g$  changes from  $\sim -1.6 \text{ km}^{-1}$  to  $\sim -2 \text{ km}^{-1}$  as the input power is increased from 2.7 kW to 4.6 kW. As already mentioned, for the Cu-HBrL as  $D_w$  is too low to be measured and hence the quantitative estimation of  $D_g (= D_c - D_w)$  is not possible. However, qualitative understanding of active medium gas lens is made by studying the rotation of fringes immediately (time  $t = 0$ ) after putting the discharge on, in the Cu-HBrL with and without HBr gas flow (in set up of Fig. 5.1a). The results are shown in Figs. 5.6 a, b & c. Gas lens power is again estimated from tilt of the fringes from a pre-set initial horizontal value (Fig. 5.6a). Since immediately after the putting the discharge on, no appreciable heating of discharge tube has taken place, the fringe rotation is exclusively due to that of gas lens. The gas lens power ( $D_g$ ) is found to be  $-2.5 \text{ km}^{-1}$  with HBr introduced (Fig. 5.6b) and  $-3.0 \text{ km}^{-1}$  without HBr (Fig. 5.6c).



*Fig. 5.6 Recorded shear fringes (a) Cold condition, no discharge (b) Cold condition, Cu-HBrL, discharge just on (c) Cold condition, CVL (no HBr), discharge just on*

In cold condition ( $T_0 \sim 300$  K), without HBr gas flow, a Cu-HBrL resembles a CVL. Hence in cold condition, the gas lens of CVL is seen to be stronger than that of a Cu-HBrL. This is consistent with the computed radial gas temperature profiles for Cu-HBrL and CVL in cold condition (Fig. 5.5b). The estimated peak/axial gas temperatures in this case are  $\sim 2280$  K and  $\sim 2300$  K for Cu-HBrL and CVL respectively. The radial temperature gradient,  $\partial T_g(r)/\partial r$ , is higher for CVL as compared to Cu-HBrL. Hence, though the gas lens in Cu-HBrL could not be measured in the present set up, it is anticipated to be weaker as compared to CVL. This is also in line with other published works for thermal lens studies in elemental CVL [43, 45, 46] and  $\text{CO}_2$  laser [187], where the thermal gas lens has become stronger with increase in electrical input power and hence increased axial gas temperature.

#### **5.4.2 Window thermal lens**

As indicated in equation 5.9, the window thermal lens depends on the thermo-optic coefficient of the window material as well as its radial temperature gradient established at equilibrium condition. The radial temperature gradient of the window depends on the net incident heat flux, the wavelength range of the radiated heat, thermal conductivity of the window material and its boundary conditions. The heat flux mainly comes from the tube wall

since the gas emissivity is negligible [11]. The heat radiation emitted by the discharge tube end can be considered to be that of blackbody type. The power radiated by it,  $P_{rad}$ , can be estimated by applying Stephen-Boltzmann law of black body radiation as,

$$P_{rad.} = A \varepsilon \sigma T_o^4 = \pi \varepsilon \sigma (R_o^2 - R_i^2) T_o^4 \quad (5.10)$$

where  $A$  = end surface area of the discharge tube,  $\varepsilon$  = emissivity of alumina ( $\sim 0.5$ ),  $\sigma$  = Stephen-Boltzmann constant =  $5.67 \times 10^{-8} \text{ W m}^{-2} \text{ K}^{-4}$ ,  $T_o$  = discharge tube wall temperature,  $R_i$  = internal radius of the discharge tube and  $R_o$  = outer radius of the discharge tube. The fraction of radiated power reaching to the laser window,  $P_{rad(w)}$ , is given as,

$$P_{rad.(w)} \approx \left( \frac{P_{rad.(w)}}{4\pi} \right) \cdot \Delta\Omega \approx \frac{\pi r_w^2 P_{rad.}}{4\pi l'^2} \quad (5.11)$$

where  $\Delta\Omega$  is the solid angle extended by the discharge tube end at the window surface of radius  $r_w$  situated at a distance of  $l'$  from the tube end. This radiated heat reaching at the window undergo absorption which is characteristic of window material and wavelength of radiation. Thus taking the absorptivity ( $\beta$ ) into consideration and simplification of equations 5.10 & 5.11 yields the radiative power absorbed by the window,  $P_{abs(w)}$ , as,

$$P_{abs.(w)} = \frac{\pi \beta \varepsilon \sigma r_w^2 (R_o^2 - R_i^2) T_o^4}{4l'^2} \quad (5.12)$$

Putting the values of  $R_i = 2.35 \times 10^{-2} \text{ m}$ ,  $R_o = 2.85 \times 10^{-2} \text{ m}$ ,  $r_w = 7.5 \times 10^{-2} \text{ m}$  and  $l' = 0.3 \text{ m}$  in equation 5.10, the heat radiated by the alumina discharge tube end are  $\sim 243 \text{ W}$  and  $\sim 15 \text{ W}$  respectively for CVL and Cu-HBrL. Out of this, heat reaching at the window is  $\sim 3.3 \text{ W}$  and  $\sim 0.21 \text{ W}$  for CVL and Cu-HBrL respectively (using equation 5.11). These radiated powers are spreaded over certain infra-red wavelength range with peak intensity corresponding to wavelength, designated as  $\lambda_{max}$ . The  $\lambda_{max}$  is a function of temperature of the body emitting radiation given by Wien's displacement law of blackbody radiation as,

$$\lambda_{max.} = \frac{b}{T_o} \quad (5.13)$$

where  $b$  is the Wien's displacement constant and is equal to  $2.898 \times 10^{-3}$  m.K. The corresponding irradiance peak lies at wavelength ( $\lambda_{\max}$ ) of  $\sim 1.61 \mu\text{m}$  and  $\sim 3.22 \mu\text{m}$  respectively for CVL and Cu-HBrL. The incident heat flux get absorbed by the respective windows, consequently these heat up. This absorption is a function of incident IR wavelength. For the fused silica windows, used in the present work, there is a peak in absorption at wavelength around  $2.7 \pm 0.5 \mu\text{m}$  due to hydroxyl ion [49]. The typical absorption fraction by the fused silica windows of thickness, 1 cm (as presently used), is about 40% at  $\lambda_{\max} \sim 1.61 \mu\text{m}$  and about 90% at  $\lambda_{\max} \sim 3.22 \mu\text{m}$  [49]. Hence, the net absorbed heat power is  $\sim 1.32$  W for windows in CVL as compared to  $\sim 0.18$  W for the Cu-HBrL. Therefore, the window of the Cu-HBrL is less heated as compared to that of CVL. So, the radial temperature gradient of the fused silica laser window,  $\partial T_w(r)/\partial r$ , is also expected to be much larger in CVL as compared to Cu-HBrL. This is line with the fact that the measured (with thermocouple) axial temperatures of the fused silica windows are  $\sim 50$  °C and  $\sim 25$  °C for CVL and Cu-HBrL respectively, for constant boundary condition of  $\sim 20$  °C (cooling water). This explains the much larger value of window thermal lens in CVL as compared to Cu-HBrL.

As already mentioned that the window thermal lens in Cu-HBrL could not be measured with this present set up, however an upper bound on its value can be anticipated. Since about 1.32 W of absorbed heat gives rise the lens power of  $+ 15 \text{ km}^{-1}$  (in CVL), hence the 0.18 W of absorbed heat in Cu-HBrL will correspond to a thermal lens power of around  $+ 2 \text{ km}^{-1}$ . This figure can be treated as an upper bound on window thermal lens of Cu-HBrL. It is also expected that employing, fluoride windows e.g.  $\text{MgF}_2$ ,  $\text{CaF}_2$  will result in much smaller thermal lensing due to their much less IR absorption corresponding to Cu-HBrL/CVL heat radiation and better thermal conductivity ( $21 \text{ Wm}^{-1}\text{K}^{-1}$  for  $\text{MgF}_2$ ,  $9.7 \text{ Wm}^{-1} \text{ K}^{-1}$  for  $\text{CaF}_2$  vs.  $1.38 \text{ Wm}^{-1}\text{K}^{-1}$  for fused silica) as compared to that of fused silica [49]. However, the cost and engineering issues associated with these materials are major factors of consideration. In

addition, the window bulging effect arising out of pressure difference across it e.g. at one side of the window the pressure is 1 atm. and at the other side it is 25-30 mbar, plays role in deciding the window thermal lensing. This is under thin window approximation as the window thickness (10 mm) is much smaller than its diameter (75 mm). The bulging effect of fused silica is expected to be lower than the commonly used material BK-7. This is due to lower value of Poisson's ratio for fused silica (0.17) as compared to that for BK-7 (0.21). However, since the present study is focused on the comparative thermal lensing behaviour of the two lasers and the pressure difference is almost same for both the cases, hence it is least likely to affect the relative thermal lensing trends of the two lasers under discussion.

#### **5.4.3 Combined thermal lens**

The combined thermal lens observations (Figs. 5.2 a - e) tell two important facts. First, the net thermal lensing is much more stronger in a CVL as compared to than in a Cu-HBrL, Second, in the investigated input power range (2.7 to 4.6 kW), the thermal lensing nature change from negative (de-focussing) to positive (focusing) in Cu-HBrL as compared to always remaining positive for CVL. From the analysis and discussion presented previous sections, it is clear that the window thermal lens dominates the overall thermal lensing behaviour in a Cu-HBrL/CVL. This is attributed to much larger magnitude of  $\partial n/\partial T$  of the window material (fused silica) as compared to that of the gaseous constituent particles (mostly dominated by neon) i.e.,  $\partial n_g/\partial T \sim -10^{-10} \text{ K}^{-1}$  for gaseous constituents [43,45,175,186] vs.  $\partial n_w/\partial T \sim +10^{-5} \text{ K}^{-1}$  for fused silica window material [49]. It is also observed that the fused silica window behaves as positive lens (focusing) whereas the gaseous active medium behaved as negative lens (defocusing). The opposite behaviour gas lens and window lens are due to opposite nature of  $\partial n/\partial T$  for gas (negative) and the window material (fused silica) used (positive). That is why, as the input power increases, the window thermal overtakes that of the gas lens and the net thermal lens becomes + ve for both the Cu-HBrL and CVL.

## 5.5 Conclusions

In conclusion, this chapter presented experimental studies and theoretical analysis on the thermal lensing characteristics of the developed Cu-HBrL using an interferometer technique. These results are also compared with that of a conventional CVL of identical discharge tube geometry and input-power/excitation conditions. It is observed that in typical operating conditions, the Cu-HBrL has much weaker thermal lens as compared to that in the CVL ( $\sim +0.95 \text{ km}^{-1}$  vs.  $\sim +13 \text{ km}^{-1}$ ). The experimental results are explained qualitatively by a comprehensive theoretical analysis on the gas thermal lens as well as the window thermal lens, taking into account the radial temperature distribution, thermal conductivity, temperature coefficient of the refractive indices of the media involved and the heat flux reaching the windows & its absorption. It is observed that the contribution of the optical windows thermal lens dominates over that of the gaseous active medium. The dominance of window thermal lens in overall thermal lensing behaviour of Cu-HBrL/CVL is attributed to higher temperature coefficient of refractive index for window material as compared to that of gaseous active medium ( $\partial n/\partial T \sim +10^{-5} \text{ K}^{-1}$  vs.  $\sim -10^{-10} \text{ K}^{-1}$ ). The overall thermal lens power of Cu-HBrL than that of CVL is due to its much lower working temperature as well as relatively flatter radial gas temperature. The analysis agrees well with the observed trends. This aspect of spatial beam characteristics of a Cu-HBrL is of crucial importance for applications requiring high beam quality laser output such as in nonlinear frequency conversion for UV generation presented in the thesis, in later chapter.

## Chapter 6

### Studies on spectral characteristics of Cu-HBr laser

#### 6.1 Introduction

The knowledge of spectral emission characteristics of a Cu-HBr laser such as line-width, frequency and their stability are very important for many of its applications in general and efficient nonlinear frequency conversion for UV generation in particular. In nonlinear frequency conversion, the conversion efficiency is maximized by ensuring that the spectral line-width of the pump fundamental beam to be well within the spectral acceptance band-width of the nonlinear crystal employed [188,189]. In this context, for the nonlinear frequency conversion, as carried out in this thesis, it is desirable to carry out a study on the spectral line-width and frequency characteristics of a Cu-HBrL. In literature, only a few studies on the line-width issues have been reported in CVL and copper bromide/chloride lasers at very low laser output power [190-195]. However, these aspects have not been paid attention in a Cu-HBrL in general and at high average laser power levels in particular. It is expected that the spectral characteristics of a Cu-HBrL would be different from other variants of copper laser due to different operating temperature, gas composition and laser gain distributions.

In view of this, the present chapter deals with a detailed experimental study and the related theoretical analysis on the spectral emission characteristics of both the green (G: 510.6 nm) and yellow (Y: 578.2 nm) radiations of a Cu-HBrL for different laser operating parameters. The Cu-HBrL spectral emission characteristics such as line-width, emission frequency & their stability are studied as a function of electrical input power, HBr concentration and optical resonator. The experimental results are explained by a comprehensive theoretical analysis followed by simulation of the spectral line-shapes of both the radiations.

#### 6.2 Theory of spectral emission of a Cu-HBr laser

The spectral composition of a Cu-HBrL can be thought of as a single emission line or

consisting of several hyperfine emission lines. These two approximations basically differ in terms of exclusion/inclusion of isotope shifts and hyperfine splitting of the energy levels associated with copper atom. The major intrinsic physical processes governing the spectral emission line-width of a Cu-HBrL are isotope shift, hyperfine splitting, line broadening and temperature & gain distribution effects associated with the energy levels of radiating copper atoms [190, 193, 194, 196].

### 6.2.1 Isotope shift and hyperfine splitting

Copper has two natural isotopes,  $^{63}\text{Cu}$  &  $^{65}\text{Cu}$ , with abundance ratio of 69% : 31%, which contribute to net observable isotope shift in both the emission lines of a Cu-HBrL. Additionally, both the isotopes have nuclear spin  $I = 3/2$ , which account for their non-zero magnetic dipole (requirement:  $I > 0$ ) as well as electric quadrupole moment (requirement:  $I \geq 1$ ). This leads to additional interactions with total electron angular moments ( $J$ ) of the atomic state, known as the hyperfine interaction, leading to further splitting of the energy levels of the copper atom. Fig. 6.1 shows the relevant energy levels of natural copper atom ( $^{63}\text{Cu}$  &  $^{65}\text{Cu}$ ) depicting the laser transitions associated with a Cu-HBrL emission spectra.

These hyperfine energy levels have a definite value of total angular momentum  $F$  ( $\vec{F} = \vec{I} + \vec{J}$ ) such that  $|J - I| \leq F \leq |J + I|$ . Both the upper and lower fine-structure energy level of the green transition i.e.  $^2P_{3/2}$  &  $^2D_{5/2}$ , split into four hyperfine components of  $F = 0, 1, 2, 3$  and  $F = 1, 2, 3, 4$  respectively. Similarly the energy levels of the yellow transition i.e.  $^2P_{1/2}$  &  $^2D_{3/2}$ , split into  $F = 1, 2$  and  $F = 0, 1, 2, 3$  respectively. However, the allowed transitions between the hyperfine levels are restricted by the selection rule  $\Delta F = 0, \pm 1$ . This leads the green component ( $^2P_{3/2} \rightarrow ^2D_{5/2}$ ) to consist of total 18 hyperfine transitions ( $a_g$  to  $i_g$  for  $^{63}\text{Cu}$  &  $a_g'$  to  $i_g'$  for  $^{65}\text{Cu}$ ) and the yellow component ( $^2P_{1/2} \rightarrow ^2D_{3/2}$ ) to consist of total 12 hyperfine transitions ( $a_y$  to  $f_y$  for  $^{63}\text{Cu}$  &  $a_y'$  to  $f_y'$  for  $^{65}\text{Cu}$ ). The frequency shifts of the hyperfine components ( $\Delta\nu^H$ ) with respect to the center frequency,  $\nu_0$ , are given by [191],

$$\Delta\nu^H = \nu_{hfs} - \nu_o = \frac{AC}{2} + \left(\frac{B}{4}\right) \left(\frac{3C(C+1) - 4I(I+1)J(J+1)}{2IJ(2I-1)(2J-1)}\right) \quad (6.1)$$

where  $A$  and  $B$  are magnetic dipole and electric quadrupole hyperfine constants respectively whereas  $C = F(F+1) - J(J+1) - I(I+1)$  whose typical values are given in Ref. 191.

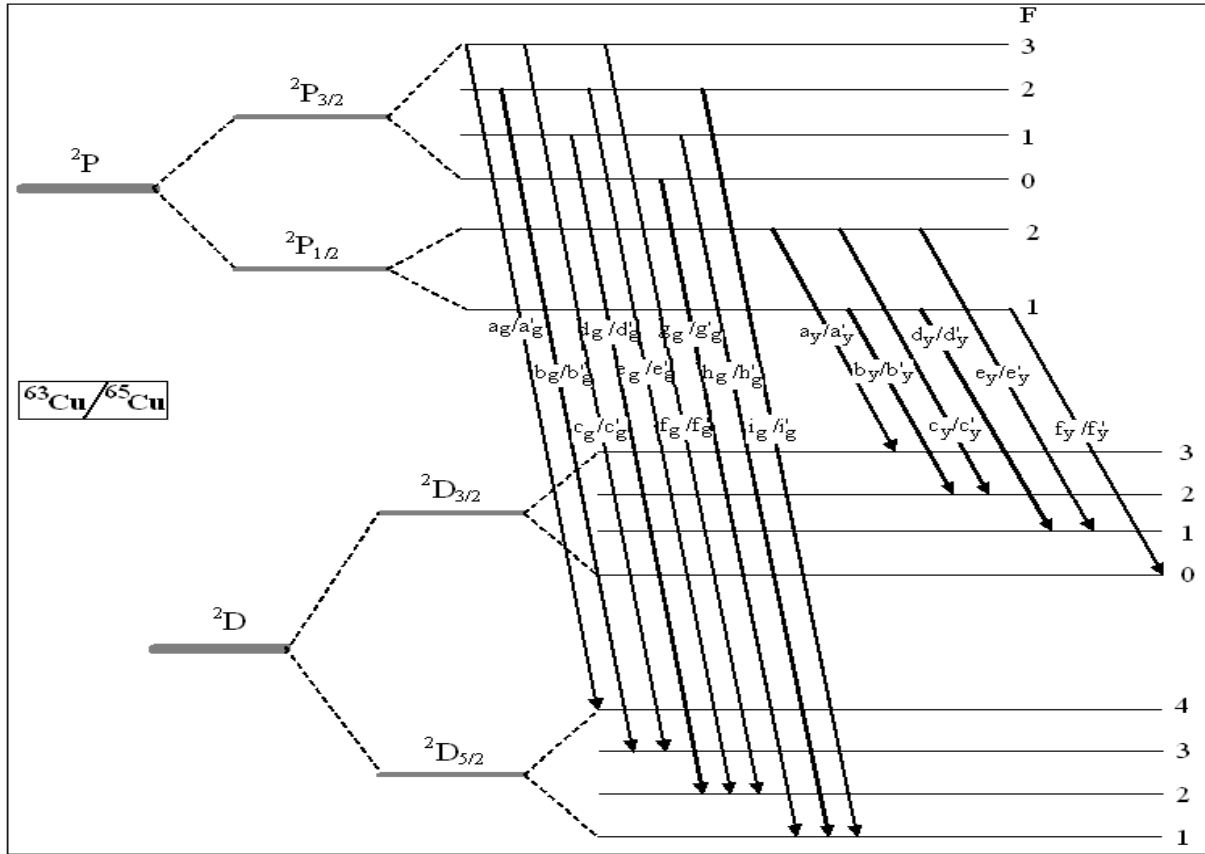


Fig. 6.1 Hyperfine energy levels and transitions in copper atom relevant to Cu-HBrL

For each of the hyperfine transitions, the relative intensity is given as [197],

$$I(JF \rightarrow J'F') \propto \beta_{iso} \frac{J(J+1)(2J'+1)(2F+1)(2F'+1)}{(2J+1)} \begin{Bmatrix} J & F & I \\ F' & J' & 1 \end{Bmatrix}^2 \quad (6.2)$$

where  $\beta_{iso}$  is the isotopic abundance factor. This is calculated using Wigner 6-J symbol (a reduced matrix of the *Clebsch-Gordan* coefficient) [198]. Table 6.1 shows the frequency shifts and the relative intensities calculated for the involved hyperfine transitions in a copper atom.

Table 6.1: Frequency shifts and relative intensities of the hyperfine components of Cu-HBrL lines based on transitions in natural copper atom

Green (510.6 nm) : G						Yellow (578.2 nm) : Y					
<sup>63</sup> Cu			<sup>65</sup> Cu			<sup>63</sup> Cu			<sup>65</sup> Cu		
Hyperfine transition	$\Delta\nu^H$ (GHz)	I <sub>rel.</sub>	Hyperfine transition	$\Delta\nu^H$ (GHz)	I <sub>rel.</sub>	Hyperfine transition	$\Delta\nu^H$ (GHz)	I <sub>rel.</sub>	Hyperfine transition	$\Delta\nu^H$ (GHz)	I <sub>rel.</sub>
a <sub>g</sub>	-2.424	1.00	a <sub>g</sub> '	-0.343	0.45	a <sub>y</sub>	-3.819	1.00	a <sub>y</sub> '	-1.868	0.45
b <sub>g</sub>	0.165	0.62	b <sub>g</sub> '	2.410	0.28	b <sub>y</sub>	0.858	0.36	b <sub>y</sub> '	3.124	0.16
c <sub>g</sub>	0.722	0.16	c <sub>g</sub> '	3.011	0.07	c <sub>y</sub>	1.872	0.36	c <sub>y</sub> '	4.211	0.16
d <sub>g</sub>	1.909	0.35	d <sub>g</sub> '	4.297	0.16	d <sub>y</sub>	4.422	0.36	d <sub>y</sub> '	6.965	0.16
e <sub>g</sub>	2.328	0.19	e <sub>g</sub> '	4.742	0.09	e <sub>y</sub>	5.436	0.07	e <sub>y</sub> '	8.051	0.03
f <sub>g</sub>	2.885	0.01	f <sub>g</sub> '	5.343	0.005	f <sub>y</sub>	6.136	0.14	f <sub>y</sub> '	8.821	0.06
g <sub>g</sub>	3.067	0.16	g <sub>g</sub> '	5.530	0.07	-	-	-	-	-	-
h <sub>g</sub>	3.259	0.15	h <sub>g</sub> '	5.765	0.07	-	-	-	-	-	-
i <sub>g</sub>	3.678	0.02	i <sub>g</sub> '	6.210	0.01	-	-	-	-	-	-

### 6.2.2 Line broadening effects

The broadening effects in a Cu-HBrL include both the homogenous and inhomogeneous components. The homogenous broadening includes mainly natural broadening, collision broadening caused by identical (Cu) atoms i.e. resonance/self-broadening, by foreign gas (Ne, HBr, H, Br etc.) particles i.e. foreign gas or Van der Waals broadening and by charged particles i.e. Stark broadening, all producing Lorentzian line shape. On the other hand the inhomogeneous broadening is mainly due to thermal Doppler broadening which produces Gaussian line shape. The FWHM (Hz) of the resonance broadening ( $R$ ), foreign gas broadening ( $W$ ), Doppler broadening ( $D$ ) and natural broadening ( $N$ ) are given by [195, 199-201],

$$\Delta\nu^R \simeq 2.97 \times 10^{-8} n_{Cu} \quad (6.3)$$

$$\Delta\nu^W \simeq \sqrt{\frac{8R_u}{\pi^3 k_B^2 \langle T_g \rangle}} \left( \frac{\sum_k \sigma_{Cu-k} P_k}{\mu} \right) \quad (6.4)$$

$$\Delta\nu^D \approx 7.16 \times 10^{-7} \nu_0 \sqrt{\frac{\langle T_g \rangle}{M_{Cu}}} \quad (6.5)$$

$$\Delta\nu^N \approx \frac{A_{ul}}{2\pi} \quad (6.6)$$

where  $A_{ul}$  = transition probability of upper laser level with respect to the lower level,  $R_u$  = the universal gas constant,  $\langle T_g \rangle$  = average gas temperature (K),  $M_{Cu}$  = mass of radiating copper atom (amu),  $\mu = (\sum_k M_k^{-1})^{-1}$  = reduced mass,  $M_k$  = mass of  $k^{\text{th}}$  colliding partner in the discharge region (Ne, HBr, H & Br etc.),  $\sigma_{Cu-k}$  = collision cross section of copper atom with  $k^{\text{th}}$  species  $\approx \frac{\pi}{4}(d_{Cu} + d_k)^2$  where  $d_{Cu}$  and  $d_k$  are diameters (m) of copper atom and  $k^{\text{th}}$  species atom/molecule,  $k_B$  = Boltzman constant,  $P_k$  = partial pressure of the  $k^{\text{th}}$  species and  $\nu_0$  = frequency of emission. The widths of the natural broadening ( $\Delta\nu^N$ ), resonance broadening ( $\Delta\nu^R$ ), foreign gas broadening ( $\Delta\nu^W$ ) & Stark broadening ( $\Delta\nu^S$ ) combine and produce the Lorentzian width ( $\Delta\nu^L$ ) given by [195],

$$\Delta\nu^L = \Delta\nu^N + \Delta\nu^R + \Delta\nu^W + \Delta\nu^S \quad (6.7)$$

The Gaussian width of the Doppler broadening ( $\Delta\nu^D$ ) is then folded with the Lorentzian width ( $\Delta\nu^L$ ) to produce the Voigt profile of width  $\Delta\nu$  which is approximated by the equation [202],

$$\Delta\nu \approx 0.5346 \Delta\nu^L + \sqrt{0.2166 (\Delta\nu^L)^2 + (\Delta\nu^D)^2} \quad (6.8)$$

The broadening mechanisms of each hyperfine component proceed independently of all other components and are combined to produce a net profile [196,200]. The convolution of the Voigt profiles of all the hyperfine components, taking their relative intensity and isotopic composition factors into consideration, produce a net line-shape of intensity distribution given as [12],

$$I(\nu) = \sum_{i,j} \alpha_j \beta_{iso.(j)} I^i(\nu_j) = \sum_j \alpha_j \beta_{iso.(j)} [I^N(\nu_j) + I^R(\nu_j) + I^W(\nu_j) + I^D(\nu_j)] \quad (6.9)$$

where  $\alpha_j$  and  $\beta_{iso.(j)}$  are the relative intensity and the isotopic composition factor of the  $j^{\text{th}}$  hyperfine component respectively.

## 6.3 Measurement of spectral characteristics of Cu-HBr laser lines

### 6.3.1 Experimental arrangement and laser parameters

Fig. 6.2 shows the schematic of the experimental arrangement for the recording the spectral characteristics of Cu-HBrL lines. The Cu-HBrL (Cu-HBrL 2) is based on a 4.7 cm bore diameter, 150 cm long discharge tube and is pumped using IGBT-solid state switch based high voltage pulse modulator at a PRR of 18 kHz. The optical resonator employed is a standard plane- plane type with a length of about 250 cm. The Cu-HBrL emission lines, G & Y, are separated using a dichroic beam splitter and sampled to a high precision Fizeau interferometer based wavelength meter (High Finesse: Angstrom WS-7) for measuring the laser line-width and transition frequency [203-204], as discussed in section 6.3.2. Long term (~1 minute) variations in spectral emission line-widths as well as the transition frequencies of both the Cu-HBrL lines are recorded for various wall plug electrical input powers (from 6 to 9.5 kW) and HBr concentrations [values corresponding to optimum (~7%), below(~5%) and above optimum (~9%) level] used. The laser discharge tube temperature is maintained at ~900 K.

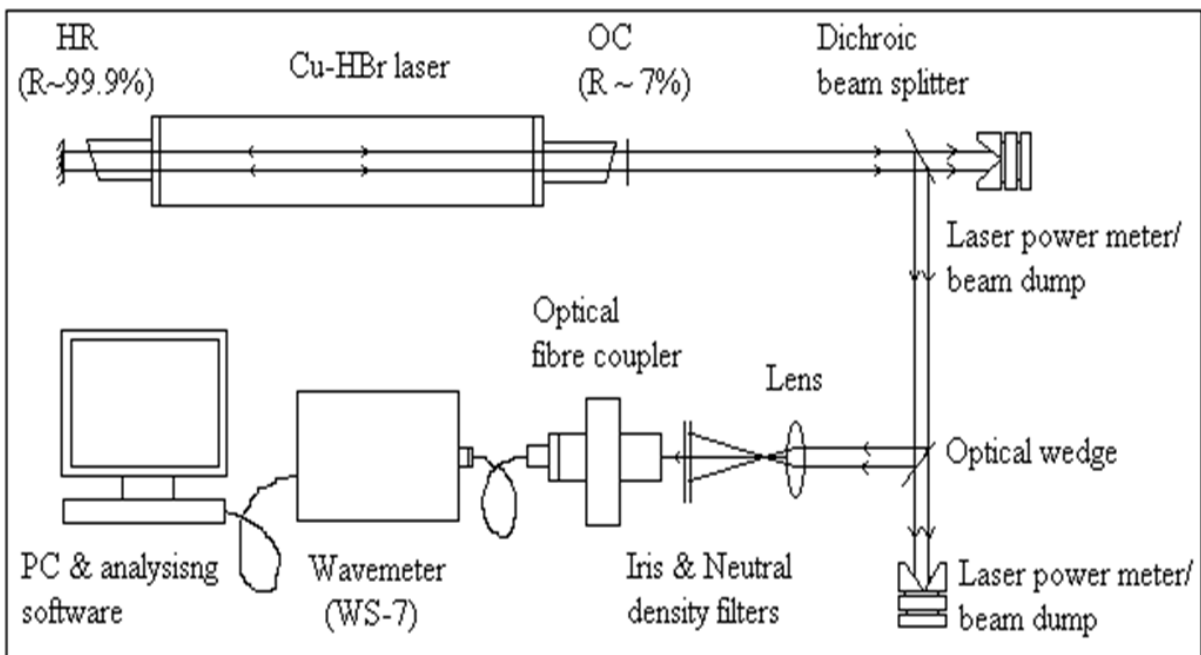


Fig. 6.2 The experimental set up for measurement of Cu-HBrL spectral characteristics

Figs. 6.3 a & b show the variation of average laser output power of the G and Y components as well as their ratios of Cu-HBr laser with variation of the electrical input power and HBr concentration respectively. It is observed that as the input power increases from 6 to 9.5 kW, the laser power of the G and Y components increase from 23 to 38 W and 15 to 34 W respectively. However, their power ratio (G/Y) decreases monotonically from 1.53 to 1.12 with increase of the input power. On the other hand, HBr concentration affects the variation of the laser power of the G and Y component as well as their ratio in a different manner. With variation of HBr concentration from ~5% to ~9%, the G component power is maximum at the optimum HBr concentration. However, the Y component power keep on increasing as the HBr concentration is changed from ~5% to ~9%. At the above optimum HBr concentration, the Y component power is higher than that of the G. With such increase in HBr concentration, the G to Y component power ratio reduces from 1.82 to 0.87.

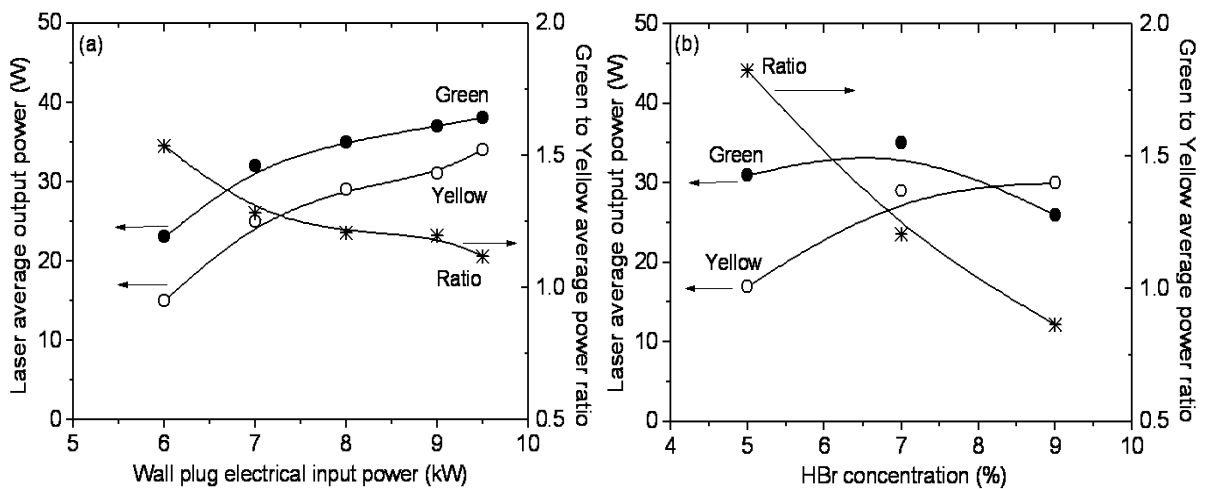


Fig. 6.3 Variation of laser output power of green and yellow component of Cu-HBr laser with  
(a) electrical input power and (b) HBr concentration

### 6.3.2 Measurement principle

The broadband Cu-HBrL lines may be considered as narrowband source with several side bands. Thus the fringes produced in the optical unit of the wave meter based on optical wedges, due to Cu-HBrL lines, are weighted sum of the fringes from many spectral components

of the light. This results in the fringes of diminished contrast as compared to that of a single frequency laser. The interference pattern thus produced are recorded by two photodiode arrays and transferred to a PC, in real-time, for estimation of the line-widths and the corresponding transition frequencies with reference to previously calibrated laser signal [203, 204]. In the PC, the laser line-width is calculated from the fringe contrast ratio whereas the frequency is calculated from the period and phase of the fringe pattern produced. These results are displayed on the monitor of the PC in real time. In the present case of Cu-HBrL, the contrast dilution is due to all the frequency components taken together. Hence the wavemeter gives a good representation of the complex line shapes. The line-width measured by the wavelength meter is in good agreement with that of conventional Fabry-Perot etalon based measurements [18, 204, 205]. The maximum upper limit of the line width measurable in the wavelength meter, primarily determined by the thickness of the Fizeau wedges used, is 10 GHz with accuracy of 200 MHz and with resolution as well as absolute accuracy of 10 MHz and 60 MHz respectively [203]. Therefore, the line-width of Cu-HBrL transitions observed is a combined effect of intrinsic physical processes associated with the laser gain medium & the finite resolution of the measuring device i.e. instrumental resolution line-width. For present set up, the later one is almost same (10 MHz) and hence the observed line-width is mainly the actual values.

## **6.4 Experimental results and analysis on the spectral behaviour of Cu-HBr laser**

### ***6.4.1 Parametric effects on spectral characteristics***

Figs. 6.4 a & b show the typical wave-meter traces of G and Y components of Cu-HBrL recorded for electrical input power of 8 kW and optimum HBr concentration. Similar wave-meter traces are recorded for variation in electrical input power and HBr concentration. The mean values of the single pulse line-widths (represented by middle lines) of the traces give the average spectral emission line-width ( $\Delta\nu$ ) whereas their standard deviation give its fluctuations [ $\delta(\Delta\nu)$ ]. For both the G and Y components, the variations of line-widths ( $\Delta\nu_g$  &  $\Delta\nu_y$ ) and their

fluctuations  $[\delta(\Delta\nu)_g \ \& \ \delta(\Delta\nu)_y]$  with respect to different electrical input powers and HBr concentrations are shown in Figs. 6.4 a & b respectively. It is observed that as the input power increases,  $\Delta\nu$  and  $\delta(\Delta\nu)$  of both G and Y components increase monotonically but the rate of increase of both  $\Delta\nu_y$  and  $\delta(\Delta\nu)_y$  are more than  $\Delta\nu_g$  and  $\delta(\Delta\nu)_g$ .

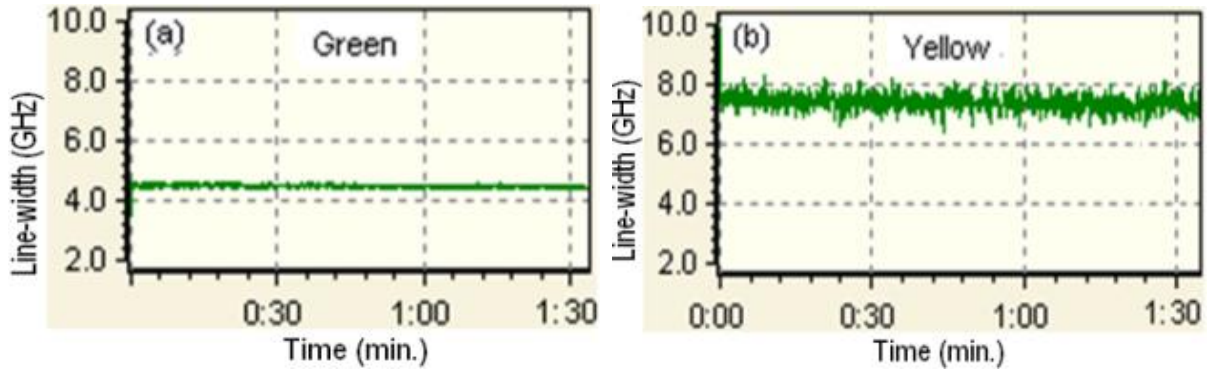


Fig. 6.4 Typical wave meter traces recorded for Cu-HBrL radiations: (a) Green & (b) Yellow

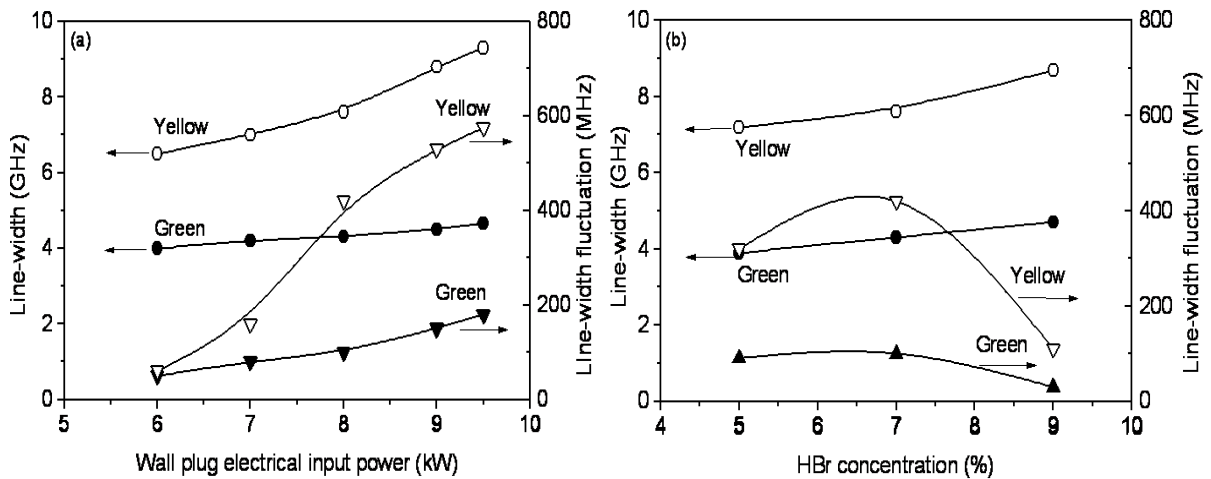
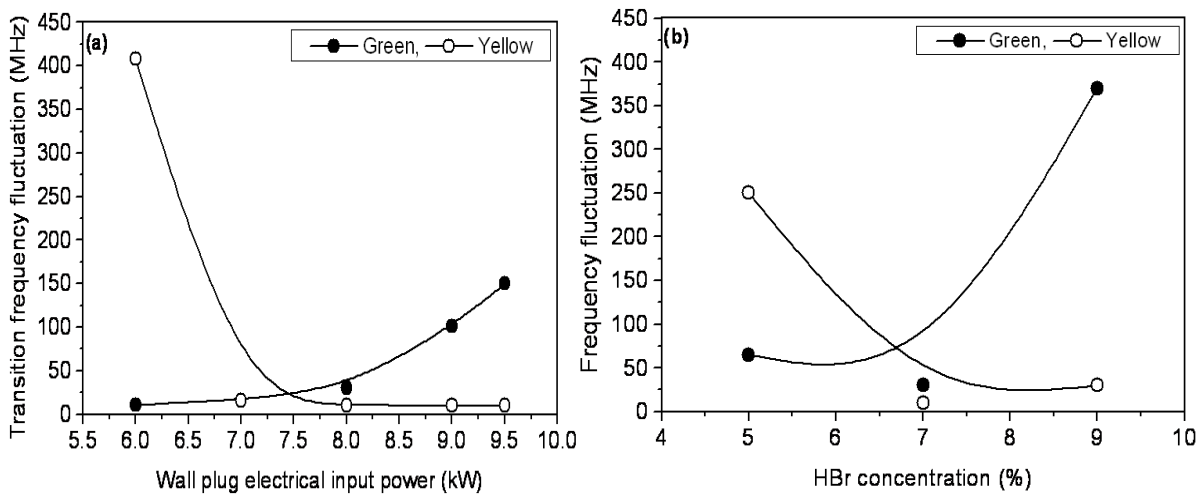


Fig. 6.5 Variation on emission line-width and its fluctuation for green and yellow component of Cu-HBr laser with (a) electrical input power and (b) HBr concentration

As the input power increases from 6 to 9.5 kW, both  $\Delta\nu_g$  and  $\Delta\nu_y$  increase from 4 to 4.7 GHz and 6.5 to 9.3 GHz respectively. Similarly both  $\delta(\Delta\nu)_g$  and  $\delta(\Delta\nu)_y$  also increase from 50 to 180 MHz and 60 to 575 MHz respectively for increase in electrical input power of 6 to 9.5 kW. On the other hand, the  $\Delta\nu$  and  $\delta(\Delta\nu)$  show opposite trends with different HBr concentrations. With the increase of HBr concentrations from ~5% to ~9%, both  $\Delta\nu_g$  and  $\Delta\nu_y$

continuously increases from 3.9 to 4.7 GHz and 7.2 to 8.7 GHz respectively. However,  $\delta(\Delta\nu)_g$  &  $\delta(\Delta\nu)_y$  are at maximum of 100 MHz and 420 MHz respectively at optimum HBr concentration (~7%). At the below and above of this concentration (i.e. ~5% & ~9% respectively), the values of  $\delta(\Delta\nu)_g$  are 90 MHz & 30 MHz and that of  $\delta(\Delta\nu)_y$  are 320 MHz, 110 MHz respectively. These line-widths can be compared with those of a conventional CVL of ~7 GHz & ~11 GHz and a CuBr laser of 5-6 GHz & 6-8 GHz respectively for the G and Y components [190-195]. The larger line widths observed in CVL are mainly due to higher gas and wall temperature leading to larger Doppler broadening widths. Figs. 6.6 a & b show the fluctuations in transition frequency [ $\delta(\nu_0)$ ] of the G & Y line of Cu-HBrL with different electrical input powers and HBr concentrations.



*Fig. 6.6 Variation in fluctuation in transition frequencies of green and yellow line of Cu-HBrL with (a) electrical input power and (b) HBr concentration*

With variation of the electrical input power from 6 to 9.5 kW, the fluctuation in central transition frequencies of both the G & Y lines show opposite trends. For the G line, the corresponding frequency fluctuation increases from ~10 MHz to ~100 MHz, centered around 587.04472, 587.04461, 587.04489 & 587.04479 THz for the respective input powers. On the other hand, for the Y line, the frequency fluctuation decreases from ~410 to ~10 MHz, centered around 518.35218, 518.35001, 518.35005 & 518.35010 THz for the respective electrical input

powers used. For both the lines, the fluctuations in the central frequencies are minimum at the optimum HBr concentration, with corresponding values of ~30 and ~10 MHz for the G and Y lines respectively. The corresponding central frequencies are 587.04463, 587.04489 & 587.04475 THz for the G line and 518.35147, 518.35005 & 518.35010 THz for the Y line, for below optimum (~5%), optimum (~7%) and above optimum (~9%) HBr concentration respectively. It is also observed that changing of the resonator, from plane-plane to unstable, does not produce any appreciable change in the spectral characteristics of the Cu-HBr laser. It is worth mentioning that proper longitudinal modes are not established in this case due to long resonator cavity & short laser gain duration that permit only 3 to 4 round trips. However, under the assumption that axial modes are established, there should be a large number of axial modes (~ 66 to ~ 78 for green and ~ 108 to ~ 155), with frequency separation of about ~60 MHz [ $c/2L_r$ :  $c$  = speed of light &  $L_r$  = length of resonator cavity (~250cm)], present within the large spectral gain width of Cu-HBrL i. e. ~ 4 to ~ 4.7 GHz (green) and ~ 6.5 to ~ 9 GHz (yellow).

#### **6.4.2 Analysis and discussion**

The observed spectral emission characteristics of a Cu-HBrL are combined effect of various intrinsic physical processes associated with the laser gain medium. The intrinsic physical processes depend on the energy coupled into the Cu-HBrL plasma as it decides the laser gain, active medium temperature distributions which are different for different input powers and HBr concentrations. The electrical power coupled/deposited into the presently used Cu-HBrL 2 discharge are already estimated in chapter 3, at various operating conditions, from the recorded voltage-current waveforms at the laser head. With the variation of the wall plug electrical input power from 6 to 9.5 kW, the deposited/coupled electrical power increases monotonically from ~2.16 to ~3.38 kW. The corresponding estimated average and axial gas temperatures also increase from ~2200 to ~2405 K and ~2410 to ~2700 K respectively. Similarly, with the variation of the HBr concentration from ~5 to ~9%, the coupled power,

average and axial gas temperature increase from ~2.56 to ~3.12 kW, ~2270 to ~2465 K and ~2470 to ~2725 K respectively.

In a Cu-HBrL, the active medium composition during the lasing period is dominated by mixture of Ne, Cu, HBr and its dissociation products such as H and Br. The Cu-HBrL 2 is operated with total pressure nearly about 30 mbar in which the HBr partial pressure is ~2 mbar. So it is judicious to assume that the equilibrium concentration of gaseous species in the discharge during the lasing period would be ~28 mbar of Ne, ~ 1 mbar of HBr, ~1 mbar of H and ~1 mbar of Br. Therefore, their contributions to the spectral emission width of Cu-HBrL are evaluated using equations 6.3 to 6.6. For typical average gas temperature of  $\langle T_g \rangle = 2200$  K, substituting values of  $A_{ul}(\text{green}) \approx 1.95 \times 10^6 \text{ s}^{-1}$ ,  $A_{ul}(\text{yellow}) \approx 1.9 \times 10^6 \text{ s}^{-1}$  [34],  $n_{Cu} \approx 10^{15} \text{ cm}^{-3}$ ,  $P_{HBr} \approx 10^2 \text{ Pa}$  (~1 mbar),  $P_H \approx 10^2 \text{ Pa}$  (~1 mbar),  $P_{Br} \approx 10^2 \text{ Pa}$  (~1 mbar),  $P_{Ne} \approx 28 \times 10^2 \text{ Pa}$  (~28 mbar),  $d_{Ne} \approx 76 \text{ pm}$ ,  $d_{HBr} \approx 141.4 \text{ pm}$ ,  $d_{Br} \approx 230 \text{ pm}$  and  $d_H \approx 50 \text{ pm}$  [206], in equations 6.3 to 6.6 we get  $\Delta v_g^N \approx 0.31 \text{ MHz}$ ,  $\Delta v_y^N \approx 0.3 \text{ MHz}$ ,  $\Delta v^R \approx 30 \text{ MHz}$ ,  $\Delta v^W \approx 0.75 \text{ MHz}$ ,  $\Delta v_g^D \approx 2475 \text{ MHz}$  and  $\Delta v_y^D \approx 2186 \text{ MHz}$ . For typical operating conditions of a Cu-HBrL for which  $n_e \sim 10^{13} \text{ cm}^{-3}$  and  $\langle T_g \rangle \sim 2200 \text{ K}$ ,  $\Delta v^S \approx 0.9 \text{ MHz}$  [199]. The equations 6.7 and 6.8 lead to the net convoluted line-width  $\Delta v \approx 2492 \text{ MHz}$  and  $2203 \text{ MHz}$  respectively for the G and Y components. So, in standard operating condition of a Cu-HBrL as that of ours, the magnitudes of individual as well as the combined contributions of natural, resonance, foreign gas and Stark broadening are significantly smaller than that of the Doppler broadening i.e.,  $\Delta v^L \approx$  few tens of MHz vs.  $\Delta v^D \approx$  few GHz. At this condition, the line-shape intensity distribution of equation 6.9 can be rewritten as [12],

$$I(\nu) \approx \sum_j \alpha_j \beta_{iso.(j)} I^D(\nu_j) \approx \sum_j I(\nu_j) e^{\left[ -\frac{4 (\ln 2) (\nu - \nu_{0j})^2}{(\Delta \nu_j^D)^2} \right]} \quad (6.10)$$

where  $I(\nu_j)$ ,  $\nu_{0j}$  and  $\Delta \nu_j^D$  are the relative intensity, central frequency and Doppler width of the  $j^{\text{th}}$  hyperfine component respectively. Using the relevant data from table 6.1, the spectral

emission line-shapes are simulated. Figs. 6.7 a & b show the representative line shape profiles of spontaneous emission, with individual hyperfine components (dull lines) as well as their convolution (bold line), for the G and Y component of Cu-HBrL, at a chosen average gas temperature of 2200 K. This exercise is repeated for various gas temperatures from 800 to

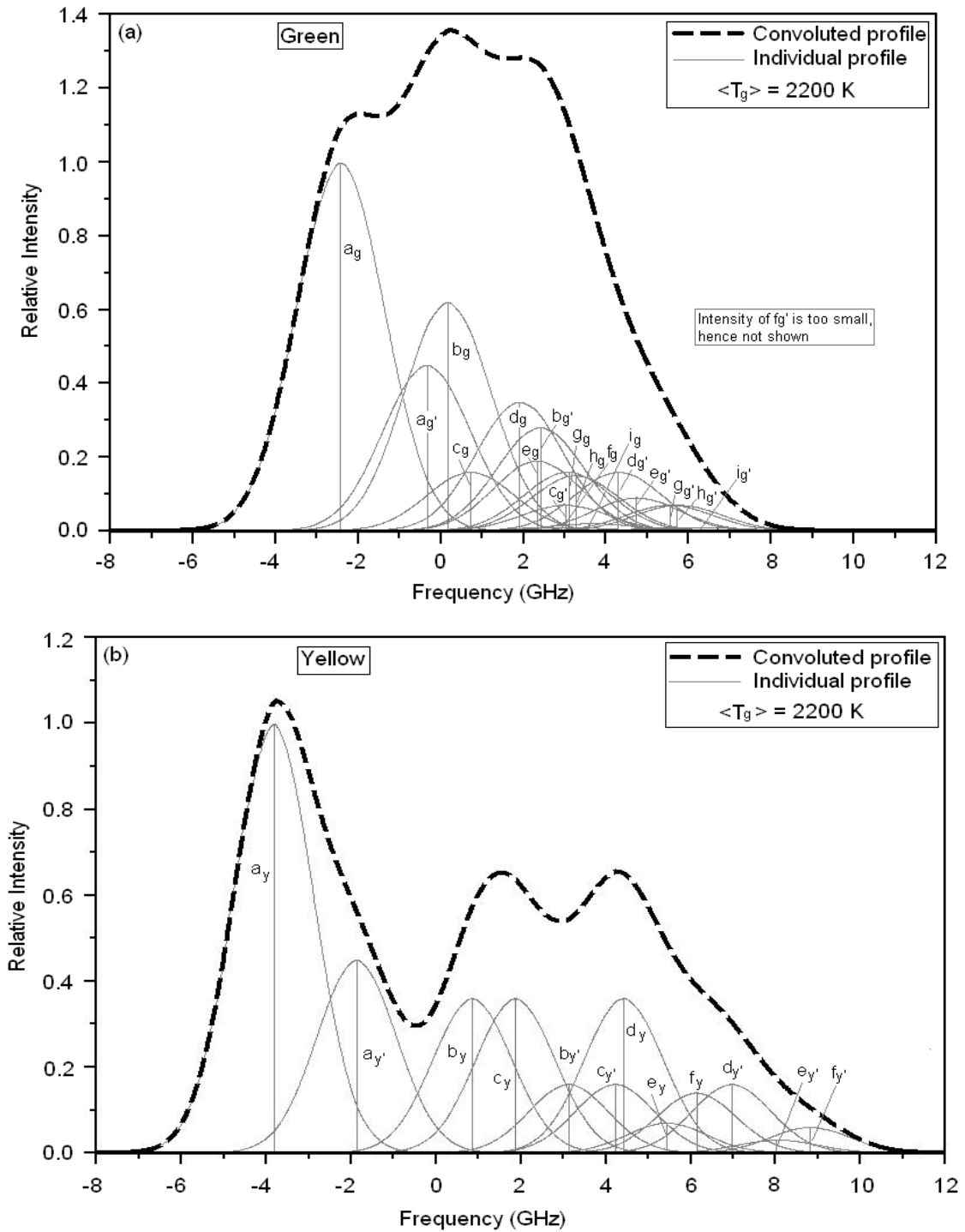


Fig. 6.7 Typical calculated spectral emission line shape with individual hyperfine components of Cu-HBr laser radiations for (a) Green line and (b) Yellow line

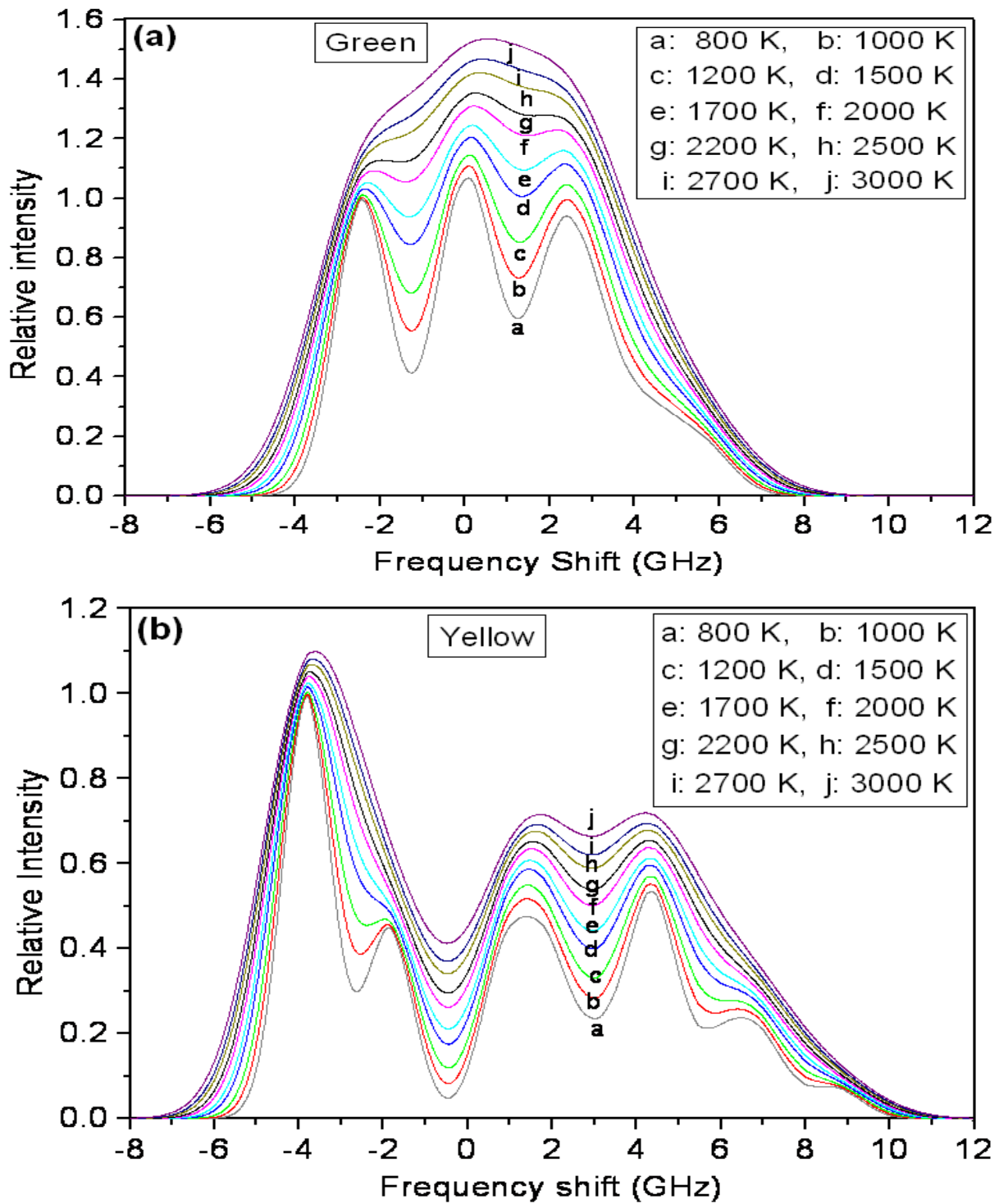


Fig. 6.8 The simulated convoluted line shapes of Cu-HBr laser emission at different average gas temperatures for (a) Green radiation and (b) Yellow radiation

3000 K, in a step of 200-300 K and the results are shown in Figs. 6.8 a & b for G and Y components respectively [13]. It is evident that the G line of Cu-HBrL is dominated by a single strong hyperfine component followed by the other three relatively weak components i.e.,

$I_{rel.}(a_g) : I_{rel.}(b_g) : I_{rel.}(a_{g'}) : I_{rel.}(d_g) = 1.00 : 0.62 : 0.45 : 0.35$  whereas the Y line is dominated by one strong component followed by four relatively weak components i.e.,  $I_{rel.}(a_y) : I_{rel.}(a_{y'}) : I_{rel.}(b_y) : I_{rel.}(c_y) : I_{rel.}(d_y) = 1.00 : 0.45 : 0.36 : 0.36 : 0.36$ . The net spread/shift of all the hyperfine components taken together for the G line ( $a_g - i_{g'}$ ) is  $\sim 8.63$  GHz and that of Y line ( $a_y - f_{y'}$ ) is  $\sim 12.64$  GHz.

Fig. 6.9 shows the variation of the convoluted FWHM line-widths of green and yellow lines with average gas temperatures from 2000 to 3000 K. For comparison, the variation of calculated line-widths (Doppler), of both the radiation components of Cu-HBr laser, under single emission line approximation (without consideration of isotope shifts & hyperfine splittings) are presented. It is seen that with increase in gas temperature, the corresponding convoluted line-widths increase from  $\sim 7.45$  to  $\sim 7.68$  GHz and  $\sim 10.35$  to  $\sim 11.45$  GHz for the green and yellow components respectively. On the other hand, for the single emission line approximation, the corresponding line-widths of green and yellow components vary from 2.36

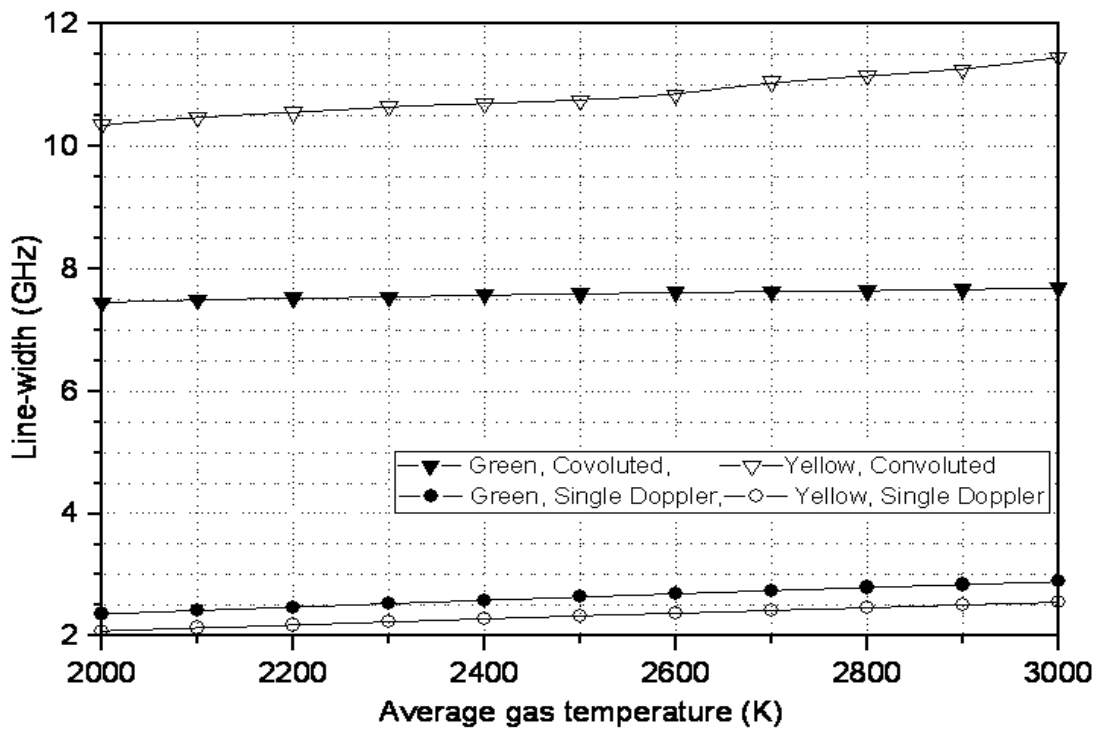


Fig. 6.9 Variation of computed emission line-widths of green and yellow radiation of Cu-HBr laser with average gas temperature

to 2.89 GHz and 2.08 to 2.55 GHz respectively. The magnitudes and trends of variation in line-widths with input powers / gas temperatures are in agreement with the analysis presented here based on isotope shift and hyperfine splitting of copper atom. However, the measured values are lower than that of the calculated values. It may be mentioned that our estimations of convoluted widths have not taken care of the exact gain distributions among the hyperfine components at different operating conditions. In addition, there are uncertainties in number density of particles in the plasma due to uncertainties in gas temperature as well as laser level pumping. All these factors might be the reason behind the discrepancies between the experimental observations and theoretical calculations [12].

In practice, the observed line-width is dependent on the operating parameters in general and the electrical power coupled into the laser discharge in particular. This is because, it decides the gain of the hyperfine components as well as their Doppler broadening widths whose convolution produces the observable line-width. As the input power increases, the gains of the hyperfine components also increase. This subsequently leads to more number of hyperfine components crossing the saturation threshold and their contribution to the net observable line-width increases. In addition, increased electrical input power and hence increased average gas temperature lead to increase of both the Doppler line-width of each hyperfine line as well as convoluted widths. In the present study, the laser is operating at high average output power which corresponds to far above saturation. This along with the fact that the hyperfine components of yellow are more widely separated in frequency domain than that of the green, explains the observed result that the line-width of the green line is lower than that of the yellow.

With increase of the input power, the gains of the relatively lower intense hyperfine components increases and go above saturation threshold. These relative lower intensity hyperfine components of yellow line are more widely separated than those of the green, which explains the observed result that the rate of increase line-width with electrical input power of

yellow is more than that of the green. Similarly, as the HBr concentration increases, it leads to decrease in inter-pulse electron density through increased DA process [121,124]. This in turn leads to increase in discharge impedance and hence the electrical energy dumped into the discharge, which are manifested in terms of increased Doppler broadening and hence the laser line-widths. In addition, increased HBr concentration also leads to increased copper density in the discharge region and hence affects the gain distribution among the hyperfine components.

The line-width and transition frequency fluctuations (standard deviation) of the Cu-HBrL lines observed may be explained as follows. In a Cu-HBrL, the line-width fluctuations may be attributed to fluctuations in refractive index of the heated active medium due to temperature and instantaneous pulse to pulse pump power variation due to repetitive pulsing. These subsequently affect the electron temperature, gas temperature and thermal speed distribution of the copper atoms inside the discharge tube and hence lower gain. In addition, several hyperfine transitions originate from the same hyperfine upper level, which lead to gain competition among the transition components. Therefore, it is possible that as the input power coupled to the discharge increases the local fluctuations in temperature and refractive indices etc. also increase. These fluctuations are likely to have more effect on the yellow lines of the Cu-HBrL line due to its lower gain than that of the green, where some of its transitions might be oscillating around the threshold level, thus leading to more observable line-width fluctuations for yellow than that of the green. Similar argument follows for the case of HBr concentrations.

The indifference in the results of spectral line-emission characteristics with the different resonators used may be attributed to the fact that the study is made at high laser average power levels. In this situation all the hyperfine transitions are far above saturation threshold and an unstable resonator is not able to suppress the lasing at any of the hyperfine transitions due to high gain values.

## 6.5 Conclusions

In conclusion, this chapter presented a detailed experimental study and the related theoretical analysis on the spectral line-emission characteristics of both the green and yellow radiations of a Cu-HBrL for different laser operating conditions. The experimental study is carried out using high precision Fizeau interferometer based wavelength meter, whereas the Cu-HBrL is operating at high average power conditions. The experimental results on the spectral line-emission characteristics such as line-width, emission frequency & their stability for different electrical input powers, HBr concentrations are studied in detail. The effect of electrical input power and HBr concentration are crucial on Cu-HBrL spectral line-emission characteristics, unlike that of the resonator used. At typical laser operating condition, the emission line-width of Cu-HBr laser varies within ~4 to ~5 GHz for green component and within ~6 to ~9 GHz for yellow component with the line-width and emission frequency (central) fluctuation of few 10s to 100s of MHz. The experimental observations are explained by a comprehensive theoretical analysis followed by simulation of the spectral emission line-shapes of both the radiations. This is carried out taking into account the isotope shift, hyperfine splitting and relevant line broadening effects (mostly Doppler) associated with the energy levels of natural copper atom. The theoretical results, in conjunction with the temperature & laser gain distribution effects, agree well with the observed trends.

## Chapter 7

### Studies on the beam divergence & pointing stability of Cu-HBr laser

#### 7.1 Introduction

The laser beam divergence and pointing stability of Cu-HBr laser radiations are crucial parameters in applications requiring finely focused beams such as second-harmonic/sum-frequency generation (SHG/SFG) for UV & its use for writing of fiber Bragg gratings (FBGs), precision material processing and tunable laser pumping (dye & Ti:Sapphire) etc. [31, 189, 207-209]. In the nonlinear UV conversion, the beam divergence of the Cu-HBrL decides its focused intensity and hence the frequency conversion efficiency. In addition, the fundamental beam divergence and pointing stability dictate the phase matching optimization in nonlinear crystal for efficient SHG or SFG of Cu-HBr laser. It is also equally important to know the long term variation in single pulse divergence & pointing angle and intensity, to plan the effective utilization of copper laser based visible/UV sources in the mentioned applications. These issues are more relevant for a Cu-HBrL due to its operation at high PRR, high specific power conditions that lead to increased power loading and thermally induced phenomena affecting the spatio-temporal laser beam characteristics. The exhaustive study of beam quality aspects of Cu-HBr laser has been missing in the field and is the focus of present chapter.

This chapter presents a comprehensive study on beam quality aspects on both the green (G) and yellow (Y) radiations of a Cu-HBrL for different laser operating conditions. The experimental results on variation of far-field divergence and pointing stability with different electrical input powers, HBr concentrations and optical resonators (plane-plane & unstable) are presented in detail for both the radiation components of the developed Cu-HBr laser. Both the time averaged and pulse to pulse variations are studied. The experimental study is augmented with near-field spatial intensity profiles & temporal pulse shapes of both the radiations. The related analysis and discussion encompass the estimation of beam divergence for different

resonators, role of spatio-temporal laser gain characteristics, thermally induced perturbations and effect of diffraction. The whole study has culminated into generation of high quality Cu-HBr laser beams as required for efficient UV generation through nonlinear optical conversion as presented in chapter 9.

## 7.2 Measurement for Cu-HBr laser beam divergence & pointing stability

### 7.2.1 Set up for measurement

Fig. 7.1 shows the schematic of set up for studying the far-field beam divergence and pointing stability characteristics of a Cu-HBrL. The laser system, Cu-HBrL 2 (Table 2.1), is based on discharge tube of 4.7cm bore dia. & 150 cm length and is excited using IGBT-solid state switch based pulser at 18 kHz PRR [156]. In the first set of measurements, the beam quality is studied for both the green & yellow radiation components of the Cu-HBrL, with a plane-plane resonator (PPR, reflectivity: ~99% & ~7%) of 250 cm cavity length ( $L_r$ ) (configuration A in Fig. 7.1). The green & yellow radiations are suitably separated by a dichroic

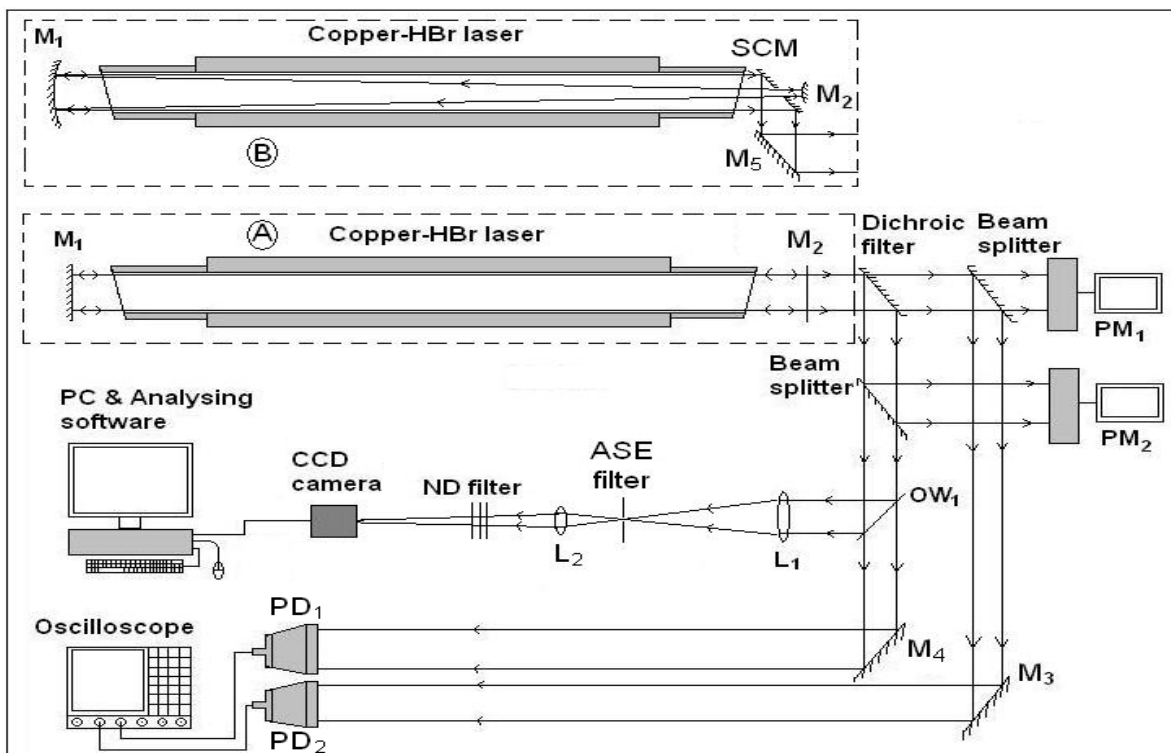


Fig. 7.1 Schematic of the set up for studying the spatial & energy characteristics of Cu-HBrL

filter and are studied sequentially for far-field beam divergence, far-field beam pointing stability, near-field radial intensity profiles, laser output powers and temporal pulse profiles for different electrical input powers (6 to 9.5 kW) and HBr concentrations (5 to 9%). The measurements are carried out by suitably sampling the laser beams with the use of beam-splitters, optical wedges and beam-steering mirrors, as described in Fig. 7.1. Then the experimental study is repeated with confocal unstable resonators (URs) of different magnifications ( $M = |F_1/F_2|$ , where  $F_1$  (250 cm) &  $F_2$  are focal lengths of mirrors  $M_1$  &  $M_2$  and are separated by a distance  $L_r = F_1 - |F_2|$ ), e.g.  $M = 12.5, 50$  &  $100$  (configuration B in Fig. 7.1) at 5 kW input power and optimized HBr concentration (~6%). The discharge tube temperature is maintained at ~900 K.

For the measurement of beam divergence and pointing stability, the reflected beam from the optical wedge ( $OW_1$ ) is focused by a lens  $L_1$  ( $f_1 = 50$  cm) and filtered for amplified spontaneous emission (ASE) noise at the focal plane of  $L_1$  using an aperture (~500  $\mu\text{m}$  diameter for PBURs & ~1500  $\mu\text{m}$  diameter for PPR). The pinholes are wide enough to allow the exit of the laser beams without limiting their spatial extent. This ASE filtered spot is then imaged, with magnification of 2.3-2.4 for PPR and 2.6-2.7 for UR at the CCD head (Pixelfly qe, PCO AG of pixel size 6.45  $\mu\text{m}$  x 6.45  $\mu\text{m}$ ) using another lens  $L_2$  ( $f_2 = 25$  cm), suitably placed. The beam intensities are suitably attenuated using suitable combinations of neutral density (ND) filters to prevent saturation & damage to the CCD. These magnification values are confirmed by calibrating the system with a known size pinhole. The far-field images are captured by a personal computer (PC) & frame grabber card set up and are analysed using in-house developed beam analysis software [210]. The CCD acquiring time is set to be 50  $\mu\text{s}$  which is little less than the inter-pulse time (~55.56  $\mu\text{s}$ ) ensuring single pulse recording. The subsequent images are acquired after time interval of 1 s at 1 Hz rate. At the end of acquiring preset number (512) of images, the individual line profiles stored in the allocated memory is saved as a

composite/stacked image. These images are then analysed for estimation of far-field beam characteristics. The error of the measurement is limited by the pixel size of the CCD camera and is estimated to be about  $\pm 5 \mu\text{rad}$ . The near-field spatial intensity profiles are recorded after suitably attenuating & imaging the laser exit on the CCD camera placed after the lens  $L_1$ . Part of the beams are also sampled to fast biplaner photo-diodes ( $PD_{1,2}$ ) (Hamamatsu: R1193U-52) for monitoring the temporal pulse characteristics, recorded with a 500 MHz oscilloscope (Lecroy: Waverunner 6050A).

### 7.2.2 Principle of measurement and base data

Figs. 7.2 a & b show the typical composite pictures (horizontal stack) of the magnified far-field spot for G and Y components of the Cu-HBr laser, with PPR and PBUR  $M=50$  respectively, at optimized conditions. The vertical stack is similar to the horizontal stack. The far-field spots of both G & Y components consist of an intense central core surrounded by low intensity outer area. The zigzag shape of the stacked picture is indicative of positional jitter of the far-field pattern and hence pointing instability of laser beam. Figs. 7.3 a & b and Figs. 7.4 a & b show the typical composite far-field intensity distributions, of the G & Y components of

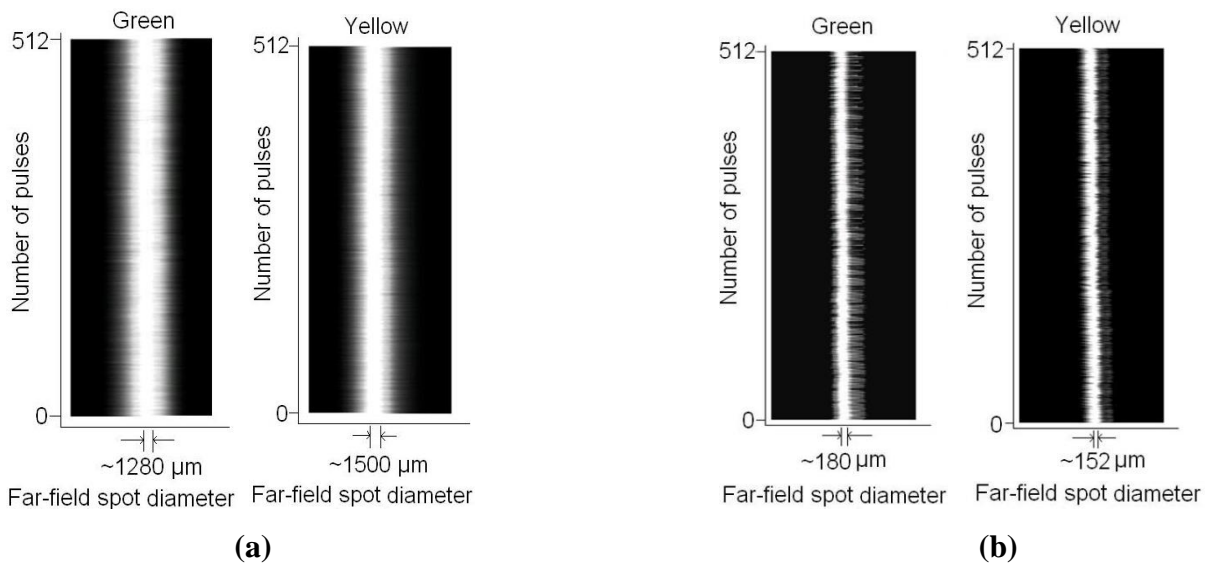


Fig. 7.2 Typical recorded composite pictures (horizontal stack, 512 pulses) of far-field spot for green and yellow component of Cu-HBr laser with PPR (a) and PBUR  $M=50$  (b)

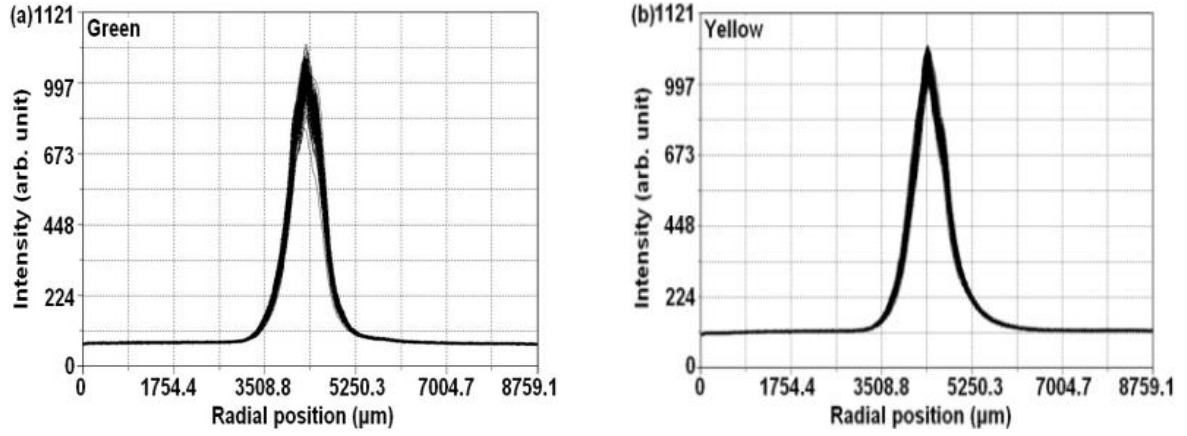


Fig. 7.3 Typical composite far-field intensity distributions (512 pulses) of green (a) and yellow(b) component of Cu-HBr laser with PPR

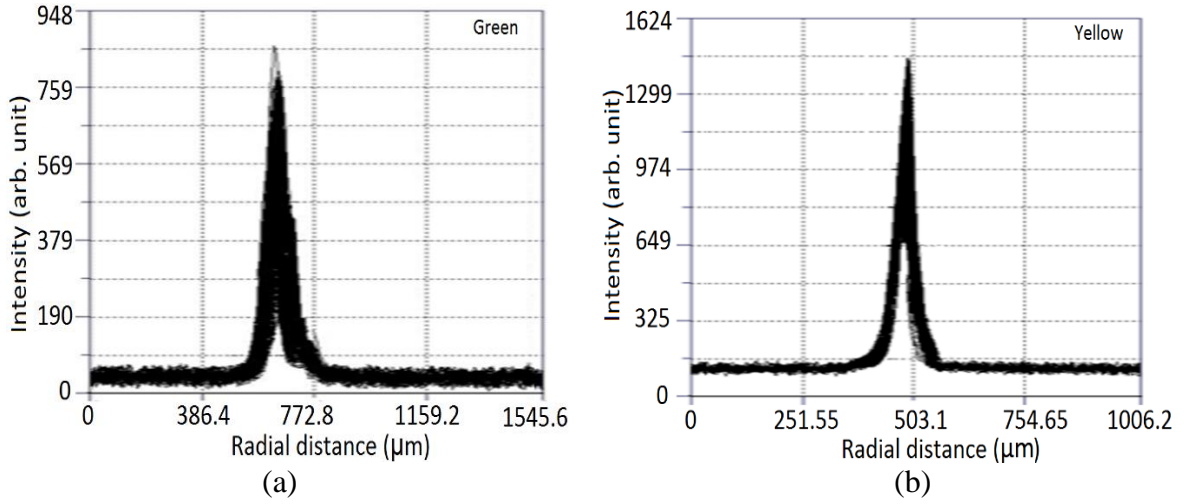


Fig. 7.4 Typical composite far-field intensity distributions (512 pulses) of green (a) and yellow (b) component of Cu-HBr laser with PBUR M=50

the Cu-HBr laser, with PPR and PBUR M=50 respectively. These are derived from Figs. 7.2 a & b. Similar exercises have been carried out for all other experimental conditions.

The beam quality parameters as evaluated as follows. For each pulse the numerical values of divergence ( $\theta_i$ ) and pointing angle ( $\delta_i$ ) are given as [13, 48],

$$\theta_i = \Delta\omega_i/d \quad (7.1)$$

$$\delta_i = \Delta s_i/d \quad (7.2)$$

where  $\Delta s_i$  = spatial displacement of the far-field intensity peak of  $i^{\text{th}}$  pulse from the mean peak position,  $\Delta\omega_i$  = width of the far-field intensity distribution at the  $1/e^2$  points of the intensity

maxima of  $i^{\text{th}}$  pulse,  $d$  = distance of the plane of minimum spot size from the lens  $L_1$ . The pointing instability ( $\delta$ ) at a given condition is taken as their mean value over all the pulses recorded. The far-field intensity data is obtained from intensity counts of the images recorded by the CCD camera. The fluctuations in far-field divergence ( $\Delta\theta$ ) and intensity ( $\Delta I$ ) are estimated as,

$$\Delta\theta = \langle \theta \rangle - \theta_{ext} \quad (7.3)$$

$$\Delta I = \langle I \rangle - I_{ext} \quad (7.4)$$

$\langle \theta \rangle$  &  $\theta_{ext}$  are the average/mean value of divergence & extreme value of the divergence,  $\langle I \rangle$  &  $I_{ext}$  are the mean value of far-field intensity count & extreme values of the intensity count respectively. These experiments and analysis are carried out for both the G & Y components of Cu-HBrL with various laser operating conditions as well as optical resonators as discussed in the following sections.

### 7.3 Spatial beam quality behaviour of Cu-HBr laser with plane-plane resonator

#### 7.3.1 Far-field beam divergence

Figs. 7.5 a & b show the typical variation of single pulse far-field beam divergence of G and Y radiations of Cu-HBrL with PPR. These are the actual corrected data after taking care of the magnification used in far-field recording. Similar graphs are generated for all other experimental conditions of electrical input powers and HBr concentrations, from which the

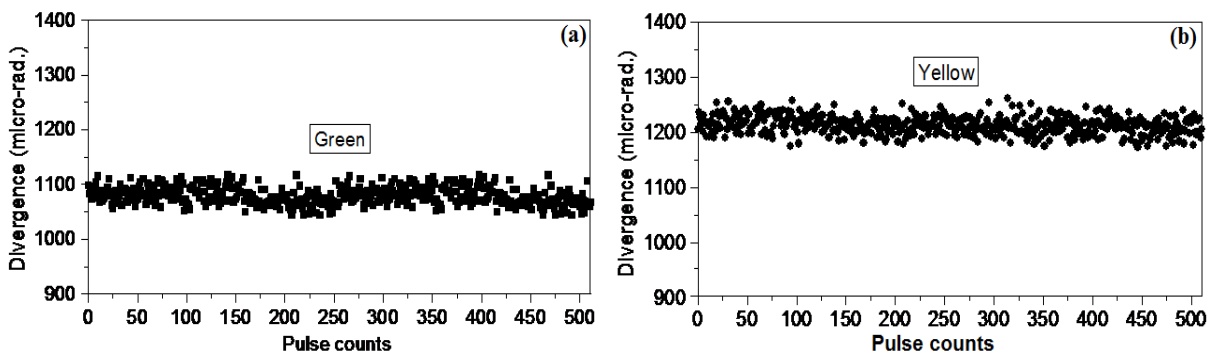


Fig. 7.5 Typical variations in single pulse far-field beam divergence of Cu-HBrL radiations with PPR: (a) Green and (b) Yellow

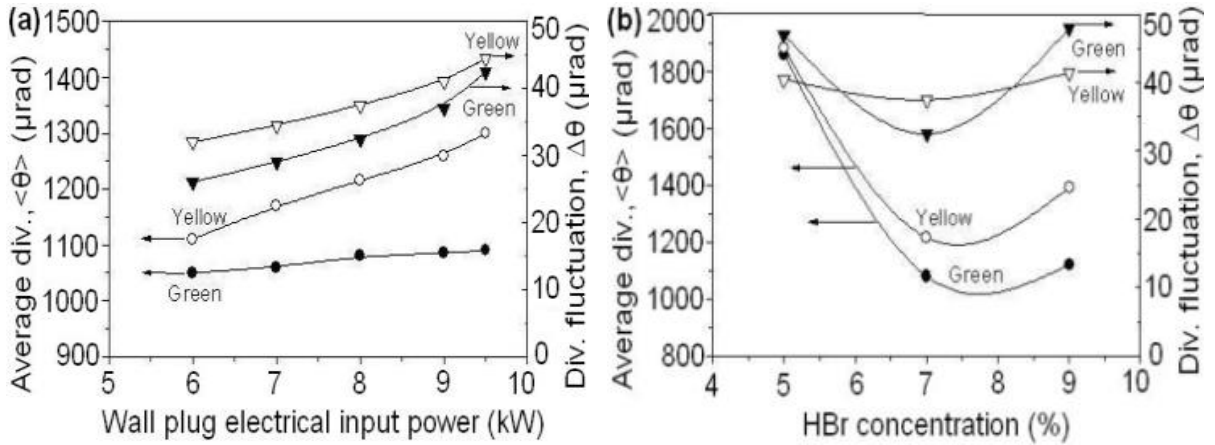


Fig. 7.6 Variation of  $\langle\theta\rangle$  and  $\Delta\theta$  of recorded 512 pulses of green and yellow component of Cu-HBrL with PPR for different (a) electrical input powers and (b) HBr concentrations

mean value of the divergences and long term divergence fluctuations are estimated (using relations 7.1 & 7.3). Figs. 7.6 a & b show the variation in mean value of divergences ( $\langle\theta\rangle$ ) and their fluctuations ( $\Delta\theta$ ) of the G & Y beams ( $\langle\theta\rangle_g$ ,  $\langle\theta\rangle_y$  and  $\Delta\theta_g$ ,  $\Delta\theta_y$ ) with respect to different electrical input powers and HBr concentrations respectively. As the electric input power increases from 6 to 9.5 kW, both  $\langle\theta\rangle_g$  and  $\langle\theta\rangle_y$  increase monotonically from 1050 to 1090  $\mu\text{rad}$  and 1110 to 1300  $\mu\text{rad}$  respectively. These account for increase of ~4% and ~17% respectively. Similarly, both  $\Delta\theta_g$  and  $\Delta\theta_y$  increase monotonically from  $\pm 26$  to  $\pm 43$   $\mu\text{rad}$  and  $\pm 32$  to  $\pm 45$   $\mu\text{rad}$  respectively with increase of the electrical input power from 6 to 9.5 kW. It may be noted that at all the input power used both  $\langle\theta\rangle_y$  and  $\Delta\theta_y$  are more than  $\langle\theta\rangle_g$  and  $\Delta\theta_g$ . However, these trends are different for different HBr concentrations used (~5%, ~7% & ~9%) as shown in Fig. 7.6 b. The value of  $\langle\theta\rangle_y$  is always higher than  $\langle\theta\rangle_g$ . These values are 1860, 1080 & 1120  $\mu\text{rad}$  for the G component and 1883, 1215 & 1392  $\mu\text{rad}$  for the Y component respectively, corresponding to HBr concentration of ~5%, ~7% and ~9% at electrical input of 8 kW. However, both  $\langle\theta\rangle_g$  &  $\langle\theta\rangle_y$  are higher at HBr concentrations far from the optimum level. On the other hand,  $\Delta\theta_g$  is about  $\pm 47$ ,  $\pm 33$  &  $\pm 48$   $\mu\text{rad}$  where as  $\Delta\theta_y$  is about  $\pm 41$ ,  $\pm 38$  &  $\pm 42$   $\mu\text{rad}$  for HBr concentrations of 5%, 7% & 9% respectively.

### 7.3.2 Far-field beam pointing stability & intensity fluctuation

Figs. 7.7 a & b and Figs. 7.8 a & b show the typical long term variation in single pulse far-field beam pointing angle and corresponding intensity of G and Y radiations of Cu-HBrL with PPR at 8 kW input power. Similar graphs are generated for all other experimental conditions of electrical input powers and HBr concentrations, from which the mean value of divergences and long term divergence fluctuations are estimated (using relations 7.1 & 7.3).

Figs. 7.9 a & b show the variation of pointing instability [ $\delta_g$  &  $\delta_y$ ] and fluctuation in far-field

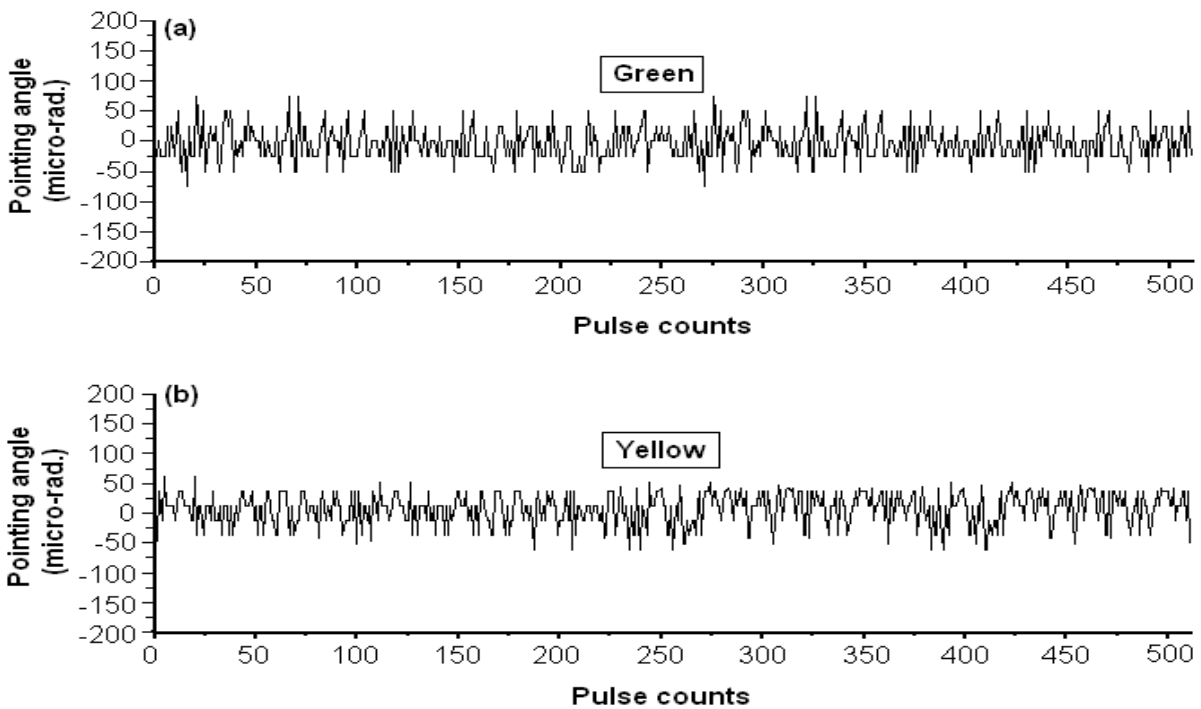


Fig. 7.7 Typical pulse to pulse variations in far-field beam pointing angle of Cu-HBrL radiations with PPR: (a) Green and (b) Yellow

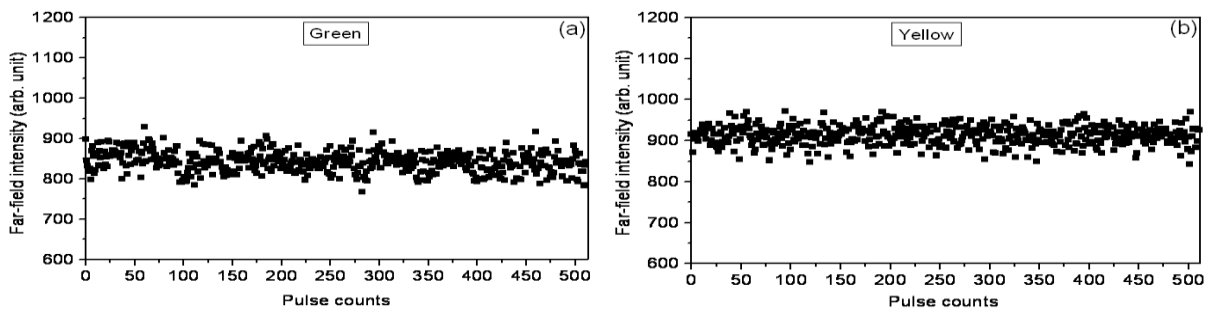


Fig. 7.8 Typical pulse to pulse variations in far-field beam intensity fluctuations of Cu-HBrL radiations with PPR: (a) Green and (b) Yellow

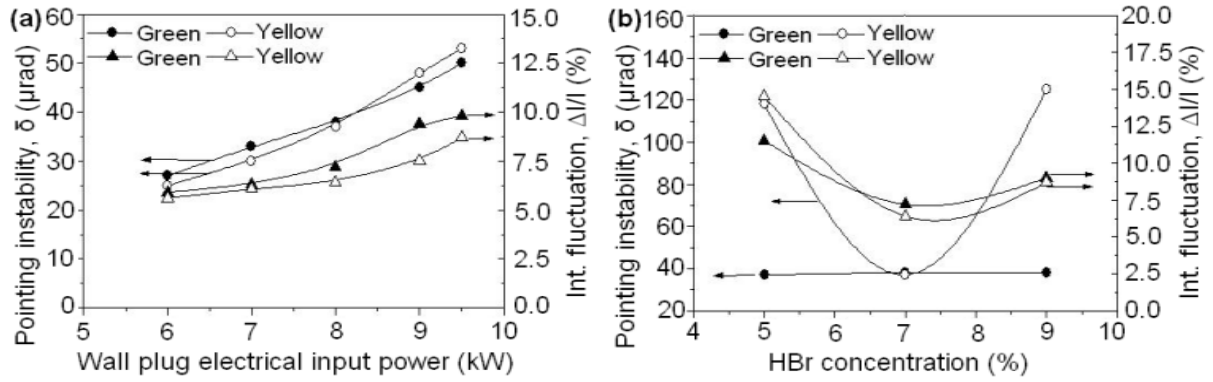


Fig. 7.9 Variation of beam pointing instability) ( $\delta$  and intensity fluctuations ( $\Delta I/I$ ) of green & yellow component of Cu-HBrL with (a) Electrical input powers & (b) HBr concentrations

beam intensity [ $(\Delta I/\langle I \rangle)_g$  &  $(\Delta I/\langle I \rangle)_y$ ] of both G & Y components with respect to electrical input powers and HBr concentrations respectively. With variation of the electrical input from 6 to 9.5 kW, both  $\delta_g$  and  $\delta_y$  increase monotonically from  $\pm 27$  to  $\pm 50$   $\mu\text{rad}$  and  $\pm 25$  to  $\pm 53$   $\mu\text{rad}$  respectively. For electrical input less than 8 kW,  $\delta_g$  is slightly higher than  $\delta_y$  where as for the input power beyond 8 kW, the trend is just opposite. Similarly, both  $(\Delta I/I)_g$  &  $(\Delta I/I)_y$  also increase from  $\pm 5.9\%$  to  $\pm 9.8\%$  &  $\pm 5.6\%$  to  $\pm 8.7\%$  respectively for corresponding increase in input power. However, for different HBr concentrations used in this study,  $\delta_g$  is almost constant at a level of  $\pm 37$ - $38$   $\mu\text{rad}$ . On the other hand,  $\delta_y$  is minimum of  $\pm 37$   $\mu\text{rad}$  for optimum HBr concentration ( $\sim 7\%$ ) and is within  $\pm 118$ - $125$   $\mu\text{rad}$  for both below and above optimum HBr concentrations. Similarly the value of  $(\Delta I/\langle I \rangle)_g$  and  $(\Delta I/\langle I \rangle)_y$  are  $\pm 11.5\%$ ,  $\pm 7.2\%$  &  $\pm 9\%$  and  $\pm 14.5\%$ ,  $\pm 6.4\%$  &  $\pm 8.7\%$  respectively for low, optimum and high HBr concentrations.

### 7.3.3 Radial and temporal intensity profiles

The far-field beam divergence and pointing stability behaviour of Cu-HBr lasers are linked with the near field radial intensity profile and the laser pulse duration as well as its temporal modulation characteristics [13]. These parameters are different for the G and Y components and are strongly dependent on the laser gain characterising operating parameters such as electrical input power as well as HBr concentrations. Figs. 7.10 a & b show the typically recorded near-field spatial intensity profiles of G & Y beams at 8 kW for optimum and below

optimum HBr concentration respectively. At all the input power used, where corresponding HBr concentration is slightly changed for maximum laser power, the profiles show similar quasi-Gaussian behaviour as in Fig. 7.10a. However, for HBr concentrations (5% & 9%) other

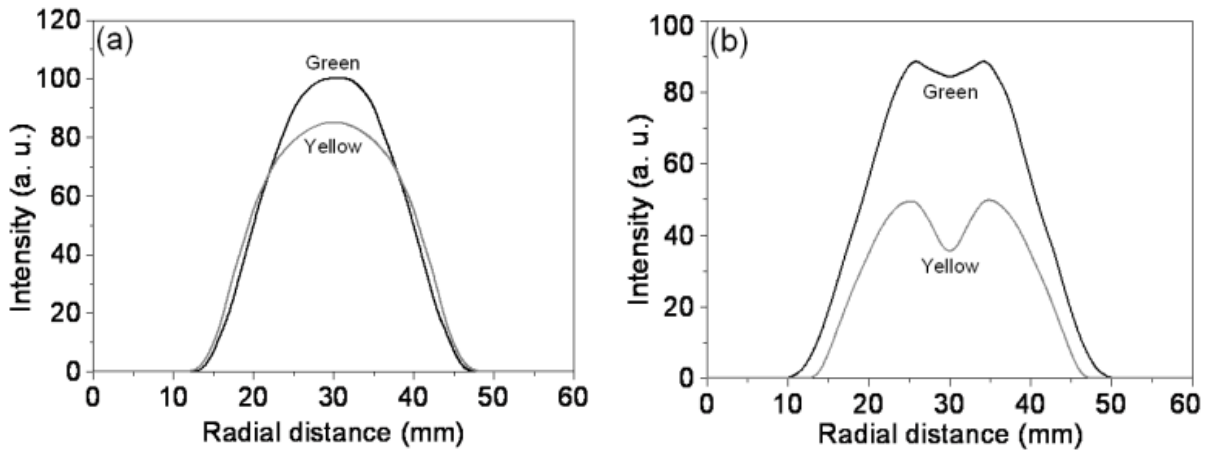


Fig. 7.10 Typical radial intensity profiles of green & yellow component of Cu-HBrL at 8 kW input power for (a) optimum HBr concentration (7%) and (b) low HBr concentration (5%)

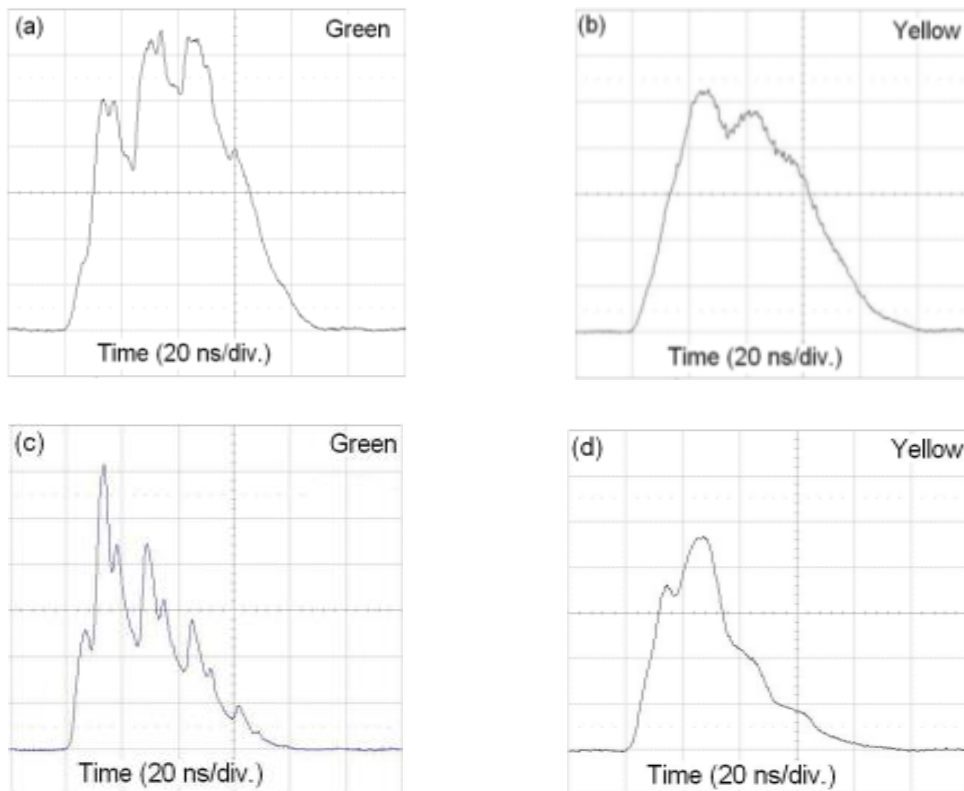


Fig. 7.11 Temporal intensity profiles of green & yellow component of Cu-HBrL at 8 kW input power for optimum HBr concentration (a & b) and low HBr concentration (c & d)

than the optimum value ( $\sim 7\%$ ), the spatial intensity profiles develop slight deep ( $<10\%$ ) in center. Figs. 7.11 a - d show the temporal evolution of laser intensity of G & Y beams for optimum & below optimum HBr concentration, at 8 kW input power. For all other input powers used, temporal profiles are more or less similar *albeit* with different durations. However, there is significant change both in shapes and durations of the G & Y components for different HBr concentrations. In all the cases, the laser beam diameters as well as the pulse durations have been estimated as the width of the  $1/e^2$  points of the maxima in the profiles.

Figs. 7.12 a & b show the variation of the laser pulse duration ( $\tau_g, \tau_y$ ) and beam diameter ( $D_g, D_y$ ) of G and Y components with variation of electrical input power & HBr concentration respectively. As the input power increases from 6 to 9.5 kW, both  $D_g$  &  $D_y$  increase from 25 to 29 mm & 26 to 30 mm respectively, whereas  $\tau_g$  &  $\tau_y$  increase from 80 to 90 ns & 78 to 100 ns respectively. On the other hand, with variation in HBr concentration from 5 to 9%, both  $D_g$  &  $D_y$  decrease from 32 to 25 mm & 30 to 25 mm respectively, whereas  $\tau_g$  &  $\tau_y$  are maximum at 7% HBr concentration and decrease to 68 ns / 64 ns & 74 ns / 82 ns for 5% & 9% HBr concentrations respectively. Similarly, with increase of the input power (6 to 9.5 kW) the respective G & Y laser power ratio decrease from 1.53 (23 W/15 W) to 1.12 (38 W/34 W) whereas with increase of HBr concentration (5 to 9%) the G to Y laser power ratios are 1.82

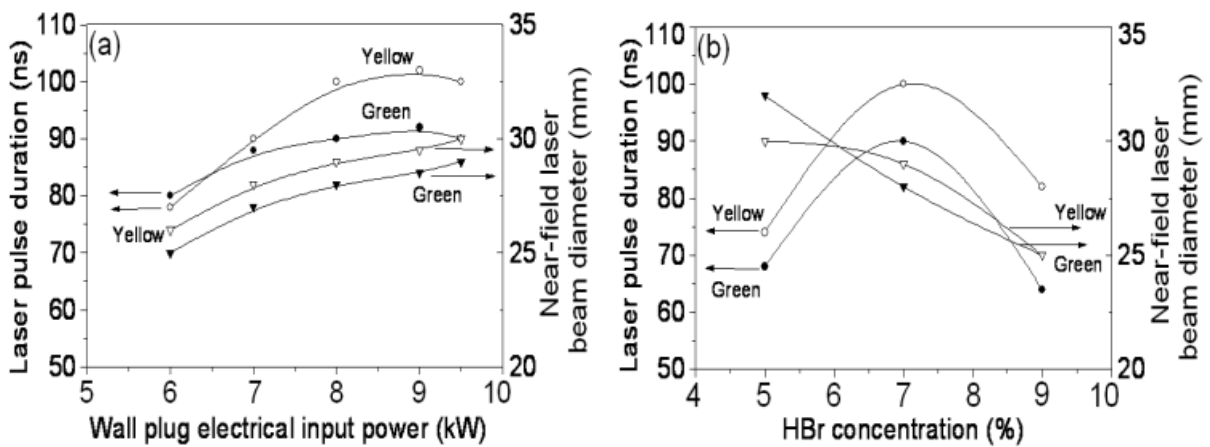


Fig. 7.12 Variation of laser pulse width and laser beam diameter of Cu-HBr laser with

(a) electrical input power and (b) HBr concentration

(31 W/17 W), 1.21 (25 W/29 W) & 0.87 (26 W/30 W) respectively. These details are described in section 6.2.1 of chapter 6 of this thesis. These are the indications of variations in their respective laser gains and are linked with Cu-HBrL kinetics as discussed in section 3.3 of chapter 3 in the present thesis [33-35, 124].

The near-field intensity profile and its width play crucial role in deciding the beam divergence in terms of its minimum attainable diffraction limit  $\theta_{DL}$ . For the quasi-Gaussian nature of near-field profiles, as measured in our case (Figs. 7.10 & 7.15 a),  $\theta_{DL}=3.05 \lambda/D$  (already discussed in section 1.4.2.3, chapter 1). Therefore, the values  $\theta_{DL}$ , for the case of different input powers used from 6 to 9.5 kW, are about 62.3 to 53.70  $\mu\text{rad}$  for G and about 67.83 to 58.78  $\mu\text{rad}$  for Y component respectively. Similarly, for HBr concentrations of 5%, 7% & 9% the values  $\theta_{DL}$  are about 48.67, 55.62 & 62.29  $\mu\text{rad}$  for G and about 58.78, 60.81 & 70.54  $\mu\text{rad}$  for Y component. The  $\theta_{DL}$  values are functions of input power or HBr concentration due to variation of near-field beam diameter, D, with these parameters (Figs. 7.12 a & b). These transform the variation in  $\langle\theta\rangle_g$  from about 16.86 to 20.30 DL and in  $\langle\theta\rangle_y$  from 16.37 to 22.11 DL respectively for the variation in input power from 6 to 9.5 kW. The variation in  $\Delta\theta_g$  is about  $\pm 0.42$  to  $\pm 0.80$  DL and in  $\Delta\theta_y$  is about  $\pm 0.47$  to  $\pm 0.77$  DL for the respective input power from 6 to 9.5 kW. However, for HBr concentrations from 5 to 9%, the values of  $\Delta\theta_g$  are about  $\pm 0.97$  to  $\pm 0.77$  DL and  $\Delta\theta_y$  are about  $\pm 0.70$  to  $\pm 0.60$  DL respectively.

## **7.4 Spatial beam quality behaviour of Cu-HBr laser with confocal unstable resonators**

### ***7.4.1 Beam divergence & pointing stability behaviour***

The far-field beam divergence, pointing stability & intensity variations as well as the near-field spatio-temporal intensity profiles are studied with confocal PBURs of three different magnifications  $M = 12.5, 50$  &  $100$ . Figs. 7.13 a - f show the variations of the of single pulse far-field beam divergence, pointing angle & intensity fluctuation of recorded 512 Nos. of pulses of G (a, c & e) and Y (b, d & f) components of Cu-HBrL with PBUR  $M = 50$ . The divergence

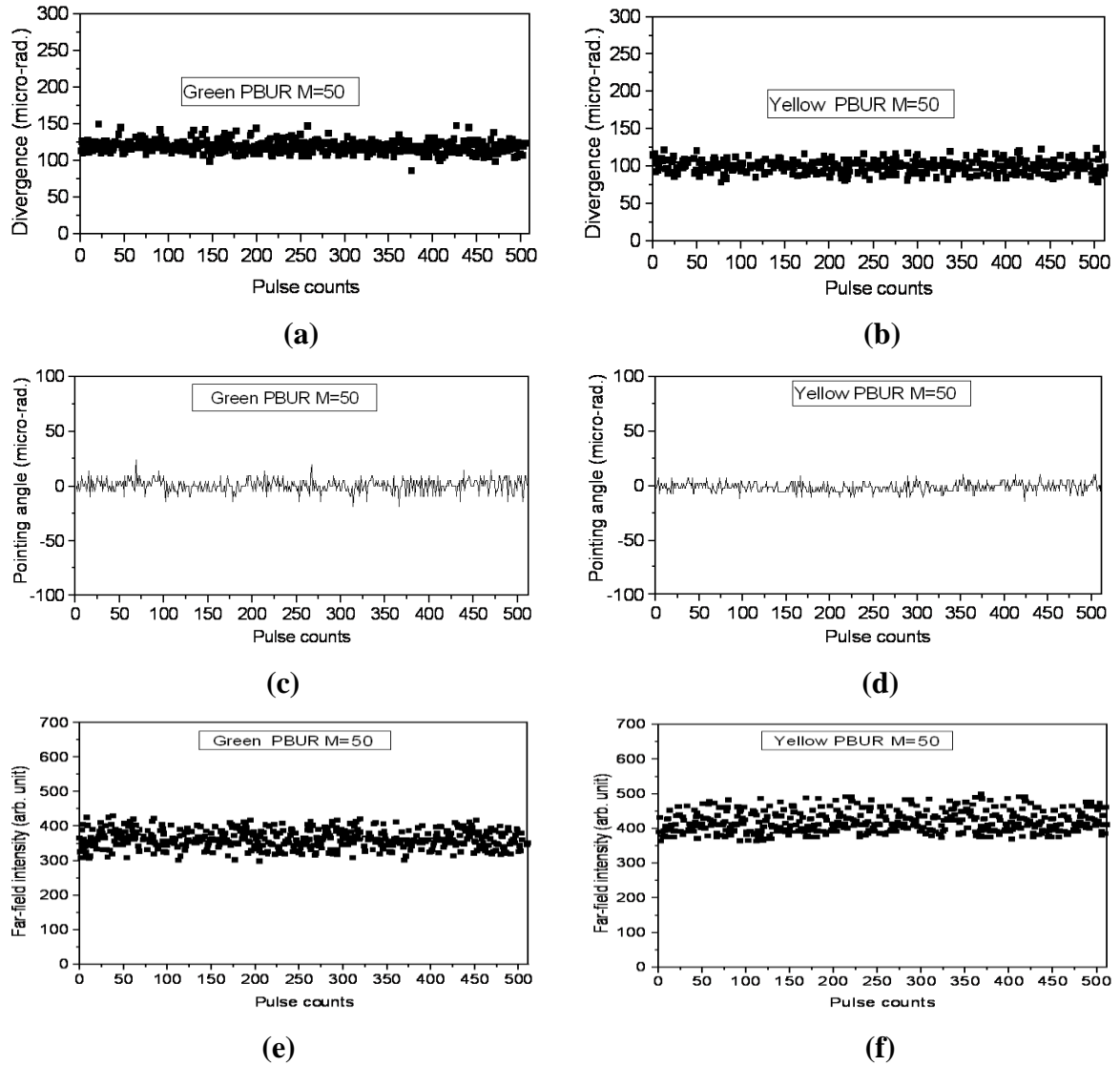


*Fig. 7.13 Variation of single pulse far-field beam divergence, pointing angle & intensity for recorded 512 pulses of Cu-HBrL with PBUR M=50 : Green (a, c & e) and Yellow (b, d & f) and pointing angle data are corrected for the magnification used in far-field recording. For the other two PBURs of M = 12.5 & 100, similar results/graphs are obtained from the recorded composite images of the far-filed spatial beam intensity profiles (outlined in section 7.2.2). However, the magnitude of the observed results are different.*

Figs. 7.14 a & b show the variation of the far-field average beam divergence & its fluctuation and the pointing stability & intensity fluctuation of Cu-HBrL radiations with different magnifications of the PBURs used. It is observed that as the magnification of the PBUR increases from 12.5 to 100, the average beam divergence ( $\langle\theta\rangle$ ) decreases rapidly from

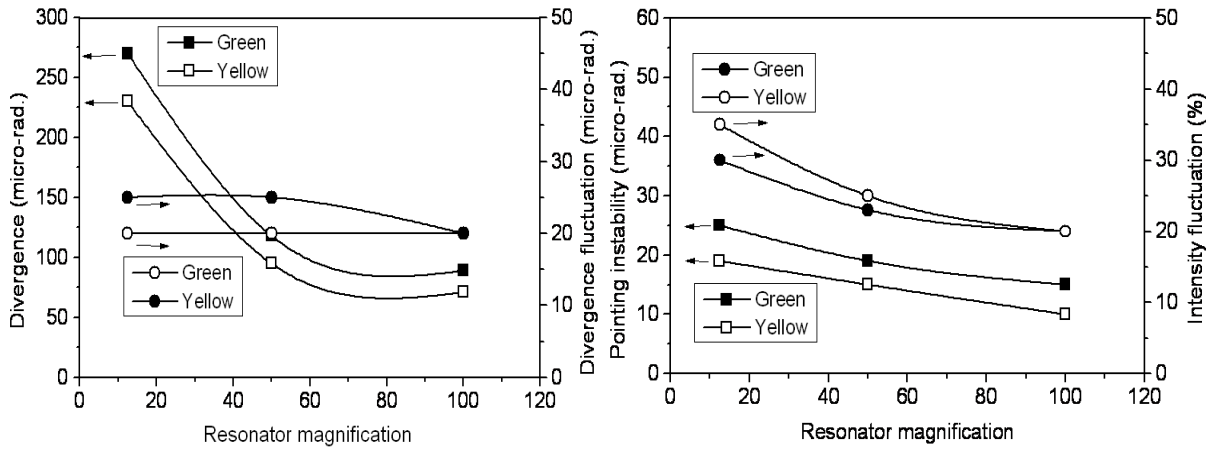


Fig. 7.14 Variation of the beam divergence & its fluctuation (a) and the pointing stability & intensity fluctuation (b) of Cu-HBrL radiations with different magnification of the PBURs

PBUR increases from 12.5 to 100, the average beam divergence ( $\langle\theta\rangle$ ) decreases rapidly from 268  $\mu\text{rad}$  to 89  $\mu\text{rad}$  for the G component and from 230  $\mu\text{rad}$  to 71  $\mu\text{rad}$  for the Y component respectively. However, the corresponding fluctuations ( $\Delta\theta$ ) remain within  $\pm 20$  to  $\pm 25$   $\mu\text{rad}$ . Similarly, with the increase of the magnification of the PBUR from 12.5 to 100, the far-field beam pointing instability as well as the long term intensity fluctuation ( $\Delta I/\langle I \rangle$ ) decreases from  $\pm 25$   $\mu\text{rad}$  to  $\pm 15$   $\mu\text{rad}$  and  $\pm 30\%$  to  $\pm 20\%$  for the G component whereas for the Y component the corresponding values decrease from  $\pm 19$   $\mu\text{rad}$  to  $\pm 10$   $\mu\text{rad}$  and  $\pm 35\%$  to  $\pm 20\%$ . It may be mentioned that the average average beam divergence & its fluctuation, pointing stability and intensity variations with PPR at this electrical input power ( $\sim 5$  kW as used for the case of URs) are 1500  $\mu\text{rad}$  & 25  $\mu\text{rad}$ ,  $\pm 30$   $\mu\text{rad}$  and  $\pm 6\%$  for the G component whereas for the Y component these values are 1400  $\mu\text{rad}$  &  $\pm 28$   $\mu\text{rad}$ ,  $\pm 27$   $\mu\text{rad}$  and  $\pm 6\%$  respectively. At this condition ( $\sim 5$  kW electrical input power), the average brightness [= Beam average power /  $\{\pi^2 \cdot (\text{beam radius})^2 \cdot \theta^2\}$ ] of the Cu-HBrL beams are estimated to be about  $5.19 \times 10^5$  W/cm<sup>2</sup>.sr,  $1.35 \times 10^7$  W/cm<sup>2</sup>.sr,  $6.52 \times 10^7$  W/cm<sup>2</sup>.sr &  $1.15 \times 10^8$  W/cm<sup>2</sup>.sr (for G component) and  $3.31 \times 10^5$  W/cm<sup>2</sup>.sr,  $1.10 \times 10^7$  W/cm<sup>2</sup>.sr,  $5.75 \times 10^7$  W/cm<sup>2</sup>.sr &  $1.03 \times 10^8$  W/cm<sup>2</sup>.sr (for Y component) corresponding to PPR, PBURs of M = 12.5, 50 & 100 respectively.

These spatial characteristics of a Cu-HBrL can be compared with that of a conventional CVL of identical size (2.8 cm bore dia. x 150 cm long tube). The far-field beam divergence, pointing instability & intensity fluctuations of the CVL [48], as reported only for the G component, with PPR are  $3000 \mu\text{rad}$ ,  $\pm 120 \mu\text{rad}$  &  $\pm 25\%$ ; with PBUR  $M = 12.5$  are  $150 \mu\text{rad}$ ,  $\pm 45 \mu\text{rad}$  &  $\pm 47\%$  whereas with PBUR  $M = 100$  these values are  $\langle\theta\rangle_g = 122 \mu\text{rad}$ ,  $\Delta\theta_g = \pm 15 \mu\text{rad}$ ,  $\delta_g = \pm 15 \mu\text{rad}$  &  $(\Delta I/\langle I \rangle)_g = \pm 30\%$  respectively. For the Y component, as reported only with PBUR  $M = 100$ , these values are  $\langle\theta\rangle_y = 108 \mu\text{rad}$ ,  $\Delta\theta_y = \pm 10 \mu\text{rad}$ ,  $\delta_y = \pm 10 \mu\text{rad}$  &  $(\Delta I/\langle I \rangle)_y = \pm 45\%$  [207]. On the other hand, these values in a Cu-HBrL are far better than that of the conventional CVL, as presented above.

#### 7.4.2 Radial and temporal intensity profiles

Fig. 7.15a shows the recorded near-field radial intensity profiles for G and Y components of the Cu-HBrL with PBUR  $M = 50$ . For PBURs of  $M = 12.5$  &  $100$ , the profiles are similar. The central dip in the intensity profiles of both the G and Y components are due to their reflection off the scraper mirror with central hole in the on-axis configuration of UR, as employed. Also, the small modulation in the spatial profiles are due to effects of diffraction by the hard edge of the scraper mirror used (Fig. 7.1, config. B). Despite the central null in

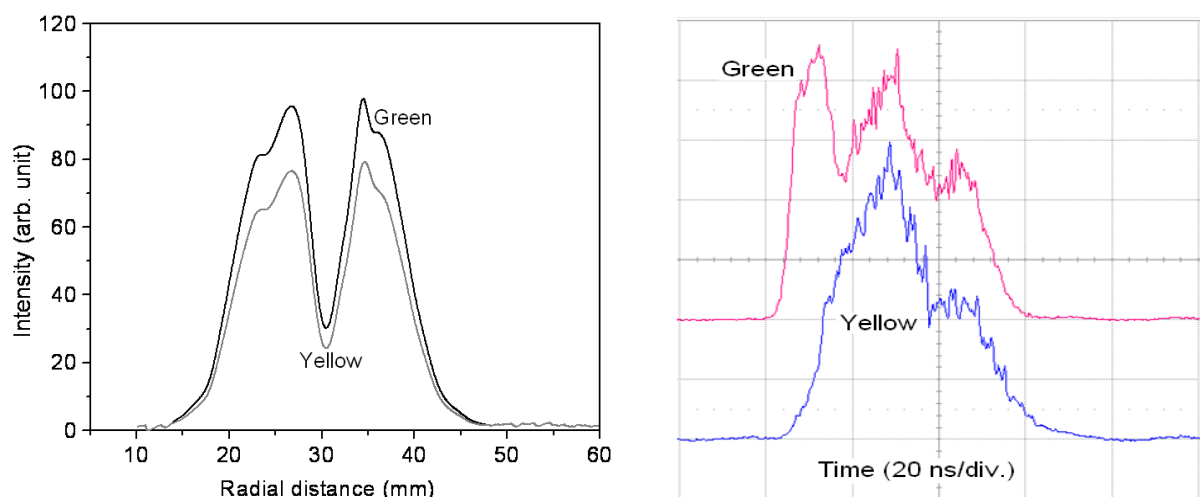


Fig. 7.15 Typical recorded intensity profiles of G & Y component of Cu-HBrL with PBUR

( $M = 50$ ): (a) radial profiles and (b) temporal profiles

the near-field intensity distribution, the far-field profiles (Fig. 7.4) are axially peaked due to almost uniphase nature of the UR beam. It is also clear that spatial profiles of the intra-resonator circulating beams are axially peaked & quasi-Gaussian in nature. The laser beam diameters for both the G and Y components are about 25 mm for PPR as well as PBURs used. For the PBURs, with both  $D_g$  &  $D_y$  of 25 mm, the variation in  $\langle\theta\rangle_g$  corresponds from about 4.3 DL to 1.45 DL and in  $\langle\theta\rangle_y$  corresponds from about 3.26 DL to 1 DL, with increase of the M of the PBURs from 12.5 to 100. However, the variations of both  $\Delta\theta_g$  &  $\Delta\theta_y$  are within  $\pm 0.3$  to  $\pm 0.35$  DL. Therefore, the changes in the beam diameters lead to variation in degrees of diffraction effects ( $\propto \lambda/D$ ), that affects the observable beam divergence.

Fig. 7.15 b shows the typical recorded laser pulses of the G and Y components of Cu-HBr laser with PBUR M=50. For the PBURs of M=12.5 & 100, the pulse shapes are similar however of different durations. The pulse durations (at  $1/e^2$ ) of the G components are ~55 ns, ~50 ns & ~44 ns and for the Y components are ~50 ns, ~45 ns & ~39 ns for the PBURs of M = 12.5, 50 & 100 respectively. It is observed that the temporal profiles of the G components show three distinctly modulated peaks, out of which the first two are almost of same heights. On the other hand, the Y component has only two modulated peaks, out of which the first one is prominent. It is also observed that the Y pulse builds up later (~5 ns) as well as slowly as compared to that of the G, but extends upto 10-12 ns after the termination of the G pulse. These phenomena are linked with the laser kinetics associated with Cu-HBrL as discussed in chapters 1 & 2 of this thesis. The temporal pulse shapes of G & Y components of PPR and UR Cu-HBr laser are further deliberated upon while discussing their SHG/SFG in the chapter 9.

## 7.5 Analysis of observed beam quality behaviour of the Cu-HBr laser

From the above experimental results following facts have emerged. First, the far-field beam divergence, pointing stability values and their fluctuations as well as far-field intensity variations scale up (degrade) with increase of the input power of Cu-HBrL. The beam quality

also degrades with change of HBr concentration away from the optimized level. Second, the beam divergence & its variation and pointing stability of both the G & Y components improve significantly with the increase of the optical resonator magnifications from  $M \approx 1$  (PPR) to  $M = 100$  (UR). At the same time, the pulse to pulse far-field intensity variation worsens when the optical resonator is changed from PPR to PBURs. Among the URs, increase of magnification leads to reduced variation in far-field intensity. Also the G & Y components have different beam quality characteristics. The observed trends (Fig. 7.5 – Fig. 7.15) need to be analyzed.

Analyzing the beam quality i.e. divergence, pointing angle and their pulse to pulse variation is a complex issue due to interconnectedness of various beam quality deciding parameters. Any change in input power or HBr concentration leads to change in near-field spatial intensity distribution, temporal laser modulation, laser gain build-up time & gain duration, beam divergence evolution, ASE present in the laser pulse, gas heating, gain medium refractive index and plasma parameters. In addition, in the present experiment, the long term beam stability, lasting over 500 seconds are recorded, where beam disturbances/wave-front distortions originating over the different time slots i.e. laser pulse duration, inter-pulse period, active medium thermal relaxation time, short & long term thermally driven fluctuations in the active medium remain present [13, 48]. The complex inter-dependence as well as the combined effects of all these factors contribute to the net observable spatial characteristics.

### ***7.5.1 Beam quality of Cu-HBrL vs. input power & HBr concentration***

The output pulse of a laser oscillator builds up from the spontaneous emission which is highly random in phase and amplitude across the beam cross section. Therefore, the beam divergence of a laser evolves with time from the optical noise/ASE seed radiation. During several transits within the optical resonator; this undergoes repeated spatial filtering (through the gain medium aperture) & amplification, and finally attains a steady state. This requires hundreds of round trips in the gain medium [13, 48]. Owing to its short inversion time and high

gain of Cu-HBrL, the steady state i.e. resonator mode establishment, is not achieved and a significant amount of ASE is expected to be present in the output of the radiations. The quality of the copper laser radiation is controlled by the ASE right from the onset of its gain [50]. The extent to which the ASE affects the spatial beam quality, depends on the gain duration, rise time & its temporal evolution dynamics. More the laser gain and faster its rise time, more will be the ASE content in the beam. So, there is a presence of significant amount of ASE in the Cu-HBrL beam. A study in CuBr + H<sub>2</sub> laser (equivalent to Cu-HBrL) revealed the presence of 20-50% ASE in the laser output pulse [211]. Also, in a Cu-HBrL, the measured single pulse divergence is an weighted average of the intra-pulse beam divergences corresponding to various round trips i.e.  $\theta = \sum_i \omega_i \cdot \theta_i$ , where  $\omega_i$  is the weighted fraction of  $i^{\text{th}}$  round trip, approximately represented by the strength of peaks of the temporal profile [13, 48, 212-214]. The later the dominant peak(s)/gain maxima occur in the laser temporal pulse profile, the better is the overall observable pulse averaged divergence.

The laser beam quality is also degraded due to wave-front distortion by the heated laser discharge plasma, high incidence laser flux on the resonator mirror and also due to acoustical perturbation originating from multi-kHz PRR pulsed power pumping [9, 13, 48, 49]. However, for the fixed PRR of the Cu-HBr laser (18 kHz in the present case), it is the relative thermal induced effect that dictates the overall wave-front distortion as input power or HBr concentration is changed. The existence of radial temperature gradient (section 5.4.1, chapter 5) in the discharge tube leads to radial refractive index variation in a Cu-HBrL plasma [11]. This leads to wavefront disturbances in terms of beam deflection, focusing/defocusing and other higher order phase profile distortions such as spherical aberration, astigmatism etc. Any thermally driven fluctuations in different time slots i.e. laser pulse duration, inter-pulse period, active medium thermal relaxation time etc. in the Cu-HBrL laser discharge plasma act as perturbation in the radial refractive index distribution and hence result in wave-front

distortions. These distortions are also manifested as pulse to pulse fluctuations in the beam position/pointing and divergence [13, 48].

Hence, referring to beam quality results (section 7.3) with increase in the input power from 6 to 9.5 kW, the energy coupled into Cu-HBrL plasma, laser gain, ASE and the heating effects increase. These result increased thermally induced adverse effects, leading to increase in  $\langle\theta\rangle$ ,  $\Delta\theta$  and  $\delta$  for both the G & Y components of Cu-HBrL, as observed. However, the rate of increase of gain, hence ASE content, with input power is expected to be higher for the lower gain Y component as compared to G. This is evident from slower gain rise of Y as compared to G (Figs. 7.11 a & b) and also from the decrease of G to Y laser power ratio from 1.53 to 1.12 (Fig. 6.6 a, chapter 6) as input power is increased from 6 to 9.5 kW. It is also evident from the laser temporal pulse profile (Figs. 7.11 a, b, c & d) that for G, as compared to Y, the dominant peak (s) occur later in time where the beam divergence has evolved to much lower values. Hence the G component has better pulse averaged divergence ( $\theta$ ) as compared to Y at all input powers. The lower beam divergence of G component also results in lower value of divergence fluctuations and high pointing instability as compared to Y.

On the other hand, for different HBr concentrations from 5 to 9%, even though the electrical input power remains same, the fractional energy coupled to the laser discharge and hence available copper density differ [12, 124]. These affect the gain rise time as well as the gain duration of both the components. As the upper laser level of Y line lies energetically lower than that of G, hence the Y transition is expected to be affected more than that of G [12, 13]. This is evident from the fact that both at higher and lower HBr concentrations, the gain duration as well as the gain build ups are lower than that for the optimum HBr concentration (Figs. 7.11 c & d). Also, the near-field spatial intensity profiles of the Y component, at both the higher and lower HBr concentrations, show slightly more centrally deep profile unlike that of the G component (Figs. 7.10 a & b). Hence, the observed results can be explained proceeding with

similar arguments as in case of the input power together with the observed intensity profiles.

### 7.5.2 Beam quality of Cu-HBrL with plane-plane & unstable resonators

For a high gain, high Fresnel number ( $N_F = D^2/\lambda L_r$ ) pulsed laser device, the evolution of far-field beam divergence for PPR & PBURs is controlled mainly by ratio of discharge tube (beam) diameter to resonator length [215, 216]. For a PPR, the beam divergence, attained after  $n^{\text{th}}$  round trip ( $2n$  passes) in the laser cavity, is given as  $\theta_n = D/2nL_r$  ( $n = 1, 2, 3, \dots$  is the round trip number &  $L_r$  = the optical resonator cavity length). Therefore, the number of round trips ( $n_o$ ) and time ( $\tau_o$ ) required to attain the DL divergence (steady state) is given as,

$$n_o = \left[ \frac{(D/2L_r)}{(\beta_p \lambda / D)} \right] = \frac{D^2}{2\beta_p \lambda L_r} \quad (7.5)$$

$$\tau_o = \frac{D^2}{\beta_p \cdot \lambda \cdot c} \quad (7.6)$$

where  $c$  is the speed of light and  $\beta_p = 3.05$  (section 1.4.2.3, chapter 1). For beam diameter  $D = 25$  mm, the values of  $n_o$  &  $\tau_o$  are  $\sim 81$  &  $\sim 1340$  ns for G and  $\sim 71$  &  $\sim 1180$  ns for Y component of Cu-HBrL. For input power variation from 6.0 to 9.5 kW in Cu-HBrL, more specifically, this corresponds to number of required round trips of 80 to 108 for G and 77 to 102 for Y components. This is because with increase in electrical input power, the electron density in the active medium also scales up. This in turn leads to enhanced filling of discharge across tube cross section and hence increase in the laser beam diameter (Figs. 7.12). For the HBr concentrations (5%, 7% & 9%), the corresponding number of round trips required are about 132, 101 & 80 for G and about 102, 95 & 71 for Y components. However, the available gain duration of the Cu-HBrL radiations (Figs. 7.12) restrict the number of cavity round trips to only 5-6 for PPR. So, with PPR, the steady state is not attainable in Cu-HBrL. Hence, the beam divergence of Cu-HBrL with PPR is comparatively large, of the order of 10s of DL (Sec. 7.3.3).

On the other hand, for PBURs, the beam divergence attained after each round trip is

reduced further by the resonator cavity magnification factor  $M$ , which after  $n^{\text{th}}$  round trip is given as  $\theta_n = D/M^n L_r$  [215, 216]. The number of cavity round trips ( $n_o$ ) as well as time ( $\tau_o$ ) required by the laser radiations to attain the DL / steady state divergence value, in such case, are given as [48,189, 215],

$$n_o = 1 + \ln M_o / \ln M \quad (7.7)$$

$$\tau_o = 2L_r \left(1 + \frac{\ln M_o}{\ln M}\right) / c \quad (7.8)$$

where  $M_o = D^2 / [\beta_p \lambda (2L_r - L_r^2 / F_1)]$ . For the PBURs of  $M = 12.5, 50$  &  $100$ , as used in our case, the values of  $\tau_o$  come out to be  $\sim 46$  ns,  $\sim 38$  ns &  $\sim 35$  ns for G and  $\sim 45$  ns,  $\sim 37$  ns &  $\sim 34$  ns for Y component respectively. These values translates to the number of required round trip values to about 3, 2.3 & 2 for both the G & Y components of Cu-HBrL with near-field beam diameter  $D = 25$  mm. In the present study, the laser pulse durations ( $1/e^2$  width) are observed to be  $\sim 55$  ns,  $\sim 50$  ns &  $\sim 44$  ns for the G and  $\sim 50$  ns,  $\sim 45$  ns &  $\sim 39$  ns for the Y component respectively for PBUR  $M = 12.5, 50$  &  $100$ . This indicates the possibility of obtaining near DL beam divergence in Cu-HBrL with the PBURs. It is also clear that higher the resonator magnification, lower will be the obtained beam divergence, as actually observed. Also, the the beam divergence & pointing instability is lower for the Y-component as compared to G due to its lower gain and lesser ASE content.

It has already been pointed out that the thermal induced perturbations are operative in high power & high PRR Cu-HBrL. The resulting wave-front distortions are manifested as fluctuations in the beam position/pointing and divergence. These distortions are also linked with the misalignment sensitivity ( $S$ ) of the resonator axis [ $S = 2M/(M-1)$ ] [48, 217]. For PPR ( $M \rightarrow 1$ ), the  $S$  value is very large high, whereas it decreases with increase of  $M$ . The  $S$  value reduces to 2.17, 2.04 and 2.02 for PBUR of  $M = 12.5, 50$  &  $100$  respectively. Also, as the resonator magnification increases, spatial filtering of the seed optical noise as well as wavefront

distortions through the gain medium aperture becomes better [218, 219]. This facilitates the optical radiations to attain steady state faster and temporal integrity of the wavefronts become better. This leads to reduction in beam divergence as well as the pointing instability with increase of the resonator magnifications from  $M \sim 1$  (PPR) to  $M=100$  (UR) as observed.

### 7.5.3 Far-field intensity variation

The observed far-field intensity variation trends of the investigated Cu-HBrL can be explained as follows. The far field peak intensity is given as [13],

$$I_{FF} = \gamma \cdot \text{Peak intensity of laser pulse on CCD face} = \gamma \cdot \frac{(E_p/\tau)}{\pi \cdot [(M' f \theta)^2/4]}$$

$$\Rightarrow I_{FF} = \frac{4\gamma}{\pi M'^2 f^2} \frac{E_p}{\tau \theta^2} \quad (7.9)$$

where  $\gamma$  = photosensitivity of the CCD,  $E_p$  = laser pulse energy falling on the CCD face,  $M'$  = magnification of the far-field laser spot at the CCD face,  $f_l = 50$  cm. In the present experiment  $\gamma$ ,  $M'$  and  $f$  are almost constant. Therefore, the fluctuations in  $E_p$ ,  $\tau$  and  $\theta$  collectively contribute to the net observable fluctuation in the far field intensity and can be written as [13],

$$\left| \frac{\Delta I_{FF}}{I_{FF}} \right| \approx \left| \frac{\Delta E_p}{E_p} \right| + \left| \frac{\Delta \tau}{\tau} \right| + 2 \left| \frac{\Delta \theta}{\theta} \right| \quad (7.10)$$

where the terms in the right hand side represent stability/fluctuations in the laser output pulse energy, laser pulse duration and far-field divergence. In a Cu-HBrL,  $\Delta \tau/\tau$  is almost negligible and hence  $\Delta I/I$  is mainly governed by  $\Delta E_p/E_p$  and  $\Delta \theta/\theta$  [13, 48, 207].

Generally, the laser pulse energy stability ( $\Delta E_p/E_p$ ) of a laser in general and a Cu-HBrL in particular, is dependent on the beam pointing stability, pump pulse energy stability, local/global fluctuations in the plasma parameters such as plasma-electron-density/plasma-impedance that decide the energy coupling, laser gain and the optimum feedback fraction of the output coupler of resonator required. In the investigated Cu-HBr laser, the role of pointing fluctuation on the pulse energy instability is negligible as the maximum beam movement ( $L_r \cdot \delta$ )

over resonator length  $L_r$  is very small (<1%) to change the single pulse resonator feedback fraction or diffraction loss to cause far field intensity variation. However, it has already been brought out (chapter 3) that any change in the input power and/or HBr concentration, will affect the coupled pump power (energy) to the gain medium. In general, either with the increase in input electrical power or moving away from optimum HBr concentration, the coupled pulse energy stability will degrade. This may be explained as follows. In a Cu-HBrL, as the input power increases, the local/global fluctuations in the plasma parameters such as in the electron and other particle density also increase. This is mainly due to increase of gas temperature [12, 13]. The enhanced gas temperature leads to increased thermal dissociation of the HBr molecule i.e.,  $\text{HBr} \rightarrow \text{H}/\text{H}_2 + \text{Br}/\text{Br}_2$ , which subsequently degrades the dissociative attachment process of electrons in the plasma [7]. This in turn leads to increased pulse to pulse fluctuation in energy coupling into the Cu-HBrL plasma. These effects lead to increased laser output pulse energy fluctuations with increase in input power and HBr concentration far from optimum. This behavior is also expected to be different for G & Y components due to different gain characteristics. This is evident from the observed  $\Delta\theta/\theta$  increase from 2.5% to 3.9% for G component and from 2.9% to 3.5% for Y component as the input power increases from 6 to 9.5 kW. Therefore, the increased divergence fluctuation and laser pulse energy instability together increase the fluctuation in the far-field intensity with increase in input power and/or change in HBr concentration.

The pulse energy stability of a laser oscillator is also influenced by the optical feedback strength of the resonator. This is linked with the reflectivity of the output coupler. Higher is the reflectivity of the output coupler, better is the energy stability as the resonator establishes more control over the cavity radiation. In a Cu-HBrL, the optimum reflectivity of the output coupler ( $R_o$ ) is inversely related with the laser gain ( $g_0l$ ) and can be represented approximately as [13],

$$g_0l \approx \left[ \frac{(1 - R_o)}{R_o} + \ln\left(\frac{1}{R_o}\right) \right] \quad (7.11)$$

For the present Cu-HBrL with PPR,  $R_o$  of ~3.5% (single side anti-reflection coated fused silica blank) have been used for maximum laser output power. On the other hand, with the change of resonator from PPR to PBUR of different magnifications, the feedback fraction also changes. The feedback fractions of PBURs are typically  $\approx (100/M^2) \%$  [48]. For the cases of PBURs of  $M=12.5, 50$  &  $100$ , this comes out to be 0.64%, 0.04% & 0.01% respectively. For this reason, the far-field intensity variation in case of PPR is better than that of PBURs. However, as the  $M$  of the PBURs increases, the variation of the divergence within a pulse becomes slower due to better spatial filtering actions for the optical noise. Similar trends in variation in intra-pulse divergence, obtained by taking streak scan of the far-field spot of CVLs with different resonators, have been observed [220]. Therefore, slightly less variation in the far-field intensity, for PBURs of higher  $M$ , is attributed to lower divergence fluctuation and slower variation in far-field divergence.

## 7.6 Conclusions

In conclusion, this chapter presented a comprehensive study on the beam divergence and pointing stability behaviour of both the green and yellow radiation components of a Cu-HBrL with different electrical input power, HBr concentration as well as optical resonators (PPR & PBURs of  $M = 12.5$  to  $100$ ). Both the time averaged and pulse to pulse variations in the beam divergence and pointing stability are studied. The experimental study is augmented with near-field spatial intensity profiles & temporal pulse shapes of both the radiations. Highly stable and diffraction limited beams of both the green and yellow radiations have been obtained with the use of unstable resonators of different magnifications. The observed results are suitably analysed and discussed encompassing the estimation of divergence for different resonators, role of spatio-temporal laser gain characteristics, thermally induced perturbations and the effect of diffraction. These high quality laser beams are required for efficient UV generation through nonlinear optical conversion as described in the chapters 8 & 9.

## Chapter 8

### Review on nonlinear frequency conversion of copper lasers

#### 8.1 Introduction

The range of applications of copper lasers is considerably broadened by the capability to shift their output radiation in frequency, particularly to ultra-violet (UV) region of the spectrum [15, 16]. The coherent mid-UV radiations (255.3, 271.2 & 289.1 nm) are obtained by nonlinear frequency conversion processes such as second harmonic & sum frequency generation (SHG & SFG) of copper laser radiations (510.6 & 578.2 nm) in nonlinear crystal [220-234]. However, the SHG/SFG based visible to UV nonlinear conversions of CVL/Cu-HBrL pose several challenges. First, the SHG/SFG conversion at high pulse repetition rate (PRR), high average power leads to limiting performances by thermal dephasing effects & crystal damage due to absorption of UV/visible radiations. Second, the low peak power / pulse energy of copper lasers require tight focusing of laser beam into the nonlinear crystal for high conversion. This requires proper focusing geometry (optical) to limit the focused beam divergence angle within angular acceptance of the nonlinear crystal. Third, there is a limited choice on nonlinear phase-matchable crystals for UV generation. In addition, nonlinear crystals with sufficiently low absorption at the frequencies involved, reasonably large angular/temperature acceptance, low walk-off and high damage threshold, are desired.

This chapter reviews the works on the SHG and SFG of copper laser radiations (G & Y). The fundamentals of SHG/SFG processes, relevant coupled wave equations and phase matching conditions are presented in brief. The criteria for choosing suitable nonlinear crystals for SHG/SFG based high repetition, high average power UV generation are presented taking into account the phase matching conditions, nonlinear coefficients, damage threshold, absorption at the involved optical frequencies, thermal effects, acceptance angle and beam walk-off effects. The experimental and theoretical works on the SHG/SFG processes of CVLs,

which are mostly carried out at 5-6 kHz PRR, are reviewed in terms of variety of nonlinear crystals, focusing geometries and pump beam quality. The limited reported studies on the SHG of green radiations of 10-18 kHz PRR as obtained from Cu-HBrL, KE-CVL & CuBrL are presented. The limiting factors of the frequency conversion process at high PRR and high average powers are discussed.

## 8.2 Basics of nonlinear frequency conversion

### 8.2.1 Nonlinear polarisation

Nonlinear frequency conversion effects are analyzed by considering the response of the dielectric material at the atomic level to the electric field of an intense light beam. The propagation of an electromagnetic wave through a material creates perturbation to its spatio-temporal electrical charge distribution creating electric dipoles whose macroscopic manifestation is the polarization. For high electric field strength (typically  $\sim 10^{11}$  V/m) as used in case of nonlinear optics/frequency-conversion processes, the magnitude of the induced instantaneous polarization per unit volume  $\mathbf{P}(t)$ , can be expressed in terms of the magnitude of the applied instantaneous electric field  $\mathbf{E}(t)$  as [235],

$$P(t) = \sum_1^n \epsilon_0 [\chi^{(n)} E^n(t)] = \sum_1^n P^{(n)}(t) \quad (8.1a)$$

$$\Rightarrow P(t) = P^{(1)}(t) + P^{NL}(t) \quad (8.1b)$$

where  $\epsilon_0 = 8.854 \times 10^{-12}$  F/m, is the electric permittivity of free space and  $\chi^{(n)}$  is dielectric susceptibility of order  $n$ , which is a tensor of rank  $n$  with  $3^{n+1}$  components. For  $n = 1$ , it describes the linear response of the material whereas for  $n \geq 2$ , it describes the nonlinear response of the material. The term  $P^{NL}(t)$ , which describes the nonlinear polarization, takes into account all the higher order polarization terms. With lasers of high intensity/electric field, the nonlinear polarization effects come into picture and corresponding radiations are observed.

Very often the dielectric susceptibility is represented by the so called  $d$ -coefficient, where  $d$  is also a tensor. For SHG/SFG, it is related to the dielectric susceptibility tensor  $[\chi^{(2)}_{ijk}]$

as  $d_{ijk} = \frac{1}{2} \chi^{(2)}_{ijk}$  [188, 235]. Most nonlinear crystals are described by only a few non-vanishing terms of  $d$ -coefficients. Furthermore, for the crystals of interest, there is usually only one predominant  $d$ -coefficient associated with a beam propagation direction which yields maximum harmonic power. For a fixed geometry i.e. for fixed propagation and polarization directions, it is possible to express the nonlinear polarization using effective  $d$ -coefficient ( $d_{eff}$ ) which depends on type of crystal (uniaxial or biaxial), its class and angle phase matching (type-I or type-II) used. For such condition,  $d_{eff}$  can be expressed readily as  $d_{eff} = \frac{1}{2} \chi^{(2)}$  [188, 235].

### 8.2.2 Coupled wave equation

The electromagnetic waves, in a nonlinear crystal (non-magnetic dielectric medium with no free charge or current), are described by Maxwell's equations given as,

$$(i) \nabla \cdot \mathbf{D} = 0 \quad (ii) \nabla \cdot \mathbf{B} = 0 \quad (iii) \nabla \times \mathbf{E} = -\frac{\partial \mathbf{B}}{\partial t} \quad (iv) \nabla \times \mathbf{B} = \mu_0 \frac{\partial \mathbf{D}}{\partial t} \quad (8.2)$$

where  $\mathbf{D} = \epsilon \mathbf{E}$  is the electric displacement vector ( $C/m^2$ ),  $\mathbf{B} = \mu_0 \mathbf{H}$  is the magnetic induction vector (also known as field strength / magnetic flux density) (tesla),  $\mathbf{H}$  is the magnetic intensity (A/m) and  $\mu_0 =$  magnetic permeability of free space =  $1.25664 \times 10^{-6}$  H/m. For a nonlinear medium,  $\mathbf{D}$  is composed of linear and nonlinear parts and are related by,

$$\mathbf{D} = \epsilon_0 \mathbf{E} + \mathbf{P} = \epsilon_0 \mathbf{E} + \mathbf{P}^{(1)} + \mathbf{P}^{NL} = \mathbf{D}^{(1)} + \mathbf{P}^{NL} \quad (8.3)$$

where  $\mathbf{D}^{(1)}$  is the linear part of the electric displacement vector such that  $\mathbf{D}^{(1)} = \epsilon_0 \mathbf{E} + \mathbf{P}^{(1)} = \epsilon \mathbf{E}$ . Coupling of the equations 8.2 and 8.3, gives rise to the *fundamental equation of nonlinear optics*, for a loss less dielectric medium as [188, 235],

$$\nabla^2 \mathbf{E} - \mu_0 \epsilon_0 \frac{\partial^2 \mathbf{E}}{\partial t^2} = \mu_0 \frac{\partial^2 \mathbf{P}^{NL}}{\partial t^2} \quad (8.4)$$

This is the equation used throughout the nonlinear optics where the nonlinear polarization  $\mathbf{P}^{NL}$  acts as a source term to couple the input waves to generate new frequencies. In the absence of source term, equation 8.4 admits solution of the form of free waves propagating with velocity

$c/n$  where the linear refractive index  $n$  satisfies the relation  $n^2 = \epsilon/\epsilon_0 = (1 + \chi)$ . For dispersive medium, the terms  $\mathbf{E}$ ,  $\mathbf{D}$  and  $\mathbf{P}^{NL}$  also become frequency dependent and each frequency component of the field must be considered separately satisfying the wave equation 8.4.

### 8.2.3 Second harmonic and sum frequency generation

The plane monochromatic waves of frequencies  $\omega_1$  and  $\omega_2$ , interacting in a nonlinear crystal, generate electromagnetic radiation at the sum frequency  $\omega_3 = \omega_1 + \omega_2$  (provided phase matching condition is satisfied). The electric fields at frequencies  $\omega_1$  and  $\omega_2$  generate polarization at  $\omega_3$  which acts as a source for generation of an electromagnetic wave at  $\omega_3$ . The electric fields associated with each frequency components i.e.  $\mathbf{E}_1$ ,  $\mathbf{E}_2$  &  $\mathbf{E}_3$ , satisfy the equation 8.4. As the beams propagate inside the interacting medium (along z-direction), the electric field amplitudes,  $E_1$  &  $E_2$  start depleting and  $E_3$  starts growing due to nonlinear polarization  $\mathbf{P}_3^{NL}$  with amplitude  $P_3^{NL} (\propto d_{eff}.E_1.E_2)$ . In the limiting case of low conversion efficiency, the fundamental beams are not significantly depleted i.e.  $\partial E_1/\partial z = \partial E_2/\partial z = 0$ . This is valid when intensity of the fundamental pump is not very high and/or the length of the interacting nonlinear medium ( $L$ ) is small. Then, the pump field amplitudes  $E_1(z)$  and  $E_2(z)$  deplete very slowly/slightly with  $z$  over  $L_{NL}$  i.e.  $E_1(z).E_2(z) \approx E_1.E_2$ . However, the time averaged amplitude  $E_3$  or the intensity  $I_3$  in SFG grows with increase of  $z$  [ $I_3(z) = 2n_3\epsilon_0c |E_3(z)|^2$ ] and at the exit plane, these are obtained by integrating the corresponding amplitude equation from  $z = 0$  to  $z = L$  as [188, 235],

$$E_3(L) = \frac{2id_{eff}.\omega_3^2 E_1 E_2}{k_3 c^2} \int_0^L e^{i\Delta k z} dz = \frac{2id_{eff}.\omega_3^2 E_1 E_2}{k_3 c^2} \left( \frac{e^{i\Delta k L} - 1}{i\Delta k} \right) \quad (8.5)$$

$$I_3(L) = I_{SFG} = 8 \left( \frac{\mu_0}{\epsilon_0} \right)^{3/2} \frac{\omega_3^2 d_{eff}^2 L^2 I_1 I_2}{n_1 n_2 n_3} \text{sinc}^2 \left( \frac{\Delta k L}{2} \right) \quad (8.6)$$

where  $\text{sinc}^2 (\Delta k L/2) = [\sin^2 (\Delta k L/2)] / (\Delta k L/2)^2$  and  $\Delta k = k_3 - (k_1 + k_2)$  is the wave vector mismatch or phase mismatch factor such that  $k_i = n_i \omega_i / c$  &  $n_i$  is the refractive index of the nonlinear medium for wave of  $i^{th}$  frequency ( $i = 1, 2, 3$ ). For SHG process, substituting  $\omega_1 =$

$\omega_2 = \omega$  and  $\omega_3 = 2\omega$ , the expression for SHG intensity ( $I_{SHG}$ ) and conversion efficiency ( $\eta_{SHG}$ ) are obtained as [235],

$$I_{SHG} = I_{2\omega} = 8 \left( \frac{\mu_o}{\varepsilon_o} \right)^{3/2} \frac{\omega^2 d_{eff}^2 L^2 I_\omega^2}{n_\omega^2 n_{2\omega}} \text{sinc}^2 \left( \frac{\Delta k L}{2} \right) \quad (8.7)$$

$$\eta_{SHG} = \eta_{2\omega} = 8 \left( \frac{\mu_o}{\varepsilon_o} \right)^{3/2} \frac{\omega^2 d_{eff}^2 L^2 I_\omega}{n_\omega^2 n_{2\omega}} \text{sinc}^2 \left( \frac{\Delta k L}{2} \right) \quad (8.8)$$

where  $I_\omega = P_\omega/A$  is the pump power per unit beam cross section area and  $\Delta k = k_{2\omega} - 2k_\omega$  is the wave vector mismatch or phase mismatch between the second harmonic & fundamental waves.

It is clear from the above equations that the SHG/SFG process is strongly dependent on the phase mismatch expressed by the  $\text{sinc}^2$  function. The harmonic power is maximum when  $\Delta k.L = 0$ , i.e. at the exact phase matching condition. For  $\Delta k.L \neq 0$ , the efficiency of the process is severely reduced. For fixed  $\Delta k$ ,  $I_{2\omega}$  increases with  $L$  along the crystal length, attains a maximum value at a distance from the face of incidence  $L_c = \pi/\Delta k = \lambda/[4(n_{2\omega} - n_\omega)]$  (called phase coherence length) and then falls to zero with a period of  $\Delta k L/2 = \pi$ . Therefore,  $L_c$  is the maximum crystal length that is useful for producing the second harmonic power which, under ordinary circumstances, is of the order of several 10s of  $\mu\text{m}$  [188, 235]. These low values of crystal length lead to very low SHG conversion efficiency i.e.  $\eta_{2\omega} \sim 10^{-4} - 10^{-8} \%$ . So, irrespective of choice on  $I_{2\omega}$  and  $L$ ,  $I_{2\omega} \rightarrow 0$  if  $(\Delta k L/2) \geq \pi$ . Thus for efficient SHG/SFG, it is very important that the phase matching condition is very closely satisfied i.e.  $\Delta k = 0$ . The phase matching processes for efficient frequency conversion in a nonlinear crystal are described in next section.

#### 8.2.4 Phase matching for SHG/SFG process

Phase matching conditions imply that the refractive indices of the nonlinear crystal at the involved frequencies should match e.g.  $n_{2\omega} = n_\omega$  for SHG ( $\Delta k = 0 \Rightarrow k_{2\omega} = 2k_\omega \Rightarrow n_{2\omega} = n_\omega$ ) and  $n_3, \omega_3 = n_1, \omega_1 + n_2, \omega_2$  for SFG ( $\Delta k = 0 \Rightarrow k_{\omega_3} = k_{\omega_1} + k_{\omega_2} \Rightarrow n_3, \omega_3 = n_1, \omega_1 + n_2, \omega_2$ ).

For normal dispersive materials, it is not possible to satisfy these refractive index matching conditions as  $n$  scales with  $\omega$ . However, when a ray enters an anisotropic/birefringent medium, it splits up into two rays: ordinary ray (o-ray) and extraordinary ray (e-ray). These rays propagate along different directions and are orthogonally polarized. The refractive indices of these two rays are different ( $n_e \neq n_o$ ), except along optic/c-axis of the crystal. The o-ray is characterized by the same velocity for all directions of propagation and hence gives rise to spherical wavefront; whereas the e-ray has different velocities along different propagation direction and hence give rise to non-spherical wavefront. The dependence of refractive index of e-wave, at a given frequency  $\omega$ , on the angle  $\theta$  between the propagation direction and the optic axis in a uniaxial crystal is given by [235],

$$\frac{1}{n_e^2(\theta)} = \frac{\cos^2\theta}{n_o^2} + \frac{\sin^2\theta}{n_e^2} \quad (8.9)$$

The phase matching/refractive index matching condition in an anisotropic crystal is satisfied by taking the two waves of different types (different  $n_o$  and  $n_e$ ). For a -ve uniaxial crystal ( $n_e < n_o$ ), it is possible to find a direction along which  $n_{o(\omega)} = n_{e(2\omega)}$ . Similarly for a +ve uniaxial crystal ( $n_e > n_o$ ) the direction would correspond to that along which  $n_{e(\omega)} = n_{o(2\omega)}$ . The angle at which this condition is satisfied is called phase matching angle,  $\theta_m$ . This situation is typically illustrated in Fig. 8.1 for a -ve uniaxial crystal such as  $\beta$ -BBO. For a -ve uniaxial crystal (o o  $\rightarrow$  e type interaction),  $\theta_m$  is given by [188, 235],

$$\theta_m = \cos^{-1} \left[ \frac{\left[ \frac{n_{o(2\omega)}}{n_{o(\omega)}} \right] \sqrt{\frac{[n_{e(2\omega)}]^2 - [n_{o(\omega)}]^2}{[n_{e(2\omega)}]^2 - [n_{o(2\omega)}]^2}}}{\left[ \frac{n_{o(2\omega)}}{n_{o(\omega)}} \right]} \right] \quad (8.10)$$

Depending on the types of waves (o-wave or e-wave) involved in SHG/SFG process, the phase matching is classified as type-I or type-II. Interactions of kind o o  $\rightarrow$  e or e e  $\rightarrow$  o are termed as type-I phase matching whereas interactions of kind e o  $\rightarrow$  o, o e  $\rightarrow$  o, e o  $\rightarrow$  e, o e  $\rightarrow$  e are termed as type-II phase matching. Similarly depending on the phase matching angle

employed, it is termed as critical phase matching ( $\theta_m \neq 90^\circ$ ) or non-critical phase matching ( $\theta_m = 90^\circ$ ). Depending on the techniques used to attain the phase matching condition, it is also categorized as angle phase matching (angle tuned) and temperature phase matching (temperature tuned). In the present thesis work, type-I critically phase matched, negative uniaxial BBO crystal is used to study SHG/SFG of Cu-HBr laser radiations.

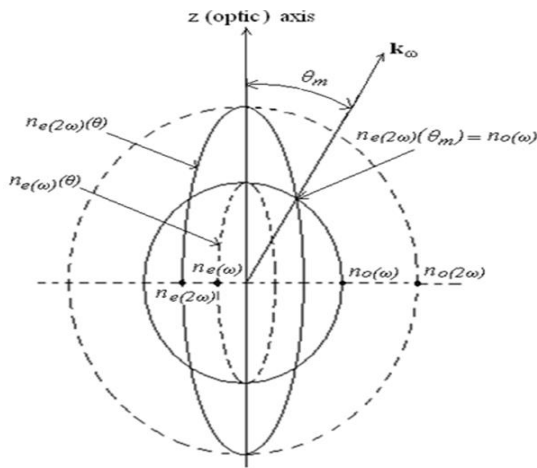


Fig. 8.1 Index surfaces for type-I critically phase matched -ve uniaxial crystal [236]

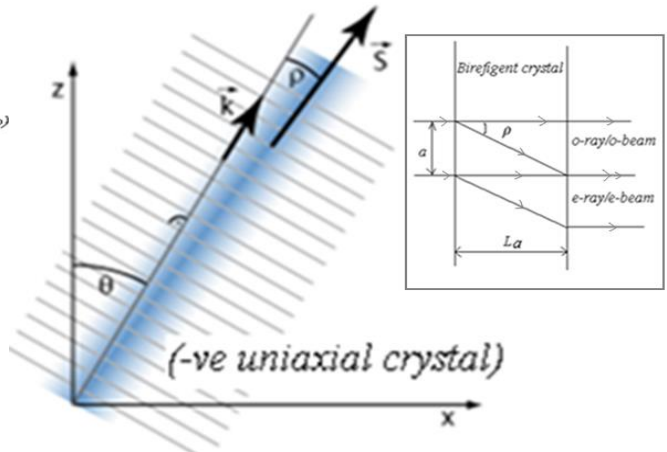


Fig. 8.2 Spatial beam walk-off in a type-I critically phase matched -ve uniaxial crystal [188]

### 8.2.5 Beam walk-off

In an anisotropic/birefringent crystal, the direction of energy flow (defined by Poynting vector  $\mathbf{S}$ ) and that of the wave vector/phase vector  $\mathbf{k}$  (defined as normal to wavefront) may not remain same throughout the crystal length, finally getting separated after certain distance (Fig. 8.2). This phenomenon is called *spatial or birefringent or Poynting vector walk-off* and is associated with some finite angle  $\rho$  (called *walk-off angle*) between  $\mathbf{S}$  and  $\mathbf{k}$ . As the fundamental and the second harmonic waves propagate along the anisotropic crystal, the power generated at the second harmonic gets separated from the fundamental, due to the effect of “spatial walk-off”. For a -ve uniaxial type-I phase matched crystal [ $n_{o(\omega)} = n_{e(2\omega)}(\theta_m)$ ], the spatial walk-off angle between the  $\mathbf{S}$  and  $\mathbf{k}$  of the e-wave (at frequency  $2\omega$ ) is given by [188],

$$\tan \rho = \frac{[n_{e(2\omega)}(\theta_m)]^2}{2} \left[ \frac{1}{[n_{e(2\omega)}]^2} - \frac{1}{[n_{o(2\omega)}]^2} \right] \sin 2\theta_m \quad (8.11)$$

The walk-off effect limits the effective length over which harmonic generation takes place. In effect, the conversion efficiency gets limited and the spatial profile of product beam is broadened and the beam quality is degraded. If the fundamental beam has transverse dimension  $a$ , then the fundamental and second harmonic beams get separated inside the nonlinear crystal after a distance  $L_a$ , called aperture length, and is given approximately as [188],

$$L_a = \frac{a}{\tan \rho} \approx \frac{a}{\rho} \quad (8.12)$$

The spatial walk-off occurs only for e-ray as its refractive index  $n_e$  and the phase velocity are dependent on the angle of propagation with respect to optic axis. A beam with ordinary polarization (where the refractive index is not dependent on the propagation angle) does not experience walk-off. It may be noted from equation 8.11 that, for noncritical phase matching ( $\theta_m = 90^\circ$ ), there is no walk-off ( $\rho = 0$ ); except for the finite beam divergence. This in turn leads to less constraint on the beam size and length of the nonlinear crystal. However, non-critical phase matching requires operation of the crystal at a temperature which is not close to room temperature. The magnitude of the walk-off angle in typical cases ranges between a few mrad and some tens of mrad [236]. The walk-off effect plays a crucial role in deciding the SHG/SFG performance in type-I critically phase matched, negative uniaxial BBO crystal, as investigated in the present thesis.

### **8.3 Issues in high average power high pulse repetition rate SHG/SFG**

For low average power and low repetition rate SHG/SFG process, the high conversion efficiency can be obtained by using appropriate fundamental laser power with proper phase matching conditions. However, for high average power, high repetition rate SHG/SFG, there are key limiting issues related with phase mismatch due thermal effects, large fundamental beam divergence, pointing instability and line-width [237]. The thermal effects are induced

primarily by optical absorption in the crystal. The nonlinear process for visible to UV frequency conversion is dominated by UV absorption. This result in thermal instability, hampering the establishment of phase matching condition except for intermittent short periods of time and the thermal gradient, which prevents simultaneous phase matching in all part of the crystal. Large beam divergence, pointing instability and line-width of high average power, high repetition rate laser systems are due to multi-transverse and axial mode operation. In angle tuned phase matching process, a small deviation from phase matching angle leads to reduction in SHG/SFG conversion efficiency. The phase mismatch factors, i.e. thermal, angular and spectral taken together, lead to large reduction in the conversion efficiency. In addition, the effect of pump beam depletion as well as walk-off effect need to be taken into account for high peak SHG/SFG conversion efficiency (>15-20%) of high power laser pulses.

The wave vector mismatch can be expressed as a function of crystal temperature  $T$ , wavelength of the interacting waves  $\lambda$  and deviation  $\theta$  from phase matching angle. The dependence of  $\Delta k$  of these parameters in the first order approximation is given as [237],

$$\Delta k(\theta, T, \lambda) \simeq \Delta k(0) + \frac{\partial(\Delta k)}{\partial\theta} \Delta\theta + \frac{\partial(\Delta k)}{\partial T} \Delta T + \frac{\partial(\Delta k)}{\partial\lambda} \Delta\lambda \quad (8.13)$$

where  $\Delta k(0)$  is the phase mismatch which equals to zero for exact phase matching. The partial derivative w. r. t. one of the arguments are taken under condition that the other two arguments are constant. In the following sub-sections the effect of these parameters on SHG/SFG processes are discussed.

### ***8.3.1 Effect of temperature***

Deviation of the crystal temperature from the phase matching condition ( $\Delta T = T - T_m$ ) decrease efficiency of the nonlinear frequency conversion process as a *sinc*<sup>2</sup> function (Fig. 8.3). To determine the extent of allowed variation of temperature on the SHG/SFG process, the wave vector mismatch  $\Delta k(T)$  is expanded in a Taylor series about the phase matching temperature ( $T_m$ ) and taking the first order approximation as [188, 237],

$$\Delta k(T) \approx \left[ \frac{\partial(\Delta k)}{\partial T} \right]_{T_m} \cdot \Delta T \quad (8.14)$$

The temperature range by which the SHG/SFG intensity reduces to half of its maximum value is called temperature bandwidth ( $\Delta T_{BW}$ ) which is related as  $\Delta k_{BW} \approx \left[ \frac{\partial(\Delta k)}{\partial T} \right]_{T_m} \cdot \Delta T_{BW} \Rightarrow \frac{0.886 \pi}{L} \approx \left[ \frac{\partial(\Delta k)}{\partial T} \right]_{T_m} \cdot \Delta T_{BW} \Rightarrow \Delta T_{BW} \approx \left( \frac{0.886 \pi}{L} \right) / \left[ \frac{\partial(\Delta k)}{\partial T} \right]_{T_m}$ . So the full temperature bandwidth, also called *acceptance temperature* ( $\Delta T_{acc}$ ) of the crystal, which is twice of the above bandwidth, for critical phase matching condition is given as [188],

$$\Delta T_{acc} = 1.772 \frac{\pi}{L} \left[ \frac{\partial(\Delta k)}{\partial T} \right]_{T_m}^{-1} \quad (8.15)$$

For a type-I phase matched –ve uniaxial crystal (o o → e), the acceptance temperature is [188],

$$\Delta T_{acc} = \frac{0.44 \lambda_{\omega} / L}{\partial [n_e(2\omega) - n_o(\omega)] / \partial T} \quad (8.16)$$

For high power SHG/SFG applications, a crystal with large value of  $\Delta T_{acc}$  is desirable.

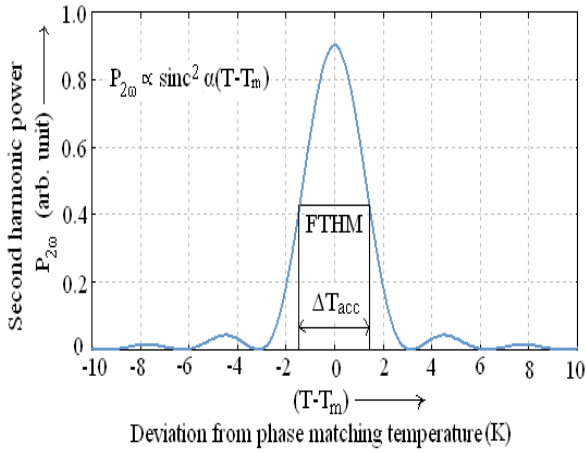


Fig. 8.3 Variation of  $P_{2\omega}$  with deviation from phase matching temperature [188]

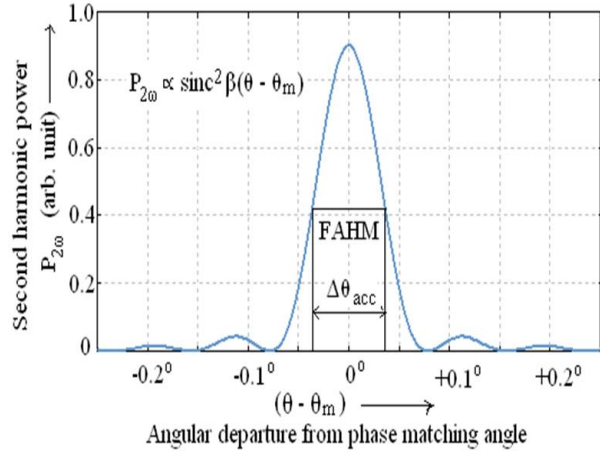


Fig. 8.4 Variation of  $P_{2\omega}$  with angular deviation from phase matching angle [188]

### 8.3.2 Effect of laser beam divergence and line-width

High average power lasers have many transverse modes which give rise to a beam of many times diffraction limited divergence; hence the resulting SHG/SFG efficiency is lower than that of the single mode laser of same laser power. In addition, the higher divergence

angles of the high power, high PRR laser beams lead to inefficient coupling of the fundamental to second harmonic wave. This fact, along with a larger power density safety margin to avoid the crystal damage, limits the SHG/SFG conversion efficiency of multimode lasers. For small angular deviation about phase matching direction ( $\theta_m$ ), the efficiency of conversion will decrease as  $\text{sinc}^2$  function and the phase velocity mismatch due to beam divergence/angular deviation  $\theta$  is obtained by first order approximation of Taylor series expansion of  $\Delta k$  as,

$$\Delta k \simeq [\partial(\Delta k)/\partial\theta]_{\theta_m} \cdot \Delta\theta \quad (8.17)$$

For critical phase matching, the full angle band width, also called *acceptance angle of the crystal*, is given as [188],

$$\Delta\theta_{\text{acc}} = 1.772 \frac{\pi}{L} \left[ \frac{\partial(\Delta k)}{\partial\theta} \right]_{\theta_m}^{-1} \quad (8.18)$$

The derivative  $[\frac{\partial(\Delta k)}{\partial\theta}]^{-1}$  used in the above equation depends on the dispersion of the refractive indices and on the type of phase matching. So for a given crystal, the acceptance angle is different for type of phase matching (type-I or type-II and critical or noncritical) and interaction (SHG or SFG) employed. For a typical case of type-I phase matched –ve uniaxial crystal (o o  $\rightarrow$  e interactions), the SHG acceptance angle is deduced to be [188],

$$\Delta\theta_{\text{acc}} = \frac{0.44 [\lambda_{\omega} \cdot n_o(\omega)/L]}{[n_o(2\omega) - n_e(2\omega)] \sin 2\theta_m} \quad (8.19)$$

The angular deviation,  $\Delta\theta$ , can also be interpreted as the beam divergence of the fundamental laser beam at which the conversion efficiency drops to one half of its peak value. When second harmonic power is plotted as a function of polar angle  $\theta$  for a uniaxial crystal, the acceptance angle is equal to the full width of the curve at 0.405 of maximum (Fig. 8.4). For angle phase matched crystal the acceptance angle is typically of the order of one mrad. For non-critical phase matched SHG crystals, the acceptance angles in the polar direction are of the order of tens of *mrad*. Uniaxial crystals have rotational symmetry around z and the acceptance angle is therefore very large in the azimuthal direction. This fact may be utilized to increase

the SHG efficiency by cylindrically focusing a beam to a line thereby managing the radiation power density at the crystal while not exceeding the acceptance angle. This approach is used in the present thesis with BBO crystal as presented in the next chapter.

Deviations of the frequency from the phase matching frequency ( $\Delta\nu = \nu - \nu_m$ ) also causes the efficiency of the frequency conversion process to decrease in a similar manner as that of the temperature and angle. Proceeding with similar manner as above, the spectral acceptance width of a nonlinear crystal is given as [188],

$$\Delta\lambda_{acc} = 1.772 \frac{\pi}{L} \left[ \frac{\partial(\Delta k)}{\partial\lambda} \right]_{\lambda_m}^{-1} \quad (8.20)$$

For a typical case of type-I phase matched –ve uniaxial crystal (o o  $\rightarrow$  e), the *acceptance spectral width* is given as,

$$\Delta\lambda_{acc} = \frac{0.44 (\lambda_\omega/L)}{\left[ \frac{\partial n_o(\omega)}{\partial\lambda_\omega} - \frac{1}{2} \frac{\partial n_e(2\omega)(\theta)}{\partial\lambda_{2\omega}} \right]} \quad (8.21)$$

It is desired to have a large value of  $\Delta\lambda_{acc}$ , particularly while planning SHG/SFG of lasers of very high bandwidth e.g. Nd-glass and dye lasers. For the Cu-HBrL, being based on atomic transitions, the line-width is relatively narrow in the range of 5-10 GHz as studied in chapter 6 of this thesis. Here, the requirement on crystal's spectral acceptance bandwidth is less stringent.

### 8.3.3 Pump beam depletion

The approximation of negligible pump beam depletion is valid only for small conversion efficiency of typically <10% [188, 235]. For large input intensity or large crystal length, the depletion of pump beam must be taken into account. Most modern laser systems generate high peak powers with good beam quality and incorporate high optical quality nonlinear crystals. These lead to higher conversion efficiencies typically 20 to 50% or more. In this case, depletion of the fundamental beam has to be considered to adequately describe and explain the experimental results. At perfect phase matching condition ( $\Delta k = 0$ ), the transfer

of energy from the input wave to the second harmonic is maximized and the conversion efficiency approaches unity. Fig. 8.5 shows the variation of depleted fundamental and second harmonic power for perfect phase matching condition ( $\Delta k = 0$ ), which are connected by expressions given by [188, 235],

$$P_{\omega}(L) = P_{\omega}(0) \operatorname{sech}^2(L/L_{NL}) \quad (8.22)$$

$$P_{2\omega}(L) = P_{\omega}(0) \tanh^2(L/L_{NL}) \quad (8.23)$$

where,

$$L_{NL} = \frac{1}{\sqrt{[8(\frac{\mu_0}{\epsilon_0})^{3/2} \omega^2 d_{eff}^2 / (n_{\omega}^2 n_{2\omega})] L^2 I_{\omega}}} \quad (8.24)$$

defines the characteristic length scale of nonlinear interaction. With perfectly phase matched SHG,  $L_{NL}$  is the length of nonlinear crystal that would produce conversion efficiency  $\sim 58\%$ .

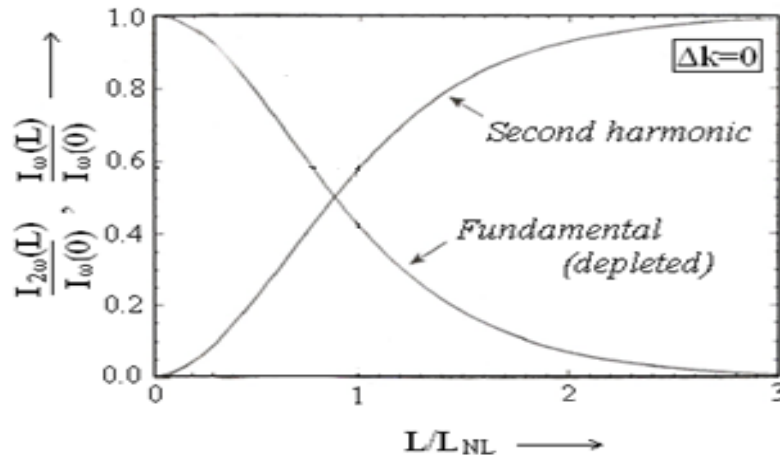


Fig. 8.5 Variation of SHG and depleted-fundamental power with interaction length in a nonlinear crystal [188]

It can be seen that  $L_{NL}$  is inversely proportional to pump intensity and  $[d_{eff}/(n_{\omega}^2 \cdot n_{2\omega})]^{1/2}$  which means the stronger the nonlinearity, shorter will be  $L_{NL}$ . It can be seen from Fig. 8.5 that as the fundamental intensity is depleted, it asymptotically approaches to zero, while the SHG efficiency approaches one. The reason for this behavior is that the fundamental intensity drives the nonlinear polarization producing SHG; as the fundamental is depleted, it becomes less effective in driving the nonlinearity. Therefore, when both the fundamental wave depletion and dephasing are considered, SHG efficiency rises with increasing drive until an optimum value

is reached. Back-conversion is the reason for the reduction of the conversion efficiency after a peak value has been attained. When the phases are not perfectly matched, power is cycled between the fundamental and harmonic waves. Thus focusing the pump beam below the optimum spot size does not lead to a further increase in conversion efficiency. Focusing the beam into the nonlinear crystal increases intensity as well as beam divergence and therefore dephasing. Hence, beyond a point, the adverse effect of dephasing on the efficiency dominates over any benefits gained from a further increase in fundamental intensity.

## **8.4 Review of results on SHG & SFG of copper lasers**

### **8.4.1 Nonlinear crystals**

The SHG and SFG of copper lasers lead to generation of coherent UV source at wavelengths of 255.3 nm, 289.1 nm & 271.2 nm with high PRR (5-20 kHz) and multi-watt average power. For this purpose, an ideal crystal for high average power SHG/SFG UV generation is one in which the frequency conversion occurs with high efficiency even when the average power level of the incident fundamental radiation is high. The ideal crystal must have reasonable birefringence (to permit phase matching at the involved wavelengths/interactions), high nonlinear coefficient ( $d_{\text{eff.}}$ ), high damage threshold (surface & bulk), low optical absorption at the involved wavelengths (visible & UV), large size with optical uniformity, large angular, spectral & temperature bandwidth, high thermal conductivity, low walk-off angle, low cost, non-hygroscopic and ease of fabrication. All these characteristics, at their best values, are seldom available in a single crystal and hence compromises need to be made. The choice of nonlinear crystal becomes even more restrictive for high power visible to UV conversion due to absorption and phase matching issues. For the efficient visible to UV SHG/SFG process of copper lasers, most of the crystals, belong to the borate family.

In the beginning, ADP (Ammonium Dihydrogen Phosphate:  $\text{NH}_4\text{H}_2\text{PO}_4$ ) and KDP (Potassium Dihydrogen Phosphate:  $\text{KH}_2\text{PO}_4$ ) were used as nonlinear frequency converter of

copper laser radiations [221, 239]. An improved variant of KDP crystal i.e. DKDP (Deuterated KDP:  $\text{KD}_2\text{PO}_4$ ) have also been used [230, 241]. The KDP & DKDP crystals provide phase matching for SHG of only yellow component and SFG of copper laser. However the borate crystals specifically BBO (Beta Barium Borate:  $\beta\text{-BaB}_2\text{O}_4$ ) as well as the newly emerged CLBO (Cesium Lithium Borate:  $\text{CsLiB}_6\text{O}_{10}$ ) provide efficient phase matching for SHG/SFG of both the green and yellow wavelengths. Multi-Watt average power UV (SHG/SFG) radiations have been realised with BBO and CLBO crystals [224-227, 229-234]. The BBO crystals are most successful for the UV generation from copper lasers, whereas the highest UV average power from copper laser frequency conversion has been obtained using CLBO crystal. The other well developed borate crystal, LBO, has good UV transmission, but its inadequate birefringence in the visible to UV region, limits phase matching for SHG/SFG of copper lasers.

A BBO is a highly efficient –ve uniaxial crystal with good transmission from 190 nm to 3600 nm and wide SHG/SFG phase matching wavelength range of 190-1750 nm. It has larger (~4 times)  $d_{\text{eff}}$  coefficient, larger (~10 times) figure of merit ( $d_{\text{eff}}^2/n^3$ ) as well as higher bulk damage threshold (~10  $\text{GW}/\text{cm}^2$ ), as compared to KDP. It is also less susceptible to UV absorption (~5%/cm) [236, 237]. The type-I phase matching angle of BBO for the nonlinear frequency conversion are  $50.6^\circ$  (SHG of green),  $46.3^\circ$  (SFG) &  $42.5^\circ$  (SHG of yellow). For 510.6 nm to 255.3 nm conversion, it has large nonlinear coefficient ( $d_{\text{eff}}$ ) ~ 1.7 pm/V, narrow acceptance angle ( $\Delta\theta_{\text{acc}}$ ) ~ 0.38 mrad-cm, large walk-off angle ( $\rho$ ) ~  $4.8^\circ$ , small acceptance temperature band width ( $\Delta T_{\text{acc}}$ ) ~ 10  $^\circ\text{C}\text{-cm}$ , large spectral acceptance bandwidth ( $\Delta\lambda_{\text{acc}}$ ) ~ 1 nm-cm and small phase matching temperature coefficient ( $d\theta_m/dT$ ) ~ 0.044 mrad/ $^\circ\text{C}$  [229]. Low peak power of copper lasers (10-100 kW) demands the fundamental beam to be focussed for efficient frequency conversion. However the BBO's narrow acceptance angle and small surface damage threshold (~1  $\text{GW}/\text{cm}^2$ ) limit the maximum pump intensity to be used. On the contrary, CLBO (type-I SHG green,  $\theta_m = 68^\circ$ ) has higher  $\Delta\theta_{\text{acc}}$  of ~1.11 mrad-cm, lower walk-

off angle of  $\sim 1.6^\circ$  and higher  $d\theta_m/dT$  of  $\sim 0.167$  mrad/ $^\circ\text{C}$ , higher  $\Delta T_{acc}$  of  $\sim 19$   $^\circ\text{C}$  and higher damage threshold than BBO [229]. These figures are particularly suitable for high power, high PRR SHG/SFG of copper lasers, even though it has lower nonlinear coefficient ( $d_{eff.} \sim 0.9$  pm/V). The highest average UV power about 15 W (255.3 nm) from SHG of green wavelength of copper laser, at 28% conversion efficiency, has been at 12 kHz PRR [229]. However, CLBO is highly hygroscopic and degrades very quickly, therefore its usage and choice is limited. In the present thesis, BBO is the crystal of choice.

#### **8.4.2 Pump focusing geometries – Spherical spot focusing & cylindrical line focusing**

The simplest pump geometry for SHG/SFG of copper lasers employs spherical focusing elements to produce circular focused pump spot at the nonlinear crystal (BBO). In order to achieve high power densities at the crystal, well above the threshold for SHG/SFG conversion (10-100 MW/cm<sup>2</sup>), focusing of high quality laser beam with short focal length lens is needed. However, the small and high intensity pump spot leads to reduced interaction length due to beam walk-off within the crystal and surface damage [237]. Attempt to use long focal length lens reduces the conversion efficiency due to reduced fundamental beam peak intensity. Nevertheless, with spherical focusing geometry, moderate UV powers and conversion efficiencies have been obtained in frequency conversion of copper laser radiations. For example, with spherical focusing of high quality ( $\sim 3$  DL) CVL beam, maximum average UV powers of 460 mW, 300 mW & 465 mW have been obtained at 255.3 nm, 289.1 nm & 271.2 nm with conversion efficiencies of 9.6%, 5.5% & 6.4% respectively at 7 kHz PRR [238]. In a Cu-HBrL, 1.3 W average power UV (255.3 nm) at 17 kHz PRR with 10.3% conversion efficiency has been generated using spherical focusing geometry, with high quality pump beam ( $\sim 1.4$  DL) [232].

It is clear that with the spherical focusing, the nonlinear conversion efficiency of copper lasers are limited to about 10%, in addition to detrimental effects of beam walk-off, non-

uniform thermal detuning & crystal damage. These limiting issues have been effectively addressed utilizing the cylindrical line focusing pump beam geometry based on the fact that in an uni-axial crystal, like BBO, the acceptance angle in azimuthal direction is large. For a typical crystal length of 1 cm and phase matching angle of  $\theta_m \approx 45^\circ$ , the acceptance angle in non-critical plane is of the order of several tens of mrad as compared to much less than one mrad in critical plane [227]. Utilising this fact, a cylindrical lens has been used to line focus the pump beam in the crystal. The beam has been focussed in noncritical plane whereas it remained collimated in the critical plane. This way the whole of the pump beam has been put within the angular acceptance range of the crystal. The cylindrical focusing also ensures longer interaction length before the beams walk-off. With this arrangement, the fundamental beam intensity becomes proportional to the fundamental beam divergence rather than its square as in the case of spherical focusing [239]. This reduces the crystal heating effect as well as chances of crystal damage. These factors, combined, has led to higher nonlinear conversion efficiencies. The maximum average conversion efficiency of 34% and peak conversion efficiency of 48-49% (instantaneous) have been demonstrated from CVLs with this cylindrical line focussing geometry [220, 227]. Also, the conversion efficiencies of 20-30%, with watt-level UV powers, are routinely available from CVLs with the line focussing geometries. Therefore, the line focussing geometry is the preferred choice for SHG/SFG conversion of copper laser radiations as also pursued in the present work.

#### **8.4.3 SHG & SFG at PRR ~5-10 kHz (conventional CVL)**

The first report of generation UV radiation from copper laser was by Isaev et. al. with spherical focussing geometry [221]. They used non-critical phase matched ADP crystal at -32 °C for SHG of green radiation of CVL and obtained about 5 mW average power at 8.3 kHz PRR and 1% conversion efficiency. The conversion efficiency degraded sharply, with temperature away from the phase matching. This was attributed to the increased thermal

dephasing as a consequence of non-uniform heating and thermal lensing. The SFG UV (271.2 nm) of average output power of 600 mW and SHG (from yellow) UV (289.1 nm) of average power of 120 mW, were generated by Polunin et. al. [240], from conventional CVL, using a KDP crystal with conversion efficiency of ~ 5%. The SFG UV output power of 750 mW with improved conversion efficiency of about 12%, was obtained using DKDP crystal [241]. This enhanced efficiency was attributed to the increased transmission at SFG wavelength, higher  $d_{eff}$  coefficient and low beam walk-off angle of DKDP over KDP and ADP. In addition, beam quality of the fundamental beam played a crucial role for increasing the SFG efficiency from 3.3% to 12%., with increase of magnification of unstable resonator from 5 to 200.

Using the then newly developed BBO crystal, UV (255.3 nm) average power of ~35 mW at 0.7% conversion efficiency was initially reported by Zhang et. al. [242]. This was later upgraded by Kuroda et al. to 230 mW at 9 % conversion efficiency, by use of high quality BBO crystal as well as high beam quality of CVL [243]. Coutts et. al. used high quality 7 kHz PRR CVL beam (~3 DL) as well as high quality focusing optics with BBO and generated maximum average powers of 460 mW, 300 mW & 465 mW at 255.3 nm, 289.1 nm & 271.2 nm with conversion efficiencies of 9.6%, 5.5% & 6.4% respectively [238]. The first multi-watt UV power of 2 W (255. 3 nm) at 7% conversion efficiency was demonstrated by Freearde and Naylor [244]. Molander et. al. used injection controlled CVL oscillator to produce 11.8 W high quality green output and obtained 2.1 W UV (255. 3 nm) average power at 18% SH conversion efficiency [222]. The UV output power was limited by thermal stresses, thermal detuning as well as crystal face damage due to high intensity with spherical focusing. With diffraction limited beam obtained using self-filtering unstable resonator (SFUR) CVL, the 255.3 nm UV radiation of average power ~ 315 mW was produced with average and instantaneous conversion efficiency of 21% and 30% respectively [245].

With use of cylindrical line focusing instead of conventional spherical focusing, a boost

in efficiency in nonlinear frequency conversion of CVL was realized by Coutts et. al. in BBO crystal coupled with improved CVL beam quality [223]. With a small scale CVL, operating at 4 kHz PRR with UR M=51, UV average output powers of 1.3 W, 0.89 W & 0.99 W were obtained at 255.3 nm, 289.1 nm & 271.2 nm, with respective conversion efficiencies of 24%, 28% & 12% respectively [223]. The UV average output powers were further scaled to 1.75 W at 255.3 nm, 1.5 W at 271.2 nm & 1.2 W at 289.1 nm using line focus geometry [227]. The average conversion efficiency of SHG of green wavelength was 34% with peak value at 48%. The same group also developed the CVL MOPA system of near DL output beam (25 W) and produced 3.6 W at 255.3 nm, 2.0 W at 289.1 nm & 3.8 W 271.2 nm with respective conversion efficiencies of 20%, 22% and 14% [224]. Thermal effects in the BBO crystal limited the UV output and reduced the conversion efficiencies. Trickett et. al. obtained 3.15 W UV at 255.3 nm at 26% conversion efficiency with 9 kHz PRR CVL (12 W green) [246]. About 1.4 W UV was generated, with a 2.5 W fundamental beam from a small SFUR CVL as oscillator and 20 mm CVL as an amplifier [247]. With generalized diffraction filtered resonator (GDFR) CVL MOPA system, 2.3 W average UV (255.3 nm) output power with conversion efficiency of 22 % was generated at the fundamental input power of 11.8 W [220]. With GDFR CVL oscillator alone, the peak and average SH conversion efficiency of 49 % & 30% was demonstrated [220] with 660 mW UV power (255.3 nm) at average pump power of 2.1 W.

The UV (255.3 nm) average power of 9.0 W was obtained by Molander et. al. [225] using two 5 mm long BBO crystals in alternative Z configuration and line focusing geometries. The CVL beam (510 .6 nm) was of average power 113 W obtained from injection seeded oscillator and power amplifier. The SH conversion efficiency was only 8 %, limited due to reflection losses and thermal effects in the crystal. Batenin et. al. [230], used a two-pass CVL amplifier beam of 25 W average power at 10 kHz PRR to study the second harmonic process with BBO and DKDP crystals. The SHG of both the G & Y radiations well as their SFG were

carried out. The SFG conversion was studied with both BBO & DKDP, whereas the SHG conversions were studied with only BBO. The SFG average UV power was 3.6 W with 24% conversion efficiency for BBO crystal and 2.1 W with 14% conversion efficiency for the DKDP crystal. The SHG average power for the green was 2.1 W (27% conv. efficiency) and 3.4 W (44% conv. efficiency). In BBO crystal, the conversion efficiencies of 28%, 23% & 17.5% at 255.3 nm, 271.2 nm & 289.1 nm have been reported from single CVL system using tunable acoustic filter [248]. In this case, the different CVL radiations and amplitudes are controlled selectively using tunable acoustic filter. Recently, the role of pulse to pulse variation of divergence, pointing and amplitude of CVL radiations on SHG/SFG was studied [207]. At PRR of 5.5 kHz with UR M=100 CVL oscillator, UV average powers of 0.94 W (255.3 nm), 0.61 W (289.1 nm) & 1.2 W (271.2 nm) were obtained at respective conversion efficiencies of 16.7%, 14.5% & 12.4%. At the same fundamental input power (2.7), the conversion efficiency of yellow was better than that of green (12.7% vs. 11%) and the reason was attributed to better far-field stability characteristics of the former radiation.

#### **8.4.4 SHG & SFG at PRR ~ 10-20 kHz (Cu-HBrL, CuBrL & KE-CVL)**

The SHG/SFG UV generation from conventional CVL radiations is restricted to typically 5-10 kHz PRR and is well studied as outlined in the previous section. Higher PRR coherent pulsed UV radiations (250-300 nm) are always desirable for many scientific and industrial applications. The high PRR variant copper lasers such as Cu-HBrL, CuBrL & KE-CVL provide means for generating the same through SHG/SFG processes. These lasers produce maximum average power in the PRR of 15-20 kHz with excellent beam quality. The conditions of SHG/SFG using a Cu-HBr laser are somewhat different from that of the conventional CVL because of its relatively higher PRR, longer pulses and lower peak power. The spatio-temporal characteristics of this laser are also different from that of the CVL and may influence its beam quality and SHG efficiency. Additionally, at higher PRR, the average

thermal effects on the crystal is expected to be more, which lead to increased thermal dephasing/detuning effects.

There are only a few reported studies on SHG of Cu-HBr laser operating at 15-20 kHz PRR range. Isaev et. al. [232] have studied the SHG of Cu-HBr laser operating at 17 kHz PRR and used a BBO crystal as nonlinear medium. This study was carried out for the 510.6 nm radiation of the Cu-HBr laser (12.6 W, ~1.4 DL) using spherical focusing geometry. They achieved around 1.3 W average power UV radiation, corresponding to average conversion efficiency of ~10.3% and peak instantaneous conversion efficiency of ~20%. The reason for limiting conversion efficiency was attributed to heating of the crystal due to absorption of either the UV output and /or the pump radiation. In another study, Huot et. al. [233] reported generation of 5.1 W average power UV (255.3 nm), with a single Cu-HBr laser beam operating at 15 kHz PRR and using two BBO crystals. With the use of two BBO crystals in parallel, under cylindrical focusing geometry, they were able to achieve conversion efficiency ~16%. However, with single BBO crystal, they obtained 3.2 W UV average powers corresponding to 20% conversion efficiency. There are no other literatures available on SHG of Cu-HBr lasers.

Few studies are also reported using KE-CVL and with CuBrL. Trickett et. al. [231] carried out experiments with KE-CVL systems using s-BBO and CLBO crystals. The laser was operated at 18 kHz and 10 kHz PRR with PBUR M=100 and produced 13.5 W and 11.5 W high beam quality green power, respectively. At 10 kHz PRR, the maximum average SHG UV power was 3.9 W (conv. eff. of ~29%) and 4.7 W (conv. eff. of ~35%) with the s-BBO crystal and CLBO crystal respectively. At 18 kHz PRR, with s-BBO crystal, the maximum average SHG UV power was 2.3 W at 20% conversion efficiency. However, in this study, CLBO degraded rapidly, due to absorption of moisture, within few hours of experiment and could not be operated at 18 kHz PRR. Larger acceptance angle of CLBO and higher UV transmission are responsible for higher conversion efficiency due to reduced thermal dephasing. Brown et. al.

[229] demonstrated 15 W average power UV (255.3 nm) through SHG of 54 W average power, high beam quality (~2.5 DL) KE-CVL MOPA operating at PRR of 12 kHz. A CLBO crystal was used and the maximum average UV power corresponded to 28% average conversion efficiency. However using BBO crystal instead of CLBO, only 3.3 W average UV power was obtained at 6 kHz PRR of 27 W KE-CVL MOPA power at 12% conversion efficiency. Beyond PRR of 6 kHz, the BBO crystal got damaged. At the fundamental power level used, the crystal temperature increased by 17 °C for CLBO where as it was 53 °C for the BBO. Because of this change in temperature, the phase matching angle also changed by ~2.84 mrad and ~2.33 mrad respectively for the CLBO and the BBO crystal used. These differing trends were attributed to the fact that CLBO has lower UV absorption thus lower temperature gradient, larger temperature acceptance bandwidth (thus minimizing the effect of thermal dephasing) and lower walk-off angle thus allowing larger crystal interaction length. These factors lead to higher SH conversion efficiency with stable operation. The output of low-power (~2.5 W) CuBr + H<sub>2</sub> laser, fitted with UR M=73.33 producing high quality beam (~155 μrad divergence), was used SHG/SFG UV generation in spherical focusing condition in BBO at 16.6 kHz PRR [249]. Frequency converted UV average output power of ~94 mW (255.3 nm), ~24 mW (289.1 nm) & ~28 mW (271.2 nm) were obtained at conversion efficiencies of ~4.8%, ~3.6% & ~0.9% respectively.

It is clear from the above review that there is a very limited study reported on the SHG/SFG of copper laser at 15-20 kHz PRR in general and that of Cu-HBrL in particular. There are only two studies reported on SHG of green radiation of Cu-HBrL. However, there are no study on SHG of its yellow component as well as SFG of both the green & yellow component of Cu-HBrL. In view of this, a detailed study on the nonlinear frequency conversion (SHG & SFG) of Cu-HBrL, operating at 18 kHz PRR, is taken up in the present thesis and presented in the next chapter.

## Chapter 9

### Studies on second-harmonic and sum-frequency generation of

### Cu-HBr laser

#### 9.1 Introduction

Development and studies on high PRR (15-20 kHz), watt-level average power, ns-second duration coherent UV (250-300 nm) radiations, produced through SHG/SFG of Cu-HBr laser radiations, have important implications both from the point of view of research in the field and their applications. The high PRR UV radiations are expected to increase the processing speed of manufacturing of photonic components, UV-photolithography, machining of semiconductors, glass/ceramics & polymers as well as photo-excitation studies of many elements [15, 16, 20, 31]. The Cu-HBr laser is one of the ideal high PRR visible sources for the same. Conventional CVL based frequency converted UV sources, limited to PRR of 5-10 kHz, are well studied, as summarised in chapter 8. However, there are only two reported studies on nonlinear frequency conversion of Cu-HBrL (SHG of green) [232, 233]. No attention has been paid on SHG of the yellow component as well as the SFG of Cu-HBrL. The conditions for SHG/SFG of a Cu-HBr laser are expected to be different due to its relatively higher PRR, longer pulses, lower peak power and better spatio-temporal beam quality behaviour. These factors are likely to affect the efficiency of the SHG and SFG processes. Studies on the beam quality aspects of Cu-HBrLs, relevant for these nonlinear frequency conversions, have already been taken up and elaborated in chapters 5, 6 & 7. In the present thesis, extensive experimental studies are carried out on SHG & SFG of Cu-HBr laser radiations.

This chapter presents detailed experimental studies and analysis on SHG of both the green and yellow radiations of the Cu-HBrL (PRR: 18 kHz) along with their SFG, in a type-I, critically phase matched BBO crystal. In order to prevent the crystal damage, the SHG/SFG study is limited to the fundamental beam average power of about 10 W. These nonlinear

frequency conversion studies are performed on Cu-HBrL with plane-plane (PPR) and unstable resonators (PBURs) of different magnifications (beam quality). The details of the experimental set up as well as the results on optimization of SHG/SFG efficiency of the Cu-HBrL as a function of pump focusing conditions for different focusing geometry (spherical & cylindrical), focal length of the focusing lens, fundamental beam optical power and optical resonator and/or their magnifications (PPR & PBUR M=12.5, 50 and 100) are presented. Temporal variation of the SHG/SFG conversion coefficients and conversion efficiencies are evaluated from analysis based on optical pulses of the fundamental and generated UV beams. The SHG process is also studied with mechanically chopped fundamental beams and the results are analysed.

## **9.2 Thermal consideration in SHG/SFG processes of a Cu-HBr laser**

The Cu-HBr lasers are high average power, high PRR (~ 20 kHz) visible laser sources. For their SHG/SFG UV conversion processes, the thermal effects i.e. dephasing, self-focusing/defocusing & crystal damage etc. in the nonlinear crystal, play crucial role in deciding the SHG/SFG conversion efficiencies and the resulting UV power. Out of these, the thermal dephasing effects are very sensitive to the pump beam power/intensity and observable even at moderate pump power level (5-10 W), in case of BBO [224, 232, 234, 237, 250]. The thermal effects are mainly caused by the absorption of the visible pump and generated UV radiations as well as by multi-photon absorption processes in the crystal [237, 250]. The multi-photon absorption is accompanied with electron transition from the valence band to conduction band i.e. free carrier generation. These free carrier generation in turn leads additional absorption [250] as well as wave-vector/phase mismatch. This wave mismatch is proportional to square of the two-photon absorbed radiation. For the SHG/SFG of high power pulsed visible to UV nonlinear conversion, the crystal defects induced by two photon absorption (TPA) of high peak power UV radiation leads to increased absorption of both visible and UV radiation [237, 250]. The negative influence of these crystal defects is accumulative for multi-kHz pulse repetition

rate visible pump pulses, where the inter-pulse period of 50-200  $\mu\text{s}$  (typical for copper lasers) is not sufficient to decay these dynamic defects whose life time is in range of 1-100 milliseconds [237, 250, 251]. In addition the thermal diffusion time for a BBO crystal is  $\sim 10\text{s}$  of millisecond [252]. Therefore, a non-uniform temperature distribution is created inside the nonlinear crystal causing refractive index variation and hence phase-mismatch. Higher the PRR (as in Cu-HBrLs), more serious is the thermal dephasing effect. However, the thermal dephasing can be partially compensated by adjusting the crystal angle.

The thermal dephasing becomes dominant if the absorbed power ( $\gamma_c LP_{av}$ ) in the crystal ( $\gamma_c$  = absorption coefficient of BBO crystal,  $L$  = length of BBO crystal &  $P_{av}$  = average power of visible-pump or generated UV beam) exceeds a certain critical value given by [221, 232],

$$P_{cr.} = \frac{K\lambda}{\partial(\Delta n)/\partial T} \quad (9.1)$$

where  $\lambda$  = wavelength of radiation involved (fundamental and/or their SHG & SFG),  $K$  = thermal conductivity of the nonlinear crystal (0.8 W/mK for BBO),  $\partial(\Delta n)/\partial T$  = change of birefringence of the crystal with temperature. For type-I phase matched BBO crystal, used in the present study in the thesis,  $\partial(\Delta n)/\partial T = \partial n_{o(\omega)}/\partial T - \partial n_{e(2\omega)}/\partial T \approx 7.3 \times 10^{-6}/\text{K}$  [251, 253, 254], the critical absorbed powers for the fundamentals & their SHG of green are  $\sim 56$  mW (510.6 nm) &  $\sim 28$  mW (255.3 nm) and for the SHG of yellow are  $\sim 63.4$  mW (578.2 nm) &  $\sim 31.7$  mW (289.1 nm) respectively. The corresponding critical power for SFG wavelength lies in between the above two figures. For the BBO crystal of length 1 cm (as used in present work) and value of  $\gamma \sim 4\%/cm$  (for 255.3 to 289.1 nm) &  $\sim 1\%/cm$  (for 510.6 nm, 578.2 nm) [251, 253, 254], the average limiting powers of propagating visible/UV beams, beyond which the thermal dephasing effects will be critical, are estimated to be  $\sim 5.6$  W (510.6 nm),  $\sim 6.3$  W (578.2 nm), 0.7 W (255.3 nm), 0.79 W (289.1 nm) & 0.74 W (271.2 nm). In view of this, in the present study, the average pump/fundamental power of Cu-HBrL is mostly limited to less than 10 W.

### 9.3 Set up for SHG/SFG of Cu-HBr laser

#### 9.3.1 The experimental arrangement

Figs. 9.1 & 9.2 show the schematic & actual photograph of the experimental arrangement for studying the SHG/SFG of Cu-HBrL. The laser is fitted with confocal PBUR containing an intra-cavity cube polarizer (BSP). For different PBURs ( $M = 12.5, 50$  &  $100$ )

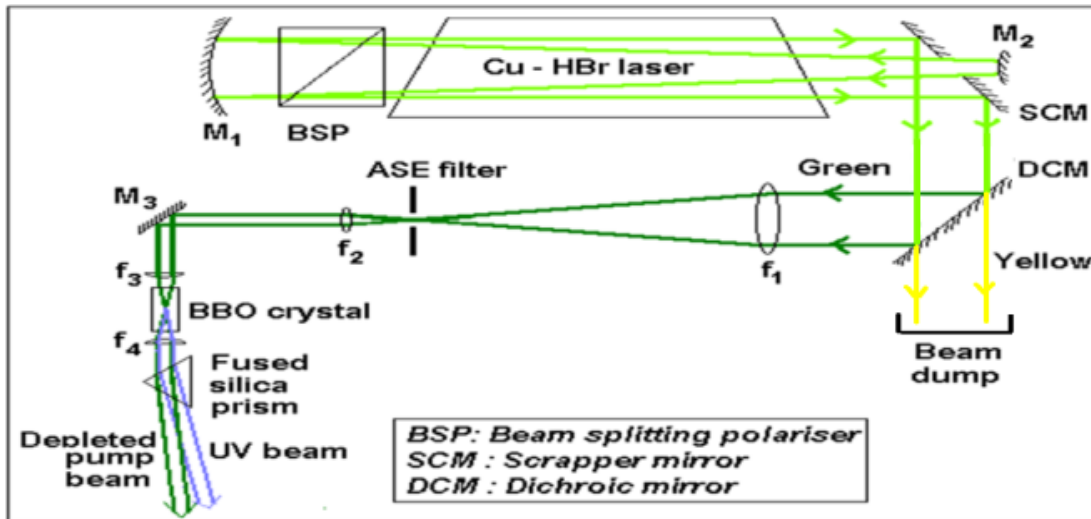


Fig. 9.1 Schematic of the experimental set up for SHG of Cu-HBr laser (G component). For SHG of Y component, a suitable DCM is used. For SFG, a broadband plane mirror is used in place of DCM and  $f_1$  &  $f_2$  are achromatic lens pair of 10X demagnification.

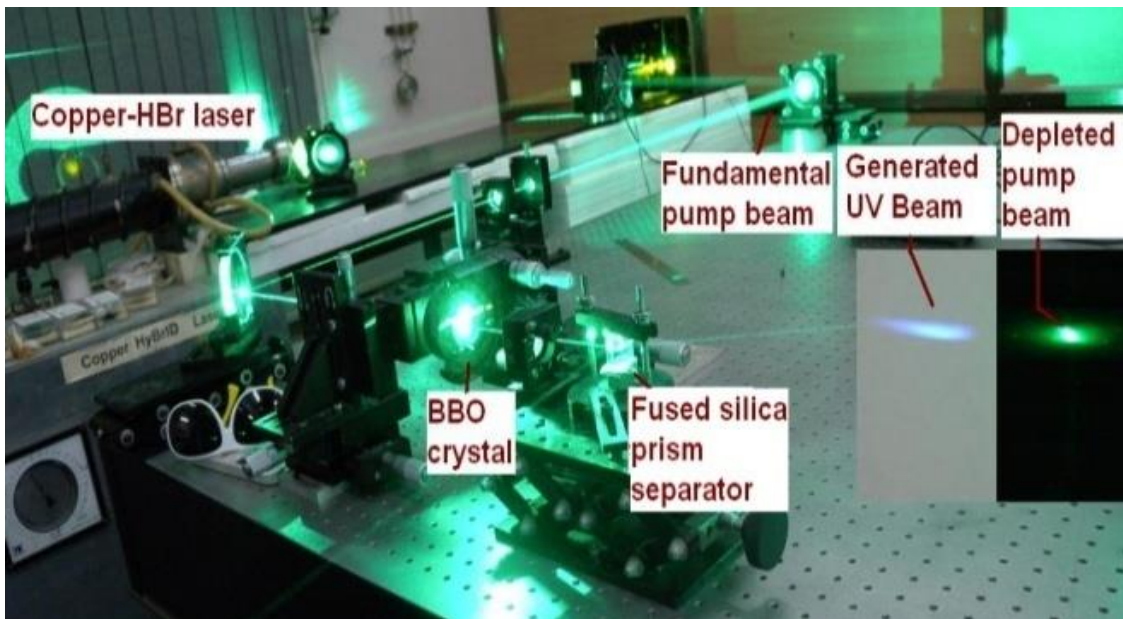


Fig. 9.2 Photograph of the experimental set up for SHG of Cu-HBr laser

used in this study, only the convex button mirror is replaced by another one of suitable focal length as detailed in chapter 7. For PPR, the mirrors  $M_1$  &  $M_2$  are replaced by high reflecting plane mirror & fused silica blank respectively. For SHG study, G or Y component is selected by suitable high reflecting dichroic mirror (DCM). However for SFG study, the DCM is replaced by a high reflecting (for both G & Y) broadband plane mirror. The selected beam (G or Y) is then compressed by 10 times to about 2.5 mm using a telescopic lens pair ( $f_1, f_2 = 100, 10$  cm) and ASE is filtered at the common focal plane with an aperture of diameter 0.5 mm for URs & of diameter 1.5 mm for PPR. For SFG, the lenses are achromats for G and Y wavelengths. The ASE filtered, collimated beam is then focused by a BK-7 cylindrical lens ( $f_3$ ) on a BBO crystal ( $6 \times 4 \times 10$  mm<sup>3</sup>, cut angle =  $47^\circ$ ). This allows angle phase matching for SHG of G ( $\theta_{pm} = 50.7^\circ$ ), SHG of Y ( $\theta_{pm} = 42.5^\circ$ ) and SFG of G + Y ( $\theta_{pm} = 46.3^\circ$ ) in a single crystal by suitably tilting it to match the type-I phase matching angle. The axis direction of the cylindrical lens is along the phase matching and walk-off directions (critical plane). The crystal is mounted on 5-axis micro-positioner for precision angle tuning. The depleted fundamental & generated UV beams are collimated using a cylindrical lens ( $f_4 = 10$  cm) and are separated using a prism, both made of fused silica (suprasil).

### ***9.3.2 Measurement techniques***

The temporal profiles of the radiations (fundamental & depleted G/Y and generated UV) are monitored using a pair of identical bi-planner photo diodes of sub-ns rise time (Hamamatsu, R1193U-52) & 500 MHz oscilloscope (Lecroy: Wave runner-6050A). The average values of the SHG & SFG UV output powers as well as fundamental pump powers are monitored using a power meter with user selectable measuring range and resolution (Gentech, TPM 300). The resolutions as well as accuracies for UV and visible power measurements are 1 mW and 0.1 W respectively. The incident pump power on the crystal is varied using a suitable combination of beam splitters. The average pump power is measured just before the focusing

lens  $f_3$ . Therefore the fundamental power taken for the SHG/SFG conversion efficiency calculations is corrected for  $\sim 8\%$  reflection losses due to both the faces of  $f_3$ . Similarly, the measured UV powers after prism are corrected for  $\sim 20\%$  reflection losses in a combination of collimating lens  $f_4$  and prism separator, in line with the practice adopted in reported literature in the field [220, 222, 224, 226-247]. The temporal variation of instantaneous peak powers of the fundamental pump beam and the generated UV beams are estimated from the digitized temporal profiles of the corresponding radiations with 1 ns resolution, averaged over 10 pulses. The wavelengths of the generated UV radiations are confirmed by recording the optical spectra of the radiations using a fiber optic spectro-photometer (Avantes). Prior to the detailed experimental study on the SHG/SFG process, the obtained SHG/SFG UV radiations are confirmed by recording the optical spectra of the radiations using a fiber optic spectro-photometer (Avantes). Figs. 9.3 a, b & c show the recorded SHG & SFG spectra, obtained by suitably tilting the BBO crystal with respect to the pump beam(s) (green and/or yellow).

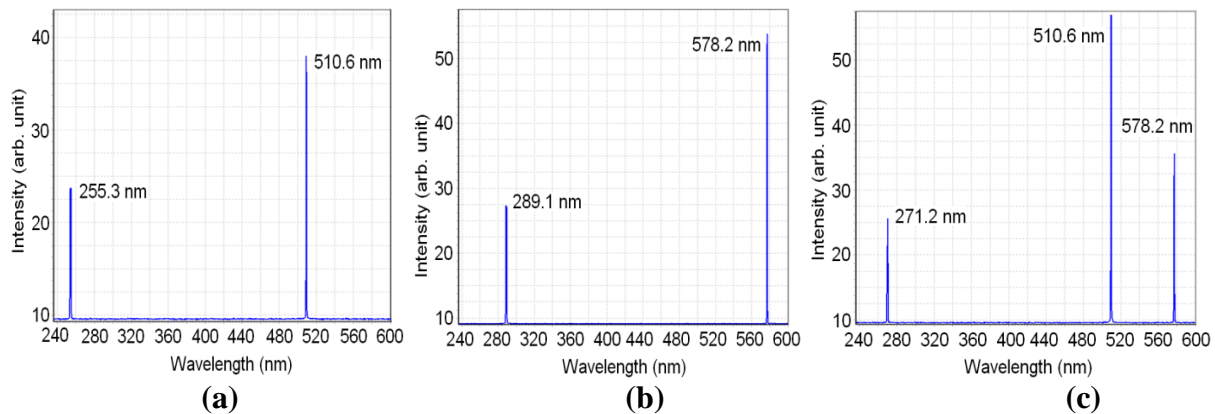


*Fig. 9.3 Spectrum of SHG & SFG radiations of Cu-HBr laser (a) SHG of green (b) SHG of yellow & (c) SFG of green & yellow*

## 9.4 Experimental results on SHG & SFG of Cu-HBr laser

### 9.4.1 Optimisation of focusing conditions

In the SHG/SFG process, Cu-HBr laser radiations need to be focused onto the nonlinear crystal to obtain the desired peak intensity and the generated UV output power depends on the pump focusing conditions. Hence, the optimization of the focusing conditions for the

SHG/SFG of G & Y beams are carried for all the resonators used (PPR,  $M = 1$  and PBURs,  $M=12.5, 50$  &  $100$ ) in Cu-HBr laser. Figs. 9.4 a & b show the variation of SHG UV average output power  $P_{2\omega(g)}$  & conversion efficiency  $\eta_{2\omega(g)}$  [ $=100\% \times (P_{2\omega(g)}/P_{\omega(g)})$ ] respectively with focal length ( $f_3$ ) of pump focusing cylindrical lens for the G-beam with all the four resonators. The maximum value of  $P_{\omega(g)}$  used are 10 W (PPR,  $M = 1$ ), 9.2 W (PBUR  $M=12.5$ ), 8.2 W (PBUR  $M=50$ ) and 6.3 W (PBUR  $M=100$ ), as obtained at exactly same electrical input power conditions of the Cu-HBr laser. It is observed that as the focal length decreases from 10 to 3 cm,  $P_{2\omega(g)}$  increases rapidly and attains maxima at focal length of 4 cm for PPR ( $M = 1$ ), PBURs of  $M = 12.5$  &  $50$ , and at 3 cm for PBUR of  $M=100$ . The maximum  $P_{2\omega(g)}$  obtained, at maximum  $P_{\omega(g)}$  mentioned above, are 0.3 W, 0.7 W, 2.05 W & 1.7 W for  $M = 1, 12.5, 50$  and  $100$  respectively. The difference in  $P_{2\omega(g)}$ , for PBUR  $M=100$ , with 3 cm and 4 cm focal lengths, are small (1.7 W vs. 1.65 W). Also the  $\eta_{2\omega(g)}$  values increase rapidly and attain maximum at focal length of 4 cm for PPR, PBURs of  $M=12.5$  &  $50$ , and at 3 cm for PBUR  $M 100$  as cylindrical lens focal length is decreased from 10 to 3 cm. With the increase of resonator  $M$  from 1 to 100, the corresponding values of maximum  $\eta_{2\omega(g)}$  are about 3%, 7.6%, 25% &

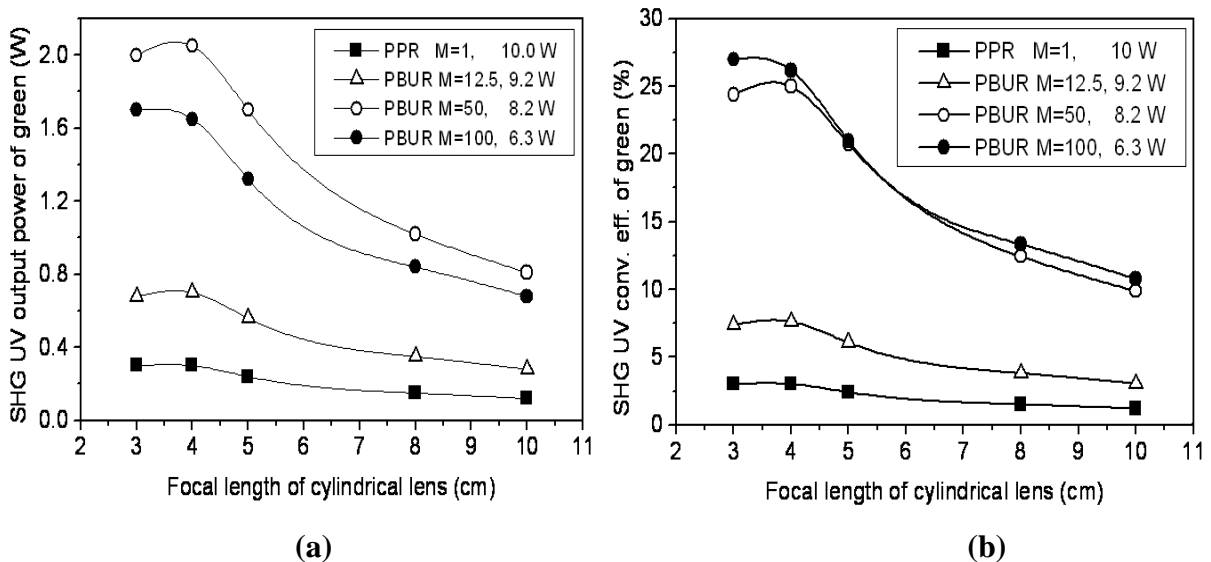


Fig. 9.4 Variation of SHG UV power (a) & conversion eff. (b) of green component of Cu-HBrL with focal length of focusing cylindrical lens for PPR and PBURs  $M=12.5, 50$  &  $100$

26.2% respectively. However, the difference in  $\eta_{2\omega}(g)$  for PBUR M 100, with 3 cm and 4 cm focal lengths are very small (26.98% vs 26.19%). Similar trends in variation of  $P_{2\omega}(y)$  and  $\eta_{2\omega}(y)$  are also observed for SHG of Y-beams of Cu-HBrL. The maximum incident average pump power of the Y-beam on the BBO crystal are 7 W (PPR), 6.4 W (PBUR M=12.5), 5.6 W (PBUR M = 50) & 5.5 W (PBUR M=100), at a fixed electrical input power to the Cu-HBrL. The maximum values of  $P_{2\omega}(y)$  are observed at focal length of 3 to 4 cm for all the four resonators with corresponding values of 0.12 W (PPR), 0.31 W (PBUR M=12.5) and 1.0 W (PBUR M=50 & 100). The corresponding values of  $\eta_{2\omega}(y)$  [=100% x  $(P_{2\omega}(y)/P_{\omega}(y))$ ] are about 1.7%, 4.8%, 17.9% & 18% respectively.

Figs. 9.5 a & b show the variation of SFG UV average output power,  $P_{\omega_3}$  & conversion for all the resonators. The average pump power (green + yellow) for these conditions are 13 W (7.6 W + 5.4 W) for PPR, 12 W (7 W + 5 W) for PBUR M=12.5, 11.9 W (7.1 W + 4.8 W) for PBUR M=50 & 9.9 W (5.5 W + 4.4 W) for PBUR M=100. The optimum focal length corresponding to the maximum SFG UV is again 3 to 4 cm. However the degradation of  $P_{\omega_3}$  and  $\eta_{\omega_3}$  are faster as the focal length of the cylindrical lens is increased upto 10 cm. The maximum values of  $P_{\omega_3}$  are about 0.3 W (PPR), 0.6 W (PBUR M = 12.5), 1.52 W (PBUR

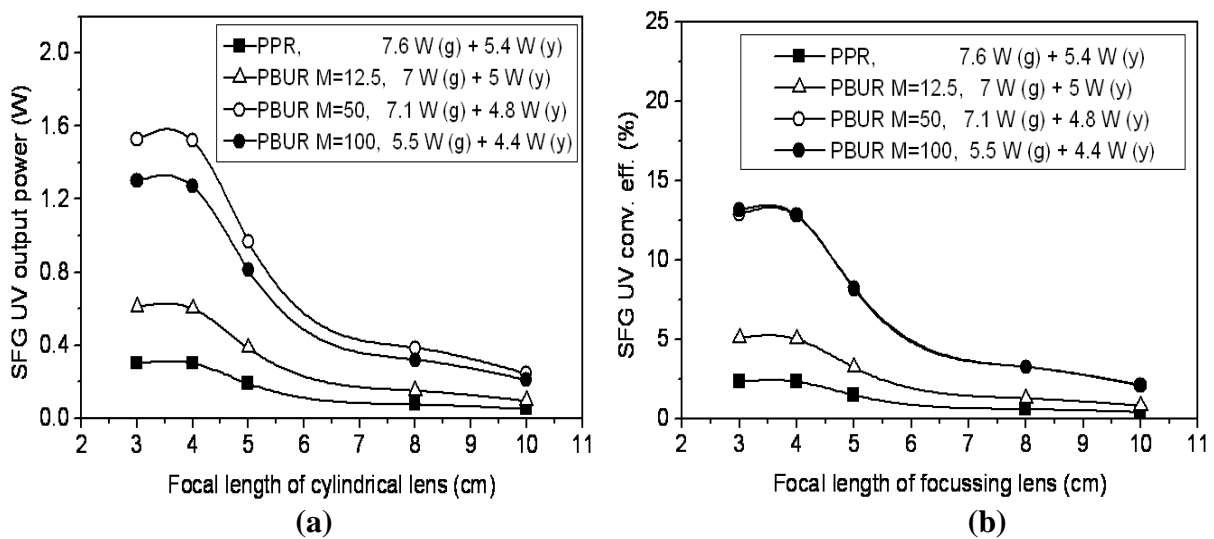


Fig. 9.5 Variation of SFG UV output power (a) & conv. efficiency (b) of Cu-HBrL with focal length of the pump focusing cylindrical lens for PPR and PBURs M=12.5, 50 & 100

M=50) [255] and 1.3 W (PBUR M=100). These translate into corresponding values of  $\eta_{\omega_3}$  to about 2.3%, 5%, 12.8% & 13% respectively. Similar studies are also carried out with spherical focusing lens of different focal lengths. However, the obtained output UV powers/conversion-efficiencies are lower than that of the cylindrical focusing. Therefore, the further studies on SHG/SFG of the Cu-HBr laser are pursued with cylindrical focusing geometry and the focal length ( $f_3$ ) of cylindrical lens is chosen to be 4 cm.

#### 9.4.2 SHG of green radiation

Fig. 9.6 a shows the variation of  $P_{2\omega}(g)$  as a function of  $P_{\omega}(g)$  for PPR and PBURs of M 12.5, 50 & 100. It is observed that  $P_{2\omega}(g)$  increases with increase of  $P_{\omega}(g)$  for all the resonators. However, the rate of increase of  $P_{2\omega}(g)$  is larger for higher resonator magnification. For PPR & PBUR M=12.5, the variations in SHG UV output power  $P_{2\omega}(g)$  are from 30 mW to 300 mW & from 31 mW to 700 mW with corresponding variations in the fundamental green pump power  $P_{\omega}(g)$  from 3 to 10 W & 1.9 to 9.2 W respectively. On the other hand, for PBURs of M=50 & M=100, the variations in  $P_{2\omega}(g)$  are from 80 mW to 2.05 W & from 81 mW to 1.65 W with corresponding variations in the fundamental green pump power,  $P_{\omega}(g)$ , from 1.6 W to 8.2 W & 1.4 W to 6.3 W respectively. Fig. 9.6 b shows the variation of the SHG UV conversion

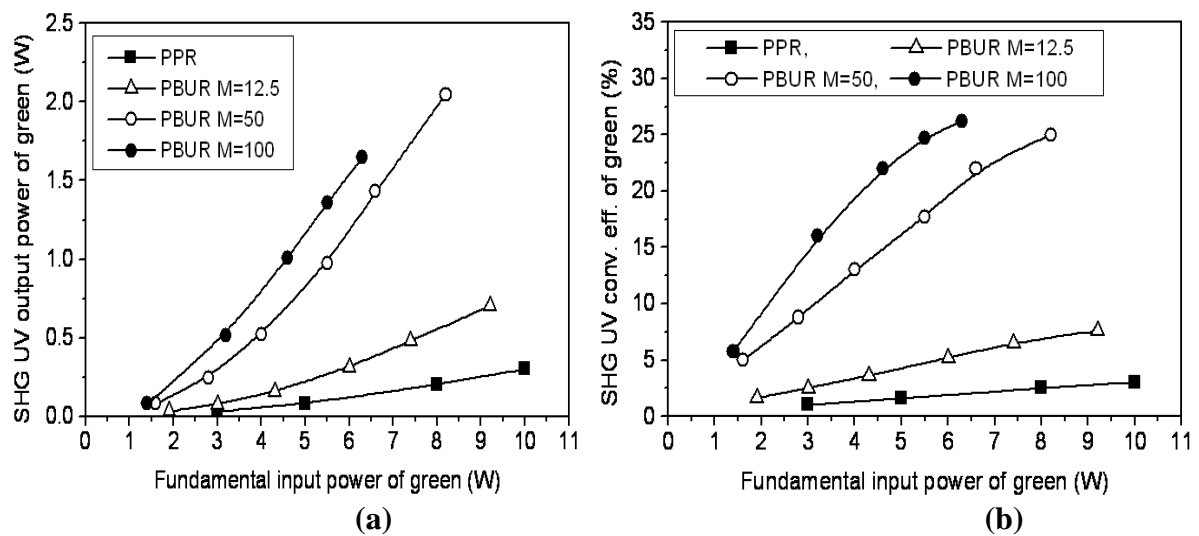


Fig. 9.6 Variation of SHG UV output power [ $P_{2\omega}(g)$ ] (a) & conversion efficiency [ $\eta_{2\omega}(g)$ ] (b), with fundamental green input power [ $P_{\omega}(g)$ ] for PPR and PBURs M = 12.5, 50 & 100

efficiency of green component of Cu-HBrL,  $\eta_{2\omega}(g)$ , for different  $P_{\omega}(g)$ . It is observed that  $\eta_{2\omega}(g)$  increases with increase of  $P_{\omega}(g)$  for all the resonators. However, the rate of increase of  $\eta_{2\omega}(g)$  is higher for higher magnification of the resonators. For PPR & PBUR M=12.5,  $\eta_{2\omega}(g)$  increases from 1% to 3% & 1.63% to 7.61% respectively, for corresponding increase in  $P_{\omega}(g)$ . However, for PBUR M=50, as the  $P_{\omega}(g)$  increases upto 6.6 W,  $\eta_{2\omega}(g)$  increases almost linearly upto 22% (1.43 W UV) and thereafter its slope slows down. At maximum used value of  $P_{\omega}(g)$  of 8.2 W,  $\eta_{2\omega}(g)$  is about 25%. On the other hand, for PBUR M=100, the slope of the graph slows down at  $P_{\omega}(g)$  of about 4.6 W [1.01 W UV &  $\eta_{2\omega}(g) \sim 22\%$ ].

### 9.4.3 SHG of yellow radiation

Fig. 9.7 a shows the variation of  $P_{2\omega}(y)$  as a function of  $P_{\omega}(y)$  for PPR, M = 1 and PBURs of M = 12.5, 50 & 100. It is observed that, like the case of SHG of green,  $P_{2\omega}(y)$  increases with increase of  $P_{\omega}(y)$  for all the resonators. The rate of increase of  $P_{2\omega}(y)$  with  $P_{\omega}(y)$  increases with increase in resonator M, however are close for M = 50 & 100. For PPR & PBUR M=12.5, the variations in SHG UV output power  $P_{2\omega}(y)$  are from about 32 mW to 120 mW & 50 mW to 310 mW with corresponding variations in the fundamental yellow pump power  $P_{\omega}(y)$  from 3.6 to 7 W & 2.6 to 6.4 W respectively. On the other hand, for PBURs of M=50 & M=100,

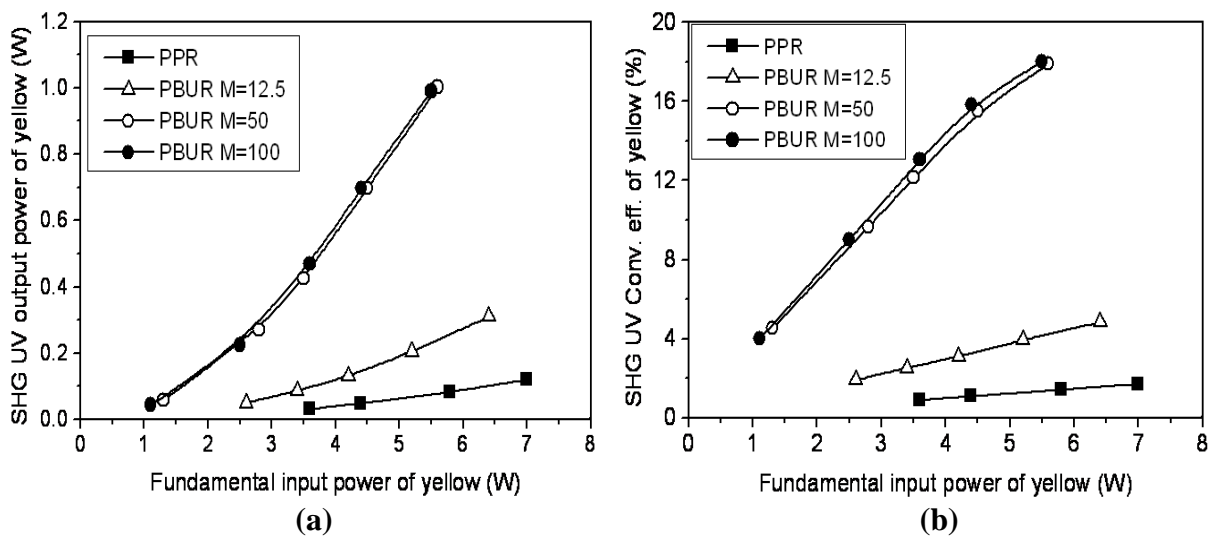


Fig. 9.7 Variation of SHG UV output power [ $P_{2\omega}(y)$ ] (a) & conversion efficiency [ $\eta_{2\omega}(y)$ ] (b), with fundamental yellow input power [ $P_{\omega}(y)$ ] for PPR and PBURs M = 12.5, 50 & 100

the variations in  $P_{2\omega(y)}$  are from 59 mW to 1.0 W & from 44 mW to 1.0 W with corresponding variations in  $P_{\omega(y)}$  from 1.3 W to 5.6 W & 1.1 W to 5.5 W respectively Fig. 9.7 b shows the variation of the SHG UV conversion efficiency of yellow component of Cu-HBrL,  $\eta_{2\omega(y)}$ , for different  $P_{\omega(y)}$ . Similar to the green component,  $\eta_{2\omega(y)}$  increases with increase of  $P_{\omega(y)}$  for all the resonators. However, the rate of increase of  $\eta_{2\omega(y)}$  is higher for larger magnification of the resonator used. For PPR & PBUR  $M = 12.5$ ,  $\eta_{2\omega(y)}$  increases almost monotonically from 0.9% to 1.71% & from 1.92% to 7.84% respectively, for corresponding increase in  $P_{\omega(y)}$ . However, for both PBUR  $M = 50$  & 100, as the  $P_{\omega(y)}$  increases upto 5.5/5.6 W,  $\eta_{2\omega(y)}$  increases almost linearly upto  $\sim 15.5\%$  ( $\sim 0.7$  W UV) and thereafter its slope slows down. At maximum used value of  $P_{\omega(y)}$  of 5.5/5.6 W,  $\eta_{2\omega(y)}$  is about 18%.

#### 9.4.4 SFG of green & yellow radiations

Fig. 9.8 a shows the variation of the SFG UV average output power,  $P_{\omega_3}$ , as a function of total average pump power [ $P_{\omega(g)} + P_{\omega(y)}$ ] for PPR and PBURs of  $M = 12.5, 50$  & 100. It is observed that, similar to the case of SHG processes,  $P_{\omega_3}$  increases almost monotonically with increase of [ $P_{\omega(g)} + P_{\omega(y)}$ ] for all the resonators and the rate of increase of  $P_{\omega_3}$  with [ $P_{\omega(g)} + P_{\omega(y)}$ ] is higher for resonator of larger magnification. For PPR,  $P_{\omega_3}$  increases from 15

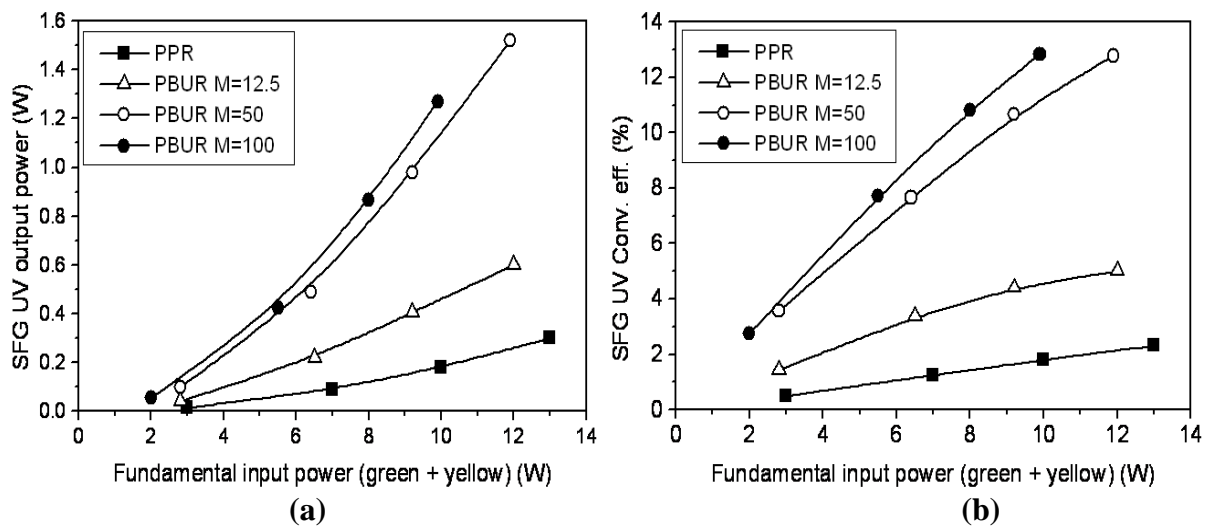


Fig. 9.8 Variation of SFG UV output power [ $P_{\omega_3}$ ] (a) and conversion efficiency [ $\eta_{\omega_3}$ ] (b) with fundamental input power [ $P_{\omega(g)} + P_{\omega(y)}$ ] for PPR and PBURs  $M = 12.5, 50$  & 100

mW to 300 mW as  $[P_{\omega(g)}+P_{\omega(y)}]$  is raised from 3 W to 13 W, whereas for PBUR M = 12.5,  $P_{\omega3}$  increases from 40 mW to 600 mW with increase of  $[P_{\omega(g)}+P_{\omega(y)}]$  from 2.8 W to 12 W. However, for the PBURs of M=50 & 100,  $P_{\omega3}$  increases from 0.1 W to 1.52 W & 0.055 W to 1.27 W with increase of  $[P_{\omega(g)}+P_{\omega(y)}]$  from 2.8 W to 11.9 W & 2 W to 9.9 W respectively. Fig. 9.8 b shows the variation of the SFG UV conversion efficiency,  $\eta_{\omega3}$ , for different  $[P_{\omega(g)}+P_{\omega(y)}]$ . It is observed that  $\eta_{\omega3}$  increases from 0.5% to 2.3% (PPR), 1.43% to 5% (for PBUR M = 12.5), 3.57% to 12.77% (for PBUR M=50) and 2.75% to 12.83% (for PBUR M=100) for the respective increase in values of their  $[P_{\omega(g)}+P_{\omega(y)}]$ .

It is clear from the average SH/SFG results presented above that the highest nonlinear conversion efficiencies are observed for SHG of green and the lowest for SFG of green and yellow. From the fundamental beam side, these differing nonlinear conversion behaviours are connected with divergence values, spot size, peak power, peak focussed intensity and temporal pulse shape/width of green and yellow components of Cu-HBr laser with different resonators. On the frequency conversion side, the average and time resolved (within pulse) behaviour of SH/SFG efficiency and the conversion coefficient need to be correlated vis-à-vis fundamental beam characteristics. With this perspective, the next section analyse the SHG/SFG experimental results of section 9.4.

## **9.5 Analysis of the result and discussion**

### ***9.5.1 Time averaged characteristics of SHG and SFG***

It is obvious from the experimental results (section 9.4.1) that there exists an optimum focal length of the cylindrical focussing lens ( $f_3$ ) for maximum SHG & SFG UV average output powers and their conversion efficiencies. This can be understood as follows. The choice on cylindrical lens focal length ( $f_3$ ) is a compromise between higher attainable peak focal plane intensity with shorter focal length vis-à-vis larger convergence/divergence angle of the smaller focus spot pump beam [227, 228]. In the present study, for less than optimum focal length ( $f_3$

< 4 cm), the UV conversion efficiency is limited by the combined effect of reduced effective interaction length (due to increased walk-off) and inefficient coupling of light within the acceptance angle of the crystal (due to increased convergence/divergence angle). At larger than optimum focal length ( $f_3 > 4$  cm), the UV conversion efficiency is reduced due to decreased pump beam intensity. At the optimised value for  $f_3$  of 4 cm, for the resonator M value of 1, 12.5, 50 & 100, the corresponding estimated peak intensities  $[I_\omega(g)]$  for G beams are  $\sim 0.62$  MW/cm<sup>2</sup>,  $\sim 3.47$  MW/cm<sup>2</sup>,  $\sim 7.72$  MW/cm<sup>2</sup> &  $\sim 8.94$  MW/cm<sup>2</sup> corresponding to the mentioned maximum average power used. In the ideal conditions of perfect phase matching,

$$P_{2\omega}(g) \propto [P_\omega(g) \cdot I_\omega(g)] \propto (L^2 P_\omega^2)/(h \cdot f \cdot \theta) \quad (9.2)$$

$$\eta_{2\omega}(g) \propto I_\omega(g) \quad (9.3)$$

$$L = \sqrt{L_a L_p} = \sqrt{a L_p / \rho} \quad (9.4)$$

where  $L$  = interaction length of the crystal,  $h$  = beam height at the focus (= 2.5 mm),  $f$  = focal length of the cylindrical focussing lens  $f_3$  and  $\theta$  = divergence of the pump laser beam,  $a$  = spot size on the crystal (=  $m f_3 \theta$ ,  $m$  is beam compression factor),  $\rho$  = walk-off angle of the crystal,  $L_a$  = aperture length of the crystal ( $\approx a/\rho$ ) and  $L_p$  = physical length of the crystal.

These standard relations closely explain the observed trends on the variation of  $P_{2\omega}(g)$  and  $\eta_{2\omega}(g)$  vs.  $f_3$  (Figs. 9.4 a & b) except in the case of  $f_3 < 4$  cm or  $M > 50$ . Lower the  $f_3$  value and/or larger the M value (reduced  $\theta$ ), higher will be conversion efficiency and larger will be slope of curve as  $\partial \eta_{2\omega} / \partial f \propto 1/f^2$  for given  $\theta$  and  $\partial \eta_{2\omega} / \partial \theta \propto 1/\theta^2$  for given  $f$ , as actually observed. However, these general trends are not observed for  $f_3 < 4$  cm or  $M > 50$ . For example, reducing  $f_3$  from 4 to 3 cm or increasing M from 50 to 100, the changes in the UV power or conversion efficiency are relatively small, both positive and negative. This is due to the fact that in both the situations, the fundamental focussed beam spot size at the crystal reduces significantly, thereby leading to restricted SHG process due to increased beam walk-

off, limited angular acceptance and increased dephasing between fundamental and generated beams in the crystal [227, 228, 220]. Similar argument follows for SHG of Y-beam as well as for SFG process. However, relatively faster decrease of SFG UV output with increase focal length, than that of SHG of G/Y case, is attributed to increased intensity and spatial mismatch of the G & Y beams at the focus pump region due to their different divergence and pointing stability characteristics, as detailed in chapter 7. From the SHG/SFG results (at fixed  $f_3 = 4$  cm; section 9.4.2 to 9.4.4), it is observed that the UV output powers increase as the fundamental input powers increase, for all the resonators. The rate of increase of UV power is higher for higher resonator magnification upto 50. The same is true for the UV conversion efficiency. However, the UV power and conversion efficiency results are very close for UR  $M = 50$  and 100. The conversion efficiency also displays a slight slowing down beyond certain pump power. These observations can again be explained on the general consideration (equations 9.2 to 9.4) as follows.

For a given pump power, as the resonator  $M$  increases,  $\theta$  as well as the spot size (width of spot) decreases and hence the peak intensity increases. This leads to increase in SHG UV power as well as the conversion efficiencies as  $M$  is increased from 1 (PPR) to 50 (UR). For example, at typical pump power of 5 W, the pump spot width on the BBO crystal ( $=10 f_3 \theta$ ) are  $\sim 600 \mu\text{m}$ ,  $\sim 107 \mu\text{m}$ ,  $\sim 47 \mu\text{m}$  and the corresponding peak intensities are  $\sim 0.31 \text{ MW/cm}^2$ ,  $\sim 1.9 \text{ MW/cm}^2$ ,  $\sim 4.7 \text{ MW/cm}^2$  for green beam of Cu-HBrL with resonator  $M=1, 12.5, 50$  respectively. Similarly for the Y component, the pump spot widths on the crystal are  $\sim 560 \mu\text{m}$ ,  $\sim 92 \mu\text{m}$  &  $\sim 38 \mu\text{m}$  and the corresponding peak pump intensities are  $\sim 0.36 \text{ MW/cm}^2$ ,  $\sim 2.4 \text{ MW/cm}^2$  &  $\sim 6.5 \text{ MW/cm}^2$  respectively. The increase in slope of  $P_{2\omega}$  vs.  $P_\omega$  and  $\eta_{2\omega}$  vs.  $P_\omega$  curves as  $M$  is increased from 1 to 50 is again due to  $\partial P_{2\omega}/\partial\theta$  or  $\partial\eta_{2\omega}/\partial\theta \propto 1/\theta^2$ . For  $M = 100$ , the pump beam width and intensity at the crystal are  $\sim 36 \mu\text{m}$  &  $\sim 7.1 \text{ MW/cm}^2$  for G beam and  $\sim 29 \mu\text{m}$  &  $\sim 10 \text{ MW/cm}^2$  for Y beam respectively. It is clear that moving from  $M=$

50 to 100, there is no major change in spot size at crystal due to almost diffraction limited divergence values (1-1.3 DL) in both the cases. Also, the spot sizes are very small (10s of microns) and the peak intensities are high, the SHG process is adversely affected due to increased beam walk-off, limited angular acceptance and increased dephasing between fundamental and generated beams in the crystal. Hence the frequency conversion performance of  $M = 50$  and  $100$  are very close. Similar arguments follow for the SFG process as well. However, the lower conversion efficiencies (12.8%) for SFG process is attributed spatial & temporal mismatch of pump intensities as brought out more clearly in section 9.5.3.

It is to be noted that the fundamental pump powers used for the SHG/SFG studies are different for the different resonators. Hence theoretically the SHG/SFG conversion efficiency is anyway expected to be different, being a function of fundamental power (section 8.2.3). Therefore, to characterize the frequency conversion processes on a uniform scale, another parameter, namely the power independent conversion coefficient (= ratio of conv. efficiency to input fundamental power) [220, 232], is to be utilized. For SHG of G/Y, at perfect phase matching condition, the conversion coefficient is given as  $C_{2\omega}(g/y) = \eta_{2\omega}(g/y)/P_{\omega(p)}(g/y)$ , where  $P_{\omega(p)}(g/y)$  is the peak power of fundamental G/Y. For SFG, this is given as  $C_{\omega 3} = \eta_{\omega 3}/[P_{(p)}(g+y)]$ , where  $P_{(p)}(g+y)$  is the peak power of combined G & Y fundamental pulses. The conversion coefficients act as a figure of merit for deciding the efficacy of the SHG/SFG conversion processes. Larger the value of the conversion coefficient, more efficient is the frequency conversion process. In ideal condition with perfect phase matching, the conversion coefficient remains constant for the SHG process with a given nonlinear crystal.

The variation of the evaluated values of  $C_{2\omega}(g)$  with  $P_{\omega}(g)$  is shown in Fig. 9.9 a. It is noticed that  $C_{2\omega}(g)$  is almost constant with a very little variation for  $M = 1$  and  $12.5$ . The  $C_{2\omega}(g)$  decreases marginally from  $0.36$  to  $0.32 \times 10^{-5} \text{ W}^{-1}$  for  $M = 1$ ,  $0.85$  to  $0.82 \times 10^{-5} \text{ W}^{-1}$  for  $M = 12.5$ . However, for PBUR  $M=50$  &  $100$ , it increases with  $P_{\omega}(g)$  and attains maximum value

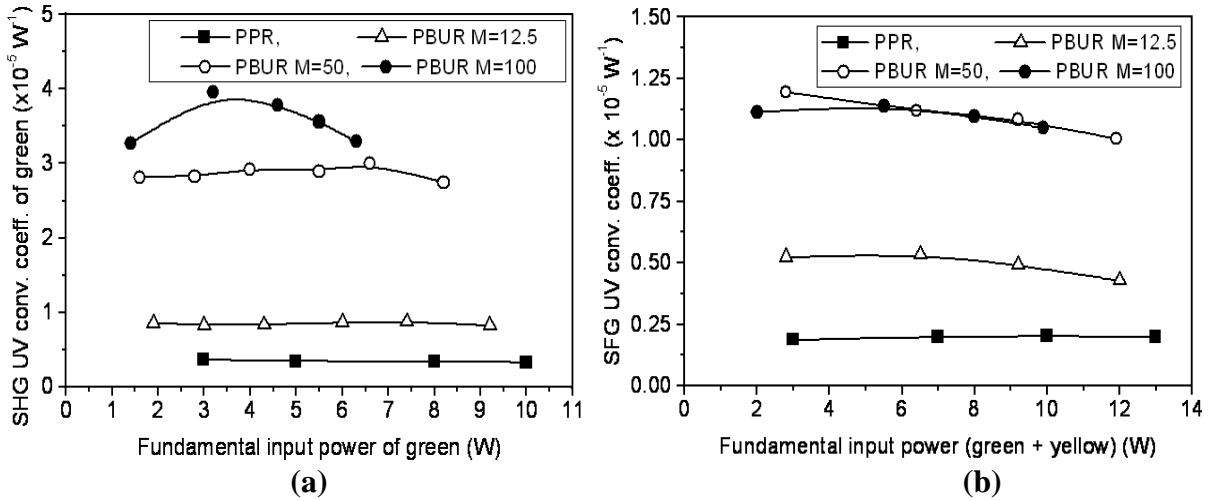


Fig. 9.9 Variation of SHG/SFG UV conversion coefficients with fundamental input powers for PPR and PBURs  $M=12.5, 50$  &  $100$ : (a) SHG of green and (b) SFG of green & yellow

& then falls. For PBUR  $M=50$ ,  $C_{2\omega}(g)$  is at maximum value of  $\sim 3 \times 10^{-5} \text{ W}^{-1}$  [ $P_{\omega}(g) = 6.6 \text{ W}$ ,  $P_{2\omega}(g) = 1.43 \text{ W}$ ] and then falls to  $\sim 2.74 \times 10^{-5} \text{ W}^{-1}$  at  $P_{\omega}(g) = 8.2 \text{ W}$  [ $P_{2\omega}(g) = 2.05 \text{ W}$ ]. On the other hand, the change of  $C_{2\omega}(g)$  with  $P_{\omega}(g)$ , for PBUR  $M = 100$ , is quite high as compared to the other resonators used. With the increase of  $P_{\omega}(g)$  from  $1.4 \text{ W}$ ,  $C_{2\omega}(g)$  increases from  $\sim 3.27 \times 10^{-5} \text{ W}^{-1}$ , attains maximum of  $\sim 3.96 \times 10^{-5} \text{ W}^{-1}$  at  $P_{\omega}(g) = 3.2 \text{ W}$  [ $P_{2\omega}(g) = 512 \text{ mW}$ ] and then decreases monotonically to  $\sim 3.29 \times 10^{-5} \text{ W}^{-1}$  at  $P_{\omega}(g) = 6.3 \text{ W}$  [ $P_{2\omega}(g) = 1.65 \text{ W}$ ]. The degree of variation of  $C_{2\omega}(g)$  with input power is indicative of the extent of phase mismatch between fundamental and UV beams as a function of input power. The variations of  $C_{2\omega}(y)$  with  $P_{\omega}(y)$  for the different resonators are more or less similar to that of the G i.e. remaining almost constant for lower resonator magnification & lower  $P_{\omega}(y)$  values. For PPR,  $C_{2\omega}(y)$  has a constant value of  $\sim 0.24 \times 10^{-5} \text{ W}^{-1}$  & for PBUR  $M=12.5$ ,  $C_{2\omega}(y)$  is almost constant at  $0.67 - 0.68 \times 10^{-5} \text{ W}^{-1}$ . However, for PBUR  $M = 50$  &  $100$ ,  $C_{2\omega}(y)$  is at almost constant level of  $\sim 2.8 \times 10^{-5} \text{ W}^{-1}$  &  $\sim 2.5 \times 10^{-5} \text{ W}^{-1}$  respectively upto  $4.4/4.5 \text{ W}$  of  $P_{\omega}(y)$  [ $P_{2\omega}(y) \sim 0.7 \text{ W}$ ] and then falls to  $\sim 2.6 \times 10^{-5} \text{ W}^{-1}$  &  $\sim 2.3 \times 10^{-5} \text{ W}^{-1}$  at  $P_{\omega}(y)$  of  $5.5/5.6 \text{ W}$  [ $P_{2\omega}(y) = 1.0 \text{ W}$ ]. However, the variations of  $C_{\omega 3}$  (SFG) are different than that of SHG. For PPR  $C_{\omega 3}$  is almost constant at  $0.19 - 2.0 \times 10^{-5} \text{ W}^{-1}$ . On the other hand for PBURs,  $C_{\omega 3}$  decreases with increase in [ $P_{\omega}(g) + P_{\omega}(y)$ ].

$C_{\omega_3}$  decreases from  $\sim 0.52 \times 10^{-5} \text{ W}^{-1}$  to  $\sim 0.43 \times 10^{-5} \text{ W}^{-1}$  (for PBUR M=12.5, increase in fundamental power from 2.8 to 12 W), from  $\sim 1.2 \times 10^{-5} \text{ W}^{-1}$  to  $\sim 1 \times 10^{-5} \text{ W}^{-1}$  (for PBUR M=50, increase in fundamental power from 2.8 to 11.9 W) and from  $\sim 1.4 \times 10^{-5} \text{ W}^{-1}$  to  $\sim 1.05 \times 10^{-5} \text{ W}^{-1}$  (for PBUR M=100, increase in fundamental power from 2 to 9.9 W). The decrease in values of conversion coefficients beyond certain UV/visible-pump power levels are in line with the thermal dephasing caused due to the absorption of radiations as discussed earlier.

The discussions presented above are based on pulse averaged picture on the SHG/SFG processes. However, in a Cu-HBrL, the fundamental beam divergence evolves in time within a pulse, as brought out in chapter 7. These evolutions are different for G & Y and hence their pump intensities are different at different time within the pulse. That is why the temporal evolution of the SHG power and conversion efficiencies are expected to be different. These issues play a crucial role for optimising and evaluating efficiency of the SH/SFG process. The time resolved behaviour are presented and discussed in the following section.

### **9.5.2 Time resolved characteristics of SHG and SFG**

Figs. 9.10 a to f show one representative case of the temporal variation (within a pulse) of instantaneous pump fundamental power [ $P_{\omega(g)}(t)$ ,  $P_{\omega(y)}(t)$  &  $P_{(g+y)}(t)$ ] & UV output power [ $P_{2\omega(g)}(t)$ ,  $P_{2\omega(y)}(t)$  &  $P_{\omega_3}(t)$ ] and UV conversion efficiencies [ $\eta_{2\omega(g)}(t)$ ,  $\eta_{2\omega(y)}(t)$  &  $\eta_{\omega_3}(t)$ ] & conversion coefficients [ $C_{2\omega(g)}(t)$ ,  $C_{2\omega(y)}(t)$  &  $C_{\omega_3}(t)$ ] for Cu-HBrL with PBUR M=50 for SHG of G (a, b), SHG of Y (c, d) and SFG of G & Y (e, f) respectively. The instantaneous conversion efficiencies are estimated as  $\eta_{2\omega(g/y)}(t) = P_{2\omega(g/y)}(t)/P_{\omega(g/y)}(t)$  for SHG &  $\eta_{\omega_3}(t) = P_{\omega_3}(t)/P_{(g+y)}(t)$  for SFG whereas the instantaneous conversion coefficients are estimated as  $C_{2\omega(g/y)}(t) = \eta_{2\omega(g/y)}(t)/P_{\omega(g/y)}(t)$  for SHG of G/Y &  $C_{\omega_3}(t) = \eta_{\omega_3}(t)/P_{(g+y)}(t)$  for SFG of G + Y. The instantaneous powers of the fundamentals (G, Y and G + Y) as well as the generated UV radiations are estimated from the averaged pulse shapes (10 pulses) recorded recorded with a 500 MHz oscilloscope. This leads to some inaccuracies in calculated

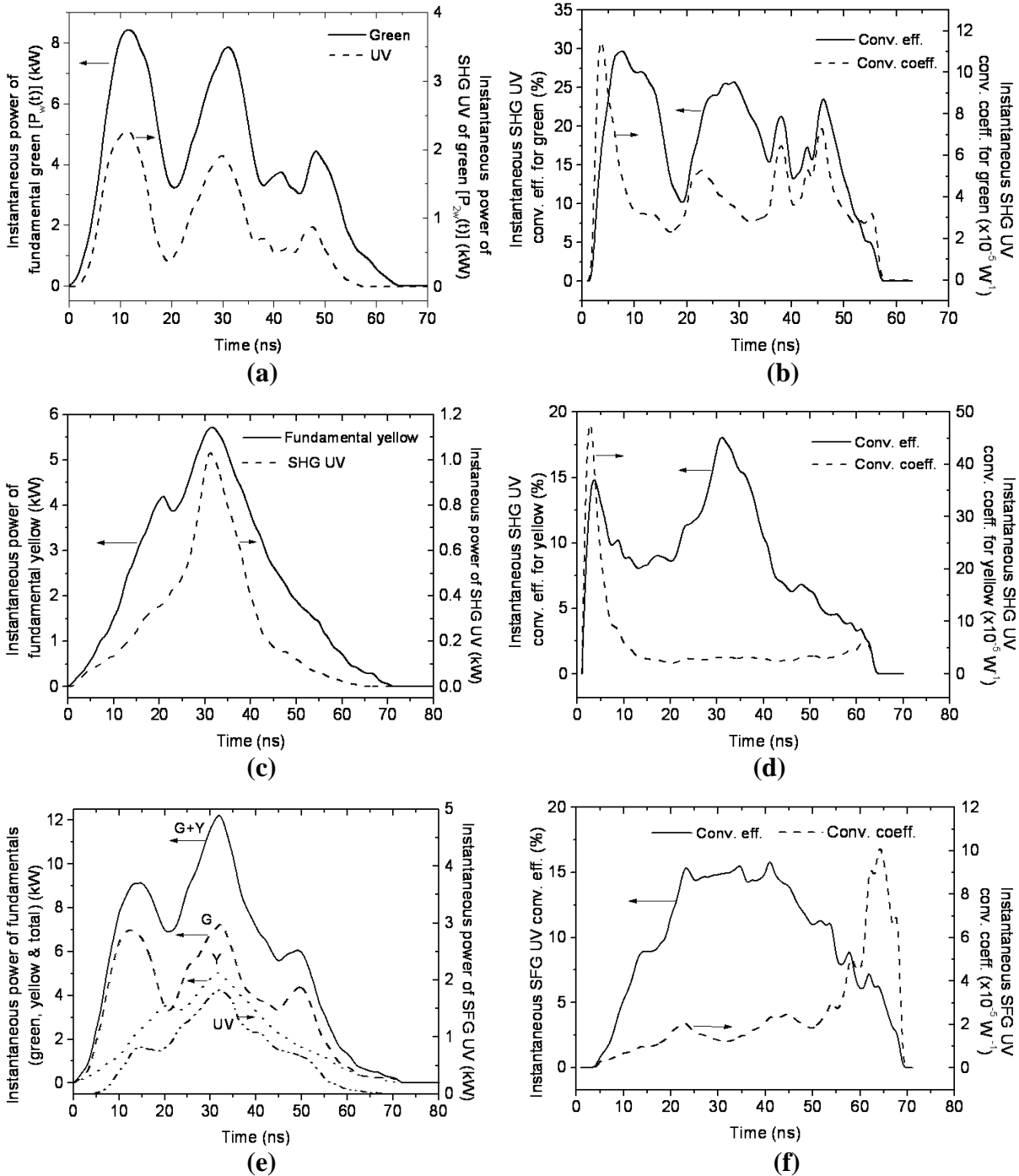


Fig. 9.10 Variation of instantaneous pump power & UV output power and UV conv. eff. & conv. coefficients for Cu-HBrL with PBUR M=50: (A) SHG of green (a, b), (B) SHG of yellow (c, d) and (C) SFG of green & yellow

conversion efficiencies as well as coefficients on their leading and trailing edges (typically 5-10 ns ns in the beginning as well as at the end). Therefore, the spikes at the start and end of the conversion coefficients (Figs. 9.10 b, d & f) are indicative of large uncertainties at the leading

and trailing edges of the light pulses owing to the fact that there are errors introduced from optical delays and detector bandwidths, and these may be exacerbated at the low light signal.

It is observed that for SHG of G (Figs. 9.10 a & b), the instantaneous UV power follows that of the fundamental G. However, the UV pulse starts with a delay of about 3-4 ns from the onset of the G pulse ( $t = 0$ ) and also ends  $\sim 10$  ns earlier than that of G pulse. Both the the G fundamental and SHG UV pulses peak at  $\sim 8.436$  kW and  $\sim 2.278$  kW respectively 10-12 ns after the onset of the G pulse, that corresponds to instantaneous conversion efficiency of 27%. However, maximum value of  $\eta_{2\omega}(g)(t)$  of  $\sim 30\%$  ( $1.93$  kW/ $6.43$  kW) is observed at  $t = 8$  ns (Fig. 9.10 b), which corresponds to the leading edge of the fundamental pulse. It is interesting to note that the values of  $\eta_{2\omega}(g)(t)$  at  $\sim 25\%$  is maintained over most of the duration of the pump pulse. The conversion coefficient,  $C_{2\omega}(g)(t)$  shows oscillatory behaviour between the values of  $2-6 \times 10^{-5} \text{ W}^{-1}$  (neglecting the values corresponding to initial  $\sim 5$  ns, owing to noise & inaccuracy). On the other hand, for the SHG of Y (Figs. 9.10 c & d), the instantaneous UV power doesn't follow that of the fundamental Y, however their peaks almost coincide in time. The SHG UV pulse of the Y builds up slowly and is finished early. Both the yellow fundamental and its SHG UV peak at  $t = 31$  ns with respective peak values of  $\sim 5.47$  kW &  $\sim 1.05$  kW, that corresponds to conversion efficiency of  $\sim 19.2\%$ . However, transient value of the conversion coefficient,  $C_{2\omega}(y)(t)$  is almost constant at  $2.7-2.8 \times 10^{-5} \text{ W}^{-1}$  (neglecting the first  $\sim 10$  ns noise, which shows a peak in conv. coefficient). This is expected, as the transient conversion efficiency values are not high to cause depletion like that of G. The values of  $\eta_{2\omega}(y)(t)$  of more than 15% exist only for 5-6 ns ( $t = 30-36$  ns). Therefore, the average conversion SHG UV efficiency of Y is lower than that of G.

The case of SFG of G and Y depends on extent of matching of their spatial and temporal intensities. Ideally, the best SFG process requires equal intensities of the G and Y components, both in space and time. In practice, it is very difficult to realise these ideal

conditions due to their different gain characteristics. However, with the use of high magnification unstable resonators, these conditions can be partly realised. It is observed that the SFG UV pulse starts with a delay of 5-6 ns than that of the fundamental pulses and is finished 7-8 ns earlier (Fig. 9.10 e). It is also observed that, the peak of SFG UV coincides with that peak of the combined G+Y with corresponding values of  $\sim 1.836$  kW [ $P_{\omega_3(t)}$ ] &  $\sim 12.335$  kW [ $P_{(g+y)(t)}$ ], corresponding to  $\eta_{\omega_3(t)} \sim 14.9\%$  at  $t=32$  ns (Fig. 9.10 f). However, the highest value of  $\eta_{\omega_3(t)}$  of  $\sim 16.3\%$  is observed at  $t=41$  ns, with values of  $P_{(g+y)(t)} \sim 6.751$  kW & that of  $P_{\omega_3(t)} \sim 1.102$  kW. In most of the duration of pump pulse (neglecting the early and end 5-10 ns values), the values of  $C_{\omega_3(t)}$  lie in the range of  $1.5 - 2.5 \times 10^{-5} \text{ W}^{-1}$ . At the highest value of  $P_{\omega_3(t)}$ , the ratio of instantaneous powers of G & Y is  $\sim 1.45$  ( $= 7.305 \text{ kW} / 5.03 \text{ kW}$ ). On the other hand, the highest value of  $\eta_{\omega_3(t)}$  corresponds to the ratio of instantaneous powers of G & Y of  $\sim 1.24$  ( $= 3.733 \text{ kW} / 3.018 \text{ kW}$ ). Under the approximation of almost constant divergence within most part of the pulse (as applicable for high magnification resonators), the ratio of pump beam spot widths of G to Y beams, on the BBO crystal, is  $\sim 1.24$  ( $= 47 \mu\text{m} / 38 \mu\text{m}$ ). The ratio of their peak intensities are  $\sim 1.17$  ( $= 6.2 \text{ MW.cm}^{-2} / 5.3 \text{ MW.cm}^{-2}$ ) &  $\sim 0.99$  ( $= 3.16 \text{ MW.cm}^{-2} / 3.18 \text{ MW.cm}^{-2}$ ) for maximum values of instantaneous SFG UV power and instantaneous conversion efficiency respectively [255]. Similar analysis for all other studied resonators explains the observed results.

## 9.6 Thermal effects on UV pulse train

In multi-kHz PRR SHG/SFG of Cu-HBr laser, the thermal dephasing is supposed to be the major performance limiting mechanism. This is due to absorption of fundamental & generated UV radiations and play detrimental role even at moderate average pump power levels. The absorption raises the temperature of the crystal in the pump region and leads to refractive index non-uniformities/mismatch & subsequent deterioration of the SHG/SFG process [237, 232, 234, 250]. For a high PRR Cu-HBrL, the temperature rise in the interaction

region is a consequence of the absorption based cumulative heating due to the optical pulse separation time ( $\sim 50 \mu\text{s}$ ) being much less than the thermal diffusion time of the crystal ( $\sim 10\text{s}$  of ms) [252]. Therefore, it is very important to probe the thermal dephasing effects in high PRR SHG/SFG UV conversion to understand the limiting mechanisms. However, it is difficult to probe this thermal effect of such high PRR lasers and has not been paid sufficient attention for direct experimental elucidations.

In view of this, we describe a simple technique based on optically chopped fundamental pump beam (510.6 nm) for probing the pulse to pulse thermal dephasing effects in a BBO crystal employed for SHG UV conversion of Cu-HBrL operating at 18 kHz PRR. Modulated bunch of fundamental green pulse trains, also called macro-pulses, are generated using a mechanical chopper (Scitech Instruments: 300 D) which are used to study the SHG UV generation processes (Fig. 9.11 b to f). The experimental observations are analysed qualitatively and the deviation of SHG UV intensity from its square dependence on the fundamental beam is taken as the mark of the onset of thermal dephasing effects. The study is carried out on Cu-HBrL with plane-plane resonator, owing to its better intensity stability as compared to unstable resonator (as discussed in chapter 7). Typical chopping frequencies of 10 to 500 Hz and average pump fundamental powers of about 4 W & 7 W are used. Lower average power is chosen purposefully to keep the SHG UV conversion efficiency low, so that the effect of saturation of SHG conversion efficiency & thermal dephasing are decoupled. The basic experimental set up (Fig. 9.11a) is similar to that of Fig. 9.1, except that the fundamental beam obtained from beam splitter is demagnified to half of its size by a telescopic lens pair of focal lengths  $f_1 = 100 \text{ cm}$  &  $f_2 = 50 \text{ cm}$ . The optical chopper, placed along the beam path after the lens  $f_2$ , blocks numbers of pump pulses in periodic interval (depending on the set chopping rate), thus generating a macro-pulse. Within the period of two consecutive macro-pulses, the BBO crystal is allowed to be cooled naturally. The compressed & collimated pump beam of

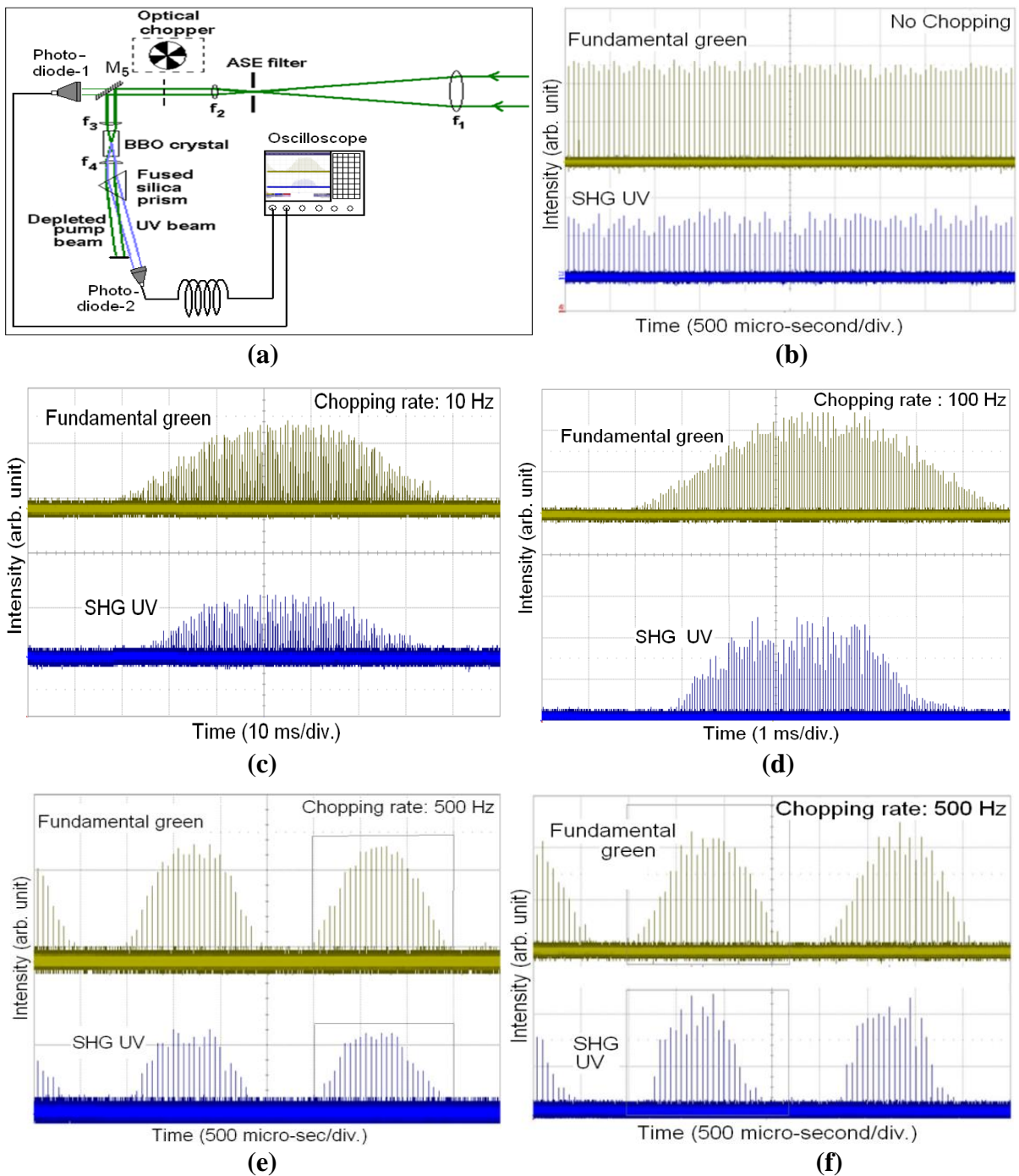


Fig. 9.11 Schematic of the SHG with chopped beam (a) and fundamental green & generated SHG UV pulse trains at 4 W (b: 0 Hz), (c: 10 Hz), (d: 100 Hz), (e: 500 Hz) & 7 W (f: 500 Hz)

12.5 mm diameter is spherically focused on the BBO crystal, by a spherical lens of focal length,  $f_3=10$  cm. At the un-chopped condition, the average SHG UV powers obtained are  $\sim 50$  mW &  $\sim 15$  mW respectively for fundamental pump power of 7 W & 4 W respectively. The pulse trains are recorded using a pair of identical biplaner photodiodes (synchronised) and a 500

MHz oscilloscope, as described earlier.

Fig. 9.11b shows the pulse trains of fundamental green and generated SHG UV radiations for unchopped conditions (chopping rate: 0 Hz) at 4 W pump power. It is observed that at the unchopped condition in steady state, the UV pulse trains do not follow the square dependence of the fundamental green pulse train completely. This could be due to pulse to pulse variation in divergence & pointing stability of the green pulses, apart from bulk heating of the crystal. Fig. 9.11c shows the fundamental and SHG UV pulse trains at chop rate of 10 Hz. It is observed that, the macro-pulse of SHG UV almost follows the fundamental pulse (neglecting the pulse to pulse effects) upto initial 30 ms, beyond which the UV macro-pulse slows down. This trend is observed for any arbitrary chosen macro-pulse bunch. Since the effect of pulse to pulse variation of beam divergence and pointing instability are statistical in nature, their role on the onset of the asymmetry on UV macro-pulse beyond 30 ms, in periodic manner, is ruled out. Also, the SHG conversion efficiency is very low ( $\sim 0.4\%$ ), therefore, the effect of any kind saturation phenomena is also ruled out. Hence, the reason of the asymmetry is attributed to onset of the thermal dephasing effects due to cumulative pulse to pulse heating with separation between pump pulse of  $\sim 55.56 \mu\text{s}$  much less than thermal diffusion time (of the crystal) of 10s of ms. To confirm the proposition, the chopping rate is further increased to 100 Hz & 500 Hz, at the same unchopped pump average power of 4 W. It is observed that, at chopping rate of 100 Hz, the asymmetry in the UV macro-pulse starts after  $\sim 4$  ms while for 10 Hz case, the asymmetry is observed after 30 ms. This is, possibly, due to increased thermal dephasing effects at 100 Hz chopping frequency as compared to that in 10 Hz case. The higher chopping rate leads to smaller time gap between two consecutive macro-pulses, thereby causing the diffusion of the deposited heat from the interaction region to be less effective. This proposition is in line with the observation of higher asymmetry/deviation (due to larger thermal dephasing effects) observed for higher chop rate of 500 Hz as well as with higher pump power

of 7 W as shown in Figs. 9.11e & f.

Hence, the thermal dephasing induced by pulse to pulse heating of the BBO crystal during the process of SHG UV conversion process, is noticeable even at moderate fundamental/UV average power much below  $P_{cr}$ . This is because the heat deposition is in a very small interaction volume ( $\sim 8 \times 10^{-5} \text{ cm}^3$  as estimated for present case, limited by beam walk-off effect) by the pump beam of peak power of the order of a few kW. Such localized heat source is strong enough to induce heating effect, change the refractive index and thereby adversely affecting the phasing between pump and SHG/SFG beams, as observed.

## 9.7 Conclusions

In conclusion, this chapter presented an extensive study on the high repetition rate ( $\sim 18$  kHz) SHG/SFG UV (255.5, 289.1 & 271.2 nm) generation of both the green (510.6 nm) and yellow (578.2 nm) radiations of Cu-HBr laser, in a type-I, critically phase matched BBO crystal. The fundamental beam average power is limited to about 10 W and the limitations based thermal constraints are discussed in detail. The details of the experimental results on the optimization of SHG/SFG UV conversion efficiency as well as conversion coefficients as a function of pump focal length of the focusing cylindrical lens, fundamental beam optical power and optical resonator and/or their magnifications (beam quality) from 1 to 100, are presented. Temporal variation of the SHG/SFG conversion efficiencies and conversion coefficients are evaluated from analysis based on optical pulses of the fundamental and generated UV beams. In order to assess the limiting thermal dephasing issues, detrimental for high repetition rate UV generation, the SHG process is also studied with mechanically chopped fundamental beams of different chop rate & pump power and the results are analysed. The SHG/SFG average UV output powers of around 2 W, 1.5 W & 1 W are achieved at 255.3 nm, 271.2 nm & 289.1 nm respectively at 18 kHz PRR. The average/peak UV conversion efficiencies achieved are about 25%/30% (255.3 nm), 18%/19.2% (289.1 nm) and 12.8%/14.9% (271.2 nm) respectively.

## Chapter 10

### Summary and future scope

#### 10.1 Summary of the thesis

The present thesis is a comprehensive research work on the technology development of high average power (upto ~110 W) and high PRR (16-18 kHz) Cu-HBr lasers (510.6 & 578.2 nm) of different active volumes followed by frequency extension to mid-UV regions (watt-level average power) through nonlinear frequency conversion. The core thesis works include detailed studies on the Cu-HBr laser system development, laser parameter studies, analysis of electrical power deposition into laser medium, HBr gas purification for enhanced laser performance, evaluation of thermal lensing behaviour, studies on spatial & spectral beam quality characteristics for both the green (510.6 nm) & yellow (578.2 nm) radiations with plane-plane & unstable optical resonators and studies on wavelength extension to high PRR coherent UV (255.3 - 289.1 nm) radiations, of 1 to 2 W average power, through efficient second harmonic & sum frequency generations. The thesis work has led to the successful technology development of Cu-HBrLs of various power levels, new research results into the field and efficient high PRR UV generation with high potential for utilization.

A Cu-HBrL system relies on successful development and integration of associated subsystems followed by a systematic parametric optimization study. In view of this, the thesis starts with a comprehensive work on design, construction/development and laser output power optimization studies on different output power versions of Cu-HBrLs. These include thermal design of the laser, mechanical design of the laser electrodes & discharge tubes, design of precision gas mixing set up for Neon & HBr gases and design & development of high-PRR, high-voltage & fast-switching electrical excitation sources. These subsystems are successfully developed, assembled and integrated for realisation of different average output power versions (40, 70, 85 & 110 W) of Cu-HBrLs (designated Cu-HBrL 1, 2, 3 & 4), differing mainly in their

active volumes. Two types of electrical power supplies e.g. thyatron and IGBT switch based pulsers are designed, developed and employed for the electrical excitation of these lasers. The safety handling of HBr is also addressed through incorporation of suitable HBr sensor and alarm system. The laser output powers have been studied for different laser operating parameters such as buffer gas pressures & flow rates, HBr concentrations, pulse repetition rates and switched electrical input powers. The results on the developed Cu-HBrLs are presented and discussed in detail. This work presents a comprehensive guideline for designing of Cu-HBrL systems. These developed Cu-HBrLs are further analyzed for electrical discharge characteristics for performance evaluation and supplemented with experimental & analytical works on spatial & spectral beam quality for the intended application of high PRR, high average power UV generation.

The electrical discharge characteristics of a Cu-HBr laser is of crucial importance for performance optimization, evaluation and understanding of the plasma processes in the active medium. Due to high electron attachment property, the HBr additive in Cu-HBrL affects the plasma electron density. This in turn influences the impedance matching and electrical power deposition into the plasma. These aspects of a Cu-HBrL are still not very well understood in the field, specifically at high average output power and/or with solid state pulser. In view of this, a comprehensive analysis on both the time resolved & time averaged electrical pulse pumping characteristics, on the developed 40 to 110 W average power Cu-HBrLs (Cu-HBrL 1 to 4), are carried out. This is implemented by numerically processing the laser discharge voltage and current waveforms, recorded for various laser operating parameters and active volumes. The fractional losses at various intermediate stages of the circuit elements as well as effective coupling for the laser excitation process are estimated. The average laser performances at various input powers are correlated with both the time resolved and average gas discharge parameters. It is observed that irrespective of the switched input power of IGBT-

solid state pulser, the fractional electrical energy coupled to the Cu-HBrL plasma is almost constant (~40%). The loss in the electrical power is mostly in MPCs, pulse transformers and other circuit elements. Based on this analysis, the Cu-HBrL tube efficiencies are estimated to be more than 2%, at the maximum laser output power. A comparative performance study between Cu-HBrL & CVL of identical geometry, pumped by thyatron pulser, is also carried out. It is concluded that energy coupling from the modulator to the laser active medium is better for Cu-HBrL plasma (~80% for Cu-HBrL vs. ~70% for CVL). This is attributed to better impedance matching in a Cu-HBr laser. The energy loss in case of the thyatron pulser is attributed to the thyatron switch. Though the IGBT solid state pulser has low overall efficiency in depositing energy into Cu-HBrL plasma, this is preferred due to their capability of high average power handling at high PRR, long life times and operational reliability. This study provides guideline for the efficient electrical pulse pumping of a Cu-HBrL vis-à-vis quick laser power optimisation by monitoring and online analysis of the laser discharge voltage & current waveforms.

The HBr gas is the most crucial component of Cu-HBrL and is responsible for high performance of Cu-HBr lasers in the copper laser family. It favourably controls the laser plasma kinetics through dissociative attachment process during the inter-pulse period and improves the laser performance. However, due to extremely corrosive/reactive nature of HBr, the impurities such as dissociation and reactant products (hydrogen and bromine) creep in during the overall process of its manufacturing, storage and handling. Therefore these impurities present in HBr gas, are likely to poison the discharge in terms of their deleterious effects on the evolution of the intra-pulse electron energy distribution and discharge parameters. These subsequently affect the laser kinetics detrimentally and degrade the laser performance. However, this issue has not been paid sufficient attention previously. In view of this, a purification process of HBr gas, by fractional distillation, is worked out and implemented. The principle of the purification

technique, development of a suitable HBr gas purification set up and their mass spectrometry analysis before/after the purification process are presented. The purified HBr gas is utilized for enhancement of the developed Cu-HBr laser, in a test set up, followed by an analysis of its discharge characteristics, to understand the physical mechanism. Around 30% improvement in the laser output power of Cu-HBrL, has been demonstrated with purified HBr gas. The effects of the distilled HBr gas on the laser output power, efficiency and beam diameter are presented. The electrical discharge characteristics such as change in discharge impedance and electrical power coupled into the discharge are analysed for both the distilled/undistilled HBr gases. The underlying physics behind the improved laser performance with purified HBr gas is discussed. This work provides an added guideline for the improved performance of a Cu-HBr laser.

Following the successful technology development of high average power Cu-HBr lasers, the next logical step is their spatial and spectral beam quality characterisation. These aspects are of crucial importance for planning of utilisation of this laser for various applications in general and for the planned SHG/SFG study in particular. Out of the four Cu-HBrL systems developed, the studies are limited to one Cu-HBrL system (Cu-HBrL 2), which are also equally valid for all other laser systems as well. The first such study, taken up, is the thermal lensing behaviour of Cu-HBrL, which originates owing to inhomogeneous radial temperature distribution. The experimental study is carried out using interferometer techniques and the results are also compared with that of a conventional CVL of identical discharge tube geometry and excitation conditions. It is observed that in typical operating conditions, Cu-HBrL has much weaker thermal lens power as compared to that in CVL ( $\sim +0.95 \text{ km}^{-1}$  vs.  $\sim +13 \text{ km}^{-1}$ ). This indicates that the wave front integrity of a Cu-HBrL beam is much better than that of conventional CVL. The experimental results are explained qualitatively by a comprehensive theoretical analysis on the gas thermal lens as well as the window thermal lens, taking into

account the radial temperature distribution, thermal conductivity, temperature coefficient of the refractive indices of the media involved and the heat flux reaching the windows & its absorption. It is observed that the contribution of the windows thermal lens dominates over that of the gaseous active medium. The dominance of window thermal lens in overall thermal lensing of Cu-HBrL/CVL is attributed to higher temperature coefficient of refractive index for window material as compared to that of gaseous active medium ( $\partial n/\partial T \sim +10^{-5} \text{ K}^{-1}$  vs.  $\sim -10^{-10} \text{ K}^{-1}$ ). The smaller overall thermal lens power of Cu-HBrL as compared to that of CVL is due to its much lower working temperature as well as relatively flatter radial gas temperature profile. The analysis agrees well with the observed trends.

The next important aspect of Cu-HBrL radiations, with particular emphasis of SHG/SFG UV generation is the knowledge of spectral emission characteristics. This aspect is not paid due attention for Cu-HBrL in literature, which is expected to be different than other copper laser variants owing to its different gas composition, operating temperature and gain distribution. In view of this, a detailed experimental study and the related theoretical analysis on the spectral emission characteristics of both the green and yellow radiations of Cu-HBrL is carried out as a function of electrical input power, HBr concentration and optical resonator (plane-plane: PPR & unstable: UR). A high precision Fizeau interferometer based wavelength meter is used in the study. It is observed that the effects of electrical input power and HBr concentration are crucial on Cu-HBrL spectral line-emission characteristics. At typical laser operating condition, the emission line-width of Cu-HBr laser varies within ~4 to ~5 GHz for green component and within ~6 to ~9 GHz for yellow component, with the line-width and emission frequency (central) fluctuation of few 10s to 100s of MHz. These trends are largely independent of the resonator used. The experimental observations are explained by a comprehensive theoretical analysis followed by simulation of the spectral emission line-shapes of both the radiations. This is carried out by taking into account the isotopic shift, hyperfine

splitting and relevant line broadening effects (mostly Doppler) associated with the energy levels of a neutral copper atom. The theoretical results, in conjunction with the temperature & laser gain distribution effects, agree well with the observed trends.

The Cu-HBr laser beam divergence & pointing stability are crucial parameters, to be elucidated, for applications requiring finely focused beams such as second-harmonic/sum-frequency UV generation, as planned in the thesis. These issues are more relevant for a Cu-HBrL due to its operation at high PRR, high specific power conditions that leads to increased power loading and thermally induced phenomena affecting the spatio-temporal laser beam characteristics. The beam quality aspects of Cu-HBr lasers have not been paid due attention in the past. In view of this, a comprehensive experimental study is carried out on beam quality aspects of both the green and yellow radiations of the Cu-HBrL for different laser operating conditions, using a time-gated CCD camera. The experimental results on variation of far-field divergence and pointing stability with different electrical input powers, HBr concentrations and optical resonators (PPR & UR M=12.5, 50 & 100) are presented in detail. Both the time averaged and pulse to pulse variations are studied. The experimental study is augmented with near-field spatial intensity profiles & temporal pulse shapes of both the radiations.

It is observed that for all the input powers & resonators used, the near-field radial intensity profiles are axially peaked (quasi-Gaussian) for both the green & yellow beams. The far-field beam divergence, pointing instability and their fluctuations as well as far-field intensity variations scales up (degrades) with increase in the input power to Cu-HBrL. The beam quality also degrades with change in HBr concentration away from the optimized level. The beam divergence & its variation and pointing stability of both the green & yellow components improve significantly with the increase of the optical resonator magnifications from  $M \approx 1$  (PPR) to  $M = 100$  (UR). At the same time, the pulse to pulse far-field intensity variation worsens when the optical resonator is changed from PPR to PBURs. Among the URs,

increase in magnification value leads to reduced variation in the far-field intensity. Also the green & yellow components have different beam quality characteristics. For same electrical input power ( $\sim 5$  kW) & optimized HBr concentration ( $\sim 6\%$ ) the far field divergence reduces from  $1500 \pm 25$   $\mu$ rad to  $90 \pm 20$   $\mu$ rad for green component and from  $1400 \pm 28$   $\mu$ rad to  $71 \pm 20$   $\mu$ rad for yellow component as resonator magnification is scaled from 1 (PPR) to 100 (UR). For the same range of resonator magnification (1 to 100), the beam pointing instability reduced from  $\pm 30$   $\mu$ rad to  $\pm 17$   $\mu$ rad for the green component and  $27$   $\mu$ rad to  $\pm 12$   $\mu$ rad for the yellow component. In terms of diffraction limit (DL), the variations in the corresponding beam divergence are  $24.08 \pm 0.4$  DL to  $1.43 \pm 0.32$  DL for the green beams and  $19.84 \pm 0.4$  DL to  $1.01 \pm 0.28$  DL for the yellow beams respectively. The observed results are suitably analysed taking into account the tube aspect ratio, theoretical divergence evolution within a Cu-HBr laser pulse, spatio-temporal laser gain characteristics, thermally induced perturbations and diffraction.

Following the successful development of Cu-HBrLs and comprehensive beam quality studies for both the G and Y radiations, the obtained high quality beams are used for high PRR (18 kHz) SHG & SFG UV (255.5, 289.1 & 271.2 nm) generation in a type-I, critically phase matched BBO crystal. The fundamental beam average power is limited to about 10 W due to thermal constraints as brought out. An extensive experimental study is carried out on the optimization of UV conversion efficiency as a function of focal length of the pump focusing cylindrical lens, fundamental optical power and optical resonator of different magnifications (beam quality) from 1 to 100. The temporal variation of SHG/SFG conversion efficiencies and coefficients are evaluated from analysis on optical pulses of the fundamental and generated UV beams. The SHG/SFG average UV output powers of around 2 W, 1.5 W & 1 W are achieved at 255.3 nm, 271.2 nm & 289.1 nm respectively at 18 kHz PRR. The average/peak UV conversion efficiencies achieved are about 25%/30% (255.3 nm), 18%/19.2% (289.1 nm) and

12.8%/14.9% (271.2 nm) respectively. The SHG process is also studied with mechanically chopped fundamental beams of different chop rate & pump power to assess the thermal dephasing issues.

In summary, the overall thesis, containing two reviews in the field and going through the stages such as technology development of high average power Cu-HBrLs (40 to 110 W @ 18 kHz PRR), thorough electrical and optical characterisation supported by appropriate analysis, the detailed study on SHG/SFG leading to highly efficient 1-2 W average UV power generation and finally ending with future scope of the work, is comprehensive and meaningful document in the field under the thesis titled “Studies on Copper - Hydrogen Bromide (Cu-HBr) laser and its nonlinear frequency conversion”. The whole work has been published in several peer reviewed journals of high impact factors as well as in book, conference proceedings & newsletters.

## **10.2 Scope for future work**

The low temperature, fast start-up time, high average power, high efficiency, high beam quality, 10s of ns duration Cu-HBr lasers, emitting coherent radiations in the green-yellow spectral region at 15-20 kHz PRR, have a lot of future scope for technology development as well as applications in the emerging research areas. From technology point of view, some of the major areas that need immediate attention, for Cu-HBrL, are exploring the possibility of sealed off operation with use of suitable chemicals and/or their combinations for in-situ generation of HBr gas inside the active region, controlling the growth of dendrites on copper pellets in the discharge region as well as window contamination due to deposition of copper compounds diffused from the hot discharge region, both of which reduce the laser power after few tens to hundreds of hour operation. Cumulative dissociation of HBr in high temperature environment of the Cu-HBrL discharge region is thought to be a limiting factor for high power operation. This issue needs to be studied further and suitable kinetic mechanism must be

explored to resolve the issue and explore the possibility of kW average power class Cu-HBrL for industrial applications. In addition, there is no reliable computer simulation studies reported so far on Cu-HBrL, due to lack up of appropriate rate constants for the physical/chemical processes involved. Necessary research works need to be carried out in this direction for further understanding of the physical mechanisms involved in Cu-HBrL.

Coupled with simple nonlinear frequency conversion for generation of discretely tunable, coherent mid-UV (255.3-289.1 nm) generation, this laser can be an efficient source for high speed precision processing of materials such as fabrication of photonics components (core/surface Bragg gratings) on photosensitive materials and micromachining of metals & ceramics. Due to excellent beam characteristics, this laser is an ideal pump source for generation of 15-20 kHz PRR, tunable UV-visible-near IR lasers, through pumping of dye & Ti:Sapphire lasers and/or their frequency doubling required for isotope selective photo-ionisation spectroscopy, without going through the route of complex optical/electronic multiplexing of CVLs. In the area of high average power, SHG/SFG UV generation, thermal dephasing issues must be suitably explored and appropriate mitigation techniques e.g. cooling of the crystals and/or beam shaping techniques etc. must be explored. Frequency doubled Q-switched solid state lasers are emerging as alternate high PRR, high average power pulsed visible sources. However, the features of high PRR Cu-HBrLs such as ease of average power scalability to 100s of watt in visible range without going through the route of nonlinear frequency doubling and capability to produce high quality laser beams, are advantageous over the solid state lasers.



## REFERENCES

- [1] E. S. Livingstone, D. R. Jones, A. Maitland and C. E. Little, *Opt. and Quant. Electron.* **24**, 73-82 (1992).
- [2] W. T. Walter, M. Piltch, N. Solimene and G. Gould, *Bull. Am. Phys. Soc.* **11**(1),113 (1966).
- [3] W. T. Walter, M. Piltch, N. Solimene and G. Gould, *IEEE J. Quant. Electron.* **QE-2(9)**, 474-479 (1966).
- [4] D. R. Jones, N. V. Sabotinov, A. Maitland and C. E. Little, *Opt. Comm.* **94**, 289-99 (1992).
- [5] D. R. Jones, A. Maitland and C. E. Little. *Opt. and Quant. Elect.* **25**, 261-69 (1994).
- [6] D. R. Jones, A. Maitland and C. E. Little, *IEEE J. Quant. Electron.* **30** (10), 2385-2390 (1994).
- [7] E. L. Guyadec, P. Countance, G. Bertrand and C. Peltier, *IEEE J. Quant. Electron.* **35(11)** 1616-22 (1999).
- [8] D. J. W. Brown, C. G. Whyte, D. R. Jones and C. E. Little, *Opt. Comm.* **137**, 158-164 (1997).
- [9] P. Countance, G. Naylor, J. P. Pique, *IEEE J. Quant. Electron.* 31(10), 1747-1752 (1995).
- [10] R. P. Mildren, D. R. Jones, D. J. W. Brown, *J. Phys. D: Appl. Phys.* **31**, 1812-16 (1998).
- [11] R. Biswal, G. K. Mishra, P. K. Agrawal, O. Prakash, S. K. Dixit and J. K. Mittal, *Opt. Engg.* **50(8)**, 084202 (2011).
- [12] R. Biswal, G. K. Mishra, P. K. Agrawal, S. V. Nakhe, S. K. Dixit, *Applied Optics* **52(14)**, 3269-78 (2013).
- [13] R. Biswal, P. K. Agrawal, O. Prakash, G. K. Mishra, S. K. Dixit and S.V. Nakhe, *IEEE J. Quant. Electron.* **50(2)**, 112-119 (2014).
- [14] R. Biswal, P. K. Agrawal, G. K. Mishra, S. V. Nakhe, S. K. Dixit and J. K. Mittal, *Pramana - Journal of Phys.* **75(5)**, 953-959 (2010).
- [15] C. E. Little ed., *Metal Vapour Lasers: Physics, Engineering and Applications* (Wiley, New York: 1999).
- [16] C. E. Little and N. V. Sabotinov eds. *Pulsed Metal Vapour Lasers: Physics and Emerging Applications in Industry, Medicine and Science* (Kluwer Academic: 1996).
- [17] G. G. Petrash ed., *Metal vapour and metal halide vapour lasers* (Nova Science: 1989).

- [18] G. K. Mishra, R. Biswal, Sachin Agrawal, O. Prakash and S. K. Dixit, *Optik - Int. J. of Light Electron Optics* **124**, 1595-1600 (2013).
- [19] M. Laubscher, P. Segonds and J. P. Pique, *Optics Comm.* **184**, 425-435 (2000).
- [20] O. Prakash, J. Kumar, R. Mahakud, S. K. Agrawal, S. K. Dixit and S. V. Nakhe, *IEEE Photonics Tech. Letters*, **26(1)**, 93-95(2014).
- [21] P. Jafarkhani, M. J. Torkamany, S. Dadras , A. Chehrghani, J. Sabbaghzadeh , *Nanotechnology* **22** (23), 235703 (2011).
- [22] V. T. Karpuhin, M. M. Malikov, T. I. Borodina, G. E. Val'Yano, O. A. Gololobova, *High Temp.* **49(5)**, 679-684 (2011).
- [23] Y. Liu, J. Li, Y. Gao and X. Yuan, *Adv. Materials Research* **443-444**, 986-995 (2012).
- [24] M. S. Fernandes De Lima, F. P. Ladario, D. Neves and A. E. Diniz, *Int. J. of Surface Science and Engg.* **5** (2-3), 98-115 (2011).
- [25] S. V. Kireev, S. L. Shnyrev, I. G. Simanovsky and S. V. Suganev, *Laser Phys. Lett.* **11(9)**, 095701 (2014).
- [26] E. V. Barmina, A. V. Simakin, and G. A. Shafeev, *Quant. Electronics* **44(8)**, 791-792 (2014).
- [27] G. S. Evtushenko, M. V. Trigub, F. A. Gubarev, S. N. Torgaev, D. V. Shiyanov, *Rev. Scient. Instru.* **85(3)**, 033111 (2014).
- [28] H. Wu, K. Nithyanandan, T. H. Lee, C. F. F. Lee and C. Zhang, *Energy & Fuels* **28(10)**, 6380-6391 (2014).
- [29] S. V. Lotarev, A. S. Lipatiev, N. V. Golubev, A. Paleari, V. N. Sigaev, *Material Lett.* **122**, 124-177 (2014).
- [30] T. Stephens, *Laser Focus World* **49(9)**, 56-58 (2013).
- [31] O. Prakash, R. Mahakud, R. Biswal, S. Gurram, H. S. Vora and S. K. Dixit, *Applied Optics* **46(24)**, 6210-6217 (2007).
- [32] L. A. Weaver, C. S. Liu and E. W. Sufov, *IEEE J. Quant. Electron.* **QE-10(2)**, 140-7 (1974).
- [33] M. J. Kushner, *IEEE J. Quant. Electron.* **17(8)**, 1555-1565(1981).
- [34] R. J. Carman, D. J. W. Brown and J. A. Piper, *IEEE J. Quant. Electron.* **QE - 30(8)** 1876-95 (1994)
- [35] M. J. Kushner and B. E. Warner, *J. Appl. Phys.* **54(6)**, 2970-2982 (1983).
- [36] C. E. Webb and G. P. Hogan, in *Pulsed Metal Vapour Lasers: Physics and Emerging Applications in Industry, Medicine and Science* (C. E. Little and N. V. Sabotinov eds.), Dordrecht: Kluwer Academic publishers, 29-42 (1996)

- [37] A. A. Isaev and G. G. Petrash, *Proc. SPIE 2110, Metal vapour Lasers and their Applications* (ed. G. G. Petrash), 2-45 (1993).
- [38] I. Smilanki, L. A. Levin and G. Erez, *Opt. Lett.* **5(3)**,93-5 (1980)
- [39] D. J. W. Brown, R. Kunemeyer and A. I. McIntosh, *IEEE J. Quant. Electron.* **QE-26(9)**, 1609-19 (1990).
- [40] P. A. Bokhan, V. I. Solomonov and V. B. Shcheglov, *Sov. J. Quant. Electron.* **7(8)**, 1032-33 (1977).
- [41] Pinhas Blau, *IEEE J. Quant. Electron.* **30(3)**, 763-769 (1994)
- [42] P. Blau, *J. Appl. Phys.* **77(6)**, 2273-2278 (1995).
- [43] V. M. Zharikov, V. V. Zubov, M. A. Lesnoi, N. A. Lyabin and A.D. Chursin, *Sov. J. Quantum Electron.* **14(5)**, 623-636 (1984).
- [44] P. Blau, I. Smilanski and S. Rosenwaks, *J. Appl. Phys.* **72(3)**, 849-854 (1992).
- [45] P. Liang, R. Hua and Q. Shen, *Appl. Phys. B* **60**, 557-563 (1995).
- [46] Q. Chen, P. Liang, J. Lei, Q. Shen and H. Ren, *J. Optics (Paris)* **27** (6), 253-258 (1996).
- [47] S. Singh and G. Sridhar, *Optics & Laser Technology* **32**, 89-91 (2000).
- [48] S. K. Dixit, R. Mahakud, O. Prakash, R. Biswal and J. K. Mittal, *Opt. Commun.* **281**, 2590-2597 (2008).
- [49] J. J. Chang, B. E. Warner, C. D. Boley & E. P. Dragon, in *Pulsed Metal Vapour Lasers: Physics and Emerging Applications in Industry, Medicine and Science* (C. E. Little & N. V. Sabotinov eds.), Dordrecht: Kluwer Academic publishers, 101-112 (1996).
- [50] D. Coutts and D. J. W. Brown, *Applied Optics* **34(9)**, 1502-1512 (1995).
- [51] R. Mahakud, O. Prakash, R. Biswal and S. K. Dixit, *Opt. Engg.* **45(2)**, 24201-7 (2006).
- [52] R. Carman, *J. Appl. Phys.* **82(1)**,71-83 (1997).
- [53] V. M. Batenin, V. A. Burmakin, P. A. Vokhmin, A. I. Evtynin, I. I. Klimovskii, M. A. Lesnoi and L. A. Selezneva, *Sov. J. Quantum Electron.* **7(7)**, 891-893 (1977).
- [54] G. P. Hogan, C. E. Webb, C.G. Whyte and C. E. Little, in *Pulsed Metal Vapour Lasers: Physics and Emerging Applications in Industry, Medicine and Science* (C. E. Little & N. V. Sabotinov eds.), Dordrecht: Kluwer Academic publishers, 67-72 (1996).
- [55] G. P. Hogan and C. E. Webb, *Opt. Commun.* **117**, 570-579 (1995).
- [56] J. J. Chang, *Applied Optics* **32(27)**, 5230-5235 (1993).
- [57] S. Gabay and I. Smilanski, *IEEE J. Quant. Electron.* **QE-16(6)**, 598-601(1980).
- [58] M. J. Withford, D. J. W. Brown and J. A. Piper, *IEEE J. Quant. Electron.* **QE-32(8)**, 1310-1315(1996).

- [59] K. Hayashi, Y. Iseki, S. Suzuki, I. Watanabe, E. Noda and O. Morimiya, *Jpn. J. Appl. Phys.* **31** part 2-Lett.(12A), L1689-1691(1992).
- [60] P. A. Bokhan and E. I. Molodykh, in *Pulsed Metal Vapour Lasers: Physics and Emerging Applications in Industry, Medicine and Science* (C. E. Little & N. V. Sabotinov eds.), Dordrecht: Kluwer Academic publishers, 137-148 (1996).
- [61] Z. G. Huang, K. Namba and F. Shimizu, *Jpn. J. Appl. Phys.* **25**(11), 1677-9(1986).
- [62] M. J. Withford, D. J. W. Brown, R. J. Carman and J. A. Piper, *Opt. Commun.* **135**, 164-170 (1997).
- [63] E. S. Livingstone and A. Maitland, *J. Phys. E: Sci. Instrum.* **22**, 63 (1989).
- [64] E. S. Livingstone and A. Maitland, *Meas. Sci. Technol.* **2**, 1119-20 (1991).
- [65] A. Ohzu, M. Kato, Y. Maruyama, *Opt. Commun.* **177**, 355-361 (2000).
- [66] H. Kimura, K. Hara, T. Iijima, T. Nayuki, E. Fujiwara and H. Saito, *Rev. Laser. Engg.* **4**(6), 670-8 (1996).
- [67] K. Oouchi, M. Suzuki and K. Fujii, *IEEE J. Quant. Electron.* **QE-27**(11), 2473-81 (1991).
- [68] S. Sakata, K. Oohori, M. Higuchi, K. Fijii,....., and H. Saito, *IEEE J. Quant. Electron.* **QE-30**(9), 2166-72 (1994).
- [69] K. Fujii, K. Uno, F. Tawada,...., and H. Saito, *Appl. Phys. Lett.* **80**(11), 1859-61 (2002).
- [70] H. Saito, Y. Shiraiwa, ....., and K. Fujii, *Appl. Phys. Lett.* **78**(15), 2113-15 (2001).
- [71] H. Kimura, M. Chinen, T. Nayuki and H. Saito, *Appl. Phys. Lett.* **71**(3), 312-4 (1997).
- [72] A. Ohzu, M. Kato, Y. Maruyama, *Appl. Phys. Lett.* **76**(21), 2979-81 (2000).
- [73] A. A. Isaev, M. A. Kazaryan and G. G. Petrash, *JETP Lett.* **16**(1), 27-9 (1972).
- [74] P. A. Bokhan, V. A. Gerasimov, V. I. Solomov and V. B. Scheglov, *Sov. J. Quant. Electron.* **8**, 1220 (1978)
- [75] B. E. Warner and M. J. Kushner, *Proc. Int. Conf. On Lasers '81*, STS press: McLean, VA, 845-52 (1982).
- [76] R. S. Anderson, B. G. Bricks, L. W. Springer and T. W. Karras, *IEEE J. Quant. Electron.* **QE-11**(9), 56D-57D (1975).
- [77] B. E. Warner, *Proc. SPIE 737* (L. R. Carlson ed.), 2-6 (1987).
- [78] B. E. Warner, *CLEO '91, Tech. Dig.*, Opt. Soc. Am., Washington, DC, 516-18 (1991).
- [79] P. A. Bokhan, V. I. Silantev and V. I. Solomonov, *Sov. J. Quant. Electron.* **10**(6), 724-7 (1980).
- [80] J. L. Emmet, W. F. Krupke and J. I. Davis, *IEEE J. Quant. Electron.* **20**, 591 (1984).

- [81] Y. Iseki, K. Hayashi, I. Watanabe, E. Noda and S. Suzuki, *Jpn. J. Appl. Phys.* **33**, Part 2(6B), L860-2 (1994).
- [82] J. J. Chang, C. D. Boley, M. W. Martinez, W. A. Molander and B. E. Warner, *Proc. SPIE* **2118** (V. N. Smiley and F. K. Tittel eds.), 2-8 (1994).
- [83] C. Konagai, H. Kimura, N. Aoki, N. Kobayashi, S. Iizuka and Y. Baba, *Proc. 15<sup>th</sup> Annual Meeting Laser Soc. Jpn.*, Osaka, **15**, 112 (1995).
- [84] R. P. Hackel and B. E. Warner, *Proc. SPIE* **1859**, Laser Isotope Separation (J. A. Paisner ed.), 120-9(1993).
- [85] M. J. Withford, D. J. W. Brown, R. J. Carman and J. A. Piper, *Opt. Lett.* **23**, 706-(1998).
- [86] M. J. Withford, D. J. W. Brown and J. A. Piper, *Opt. Lett.* **23**, 1538-(1998).
- [87] R. P. Mildren, M. J. Withford, D. J. W. Brown, R. J. Carman, and J. A. Piper, *IEEE J. Quant. Electron.* **34**, 2275-(1998).
- [88] M. J. Withford, D. J. W. Brown, R. J. Carman and J. A. Piper, *Opt. Commun.* **154**, 160-(1998).
- [89] G. D. Marshall and D. W. Coutts, *IEEE Sel. Topic Quant. Electron.* **6**, 623(2000).
- [90] M. J. Withford, D. J. W. Brown, R. P. Mildren, R. J. Carman, G. D. Marshall and J. A. Piper, *Prog. In Quant. Electron.* **28**, 165-196 (2004).
- [91] R. P. Mildren, G. D. Marshall, M. J. Withford, D. W. Coutts and J. A. Piper, *IEEE J. Quant. Electron.* **39** (6), 773-777 (1998).
- [92] E. L. Guyadec, P. Nouvel and P. Regnard, *IEEE J. Quant. Electron.* **41**(6), 879-884 (2005).
- [93] C. S. Liu, E. W. Sucof and L. A. Weaver, *Appl. Phys. Lett.* **23**(2),92-3(1973).
- [94] C. J. Chen, N. M. Nerheim and G. R. Rusell, *Appl. Phys. Lett.* **23**(9),514-15 (1973).
- [95] N. V. Sabotinov, in *Pulsed Metal Vapour Lasers: Physics and Emerging Applications in Industry, Medicine and Science* (C. E. Little & N. V. Sabotinov eds.), Dordrecht: Kluwer Academic publishers, 113-124 (1996).
- [96] N. C. Perry and R. C. Tobin, *Appl. Phys. Lett.* **45**, 727 (1984).
- [97] A. J. Andrews, C. E. Webb, R. C. Tobin and R. G. Denning, *Opt. Commun.* **22**, 272 (1977).
- [98] S. Gabay, I. Smilanski, L. A. Levin and G. Erez, *IEEE J. Quant. Electron.* **QE-13**(5), 364-6 (1977).
- [99] D. N. Astadjov, N. V. Sabotinov and N. K. Vuchkov, *Opt. Commun.* **56**(4),279-82 (1985).

- [100] D. N. Astadjov, N. K. Vuchkov, A. A. Isaev, G. G. Petrash, I. V. Ponomarev and N. V. Sabotinov, *Sov. J. Quant. Electron.* **17**(2), 245-7 (1987).
- [101] D. N. Astadjov, A. A. Isaev, G. G. Petrash, I. V. Ponomarev, N. V. Sabotinov and N. K. Vuchkov, *IEEE J. Quant. Electron.* **QE-28**, 1966-9 (1992).
- [102] K. I. Zemskov, A. A. Isaev and G. G. Petrash, *Quant. Electron.* **27**(7), 579-83 (1997).
- [103] V. F. Elaev, G. D. Lyakh and V. P. Pelenkov, *Atm. Opt.* **29**(11), 1045-7(1989).
- [104] D. N. Astadjov, K. D. Dimitrov, D. R. Jones, V. Kirkov, C. E. Little, N. V. Sabotinov and N. K. Vuchkov, *IEEE J. Quant. Electron.* **QE-33**(5), 705-9 (1997).
- [105] D. V. Shiyarov, V. B. Sukhanov, G. S. Evtushenko and O. S. Andrienko, *Quant. Electron.* **34**(7), 625-9 (2004).
- [106] D. V. Shiyarov, G. S. Evtushenko, V. B. Sukhanov and V. F. Fedorov, *Quant. Electron.* **37**(1), 49-52 (2007).
- [107] E. B. Gordon, V. G. Egorov and V. S. Pavlenko, *Sov. J. Quant. Electron.* **9**(12), 1526-32 (1979).
- [108] C. J. Chen and G. D. Russell, *Appl. Phys. Lett.* **26**(9), 504-5 (1975).
- [109] M.A. Kazaryan and A. N. Trofimov, *Sov. J. Quant. Electron.* **89**(11), 1390-1 (1978).
- [110] D. N. Astadjov, K. D. Dimitrov, D. R. Jones, V. Kirkov, L. Little, C. E. Little, N. V. Sabotinov and N. K. Vuchkov, *Opt. Commun.* **135**, 289-94 (1997).
- [111] C. E. Little, D. R. Jones, S. A. Fairlie and C. G. Whyte, in *Pulsed Metal Vapour Lasers: Physics and Emerging Applications in Industry, Medicine and Science* (C. E. Little & N. V. Sabotinov eds.), Dordrecht: Kluwer Academic publishers, 125-136 (1996).
- [112] R. P. Mildren, K. E. Osgood and J. A. Piper, *Opt. And Quant. Electron.* **29**, 991-998 (1997).
- [113] N. V. Sabotinov, F. Akerboom, D. R. Jones, A. Maitland and C. E. Little, *IEEE J. Quant. Electron.* **31**(4), 747-753 (1995).
- [114] P. Countance and J. P. Pique, *IEEE J. Quant. Electron.* **34**(8), 1340-1346 (1998).
- [115] F. Girard, E. L. Guyadec and P. Delaporte, *J. Appl. Phys.* **89**(2), 843-848 (2001).
- [116] L. Little and C. E. Little, *Proc. SPIE* **3092**, 285-288 (1997).
- [117] H. M. Rosenstock, J. R. Sites, J. R. Walton and R. Baldock, *J. Chem. Phys.* **23**, 2442 (1955).
- [118] M. A. Kazaryan, G. G. Petrash and A. N. Trofimov, in *Proc. Lebedev Phys. Inst.* **181** (G. G. Petrsh ed.), Nova Science Publ.: Commack, 178-82 (1989).
- [119] K. P. Huber and G. Herzberg, *Molecular Spectra and Molecular Structure. IV. Constants of Diatomic Molecules*, Van Nostrand Reinhold: New York (1979).

- [120] D. R. Jones, S. N. Halliwell and C. E. Little, *Opt. Commun.* **111**, 394-402 (1994).
- [121] A. A. Isaev, D. R. Jones, C. E. Little, G. G. Petrash, C. G. Whyte and K. Zemskov, *IEEE J. Quant. Electron.* **33(6)**, 919-26 (1997).
- [122] D. R. Jones, A. Maitland and C. E. Little, *Proc. SPIE* **2118**, 42-50 (1994).
- [123] R. Riva, J. T. Watanuki, C. L. dos Santos, N. A. S. Rodrigues and C. Schwab, *Proc. SPIE* **4184**, 219-223 (2001).
- [124] R. Biswal, P. K. Agrawal, G. K. Mishra, S. K. Dixit and S. V. Nakhe, *J. of Russ. Laser Res.* 33(4), 319-335 (2012).
- [125] R. J. Carman, R. P. Mildren, J. A. Piper, G. D. Marshall and D. W. Coutts, *Proc. SPIE* **4184**, 215-218 (2001).
- [126] D. N. Astadjov, N. K. Vuchkov and N. V. Sabotinov, *IEEE J. Quant. Elect.* **24(9)** 1927-35 (1988).
- [127] R. Biswal, P. K. Agrawal, S. K. Dixit and S. V. Nakhe, *Opt. Engg.* **51** (11), 114203 (2012).
- [118] G. P. Hogan and C. E. Webb, *Opt. Commun.* **117**, 570-9 (1995).
- [129] B. L. Borovich, *Proc. SPIE* **2110** (G. G. Petrash ed.), 46-63 (1993).
- [130] R. P. Mildren, *IEEE J. Quant. Electron.* **36(10)**, 1145-1150 (2000).
- [131] L. Little and C. E. Little, *Proc. SPIE* **3092**, 62-67 (1997).
- [132] N. K. Vuchkov, N. V. Sabotinov and D. N. Astadjov, *Opt. Quant. Electron.* **20**, 433-8 (1988).
- [133] N. K. Vuchkov, D. N. Astadjov and N. V. Sabotinov, *Opt. Quant. Electron.* **23**, S549-53 (1991).
- [134] V. B. Vorob'ev, S. V. Kalinin, I. I. Klimovskii, ....., O. Marazov, *Sov. J. Quant. Electron.* 21(10), 1067-8 (1991).
- [135] D. N. Astadjov, K. D. Dimitrov, C. E. Little, N. V. Sabotinov and N. K. Vuchkov, *IEEE J. Quant. Electron.* **QE-30(6)**, 1358-60 (1994).
- [136] A. A. Isaev, D. R. Jones, C. E. Little, G. G. Petrash, C. G. Whyte and K. I. Zemskov, *Opt. Commun.* **132**, 302-306 (1996).
- [137] N. Huot, C. Jonin, N. Sanner, E. Baubeau, E. Audouard and P. Laporte, *Opt. Commun.* **211**, 277-282 (2002).
- [138] S.V Kireev, S. L. Shnyrev, I. G. Simanovsky and S. V. Suganeev, *Laser Phys. Lett.* **11(7)**, 075701 (2014).
- [139] E. V. Barmina, I. A. Sukhov, N. M. Lepekhin, ....., A. V. Simakin and G. A. Shafeev, *Quantum Electronics* **43(6)**, 591-596 (2013)

- [140] S. V. Lotarev, A. S. Lapat'Ev, N. V. Golubev, ..., A. Paleari and V. N. Sigaev, *Glass and Ceramics* **70**(3-4), 130-134 (2013).
- [141] M. J. Torakmany, P. Jafarkani, S. Dadras and A. Koohian, *Radiation Effects and Defects In Solids* **167**(6), 448-454 (2012).
- [142] N. A. Kirichenko, I. A. Sukhov, G. A. Shafeev and M. E. Shcherbina, *Quant. Electron.* **42**(2), 175-180 (2012).
- [143] Y. M. Mokrushin and V. A. Parfenov, *J. Opt. Techno.* **75**(7), 476-77 (2008).
- [144] B. Zhang, T. H. Zhang, Z. Huang, ...K. H. Yuan and Z. Q. Hu, *Photodiagnosis and Photodynamic Therapy* **11**(4), 491-497 (2014).
- [145] I. P. Son, K. Y. Park, B. Kim and M. N. Kim, *Annals of Dermatology* **26**(2), 156-161 (2014).
- [146] R. K. Kim, T. Lee, S. Lee, ..., H. Eun and Y. Huh, *J. Korean Phys. Soc.* **64**(5), 755-758 (2014).
- [147] K. Gao, Z. Huang, K. H. Yuan, B. Zhang and Z. Q. Hu, *British J. Dermatlogy* **168**(5), 1040-1046 (2013).
- [148] A. G. Filonov and D. V. Shiyanov, *Instru. And Expt. Techniques* **56**(3), 349-52 (2013).
- [149] B. Singh, *Rev. Scient. Instru.* **83**(12), 123101 (2012).
- [150] A. N. Soldatov, S. J. Mirza, J. P. Polunin, A. S. Shumeyko and I. C. Kostadinov, *J. Appl. Spectro.* (In press) (2015).
- [151] M. Zhand and K. Khorasani, *J. Russ. Las. Research* **35** (3), 268-272 (2014).
- [152] V. O. Nekhoroshev, V. F. Federov, G. S. Evtushenko and S. N. Torgaev, *Quant. Electron.* **42**(10), 877-879 (2012).
- [153] L. B. Direktor, M. M. Malikov, S. N. Skovorod'ko, V. A. Fomin, E. M. Shelkov and E. E. Shpil'rain, *Teplofizika Vysokikh Temperatur* **21**(1), 162-166 (1983).
- [154] S. Cavalieri, R. Pini, R. Salimbeni, U. Vanni, M. Vannini, P. Burlamachhi and L. Fini, *Laser and Particle Beams* **7**, 333-344 (1989).
- [155] G. G. Petrash, *Proc. SPIE* **2619**, 68-75 (1995).
- [156] R. Biswal, S. K. Agrawal, P. K. Agrawal, G. K. Mishra, S. K. Dixit and S. V. Nakhe, *Proc. DAE-BRNS National Laser Symposium*, CGC, Anna University, Chennai, 16-19 (2012).
- [157] P. K. Agrawal, S. V. Nakhe, R. Biswal, and J. K. Mittal, *Proc. of DAE-BRNS National Laser Symposium*, BARC, Mumbai, Jan. 13-16, art. No.: CP-01-06 (2010).
- [158] R. Biswal, *RRCAT Newsletter* **27**(2), 35-44 (2014).

- [159] A. A. Isaev and G. Y. Lemmerman, in *Proc. Lebedev Phys. Inst.* **181** (G. G. Petrsh ed.), Nova Science Publ.: Commack (1989).
- [160] R. Biswal, P. K. Agrawal, S. V. Nakhe, S. K. Dixit and J. K. Mittal, in *Laser and Bose Einstein Condensation Physics* (Man Mohan, Anil Kumar, A. B. Bhattacharjee, A. K. Razdan eds.), Narosa Publishing, New Delhi, 149-160 (2010).
- [161] R. Biswal, P. K. Agrawal, G. K. Mishra, S. V. Nakhe, S. K. Dixit and J. K. Mittal, *Proc. DAE-BRNS National Laser Symposium*, BARC, Mumbai, Jan. 13-16, art. No.: CP-01-26 (2010).
- [162] R. Biswal and P. K. Agrawal, *RRCAT Newsletter* **22(2)**, 5 (2009).
- [163] MSDS for HBr; <https://apdirect.airproducts.com/msds/DisplayPDF.aspx?docid=63386>
- [164] <https://www.osha.gov>
- [165] R. Biswal, S. K. Agrawal, P. K. Agrawal, G. K. Mishra, S. K. Dixit, and S. V. Nakhe, *Proc. DAE-BRNS National Laser Symp.*, CGC, Anna University, Chennai, Jan. 9-12, 16-19 (2012).
- [166] P. A. Bokhan and V. A. Girasimov, *Sov. J. Quant. Electron.* **9**, 273-275 (1979).
- [167] R. P. Mildren, *IEEE J. Quant. Electron.* **39(4)**, 592-599 (2003).
- [168] S. V. Nakhe, B. S. Rajanikanth and R. Bhatnagar, *Meas. Sci. Tech.* **14**, 607-613 (2003).
- [169] M. Nehmadi, Z. Kramer, Y. Ifrah and E. Miron, *J. Phys. D: Appl. Phys.* **22**, 29-34 (1989).
- [170] L. Druckmann, S. Gabay and I. Smilanski, *IEEE Power Modulator Symposium*, 213-216 (1992).
- [171] A. Ohzu, M. Kato and Y. Maruyama, *Jpn. J. Appl. Phys.* **39** (part I, No. 9A) 5118-23 (2000).
- [172] D. N. Astadjov and N. K. Vuchkov, *J. Phys. D : Appl. Phys.* **30**, 1507-14 (1997).
- [173] A. J. Seymour, C. L. Wyse, J. L. Yao, P. Jha, E. W. Olsen, M. W. Raynor and R. Torres, *ECS Transactions* **13** (8), 71-77 (2008)
- [174] P. Albert, A. Amato, A. M. Brzychcy, Y. Chen, E. Flaherty, L. Johns and W. Sanborn, *IEEE/SEMI Adv. Semicond. Manufact. Conf. and Workshop*, 86-91 (1993)
- [175] W. Braker and A. L. Mossman, *Matheson gas data book*, Matheson, East Rutherford, New Jersey (1980).
- [176] <http://www.aip.org/avsguide/refguide/vapor.html>
- [177] [http://en.wikipedia.org/wiki/Hydrogen\\_bromide](http://en.wikipedia.org/wiki/Hydrogen_bromide)
- [178] R. E. Dickerson ed., *Molecular thermodynamics*, Benjamin-Cummings Publishing Co., USA (1969).

- [179] Instruction manual, Dataquad-2, Anglo Scientific Instruments, UK
- [180] O. D. Sparkman, *Mass spectrometry desk reference*, Global View Publishers, California (2000).
- [181] O. S. Andrienko, V. A. Dimaki, G. S. Evteshenko, V. B. Sukhanov, V. O. Troitskiy and D. V. Shiyanov, *Opt. Engg.* **44**(7), 071204 (2005).
- [182] A. M. Boichenko, G. S. Evteshenko, S. I. Yakovlenko and O. V. Zhdaneev, *Laser Phys.* **14**(6), 835-846 (2004).
- [183] M. Amit, S. Lavi, G. Grez and E. Miron, *Opt. Commun.* **62**(2), 110-114 (1987).
- [184] S. K. Dixit, J. K. Mittal, B. Singh, P. Saxena, H. Vora and R. Bhatnagar, *Opt. Commun.* **88**(4-6), 397-402 (1992).
- [185] M.V.R.K. Murthy, in *Optical shop testing* (D. Malacara ed.), 123-72, John Wiley & Sons, New York (1992).
- [186] G.W. C. Kaye and T. H. Laby, *Tables of physical and chemical constants and some mathematical functions*, 14th ed., Longmans, London (1973).
- [187] M. G. Galushkin, V. S. Golubev, Y. N. Zavalov, V. E. Zavalov and V. Y. Panchenko, *Quantum Electronics* **27**(3), 217-220 (1997).
- [188] R. L. Sutherland, *Handbook of Nonlinear Optics*, Marcel Dekker, Inc. New York (2003).
- [189] A. A. Isaev, in *Pulsed Metal Vapour Lasers: Physics and Emerging Applications in Industry, Medicine and Science* (C. E. Little & N. V. Sabotinov eds.), Dordrecht: Kluwer Academic publishers, 289-301(1996).
- [190] J. Tenenbaum, I. Smilanski, S. Gabay, L. A. Levin, G. Erez and S. Lavi, *Opt. Comm.* **32**(3), 473-477 (1980).
- [191] D. C. Gerstenberger, E. L. Latush and G. J. Collins, *Opt. Comm.* **31**(1), 28-30 (1979).
- [192] N. Singh and H. S. Vora, *Opt. Comm.* **282**, 1393-1398 (2009).
- [193] W. Yube, M. Bangning, C. Li, W. Limin, P. Bailiang, *Opt. Comm.* **278**, 138-141 (2007).
- [194] W. Yongjiang, S. Shengpen, X. Tiejun, and W. Zhehua, *Appl. Phys. B* **46**, 191-195 (1988).
- [195] C. J. Chen, *Phy. Rev. A* **18**(5), 2192-2195 (1978).
- [196] N. M. Nerheim, *J. Appl. Phys.* **48**(8), 3244-3250 (1977).
- [197] E. U. Condon and G. H. Shortley, *The Theory of Atomic Spectra*, Cambridge University press (1935).
- [198] I. I. Sobelman, *Introduction to the theory of atomic spectra*, Pergaman Press, Oxford (1981).

- [199] W. C. Martin and W. L. Wiese, *Atomic Spectroscopy*, <http://www.nist.gov/pml/pubs/atspec/index.cfm> (2013).
- [200] A. A. Isaev, in *Metal vapor and metal halide vapor lasers* (G. G. Petrash ed.), Nova Science, 49-74 (1989).
- [201] P. W. Milonni and J. H. Eberly, *Laser Physics*, John Wiley & Sons (2010).
- [202] J. J. Olivero and R. L. Longbothum, *J. Quant. Spectro. Radiat. Transfer* **17**, 233-236 (1977).
- [203] WS-7 manual, <http://www.highfinesse.com/en/wavelengthmeter/ws7.php>
- [204] C. Reiser and P. Esherick, *Opt. Lett.* **13** (11), 981-983 (1988)
- [205] O. Prakash, R. Mahakud, P. Saxena, V.K. Dubey, S.K. Dixit and J.K. Mittal, *Opt. Commun.* **283**, 5099-5106 (2010).
- [206] "Atomic radii of the elements", <http://en.wikipedia.org> (2013).
- [207] O. Prakash, R. Mahakud, S. V. Nakhe and S. K. Dixit, *Opt. and Laser. Techno.* **50**, 43-50 (2013).
- [208] D. W. Coutts, A. C. J. Glover, E. K. Illy, D. J. W. Brown, J. A. Piper, in *Pulsed Metal Vapour Lasers: Physics and Emerging Applications in Industry, Medicine and Science* (C. E. Little & N. V. Sabotinov eds.), Dordrecht: Kluwer Academic publishers, 365-376 (1996).
- [209] R. Mahakud, J. Kumar, O. Prakash, H. S. Vora, S. V. Nakhe, S. K. Dixit, *Opt. & Laser Tech.* **44** (2), 412-420 (2012).
- [210] H. S. Vora and N. Singh, *Opt. Commun.* **282**(21), 4259-4265 (2009).
- [211] P. G. Foster, P. E. Davis, D. McCoy, J. Munch, *IEEE J. Quant. Electron.* **37**(12), 1531-1536 (2001).
- [212] D. W. Coutts, M. D. Ainsworth and J. A. Piper, *Opt. Commun.* **87**(5,6), 245-8 (1992).
- [213] D. W. Coutts, D. J. W. Brown and J. A. Piper, *Appl. Opt.* **32**(12), 2058-61(1993).
- [214] D. W. Coutts, *IEEE J. Quant. Electron.* **QE-34**(2), 330-42 (1995).
- [215] S. K. Dixit, B. Singh, J. K. Mittal, R. Choube and R. Bhatnagar, *Opt. Engg.* **33**, 1908-1920 (1994).
- [216] J. J. Chang, *Appl. Opt.* **33**(12), 2255-65 (1994).
- [217] W. F. Krupke and W. R. Sooy, *IEEE J. Quant. Electron.* **5**, 525 (1969).
- [218] Y. A. Anan'ev, *Resonator and Beam Divergence Problems*, 203, Adam Hilger, Bristol, Philadelphia (1992).
- [219] A. E. Siegman, *Lasers*, Oxford university press (1986).
- [220] O. Prakash, S. K. Dixit and R. Bhatnagar, *IEEE J. Quant. Electron.* **38**, 603-613 (2002).

- [221] A. A. Isaev, G.Y. Lemmerman and G. L. Malafeeva, *Soviet J. Quant. Electron* **10(8)**, 983-6 (1980).
- [222] W. Molander, M. Norton and J. Chang, *CLEO '91, Tech. Dig.*, OSA, Washington DC, 818-19 (1991).
- [223] D. W. Coutts and J. A. Piper, *IEEE J. Quant. Electron.* **QE-28(8)**, 1761-64 (1992).
- [224] J. A. Piper, in *Pulsed Metal Vapour Lasers: Physics and Emerging Applications in Industry, Medicine and Science* (C. E. Little & N. V. Sabotinov eds.), Dordrecht: Kluwer Academic publishers, 277-288 (1996).
- [225] W. Molander, *CLEO '94, Tech. Dig.*, OSA, Washington DC, 363 (1994).
- [226] M. J. Withford and D. J. W. Brown, *IEEE Sel. Topics in Quant. Electron.* **1(3)**, 779-83 (1995).
- [227] D. W. Coutts, *IEEE J. Quant. Electron* **QE-31(12)**, 2208-14 (1995).
- [228] T. Omatsu, K. Kuroda, T. Shimura, M. Chihara, M. Itoh and I. Ogura, *Opt. Commun.* **79(1 & 2)**, 125-130 (1990).
- [229] D. J. W. Brown and M. J. Withford, *Opt. Lett.* **26(23)** 1885-1887 (2001).
- [230] V. M. Batenin, V. T. Karpukhin and M. M. Malikov, *Quant. Electron.* **35(9)**, 844-848 (2005).
- [231] R. I. Trickett, M. J. Withford and D. J. W. Brown, *Opt. Lett.* **23(3)**, 189-191 (1998).
- [232] A. A. Isaev, D. R. Jones, C. E. Little, G. G. Petrash, C. G. Whyte and K. I. Zemskov, *Opt. Commun.* **132**, 302-306 (1996).
- [233] N. Huot, C. Jonin, N. Sanner, E. Baubeau, E. Audouard and P. Laporte, *Opt. Commun.* **211**, 277-282 (2002).
- [234] O. Prakash, S. K. Dixit and R. Bhatnagar, *Appl. Optics* **44(9)**, 1719-1725 (2005).
- [235] R. W. Boyd, *Nonlinear Optics* (3rd ed.), Academic Press, San Diego, CA (2009).
- [236] V. G. Dmitriev, G. G. Gurzadyan and D. N. Nikogosyan, *Handbook of nonlinear optical crystals*, Springer, Berlin (1997).
- [237] D. Hon, in *Laser Handbook* (3rd ed., M. L. Stitch ed.), North Holland Publishing Co., Amsterdam, 421-484 (1979).
- [238] D. W. Coutts, M. D. Ainsworth and J. A. Piper, *IEEE J. Quant. Electron.* **QE-26(9)**, 1555-8 (1990).
- [239] D. W. Coutts and D. J. W. Brown, *IEEE J. of Selected topics in Quant. Electron.* **1(3)**, 768-778 (1995).
- [240] Y. P. Polunin and V. O. Troitskii, *Sov. J. Quant. Electron.* **17(11)**, 1433-34 (1987).

- [241] V. T. Kapurkhin, Y. B. Konev and M. M. Malikov, *Sov. J. Quant. Electron.* **28**, 788 (1988).
- [242] G. Zhang, C. Jin, F. Lin, C. Chen and B. Wu, *Acta Opt. Sin.* **4**(6), 513-16 (1984).
- [243] K. Kuroda, T. Omatsu, T. Shimura, M. Chihara and I. Ogura, *Opt. Commun.* **75**(1), 42-46 (1990).
- [244] T. G. M. Freearde and G. A. Naylor, *CLEO '90, Tech. Dig.*, OSA, Washington DC, 436 (1990).
- [245] R. Pini, R. Salimbeni, G. Toci and M. Vannini, *Appl. Opt.* **31**(15), 2747-51 (1992).
- [246] R.I. Trickett, M. J. Withford and D. J. W. Brown, *IQEC'96 Tech. Dig.*, OSA, Washington DC, 259 (1996).
- [247] E. K. Illy, D. J. W. Brown, M. J. Withford and J. A. Piper, *IEEE J. Sel. Top. Quantum Electron.* **5**, 1543 (1999).
- [248] Y. G. Gradoboev, Y. V. Gulyaev, M. A. Kazaryan, S. V. Kruzhalov, N. A. Lyabin, M. Morkusin and O. V. Shakin, *Quant. Electron.* **34**(12), 1133-7 (2004).
- [249] T. S. Petrov, V. V. Sabotinov, S. T. Trendafilov, L. Fucheng and Z. Guiyan, *J. Phys. D: Appl. Phys.* **25**, 1169-1171 (1992).
- [250] M. Takahashi, A. Osada, A. Dergachev, P. F. Moulton, M. Cadatal-Raduban, T. Shimizu and N. Sarukura, *Jpn. J. Appl. Phys.* **49**, 080211 (2010).
- [251] O. Prakash, R. Mahakud and S. K. Dixit, *Opt. Engg.* **50**(11), 114201 (2011).
- [252] A. P. Sukhorukov, in *Proc. Int. Conf. and School on Lasers and Applications: Part 1* (I. Ursu and A. M. Prokhorov eds.) CIP Press, Bucharest, Romania, 243-266 (1983).
- [253] D. Eimerl, L. Davis, and S. Velsko, *J. Appl. Phys.* **62**(5), 1968-1983 (1987).
- [254] Technical leaflet of BBO, [http://www.castech.com/products\\_detail](http://www.castech.com/products_detail)
- [255] R. Biswal, P. K. Agrawal, S. K. Dixit and S. V. Nakhe, *Applied Optics*, (2015) (In press: Article No. 247026, posted online 15th October, 2015)